Deterministic and probabilistic analyses of supported excavations

Tingting Zhang

THÈSE

Pour obtenir le grade de

DOCTEUR DE L'UNIVERSITÉ GRENOBLE ALPES

École doctorale : I-MEP2 - Ingénierie - Matériaux, Mécanique, Environnement, Energétique, Procédés, Production
Spécialité : 2MGE - Matériaux, Mécanique, Génie civil, Electrochimie
Unité de recherche : Laboratoire Sols, Solides, Structures et Risques

Analyses déterministes et probabilistes de parois de soutènement

Deterministic and probabilistic analyses of supported excavations

Présentée par :

Tingting ZHANG

Direction de thèse :

Daniel DIAS PROFESSEUR DES UNIVERSITES, Université Grenoble Alpes	Directeur de thèse
Julien BAROTH MAITRE DE CONFERENCES HDR, Université Grenoble Alpes	Co-encadrant de thèse

Rapporteurs :

Sidi Mohammed ELACHACHI
PROFESSEUR DES UNIVERSITES, Université de Bordeaux
Richard GIOT
PROFESSEUR DES UNIVERSITES, Université de Poitiers

Thèse soutenue publiquement le **5 juin 2023**, devant le jury composé de :

Sidi Mohammed ELACHACHI PROFESSEUR DES UNIVERSITES, Université de Bordeaux	Rapporteur
Richard GIOT PROFESSEUR DES UNIVERSITES, Université de Poitiers	Rapporteur
Zhibin SUN ASSOCIATE PROFESSOR, Hefei University of Technology	Examinateur
Yann MALECOT PROFESSEUR DES UNIVERSITES, Université Grenoble Alpes	Examinateur
Farimah MASROURI (**Président de jury**) PROFESSEUR DES UNIVERSITES, Université de Lorraine	Présidente
Eric ANTOINET INGENIEUR DOCTEUR, Antea Group	Examinateur
Daniel DIAS PROFESSEUR DES UNIVERSITES, Université Grenoble Alpes	Directeur de thèse

Invités :

Julien BAROTH
MAITRE DE CONFERENCES, Université Grenoble Alpes

Deterministic and probabilistic analyses of supported excavations

submitted by

Tingting ZHANG

Grenoble, June 2023

Abstract

Supported excavations are mainly concerned with base instability, horizontal wall displacements and ground deformations in geotechnical design. Their stability assessment is essential to prevent damages to adjacent infrastructures and people's lives. Uncertainties in soil properties are also widely encountered in the field of geotechnical engineering and it is necessary to implement a probabilistic analysis to provide more rational and supplementary results.

This work attempts to assess the excavations stability in deterministic and probabilistic frameworks. Two kinds of supported excavations, including rectangular- and circular-shaped cross-sections, are considered. For the deterministic part, several models based on the upper bound limit analysis and numerical simulations are proposed to evaluate the supported excavations stability under (un)drained conditions. For the probabilistic part, the random variable and random field approaches are used to model parameter uncertainties. A comprehensive and efficient analysis framework based on the surrogate models is then proposed, which allows to accurately estimate the excavation failure probability and statistical moments within a significantly reduced computational time. Polynomial Chaos Kriging and Sparse Polynomial Chaos Expansions are mainly used for the surrogate model construction. Besides, a versatile and flexible sample-wised probabilistic method based on the Artificial Neural Network is developed to further improve the probabilistic assessments efficiency. In addition, some issues that are still unknown or unclear in the field of the supported excavations stability analysis, are discussed, mainly including: the soil-wall interface and its uncertainties on the excavations stability; the stability analysis of a real great-depth (32 m) excavation case; the soil non-homogeneity and hydraulic effects on the circular shafts stability; the anisotropy of the hydraulic permeability coefficient on the circular shafts stability and a global sensitivity analysis for the parameter importance determination.

This work presents a good supplement to the existing studies on the stability assessment of supported excavations. It allows to better understand and design practical geotechnical problems.

Keywords: Supported excavations; Basal heave stability; Horizontal wall deflection; Reliability analysis; Sensitivity analysis; Polynomial Chaos Kriging; Artificial Neural Network

Résumé

L'excavation soutenue est principalement concernée par l'instabilité de la base, les déplacements horizontaux des parois et les déformations du sol dans la conception géotechnique. L'évaluation de la stabilité correspondante est essentielle pour prévenir les dommages aux infrastructures adjacentes et à la vie des personnes. Les incertitudes dans les propriétés du sol sont également largement rencontrées dans le domaine de l'ingénierie géotechnique et il est nécessaire de mettre en œuvre une analyse probabiliste pour fournir des résultats plus rationnels et complémentaires.

Ce travail tente d'évaluer la stabilité des excavations dans des cadres déterministes et probabilistes. Deux types d'excavations soutenues, comprenant des sections rectangulaires et circulaires, sont considérés. Pour la partie déterministe, plusieurs modèles basés sur l'analyse de la limite supérieure et des simulations numériques sont proposés pour évaluer la stabilité des excavations soutenues dans des conditions (non)drainées. Pour la partie probabiliste, les approches de variables aléatoires et de champs aléatoires sont utilisées pour modéliser les incertitudes des paramètres. Un cadre d'analyse complet et efficace basé sur les modèles de substitution est ensuite proposé, ce qui permet d'estimer avec précision la probabilité de défaillance de l'excavation et les moments statistiques dans un temps de calcul considérablement réduit. Le krigeage du chaos polynomial et les expansions du chaos polynomial éparses sont principalement utilisés pour la construction du modèle de substitution. En outre, une méthode probabiliste polyvalente et flexible basée sur le réseau neuronal artificiel est développée pour améliorer l'efficacité des évaluations probabilistes. En outre, certaines questions encore inconnues ou peu claires dans le domaine de l'analyse de la stabilité des excavations soutenues sont discutées, notamment: l'interface sol-paroi et ses incertitudes sur la stabilité des excavations; l'analyse de la stabilité d'un cas réel d'excavation à grande profondeur (32 m); la non-homogénéité du sol et les effets hydrauliques sur la stabilité des puits circulaires; l'anisotropie du coefficient de perméabilité hydraulique sur la stabilité des puits circulaires; l'analyse de sensibilité globale pour la détermination de l'importance des paramètres.

Ce travail peut constituer un bon complément aux études existantes sur l'évaluation de la stabilité des excavations soutenues. Les résultats obtenus devraient permettre de mieux résoudre les problèmes géotechniques pratiques.

Mots clés: Excavations soutenues; Stabilité du soulèvement de la base; Déviation horizontale de la paroi; Analyse de fiabilité; Analyse de sensibilité; Krigeage du Chaos Polynomial; Réseau de Neurones Artificiels

Acknowledgements

First, I would like to extend my sincere gratitude to my supervisor, Prof. Daniel DIAS. We met in 2017 when I was in my master, and his extensive knowledge and kindness impressed me a lot. I did not hesitate to apply to be his PhD candidate and thank him to give me this chance to work and study in deterministic and probabilistic analysis of supported excavations. Over the past 3 years, his constructive advice, patient guidance and optimistic mindset help me to make progress and contributions to my doctoral subjects. His suggestions on outdoor activities (hiking, skiing, and running routes, etc.) also helped me to have a pleasant life in Grenoble.

I am also extremely grateful to my co-supervisor, Assoc. Prof. Julien BAROTH. His professional advice on probabilistic analysis, efficient help when I have a problem, and kind encouragements help me to finish my PhD subjects. I am also deeply impressed by his professionalism and serious attitude toward research, which also influence my research and career life. He also helps me a lot in life, a birthday gift let me really touched, and he finds financial support for me when my scholarship is stopped. Many thanks to him and it is my great honor to work with him.

I would also like to thank my CSI committee formed by Professors Frédéric DUFOUR, Mbarka SELMI and Robert PEYROUX, who each year provide useful comments on the progress of my work and take an interest in the problems in my life and research. Besides, I am grateful to the 3SR lab for providing me with a comfortable working environment and a platform to interact with people from all over the world.

I shall extend my thanks to my colleagues, Dr. Xiangfeng GUO, Dr. Chunjing MA, Ms. Jiamin ZHANG, Ms. Lu An, Mr. Chuanqi LI and Dr. Khadija Nejjar. Through the collaboration with them, my knowledge and insights on my subjects are also improved.

The financial support: China Scholarship Council (CSC No. 201906690049) and INPG Entreprise S.A. are greatly appreciated.

Finally, I would like to thank my family for their unconditional love and encouragement. I am so lucky to have super amazing parents, older sister, and younger brother, who always support me to pursue my desired life.

Contents

Abstract 2

Résumé 3

Acknowledgements 4

Contents 5

List of Tables 9

List of Figures 11

List of symbols 16

Acronyms 16

Notations: Supported excavation 18

Notations: Probabilistic analysis 20

General introduction 21

Background and motivation 21

Objectives and outline of the thesis 25

Publications and communications 27

Chapter 1 29

1.1 Introduction 30

1.2 Deterministic analysis of supported excavations 30

1.2.1 Rectangular-shaped excavations 30

1.2.2 Circular shafts 44

1.2.3 Basal instability due to an hydraulic uplift 46

1.2.4 Soil-wall interaction 48

1.3 Probabilistic analysis of supported excavations 50

1.3.1 Reliability theory 50

1.3.2 Characterization of the soil variability 52

1.3.3 Reliability analysis methods 53

1.3.4 Sensitivity analysis methods 58

1.3.5 Previous studies about probabilistic analysis of supported excavations 60

1.4 Machine learning-based excavation analyses 68

1.5 Conclusion 72
Chapter 2 73
2.1 Introduction 74
2.2 Development of limit analysis model 74
2.2.1 Improved limit analysis 74
2.2.2 Deterministic model comparison 78
2.3 Proposed probabilistic analysis framework 84
2.3.1 Polynomial Chaos Kriging 84
2.3.2 Probabilistic analysis framework 86
2.3.3 Comparison and discussion of the probabilistic results 88
2.4 Parametric study 91
2.5 Conclusion 93
Chapter 3 95
3.1 Introduction 96
3.2 Presentation of the FIVC excavation 97
3.3 Deterministic analysis 99
3.3.1 Finite Element Modelling 99
3.3.2 Comparison and discussion 101
3.4 Probabilistic analysis 105
3.4.1 Definition of the limit state function and statistical parameters 105
3.4.2 Probabilistic results 106
3.4.3 Probabilistic distributions of the wall deflection and ground surface settlement 112
3.4.4 Relation between the maximum wall deflection and ground surface settlement 119
3.4.5 Probabilistic serviceability assessment 121
3.4.6 Soil-wall interaction effects 123
3.5 Conclusion 124
Chapter 4 126
4.1 Introduction 127
4.2 Problem statement 127
4.2.1 Circular shaft 127

4.2.2 Uncertainty consideration 130
4.3 Model of non-homogeneity and comparison 130
4.3.1 Deterministic computational model 130
4.3.2 Deterministic FELA model verification 132
4.4 Probabilistic discussions 134
4.4.1 Probabilistic results of the reference case 135
4.4.2 Importance of the uncertainty consideration 136
4.4.3 Influence of the soil-wall adhesion 138
4.4.4 Influence of the soil non-homogeneity 140
4.5 Conclusion 142
Chapter 5 144
5.1 Introduction 145
5.2 Problem statement 145
5.2.1 Circular shaft against an hydraulic uplift 145
5.2.2 Uncertainty consideration 147
5.3 Deterministic analysis 148
5.3.1 Numerical model construction 148
5.3.2 Influence of the permeability anisotropy 149
5.3.3 Influence of soil-wall interaction 153
5.4 Probabilistic analysis 155
5.4.1 Probabilistic results for the reference case 155
5.4.2 Influence of permeability anisotropy 158
5.4.3 Influence of soil-wall interaction 161
5.5 Conclusion 162
Chapter 6 164
6.1 Introduction 165
6.2 Random finite element analysis 165
6.2.1 Random field generation 165
6.2.2 *b*SPCE method 167
6.2.3 Procedure 168
6.3 Results and discussions 170

6.3.1 Results and comparison 170
6.3.2 Probabilistic distributions of the wall deflection with consideration of the soil spatial variability 173
6.3.3 Probabilistic serviceability assessment 176
6.3.4 Influence of the autocorrelation lengths 177
6.4 Conclusion 177
Chapter 7 180
7.1 Introduction 181
7.2 Proposed hybrid SPAA approach 181
7.2.1 ASO-ANN method 181
7.2.2 Data preparation 185
7.2.3 SPAA procedure 186
7.3 Example and application 189
7.3.1 Case 1: drained circular shaft stability against hydraulic uplift 189
7.3.2 Case 2: undrained circular shaft stability in non-homogeneous soils 194
7.3.3 Case 3: circular shaft stability considering soil spatial variability 198
7.4 Discussion 200
7.4.1 Accuracy and efficiency survey 200
7.4.2 Initial samples determination 202
7.5 Conclusion 202
Chapter 8 202
8.1 Conclusions and recommendations 204
8.2 Limitations and perspectives 208
Bibliography 210

List of Tables

Table 1.1 Summary of numerical analysis of rectangular-shaped excavations. 39

Table 1.2 Commonly-used univariate probability distributions (Marelli and Sudret, 2014)..... 51

Table 1.3 Summary of previous probabilistic basal heave stability analysis. 60

Table 1.4 Summary of probabilistic basal heave analyses considering spatial variability. 64

Table 1.5 Summary of probabilistic serviceability assessment considering spatial variability. 66

Table 1.6 Application of the machine learning methods on the supported excavations. . 68

Table 2.1 Statistical properties of input random variables. 89

Table 2.2 Comparison of probabilistic results. 90

Table 3.1 Excavation stages. 99

Table 3.2 Soil parameters of each layer (Nejjar and Dias, 2019). 100

Table 3.3 Properties of the structural support elements (Nejjar and Dias, 2019). 100

Table 3.4 Statistical properties of input random variables. 106

Table 3.5 Four cases for probabilistic analysis. 112

Table 4.1 Summary of soil, wall and geometric input parameters of the reference case. 129

Table 4.2 Statistical properties of input random variables. 130

Table 4.3 Comparison of the safety factors for non-homogeneous circular shafts. 133

Table 5.1 Parameters summary of the reference case. 147

Table 5.2 Statistical properties of input random variables. 147

Table 5.3 Results for the reference case. 156

Table 5.4 Design points for the reference case. 156

Table 6.1 Probabilistic analysis with consideration of the spatial variability. 178

Table 7.1 Probabilistic analysis iterative results of case 1. 190

Table 7.2 Failure probability comparison of case 1. 194

Table 7.3 Probabilistic analysis iterative results of case 2. 195

Table 7.4 Failure probability comparison of case 2. 196

Table 7.5 Probabilistic analysis iterative results of case 3. 199

Table 7.6 Failure probability comparison of case 3. 200
Table 7.7 Parameters of ASO-ANN model. 201

List of Figures

Fig. 1.1 Typical deformation profiles for excavations (Clough and O'Rourke, 1990). ... 31

Fig. 1.2 Proposed settlement diagrams behind the wall. ... 32

Fig. 1.3 Comparison of actual and predicted wall movements. ... 33

Fig. 1.4 Relationship between the lateral deformation with the system stiffness and ... 33

Fig. 1.5 Schematic diagram of experimental setup within-flight excavator (Lam et al., 2014) ... 35

Fig. 1.6 Incremental displacements in braced excavations (O'Rourke, 1993) ... 36

Fig. 1.7 Terzaghi models. ... 41

Fig. 1.8 Bjerrum & Eide method model (BE). ... 42

Fig. 1.9 Slip circle method model (SC). ... 43

Fig. 1.10 Limit analysis failure mechanism. ... 44

Fig. 1.11 Circualr shaft construction. ... 45

Fig. 1.12 Centrifuge model package for the excavation basal heave stability ... 47

Fig. 1.13 Schematic illustration of the safe/failure region and LSS (Wang et al., 2021). 51

Fig. 1.14 Comparison of RV and RF generation. ... 52

Fig. 1.15 Approximation of the LSS by FORM (Wang et al., 2021). ... 53

Fig. 1.16 Generated samples from MCS and SS (*R*-*S* problem) (Guo, 2020). ... 56

Fig. 1.17 Influence of threshold values (Zhang et al., 2015b). ... 62

Fig. 1.18 System probability of serviceability failure contour at various combinations of limiting wall deflection and limiting ground surface settlement (Luo and Das, 2015) ... 63

Fig. 1.19 RF realizations of Normalized undrained shear strength for different scales of fluctuation (Luo et al., 2012b). ... 64

Fig. 1.20 Spatial variability effects on the variability of excavation responses (Dang et al., 2014). ... 66

Fig. 1.21 The procedure presented in (Lü et al., 2012). ... 71

Fig. 2.1 Limit analysis failure mechanism. ... 75

Fig. 2.2 Flowchart of the safety factor optimization. ... 78

Fig. 2.3 A FELA model for D=5 m, H=10 m, B=20 m, S_u=40 kPa, and r_i=1. ... 79

Fig. 2.4 Safety factors comparison for different values of H/B with B=20 m, D=5 m. ... 80

Fig. 2.5 Safety factors comparison for different values of H/B with H=20 m, D=5 m.... 81

Fig. 2.6 Safety factors comparison for different values of D with H=20 m..... 82

Fig. 2.7 Safety factors comparison for different values of r_i with H=20 m and S_u=40 kPa. 83

Fig. 2.8 Optimal PCK metamodel construction. 86

Fig. 2.9 Flowchart of the proposed metamodel-based stochastic analysis procedure PCK-PA. 88

Fig. 2.10 PCK metamodel construction process with the enrichment samples increase. 89

Fig. 2.11 PDFs of safety factor obtained by the PCK-based MCS and the direct MCS.. 90

Fig. 2.12 Effect of the COV_{Su} on the failure probability. 91

Fig. 2.13 Effect of the soil-wall adhesion coefficient on the failure probability. 92

Fig. 2.14 Effect of the embedment depth D on the failure probability. 93

Fig. 3.1 Location and aerial photo of the FIVC excavation. 96

Fig. 3.2 Top view and supporting system of the FIVC excavation. 98

Fig. 3.3 Section D layout. 98

Fig. 3.4 FEM model of the FIVC excavation. 99

Fig. 3.5 Comparison between measured and predicted excavation responses. 102

Fig. 3.6 Relationships between the excavation depth and maximum horizontal wall deflection, and maximum ground surface settlement. 104

Fig. 3.7 Locations of maximum wall deflection and maximum ground surface settlement 105

Fig. 3.8 PCK metamodel construction process with the enrichment samples increase. 107

Fig. 3.9 Maximum horizontal wall deflection comparison using FEM and PCK methods. 107

Fig. 3.10 PDF and CDF of maximum wall deflections of PCK-MCS. 108

Fig. 3.11 Sensitivity analysis results of PCK-GSA. 108

Fig. 3.12 Influences of layers MM and PC friction angles on the plastic zone distributions. 109

Fig. 3.13 Influences of MM and PC friction angles on the wall bending moment 111

Fig. 3.14 Mean values of the maximum wall deflection and maximum ground surface settlement 113

Fig. 3.15 Numerical convergence of mean values of maximum wall horizontal deflection 114

Fig. 3.16 Wall deflection contours using deterministic and probabilistic analyses. 115

Fig. 3.17 Ground surface settlement contours using deterministic and probabilistic analyses. 116

Fig. 3.18 PDF and CDF of maximum wall deflections and ground surface settlements. 116

Fig. 3.19 Frequency of the maximum horizontal wall deflection location. 117

Fig. 3.20 Frequency of the maximum ground surface settlement location. 118

Fig. 3.21 Relationship between the maximum wall deflection and maximum ground surface settlement under different cases. 121

Fig. 3.22 Effect of parameters uncertainties on the probability of exceeding specified 122

Fig. 3.23 Effect of parameters uncertainties on the sensitivity indices. 123

Fig. 3.24 Effects of the soil-wall interface on failure probability. 124

Fig. 4.1 Introduction of the supported circular shaft of the geometry and evolution of the undrained shear strength with depth. 128

Fig. 4.2 FELA model of the reference circular shaft with adaptive mesh refinement. .. 131

Fig. 4.3 Comparison of the safety factors (left vertical axis, black curves) and computational time (right vertical axis, blue curves) considering the cases with and without adaptive mesh refinement. 132

Fig. 4.4 Comparison of the safety factors for homogeneous circular shafts. 133

Fig. 4.5 Comparison of the safety factors for different values of soil-wall adhesion factor *m*. 134

Fig. 4.6 PDF and CDF of the obtained safety factor F_s. 135

Fig. 4.7 Sensitivity analysis results: undrained shear strength at the ground surface S_{u0}, strength gradient k, unit weight γ and soil-wall adhesion factor r_i. 136

Fig. 4.8 Comparison of the safety factors estimated by FELA and PCK metamodel. ... 136

Fig. 4.9 Coefficient of variation of (a) S_u (b) r_i (c) k (d) γ effects on the failure probability 137

Fig. 4.10 Soil-wall adhesion factor effects under different undrained shear strengths. . 138

Fig. 4.11 Sensitivity analysis for different soil-wall adhesion coefficients. 139

Fig. 4.12 Soil-wall adhesion factor effects under different embedment depths. 140

Fig. 4.13 Sensitivity indices under different embedment depths. 140

Fig. 4.14 Soil non-homogeneity effects under different undrained shear strengths. 141

Fig. 4.15 Sensitivity analysis for different non-homogeneity coefficients. 142

Fig. 5.1 Cross-section of the circular shaft. 146

Fig. 5.2 Deterministic FELA model with adaptive mesh refinement. 149
Fig. 5.3 Effects of r_k and r_t on F_s. 149
Fig. 5.4 Flow vectors for different r_k values. 150
Fig. 5.5 Water pressure distributions for different r_k values. 151
Fig. 5.6 Water head distributions for different r_k values. 152
Fig. 5.7 Effects of r_i and r_t on F_s. 153
Fig. 5.8 Effects of r_i and r_k on F_s. 154
Fig. 5.9 Shear dissipation distribution for different r_k values (r_i =1). 154
Fig. 5.10 Comparison between average and 15-node Gauss solutions. 156
Fig. 5.11 PDF and CDF of F_s. 157
Fig. 5.12 Sensitivity analysis results based on the FORM and GSA. 157
Fig. 5.13 F_s comparison obtained by FELA and PCK models. 158
Fig. 5.14 Effects of r_k and r_t on probabilistic analysis results. 159
Fig. 5.15 Effects of COV_{rk} on probabilistic analysis results. 160
Fig. 5.16 PDF of r_k for different cases. 160
Fig. 5.17 Effects of r_i and r_t on probabilistic analysis results. 161
Fig. 5.18 Effects of r_i and r_k on P_f. 162
Fig. 6.1 Flowchart of the probabilistic analysis with consideration of the spatial variability 170
Fig. 6.2 FEM model of the FIVC excavation considering the spatial variability 171
Fig. 6.3 PDF and CDF of δ_{hm} 172
Fig. 6.4 δ_{hm} comparison obtained by FEM and SPCE models. 173
Fig. 6.5 Wall deflection contours with consideration of the spatial variability. 174
Fig. 6.6 Frequency of the maximum horizontal wall deflection location. 175
Fig. 6.7 Effect of autocorrelation lengths on the probability of exceeding specified limiting wall deflection 177
Fig. 6.8 PDFs for different autocorrelation lengths 178
Fig. 7.1 The architecture of artificial neural networks. 182
Fig. 7.2 Atomic motion theory model. 183
Fig. 7.3 Comparison of samples generated by the LHS and uniform methods. 186
Fig. 7.4 Flowchart of the proposed SPAA. 188

Fig. 7.5 Pearson correlation coefficients between the influential factors (r_k: permeability anisotropy coefficient, c: the soil cohesion, φ: friction angle, r_i: the soil-wall interface coefficient). 191

Fig. 7.6 Comparison of the predictions and numerical simulations for case 1. 191

Fig. 7.7 Predictions error distribution of case 1. 192

Fig. 7.8 PDF, CDF and statistical moments of F_s comparison of case 1..... 193

Fig. 7.9 Sensitivity indices comparison of case 1. 193

Fig. 7.10 Comparison of the predictions and numerical simulations for case 2. 195

Fig. 7.11 Predictions error distribution of case 2. 196

Fig. 7.12 PDF, CDF and statistical moments of F_s comparison of case 2..... 197

Fig. 7.13 Sensitivity indices comparison of case 2. 197

Fig. 7.14 One realization of the random field for cohesion. 198

Fig. 7.15 Validation of the SPAA model for high-dimensional case..... 199

Fig. 7.16 PDF, CDF and statistical moments of F_s comparison of case 3..... 200

Fig. 7.17 Comparison of deterministic simulations number and P_f of 3 cases. 201

List of symbols

Acronyms

ANN	Artificial Neural Network
ASO	Atom Search Optimization
BE	Bjerrum & Eide method
BF	Backfill
b(S)PCE	Bootstrap (Sparse) Polynomial Chaos Expansions
CDF	Cumulative Distribution Function
CK	Chalk
COV	Coefficient of Variation
DA	Deterministic Analysis
DP	Design Point
ED	Experimental Design
FBR	Fraction of Bootstrap Replicates
FIVC	Fort d'Issy-Vanves-Clamart
FELA	Finite Element Limit Analysis
FEM	Finite Element Method
FORM	First Order Reliability Method
GSA	Global Sensitivity Analysis
HL	Hard Limestone
HS	Hardening Soil model
IS	Importance Sampling
K-L expansion	Karhunen-Loève expansion
LA	Limit Analysis
LAR	Least Angle Regression
LB	Lower Bound
LEM	Limit Equilibrium Method
LHS	Latin Hypercube Sampling
LOO	Leave-One-Out error
LSS	Limit State Surface
MCS	Monte-Carlo Simulation

MBE	Modified Bjerrum & Eide method
MLP	Multilayer Perceptron
MM	Meudon Marls
MT	Modified Terzaghi Method
OCR	Over Consolidation Ratio
PA	Probabilistic Analysis
PC	Ypresian Plastic Clay
PDF	Probability Density Function
PCK	Polynomial Chaos Kriging
RF	Random Field
RV	Random Variable
SC	Slip Circle Method
SLS	Serviceability Limit State
SOCP	Second-Order Conic Programming
SPAA	Sample-wised Probabilistic Approach based on the ANN
SS	Subset Simulation
Std.	Standard deviation
UB	Upper Bound
ULS	Ultimate Limit State

Notations: Supported excavation

B	Excavation Width
B_1	Distance from the wall to the vertical failure surface *fi*
c	Cohesion
D	Wall embedment depth
E	Energy dissipation
E_u	Young's modulus
E_{50}^{ref}	Secant stiffness
E_{oed}^{ref}	Tangent oedometer stiffness
E_{ur}^{ref}	Unloading/reloading stiffness
F_s	Safety factor
f_t	soil tensile strength
H	Excavation Depth
h_w_1	Groundwater level below the ground surface
h_w_2	Groundwater level inside the excavation
k	Undrained shear strength increase gradient
k_0	Initial earth pressure coefficient at rest
k_x	Horizontal permeability coefficient
k_y	Vertical permeability coefficient
R_c	Circular shaft diameter
r_i	Soil wall adhesion factor
r_k	Permeability anisotropy coefficient
r_t	Tensile strength cut-off coefficient
S_u	Undrained shear strength
S_{u0}	Undrained shear strength at ground surface
T	Depth from the wall bottom tip to the hard stratum
T_c	Critical hard stratum depth from the wall bottom tip
t_w	Wall thickness
v	Velocity of plastic flow
W	External work rate
φ	Friction angle
γ	Unit weight

γ_{dry}	Unsaturated unit weight
γ_{sat}	Saturated unit weight
υ_{wall}	Poisson's ratio of wall
υ_{soil}	Poisson's ratio of soil

Notations: Probabilistic analysis

b_j	Bias of the neural network
COV_{P_f}	Coefficient of variation of P_f
Err_{LOO_tg}	Threshold values of LOO
$Err_{P_f\_tg}$	Threshold values for failure probability
F_i	Interaction forces in ASO
G_i	Constraint forces in ASO
I_k	Indicator function in MCS
$M^{PCK}(\boldsymbol{x})$	Model output approximation using PCK
m_i	Mass of i^{th} atom in ASO
n_{ij}	Neuron in the hidden layer
N_l	Number of samples at each level of SS
P^*	Design point
P_f	Failure probability
$P(F_1)$	Failure probability corresponding to the first level of SS
$P(F_i\|F_{i-1})$	Intermediate conditional failure probability
Si	First-order Sobol index
St	Total Sobol index of input variables
w_{ij}	Weight of the neural network
$\boldsymbol{x}$	Vector with input random variables
$Z(\boldsymbol{x})$	Zero mean, unit variance stationary Gaussian process
α_i	Unknown coefficients of polynomials
$\Phi_i(\boldsymbol{x})$	Multivariate polynomial basis
σ^2	Variance
θ	Hyper-parameter for autocorrelation function
β_{HL}	Hasofer-Lind reliability index

General introduction

Background and motivation

There is a fast-growing need for transportation with the continued urbanization over these last decades. Mass transportation systems operating on the surface may lead to traffic congestion, land shortage, noise or air pollution, particularly when the urban population exceeds one million (Cui and Nelson, 2019). Underground railway transportation is receiving much attention and plays a significant role in relieving traffic congestion. Utilizing the underground space is consequently preferred to ease problems without affecting the existing ground surface activities and can help people to reach their destinations within a reasonable time. Among the underground infrastructures, the supported excavations are necessary as they can facilitate tunnel boring machine works and can be used as ventilation systems (Faustin et al., 2018), subway stations (Celestino et al., 2009), underground car parks (Marten and Bourgeois, 2006) or emergency exits (Le et al., 2019). Rectangular- and circular-shaped cross-sections as shown in Fig. i(a) and (b) are common in practice (Chehadeh et al., 2015; Dias et al., 2015), and will be considered in this work.

(a) Rectangular (b) Circular

Fig. i Two common types of excavations

The urban environments complexity and uncertain geological conditions around the excavation can pose a threat to public safety. Once construction accidents occur, severe consequences can occur. For example, the excavation collapse accident at Xianghu station of Hangzhou metro line 1 caused 21 deaths, 24 injuries, and a direct economic loss of 49.62 million RMB (Lin et al., 2021). Safety assessments of the supported excavation stability are thus important to prevent damage to adjacent infrastructures. The geotechnical design, which takes into account the soil and rock conditions at a construction site, is often considered in the supported excavation

engineering designs (Luo et al., 2018b). It includes the Serviceability Limit State (SLS) which is related to the excavation-induced maximum lateral wall deflection and maximum ground surface settlement and the Ultimate Limit State (ULS) which corresponds to the foundation pit stability and can often be evaluated by the basal heave safety factor. The excavation is considered safe when the stability indicators (i.e. wall deflection, surface settlement, safety factor, etc.) satisfy the requirements specified in design codes or criteria (Zhou et al., 2020). Otherwise, the excavations should be strengthened. Besides, undrained and drained conditions exist in excavation construction according to the soil type and geological formation. Undrained conditions usually govern the excavation stability immediately after construction for clays and silts because the pore water in the soil does not dissipate immediately due to the low hydraulic conductivity (Faheem et al., 2003), while drained conditions are more common in coarse-grained materials. The design strength properties under drained and undrained conditions are different (drained: cohesion and friction angle; undrained: undrained shear strength) and the corresponding stability performance should be discussed.

In addition, failures may still occur even though the stability indicators are greater than the values specified in design codes (Luo et al., 2012a). This is because the geotechnical engineering variability is complex property and can result from many different sources of uncertainty as presented in Fig. ii. Among them, the inherent variability (which results from the natural geologic processes), measurement error (which is caused by limited amounts of information, equipment, operator, and random testing effects), and transformation uncertainty (during the transformation from measurements into design soil properties using empirical or other correlation models) are the main three primary sources (Phoon and Kulhawy, 1999).

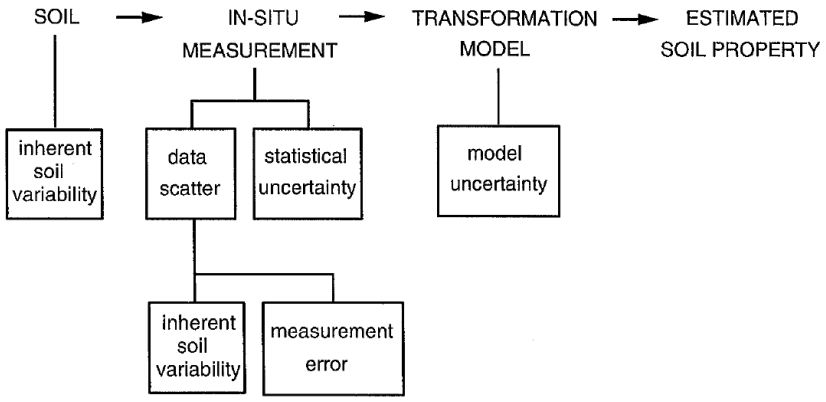

Fig. ii Uncertainty in soil property estimates (Phoon and Kulhawy, 1999)

Probabilistic analysis, which can rationally take into account these variabilities, is a more rational tool to assess excavation stability (Goh et al., 2019b). Instead of the single safety factor (or wall deflection, ground surface settlement) in deterministic analysis, a variety of supplementary results can be provided in probabilistic analysis, such as the failure probability (P_f), probability density function (PDF), cumulative distribution function (CDF), statistical moments of the system response from Monte Carlo Simulation (MCS), or the reliability index and design point obtained by the First Order Reliability Method (FORM). A sensitivity analysis can also be implemented to provide the importance information about the involved random variables. There is no doubt that having more analysis results are beneficial to the designs and constructions. For example, a high value of failure probability (or a low value of reliability index) corresponds to low-performance level as presented in Table i, which can result in more casualties and economic damages (Zhou et al., 2020). Strengthened measurements should then be performed.

Table i Target reliability indices (Kamien, 1997)

Performance level	β	P_f
High	5.0	2.87e−7
Good	4.0	3.17e−5
Above average	3.0	1.35e−3
Below average	2.5	6.21e−3
Poor	2.0	2.28e−2
Unsatisfactory	1.5	6.68e−2
Hazardous	1.0	1.59e−1

It is therefore of interest to investigate the supported excavation stability in deterministic and probabilistic frameworks. A general framework is illustrated in Fig. iii. For the deterministic analysis, the construction of supported excavation model is essential. The model response (such as the basal heave safety factor, wall deflection and ground surface settlement) can then be provided. Considering the probabilistic analysis, the considered input parameters and the corresponding uncertainties should be identified first. The input samples can be generated based on the statistical information (such as the distribution, mean value, and coefficient of variation, etc.) and then mapped to the numerical models to obtain the output values. The reliability and sensitivity analyses are implemented to give a variety of valuable results.

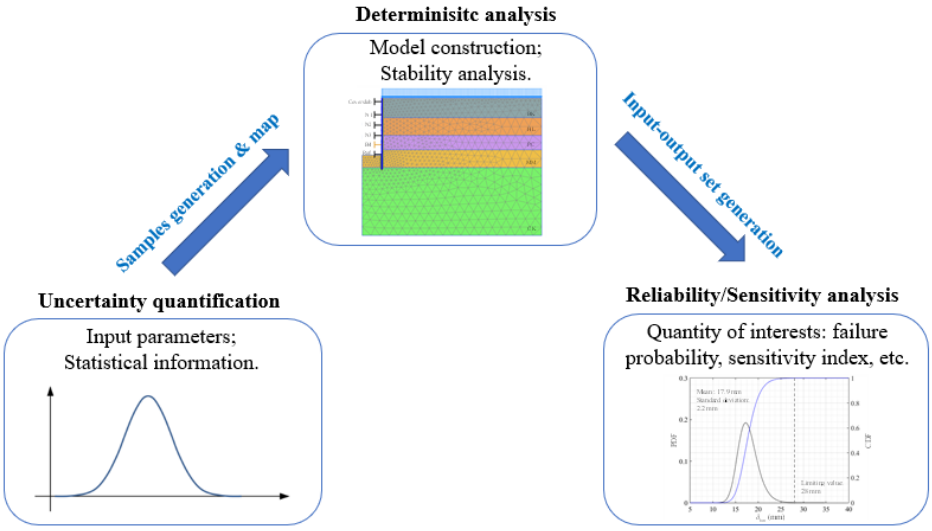

Fig. iii Framework for the deterministic and probabilistic analyses.

Several related works were done and provided a better understanding of the excavation stability assessment. However, there are still some limitations that should be addressed (more information about the literature review can be found in Chapter 1), including (1) most of the rectangular-shaped excavation studies are related to hypothetical design examples and focus on small-depth excavations from 6 m to 20 m, whereas studies on excavations at large depths (greater than 30 m) are rarely discussed; (2) there are several analytical solutions for the basal heave stability of the excavations under undrained conditions, however, they can be limited during the analysis, for instance, the Terzaghi (1943) method may give biased results for narrow excavations, the slip circle method (Tang and Kung, 2011) cannot explain the excavation width effect. Analytical methods improvements, which can be used in a wide range of applications (with consideration of the excavation depth, excavation width, wall penetration depth and soil-wall interface strength), is thus necessary; (3) the circular shafts are less discussed compared to the rectangular-shaped excavations in the literature. It is noted that circular shafts are preferred in cases of restricted space or unfavorable ground conditions due to their high structural stiffness through hoop forces, which make them inherently stiffer than rectangular cross-sections (Le et al., 2019). Circular shafts analyses are also essential; (4) for the reliability analysis, the MCS, which lacks computational efficiency, and FORM, which may fail to give accurate estimates for non-linear limit state surface cases, are commonly used. There are no studies to improve the calculation efficiency of the reliability analyses; (5) there is no Global Sensitivity Analysis (GSA) for the determination of the involved random variables contributions.

Objectives and outline of the thesis

The importance of the supported excavations safety assessment and the common limitations of the existing studies are detailed in the above section. Motivated by the mentioned points, this research work aims to evaluate efficiently the supported excavations stability in deterministic and probabilistic frameworks. For the deterministic analysis, the stability of rectangular excavations and circular shafts in undrained and drained conditions are respectively analysed by considering the great-depth effects, the destabilizing effect of the seepage forces, and of the soil non-homogeneity. For the probabilistic analysis, advanced surrogate-model techniques are adopted to obtain results in an affordable time. The main objectives of this work can be summarized as follows:

- Some issues that remain unclear for the supported excavation stability analyses are discussed. The issues addressed in this work include: **Rectangular-shaped Excavation (RE) in undrained conditions**: improvements of the analytical methods based on the limit analysis method; **RE in drained conditions**: great depth consideration based on a real supported excavation case; **Circular Shaft (CS) in undrained conditions**: non-homogeneity consideration survey; **CS in drained conditions**: investigation of the hydraulic effects and the anisotropy consideration for the permeability coefficients. Besides, as a soil-structure interaction problem, the soil-wall interface interaction effects on the supported excavations stability are also discussed,
- Present a comprehensive and efficient probabilistic analysis for the supported excavations by applying surrogate model-based probabilistic methods. Polynomial Chaos Kriging (PCK) and Sparse Polynomial Chaos Expansions (SPCE) are introduced for the metamodel construction. The Sobol-based GSA is implemented for the parameter importance determination,
- Develop a versatile and flexible sample-wised probabilistic method based on the Artificial Neural Network (ANN) to further improve the probabilistic assessments efficiency.

Based on the obtained results, some recommendations for future studies or practical engineering design on supported excavations are provided. The manuscript is organized as follows:

Chapter 1 provides a brief overview of the deterministic and probabilistic analyses of supported excavations (RE and CS). In the deterministic part, the theoretical and empirical methods, laboratory tests and field observations, and numerical modellings are given. For the probabilistic

part, the methods commonly used in geotechnical engineering are provided first, which is followed by the applications on the circular shaft stability analysis.

Chapter 2 is devoted to the stability analysis of RE under undrained conditions. An improved limit analysis mechanism is proposed first based on the existing limit analysis mechanism. A comparative study with numerical simulations and existing analytical methods is carried out to validate the effectiveness of the proposed mechanism. The Polynomial Chaos Kriging metamodel-based probabilistic analysis is then introduced to improve the efficiency of the probabilistic results estimation.

Chapter 3 discusses great depth RE in c-φ soils based on a real case of the Grand Paris Project: the Fort d'Issy-Vanves-Clamart (FIVC) excavation. The probabilistic distributions of the wall deflection and ground surface settlement are given. The correlation between the maximum wall deflection and ground surface settlement is also provided. The probabilistic serviceability assessment with different limiting criteria and the sensitivity analysis for the considered parameters are followed.

Chapter 4 explores the circular shaft stability in undrained and non-homogeneous clayey soils. The uncertainty influences of the soil undrained shear strength at the ground surface, non-homogeneity coefficient, unit weight and soil-wall adhesion factor on the circular shaft stability are discussed.

Chapter 5 gives the deterministic and probabilistic analyses of supported circular shafts in clayey soils subjected to hydraulic uplifts. The effects of the permeability anisotropy coefficient, the soil-wall interface strength coefficient and the soil tension cut-off coefficient are discussed.

Chapter 6 aims to discuss the supported excavations stability in a probabilistic framework with consideration of the soil spatial variability. Great depth supported excavation are discussed. The random field generation and an effective surrogate-model based probabilistic framework are introduced, followed by a discussion of the spatial variability effects.

Chapter 7 proposes a sample-wised probabilistic approach SPAA based on the Atom Search Optimization (ASO)-ANN. The ASO-ANN surrogate model with self-adaptive convergence and high efficiency, is constructed to replace the time-consuming numerical simulations. The initial samples are generated by the Latin Hypercube Sampling method and the iterative samples enrichment allows searching the most representative points for the ASO-ANN model

construction. Two low-dimensional random variable cases and a high-dimensional random field problem are then considered and discussed based on the proposed hybrid SPAA approach.

Chapter 8 summarizes this research work and gives the major findings from each chapter. Some recommendations for the future research are also provided.

Publications and communications

Publications and communications related to this thesis are listed.

Publications

Two papers are published, including '*Tingting Zhang, Julien Baroth and Daniel Dias. (2021). Probabilistic basal heave stability analyses of supported circular shafts in non-homogeneous clayey soils. Computers and Geotechnics, 140, 104457*.' and '*Tingting Zhang, Julien Baroth and Daniel Dias. (2022). Deterministic and probabilistic basal heave stability analysis of circular shafts against hydraulic uplift. Computers and Geotechnics, 150, 104922*.', which are respectively related to Chapters 4 and 5.

Papers related to the remaining chapters are under review or in preparation.

In addition, I had the opportunity to collaborate with other researchers in the field of slopes, tunnels and dams. The published contents are presented below,

Tingting Zhang, Xiangfeng Guo, Julien Baroth and Daniel Dias (2021). Metamodel-Based Slope Reliability Analysis - Case of Spatially Variable Soils Considering a Rotated Anisotropy. Geosciences, 11(11), 465.

Tingting Zhang, Xiangfeng Guo, Daniel Dias and Zhibin Sun. (2021). Dynamic probabilistic analysis of non-homogeneous slopes based on a simplified deterministic model. Soil Dynamics and Earthquake Engineering, 142, 106563.

Chunjing Ma, Alice Di Donna, Daniel Dias and Tingting Zhang (2021). Thermo-hydraulic and sensitivity analyses on the thermal performance of energy tunnels. Energy and Buildings, 249, 111206.

Communications at international conferences

Tingting Zhang, Xiangfeng Guo, Daniel Dias and Zhibin Sun. An efficient procedure for seismic slope stability analysis considering input uncertainties and soil spatial variability, 8th International Symposium for Geotechnical Safety & Risk (ISGSR 2022). Newcastle, Australia.

Chapter 1

Overview of supported excavations analyses

Contents

1.1 Introduction 30

1.2 Deterministic analysis of supported excavations 30

1.2.1 Rectangular-shaped excavations 30

1.2.2 Circular shafts 44

1.2.3 Basal instability due to an hydraulic uplift 46

1.2.4 Soil-wall interaction 48

1.3 Probabilistic analysis of supported excavations 50

1.3.1 Reliability theory 50

1.3.2 Characterization of the soil variability 52

1.3.3 Reliability analysis methods 53

1.3.4 Sensitivity analysis methods 58

1.3.5 Previous studies about probabilistic analysis of supported excavations 60

1.4 Machine learning-based excavation analyses 68

1.5 Conclusion 72

1.1 Introduction

This chapter aims to provide a comprehensive introduction of the supported excavation stability in deterministic and probabilistic frameworks. A general review of deterministic and probabilistic methods commonly used in supported excavations analyses and an overview of the corresponding previous studies are provided.

Firstly, the deterministic methods (e.g., field observations, laboratory-scale physical tests, analytical/empirical methods and numerical simulations) and previous studies used for two kinds of supported excavations, i.e., rectangular excavation (RE) and circular shaft (CS), are given. Then, the probabilistic methods are summarized and the previous probabilistic studies of supported excavations are reviewed. The advantages and limitations of the existing studies are discussed.

1.2 Deterministic analysis of supported excavations

1.2.1 Rectangular-shaped excavations

For rectangular-shaped excavations, there are two major concerns: serviceability assessment of excavations and basal heave stability analyses. Previous studies on these two aspects are reviewed and the major limitations of previous works are identified.

1.2.1.1 Serviceability assessment

The excavation-induced lateral wall deflection and ground surface settlement should be considered when the Serviceability Limit State (SLS) is verified. It has been investigated by numerous researchers using field investigation, laboratory-scale physical tests, analytical/empirical methods, and numerical simulations.

Field investigation

A number of case histories have been reported worldwide and well-documented field data, such as Chicago (Finno et al., 1989), the UK (Long, 2001), Singapore (Young and Ho, 1994; Zhang and Goh, 2016), Paris (Khadija et al., 2021) and Shanghai (Hong et al., 2015a; Liu et al., 2011; Ng et al., 2012; Wang et al., 2010, 2005).

Clough & O'Rourke (1990) summarized the profiles of lateral wall movement and ground surface settlement based on field observations from several case histories. As shown in Fig. 1.1(a), the cantilever movement can be observed before the installation of the first prop, and the corresponding settlement behind the wall can be represented by a triangular shape. The deformation profile of the wall changes from cantilever to deep inward (Fig. 1.1(b)) and the maximum lateral wall displacement is near the excavation bottom. The settlement also changes from a triangular shape to a trapezoidal shape.

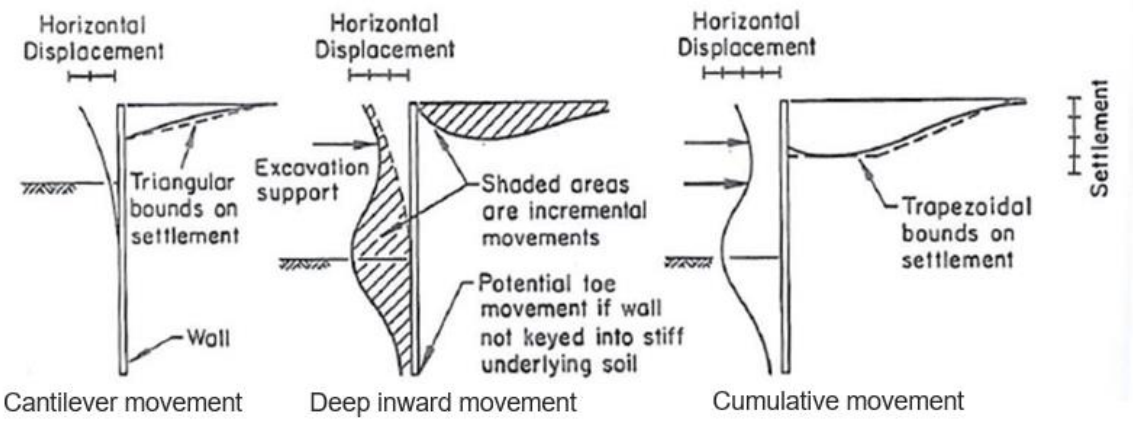

Fig. 1.1 Typical deformation profiles for excavations (Clough and O'Rourke, 1990).

Ou et al. (1998) proposed two types of settlement profiles during excavations based on some field observations, including the spandrel shape and the concave shape as presented in Fig. 1.2(a) and (b), respectively. The spandrel shape was proposed by 10 cases from Taipei, and the maximum settlement occurs close to the wall, while for the concave one, the maximum settlement occurs at a certain distance away from the wall. The concave settlement near the wall is estimated as 0.5 times the maximum ground surface settlement based on the field data (Clough and O'Rourke, 1990) and the primary influence zone of the settlement trough is considered as twice the excavation depth. Ou (2006) suggested that the spandrel surface settlement profile may occur with the cantilever mode of wall movements, while the concave surface settlement profile may occur with the deep inward movement pattern.

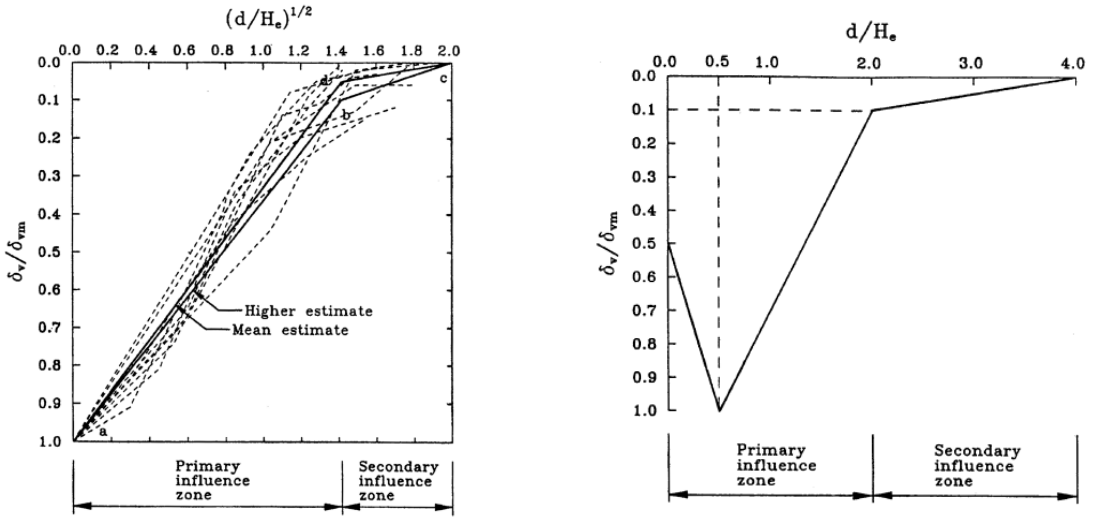

(a) Spandrel shape (b) Concave shape

Fig. 1.2 Proposed settlement diagrams behind the wall.

Long (2001) used a monitoring system consisting of inclinometers attached to the steel cages in the piles, levelling stations and ground movement monitoring stations, to monitor the wall deflection and ground movement for the National Gallery excavation in London. Several numerical simulations with London Clay constitutive model with small strain stiffness model and BRICK model were then performed. Fig. 1.3 indicate that the excavation responses are considerably over-predicted using these three models. However, the constitutive model BRICK can predict a displacement profile that are much closer to the measured results.

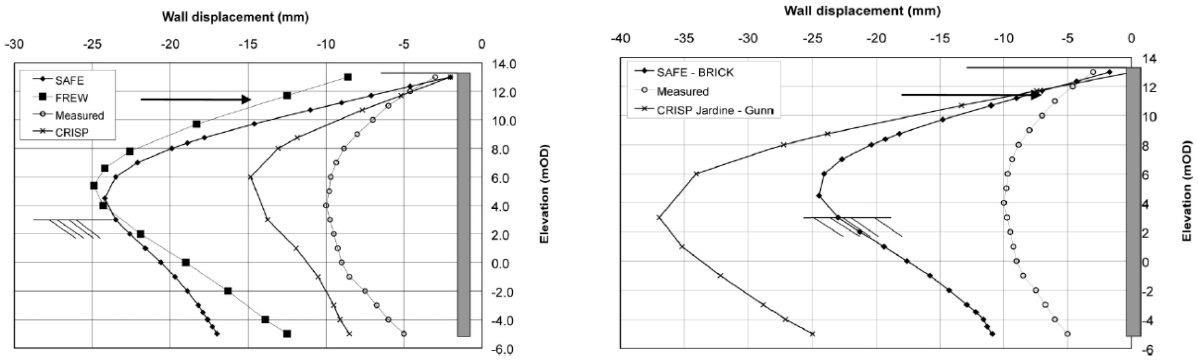

(a) Mohr-Coulomb model (b) London Clay constitutive model

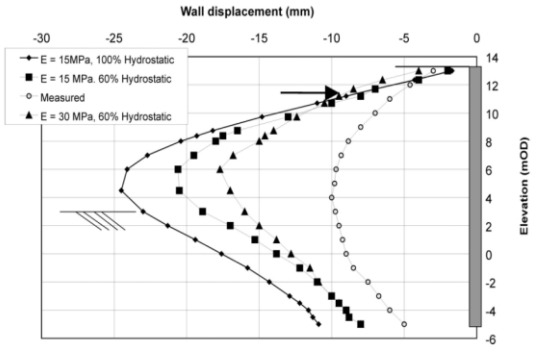

(c) BRICK model

Fig. 1.3 Comparison of actual and predicted wall movements.

Moormann (2004) analysed the lateral wall displacement and ground surface settlement based on 530 cases. The results show that the maximum horizontal wall displacement lies between 0.5%H (H: excavation depth) to 1.0%H, with a mean value of about 0.87H. The maximum vertical settlement behind a retaining wall was located between 0.1%H and 10%H, with a mean value of about 1.1H. The maximum ground surface settlement usually varies between 0.5~1 times the maximum wall deflection. Besides, it is also found that the excavation deformation in soft clay seems to be largely dependent on the basal heave safety factor compared to the system stiffness of the retaining system as shown in Fig. 1.4. Wang et al. (2010) indicated that the ratio between the maximum wall deflection and the excavation depth varies considerably (in the range of [0.5%, 1.4%]) and the value depends on the soil properties and the retaining structure types.

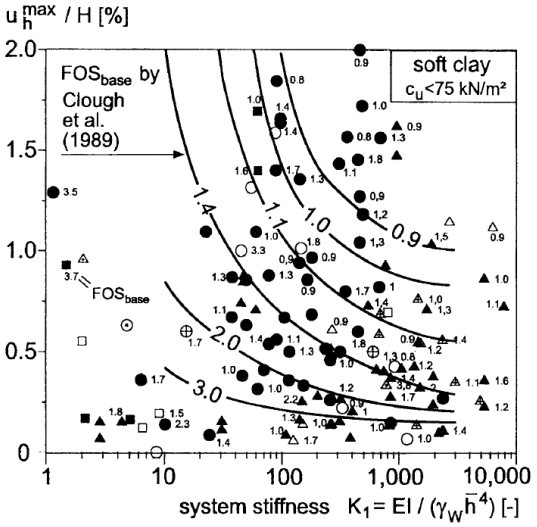

Fig. 1.4 Relationship between the lateral deformation with the system stiffness and basal heave safety factor.

Tan and Wei (2012) investigated the performance of a long sword-shaped deep excavation in soft clay using the cut-and-cover technique in Shanghai, China. Based on the long-term comprehensive instrumented field data, the over-excavation, long construction duration, or large

exposure period without support would induce significant retaining wall and ground movements; Ng et al. (2012) monitored a multi-propped excavation in a greenfield site in Shanghai. The lateral wall displacements, lateral ground displacements and surface ground settlements were measured. The results show that the ratio between the maximum wall deflection to ground surface settlement ranges from 0.2 to 1.2; Xu et al. (2016) present a case study of dynamic control of excavation deformations. Various deformation control measures such as strengthening the chamfer of the retaining structure, adjusting the excavation sequence and strengthening the support nodes were adopted to reduce the horizontal displacement of the retaining wall. The monitored excavation performance indicates that these remedial measures are feasible and effective in controlling excavation-induced deformation and reducing the associated risks; W. Zhao et al. (2019) carried out a long-term field measurement to understand the behaviour of an anchored sheet pile wall structure. The field measurements show that the soil excavation has a greater effect on the anchored sheet pile deflection than the backfilling procedure.

In general, the wall deflection is usually measured with inclinometers, and the maximum wall deflection and surface settlement depend on various factors such as the soil properties, the retaining system type and stiffness, the construction method (top-down, bottom-up and open-cut) and the quality of the workmanship. Field investigation is an effective method, whereas it is expensive as it takes a long time to obtain data and the process is not repeatable. In addition, it cannot be used for forecasting.

Laboratory-scale physical tests

Laboratory tests have the advantage of allowing quantitative control of the factors affecting the results. Small-scale centrifuge model tests have been used to study excavation behaviours. Takemura et al. (1999) carried out the centrifuge model tests of a vertical excavation in normally consolidated soft clay to evaluate the settlements of the ground surface behind the wall, earth pressures on the wall and strains along the wall. It was found that the deformation after a certain excavation depth is mainly determined by the mechanical properties of the sand. The support prevents significant increases in settlement and wall displacement, and once deformation has occurred it is difficult to recover by increasing the support (i.e., preload). The non-linear behaviour of the soil is one of the main reasons; Lam et al. (2014) conducted the centrifuge model tests of deep excavations in slightly over-consolidated soft clay to understand the mechanisms involved in soil excavations. The schematic diagram of experimental setup is

presented in Fig. 1.5. The ground surface settlements and changes in pore water pressure are monitored. Besides, the effects of prop stiffness, wall rigidity, and excavation geometry on the characteristics of ground deformation and soil-structure interaction were discussed. The results indicate that a reduction in strut stiffness increases wall deflection above the foundation level; Chen et al. (2022) performed a series of centrifuge model tests to investigate the interaction between successively constructed adjacent foundation pits. The stress and deformation of retaining structures and the settlement of the soil between the two adjacent pits were investigated. The results show that the deformation of the retaining structure in the pit constructed first was greater than that in the pit constructed later; Shoari Shoar et al. (2023) carried out a series of centrifuge tests to evaluate surcharge effects on the behaviour of nailed vertical excavations. The mechanism of failure surface development was observed. It is found that the shapes of failure surfaces are bilinear and that the surcharge affects on the development of failure surfaces. The pull-out mechanism was observed in the nails during failure without bending.

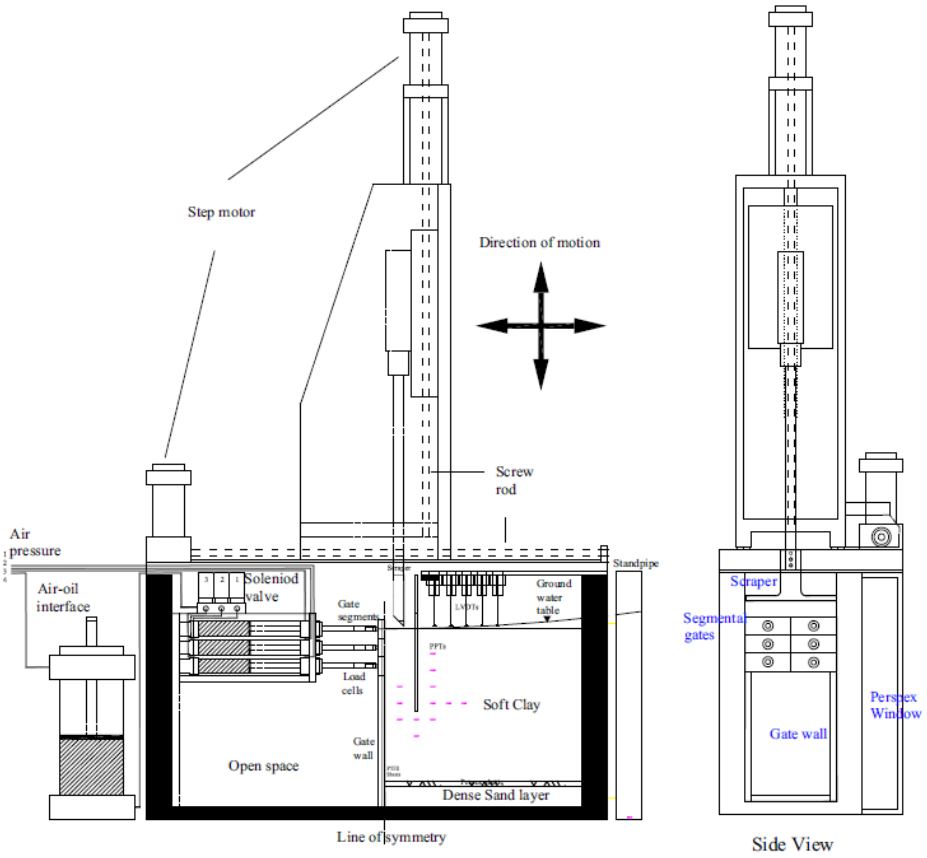

Fig. 1.5 Schematic diagram of experimental setup within-flight excavator (Lam et al., 2014).

It should be noted that centrifuge modelling allows the provision of a correctly scaled physical model to effectively investigate the mechanisms of soil deformation during excavation.

Compared to full-scale projects, the tests are valid and can be repeated until they fail. However, centrifuge teste also have some limitations and drawbacks, for instance, only relatively simple models can be considered, the process is expensive due to the high cost of equipment and the specialized operations skills, or the environmental conditions used in centrifuge modelling (such as soil moisture, temperature, and chemical conditions) are difficult to control and maintain precisely.

Analytical/empirical methods

Several analytical/empirical methods were proposed to estimate the wall displacements (Addenbrooke et al., 2000; Clough and O'Rourke, 1990; Hashash and Whittle, 1996; O'Rourke, 1993; Zapata-Medina, 2007; Zhang et al., 2015a) and the ground surface settlements (Hsieh and Ou, 1998; Kung et al., 2007c; Ou and Hsieh, 2011; Peck, 1969).

O'Rourke (1993) assumed the incremental displacement profile of the multi-propped wall in soft and undrained clay to be a cosine function as shown in Fig. 1.6, which can be defined as

$$\delta h = \frac{\delta h \max}{2}\left(1-\cos\left(\frac{2\pi y}{\lambda}\right)\right) \tag{1.1}$$

where δh is the incremental wall displacement at any distance below the lowest support, $\delta h \max$ is the maximum incremental displacement, λ is the wavelength of the deformation, which is defined as the distance from the lowest support level to the fixed base of the wall.

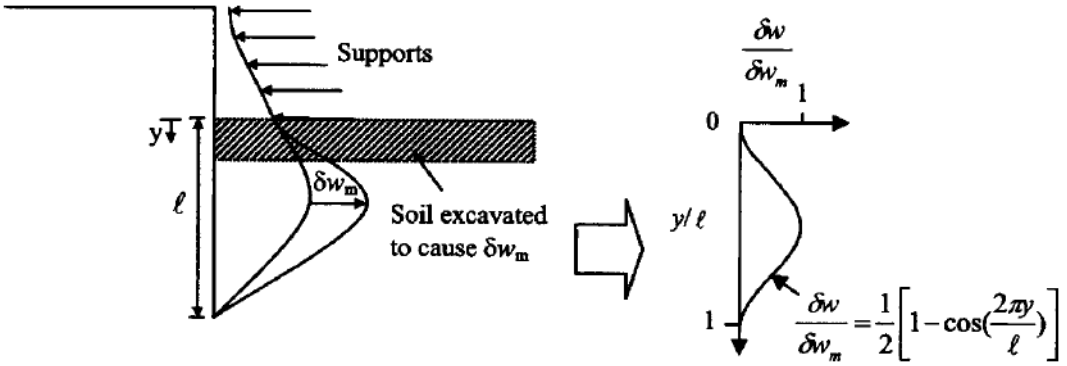

Fig. 1.6 Incremental displacements in braced excavations (O'Rourke, 1993).

Osman and Bolton (2006) proposed that the wavelength of the deformation presented in Eq. (1.1) depends on the wall end-fixity conditions, and is defined as

$$\lambda = \alpha s \tag{1.2}$$

where α is a dimensionless value and *s* is the length of the wall beneath the lowest support. When the wall is embedded into a stiff layer beneath the soft clay, the wall tip is fully fixed, in such case, α should be considered as 1. For short walls embedded in deep very soft clay, the maximum wall deformation occurs at the tip of the wall and α is equal to 2. For the intermediate cases, for instance a wall is embedded in soft or medium stiffness soil where its end is not fixed, the maximum displacement often occurs below the excavation level and α is set in the range of (1,2); Osman and Bolton (2006) proposed a new approach for ground movement estimation that can consider the actual stress-strain data and the undrained shear strength profile of the soil on site; Clough et al. (1989) proposed a semi-empirical procedure to determine the wall movement. The maximum lateral wall deflection is related to the basal heave safety factor and system stiffness. However, the proposed wall movement curves depend on good condition and workmanship, and the cantilever deformation of the wall contributes only a small fraction of the total movement.

Hsieh and Ou (1998) considered the concave settlement profile as presented in Fig. 1.2 as the bi-linear relationship and the surface settlements in the primary influence zone and the secondary influence zone can be predicted by

$$\begin{cases} \delta v = (-0.636\sqrt{\frac{d}{H}} + 1)\delta v\max, \text{if } \frac{d}{H} \le 2 \\ \delta v = (-0.171\sqrt{\frac{d}{H}} + 0.342)\delta v\max, \text{if } \le \frac{d}{H} \le 4 \end{cases} \quad (1.3)$$

where δv and $\delta v\max$ are respectively the surface settlement and maximum surface settlement, *d* is the distance from the wall. Ou and Hsieh (2011) further suggested new surface settlement patterns to consider the excavation depth, excavation width and the hard stratum depth.

The analytical method is simple and easy to implement. However, this method can only represent ground settlement or wall displacement perpendicular to the direction of the retaining wall. Besides, due to the assumptions, the methods cannot consider properly the soil non-linear properties, specific ground conditions, retaining systems or construction sequence.

Several empirical methods have been developed. Based on a database of 33 cases and several results from finite element analyses, G. T. C. Kung et al. (2007b) developed a semi-empirical model to determine the maximum wall deflection and ground surface settlement caused by a braced excavation in soft to medium clays; Zhang et al. (2015a) proposed a simple polynomial

regression model to estimate the maximum wall deflection considering the excavation geometry, soil strength and stiffness, and the wall stiffness. The wall deflections calculated using this method are consistent with some field measurements and published records; Goh et al. (2017) developed a semi-empirical logarithmic regression model to estimate the maximum wall deflection for braced excavations. The soil properties, wall stiffness, excavation length, excavation depth, and wall embedment depth are considered in this method. However, it should be noted that empirical methods need to capture the isolated effects of various factors, therefore a large of field measurements or numerical simulations are necessary. Assessing and analyzing such a large amount of comprehensive and detailed data are difficult.

Numerical analyses

Numerical simulations, which can consider both the geotechnical and structural aspects (such as the wall stiffness, complex soil behaviours, struts and soil-wall interactions), permit to provide more accurate and rational information on excavations performance (Sert et al., 2016). It can also be used to predict the excavations behaviour and provide guidance for the design and construction. Mana and Clough (1981) carried out a numerical parametric study to investigate the effects of wall stiffness, prop spacing, stiffness and prestress, and soil stiffness on ground deformations. The excavation geometry (such as excavation width and depth) effects were also discussed; Clough and O'Rourke (1990) implemented several finite element studies and indicated that wall stiffness and prop spacing have a small influence on deformations around excavations in stiff clay. Conversely, soil modulus and lateral earth pressure coefficients have a greater influence on ground movement than the stiffness of the retaining system; Jen (1998) performed numerical parametric studies to study the effects of excavation geometry, retaining system and stress history of clay on ground deformations due to excavation. Besides, a design chart was proposed to correlate ground settlement to excavation depth, wall length, depth of hard stratum and soil profile. With the development of the numerical analysis software, more studies are conducted and It is seen from this table that most of the above excavations were mainly at depths of around 20 m, with little discussion of depths above 30 m. However, with the urbanization acceleration, the development of underground space is characterized by large, deep, fast and dense. Besides, the complexity of the stratigraphy, the surrounding structures and the variety of construction procedures may increase the potential risks associated with deep excavation construction. The previous experiences and case histories cannot be used as a reference due to the small depth.

Table 1.1 summarizes some recent numerical studies including the excavation depth, the soil constitutive models and the analysis methods. It is seen from this table that most of the above excavations were mainly at depths of around 20 m, with little discussion of depths above 30 m. However, with the urbanization acceleration, the development of underground space is characterized by large, deep, fast and dense. Besides, the complexity of the stratigraphy, the surrounding structures and the variety of construction procedures may increase the potential risks associated with deep excavation construction. The previous experiences and case histories cannot be used as a reference due to the small depth.

Table 1.1 Summary of numerical analysis of rectangular-shaped excavations.

No.	Case	Excavation depth (m)	Soil constitutive models	Analysis method
1	An excavation in the UK (Ng et al., 1998)	10	Mohr-Coulomb model	Numerical method
2	O6 station, China (Hsiung, 2009)	19.6	Mohr-Coulomb model	FDM
3	An excavation in Japan (Konda et al., 2010)	21.55	Mohr-Coulomb model	FEM
4	An academic case (Baroth and Malecot, 2010)	6	Mohr-Coulomb model	FEM
5	Formosa case (Tang, 2011)	18.45	Sands: hyperbolic model clays: pseudo-plastic model	FEM (PLAXIS)
6	TNEC in Taipei (Luo et al., 2011a)	19.7	MPP soil model (modified pseudo-plasticity)	FEM (PLAXIS)
7	An academic case (Papaioannou and Straub, 2012)	5	Mohr-Coulomb model	FEM (SOFiSTiK)
8	Bangkok MRT (Likitlersuang et al., 2013)	21	Mohr-Coulomb model, Soft Soil Model, Hardening Soil model Small Strain Stiffness model	FEM (PLAXIS)
9	Formosa case (Luo and Das, 2015)	18.45	Sands: hyperbolic model clays: MPP model	FEM (PLAXIS)
10	An academic case (Sert et al., 2016)	5	Hardening Soil model	FEM (PLAXIS)

11	An excavation in Shanghai (Dong et al., 2016)	24	Hardening Soil model with small strain	FEM
12	An excavation in Boston (Rouainia et al., 2017)	13~17	Mohr-Coulomb model, Modified Cam Clay, Kinematic Hardening Model	FEM (PLAXIS)
13	Formosa case (Luo et al., 2018a)	18.45	Small-strain stiffness model	FEM (PLAXIS)
14	Cashew station excavation (W. Zhang et al., 2018)	20	Hardening Soil model	FEM (PLAXIS)
15	An academic case (Luo et al., 2018b)	6	Hardening Soil model	FEM (PLAXIS)
16	An excavation in Iran (Johari and Kalantari, 2021)	20	Mohr-Coulomb model	FDM (FLAC)
17	Sukhumvit Station in Bangkok (Nguyen and Likitlersuang, 2021)	21	Mohr-Coulomb model	FEM (PLAXIS)
18	An excavation in Shanghai (Yang et al., 2022)	24	Mohr-Coulomb model	FEM

1.2.1.2 Basal heave stability analyses

Considering the Ultimate Limit State (ULS), the evaluation of safety factors against base heave failure is important in excavation designs. Numerical methods are often used since they permit to provide a comprehensive framework considering complicated geotechnical and geometrical characteristics. Goh (1994) implemented finite element analyses to discuss the effects of the thickness of the clay layer beneath the bottom of the excavation, the depth of the wall below the bottom of the excavation, the width/height ratio, and wall stiffness; Faheem et al. (2003) employed the finite element method with the strength reduction technique to analyse the basal heave stability of excavations, and indicated that the base stability is significantly influenced by the depth, width of the excavations, the walls depth embedded below the excavation base, and the wall stiffness; Goh (2017a) carried out finite element analyses to assess the basal heave safety factor for excavations in soft clays supported by jet grout slabs. The results indicate that the interface friction between the jet grout slab and the wall is a key component contributing to

the resistance of the excavation system to basal heave failure; Goh et al. (2019b) implemented different excavation cases with various geometrical properties, wall and soil properties to assess the basal heave safety factor using finite element software.

Alternatively, the analytical methods are also popular for basal heave stability analyses. Several limit equilibrium methods were proposed and improved. Terzaghi (1943) proposed a mechanism with a soil column outside the excavation as depicted in Fig. 1.7(a). The failure is resisted by the weight of the corresponding soil column inside the excavation and the adhesion acting along the vertical edges of the mechanism. It is suitable for wide excavations (the excavation width B is equal to or larger than the excavation depth H) and the basal heave safety factor (F_s) can be expressed as

$$F_{s-\mathrm{T}} = \frac{5.7 S_u B_1}{\gamma H B_1 - S_u H} \tag{1.4}$$

where B_1 refers to the distance from the wall to the vertical failure surface and can be determined by $B_1 = B/\sqrt{2}$, S_u is the undrained shear strength (kPa) and γ is the unit weight of the soil (kN/m^3). However, it ignores the wall embedment effects. An improved mechanism is then proposed with consideration of the embedment wall as shown in Fig. 1.7(b). The resistance of the embedment wall is determined from the soil-wall adhesion $r_i S_u$ (r_i: soil-wall interface coefficient) and the F_s of the modified Terzaghi method (MT) is (Goh et al., 2019b)

$$F_{s-\mathrm{MT}} = \frac{5.7 S_u B_1 + S_u H + S_u D + r_i S_u D}{\gamma H B_1} \tag{1.5}$$

where D is the wall embedment depth.

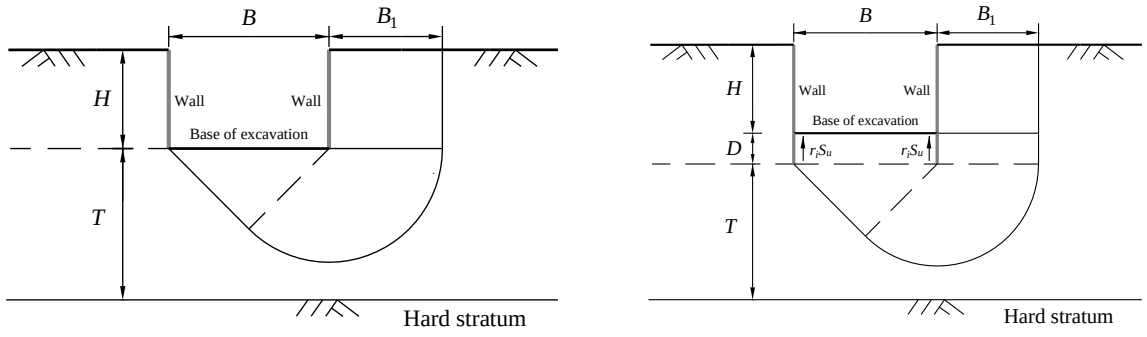

(a) Terzaghi (b) Modified Terzaghi (MT)

Fig. 1.7 Terzaghi models.

Bjerrum and Eide (1956) proposed a basal heave stability analysis method for deep excavations (H>B) as illustrated in Fig. 1.8 and the safety factor can be determined by

$$F_{s-\mathrm{BE}} = \frac{S_u N_c}{\gamma H} \tag{1.6}$$

where N_c is Skempton's bearing capacity factor and for the case with (H+D)/B<2.5, it can be approximated as $N_c = 5(1+0.2B/L)\times[1+0.2(H+D)/B]$, where L is the excavation length (Goh et al., 2008). The modified Bjerrum & Eide method (MBE) which considers the wall embedment depth resistance can be determined by

$$F_{s-\mathrm{MBE}} = \frac{S_u N_c + 2mS_u D(1+B/L)/B}{\gamma H} \tag{1.7}$$

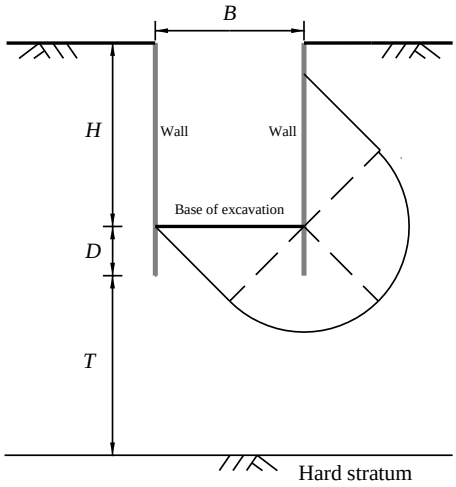

Fig. 1.8 Bjerrum & Eide method model (BE).

It is noted that the methods developed by Terzaghi and Bjerrum & Eide are based on the bearing capacity theory, which assumes the soil as homogeneous and is difficult to consider soil non-homogeneity (Wu et al., 2012). The slip circle method is then proposed as shown in Fig. 1.9 (Chowdhury, 2017; Tang and Kung, 2011). The safety factor can be defined by the ratio of the resisting moment to the driving moment and is given by

$$F_{s-\mathrm{SC}} = \frac{M_r}{M_d} = \frac{R\int_0^{\delta+\pi/2} S_u(Rd\theta)}{W_s \cdot R/2} \tag{1.8}$$

where M_r and M_d are respectively the resisting moment and driving moment (kN·m), R is the radius of the slip circle (m), W_s is the weight of clay behind the wall and above the excavation level (kN), δ is the angle of failure arc in excavation zone and it can be obtained by $\delta = \cos^{-1}(h/R)$, where h is the distance (m) from the lowest strut level to the final excavation level, it is set to be 3 m based on engineering practice.

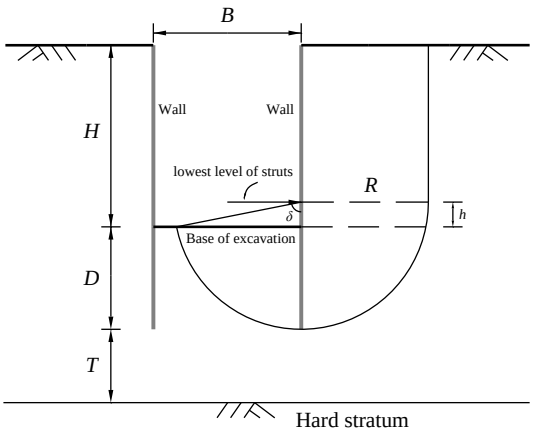

Fig. 1.9 Slip circle method model (SC).

This method allows investigating the influence of soil non-homogeneity. However, it cannot account for the excavation width effect on the basal heave stability.

Another widely used analytical method is the upper bound limit analysis and the safety factor can be determined by equating the external work rate to the energy dissipation for assumed deformation modes (or velocity fields) that satisfy velocity boundary conditions (Mollon *et al*., 2011; Mollon *et al*., 2010). Several researches about the basal heave stability of excavations were based on the limit analysis method (Cai et al., 2018; Chang, 2000). The Prandtl mechanism is often used as the failure mechanism and the work rates are then calculated to determine the stability (Cai *et al*., 2018). The corresponding failure mechanism can be found in Fig. 1.10. The mechanism consists of a 90^{o} circular arc (*jkh*) sandwiched between two 45^{o} isosceles wedges (*ijk* and *gjh*), soil columns *efij* and *mljg*. *v* is the velocity of plastic flow and the safety factor can be determined by the ratio of the internal energy dissipation *E* and the external work rate *W*. It is noted that $B_1=B$ when a hard stratum is present at a depth of $T \geq T_c$, otherwise, $B_1=\sqrt{2}T$ ($T < T_c$), T_c is the critical hard stratum depth from the wall bottom tip and is equal to $B/\sqrt{2}$. The wall is assumed to be fully rigid and the lateral resistance afforded by the wall is not considered, which means that the wall moves along the vertical direction while it is motionless in the horizontal direction (Faheem et al., 2003; Huang et al., 2018).

$$F_{s\text{-ELA}} = \frac{E}{W} = \frac{H + 4D + 6.14B_1}{\gamma H B_1} S_u \tag{1.9}$$

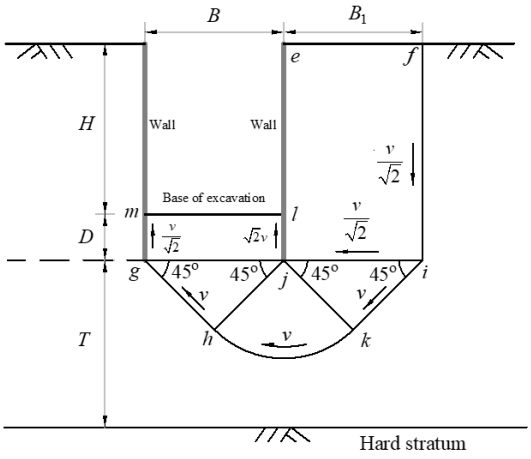

Fig. 1.10 Limit analysis failure mechanism.

It should be noted that the triangular wedges *ijk* and *gjh* of the existing failure mechanism are defined by a constant angle of 45°. However, this angle may change in different excavations with different parameters (such as the soil properties). To assess excavation stability more accurately, improvements to the failure mechanism are necessary.

1.2.2 Circular shafts

The "self-stabilizing effect" of circular excavations is known to exist (Xiao et al., 2022), which can give circular shafts an inherent stiffness over rectangular shafts. They are preferred in urban areas where space is limited or ground conditions are unfavourable, and have been used for underground car parks (Marten and Bourgeois, 2006), metro stations (Celestino et al., 2009), tunnel boring machine lunch and electricity infrastructure projects (Aye et al., 2014; Faustin et al., 2018; Furlani et al., 2011; Le et al., 2019; Tang, 2020). Some circular shaft cases are given in Fig. 1.11. Concerning the stability analyses of circular shafts, most of the existing studies focus on ground stresses, ground movements and wall displacements assessments. The field investigation (McNamara et al., 2008; Schwamb et al., 2016; Tang, 2020; Wong and Kaiser, 1988), laboratory-scale physical tests (Le et al., 2019), analytical/empirical methods (Faustin et al., 2018) and numerical simulations (Arai et al., 2008; Aye et al., 2014; Dias et al., 2015; Furlani et al., 2011; Schwamb and Soga, 2015; Xiao et al., 2022) were implemented for the circular shaft analyses. Whereas, the basal heave stability, which is also essential when verifying the ULS, is rarely discussed and it will be considered in this study.

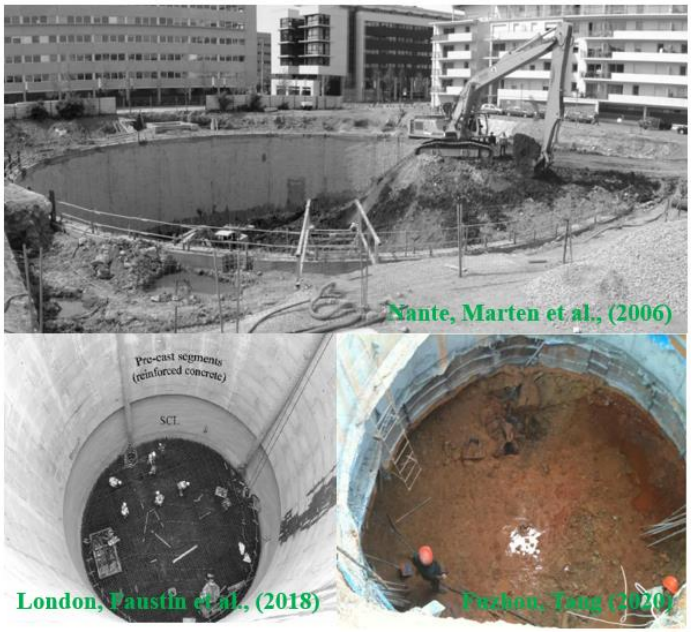

Fig. 1.11 Circualr shaft construction.

1.2.2.1 Basal heave stability analyses

There are sevreral analytical methods for the basal heave stability analysis of the rectangular-shaped excavations, such as the Terzaghi method, Bjerrum and Eide method as presented in Section 1.2.1.2. For circular excavations, a modification factor 1.2 is applied to the safety factor to consider the shape effect (Cai et al., 2002). However, this method cannot take into account the wall stiffness effects and the modification may vary with soil and geometric conditions; M. Zhang et al. (2018) proposed an axisymmetric arc sliding method based on the circular arc sliding model of the limit equilibrium method to analyse the basal heave stability of braced circular excavations. It combined the stiffness of the enclosure structure and considered spatial effects. However, the performance of numerical simulations is still required to provide the deformation distribution of the enclosure structure during the safety factor calculations.

The numerical simulations are more reasonable and an axisymmetric model is often used due to the circular shape. Cai et al. (2002) implemented the finite element method to analyse the circular shaft stability and noted that the substrate stability of circular excavations in soft clay soils is expected to be greater than rectangular excavations due to shape effects; Goh (2017b) used the finite element method to assess the basal heave stability of diaphragm wall supported circular excavations. The results show that the basal heave safety factor is related to the undrained shear strength of the clay, the geometrical properties of the excavation system and the thickness of the soil stratum; Keawsawasvong and Ukritchon (2019) focused on the stability

analysis of braced circular excavations in non-homogeneous clays using the lower bound finite element limit analysis. The above-mentioned studies mainly analyse the effects of the excavation geometry or soil properties on the shaft stability, and rarely discuss the hydraulic or interface effects, which are described in detail in the following sections.

1.2.3 Basal instability due to an hydraulic uplift

As the excavation depth increases, the stability and serviceability of the work site and of the adjacent buildings would be influenced by water pressure, particularly in coastal cities. The main failure mechanisms caused by seepage include heave, uplift, internal erosion or piping. Heave occurs when the seepage forces generated by groundwater flow lift the soil on the downstream side. Uplift failure can occur when seepage forces act on the subsoil are higher than the effective soil weight. Internal erosion or piping may occur with the transport of soil grains within a soil layer at the interaction surface (between soil and structure) by groundwater flow (Ouzaid et al., 2020). The occurrence of seepage failure has the highest distribution (over 60%) among the types of excavation accidents, the excavation stability analyses subjected to hydraulic effects are thus important (Ye-Shuang et al., 2019).

Field investigations are often carried out for the excavation stability analysis. Milligan and Lo (1970) collected eight case histories in Canada with base instability caused by hydraulic uplift. The results indicate that the base instability due to the hydraulic uplift is associated with excessive basal heave, wall inward movement and ground surface settlement behind the wall; Moore and Longworth (1979) reported an excavation with hydraulic uplift failure in Oxford Clay and pointed out that there is a large upheaval displacement on the excavation base due to the artesian pressure; Qu et al. (2002) provided a case history in Shanghai and carried out pumping tests to study ground settlement induced by artesian release; Shi et al. (2018) conducted a comprehensive monitoring program to study the responses of far-field ground and groundwater to pumping of artesian water in deep excavations.

Analytical methods were also proposed for the basal heave stability analysis. The pressure balance method (PBM), which indicates that the pore water pressure beneath a low permeability stratum is greater than the average overburden pressure, is mainly used (Terzaghi, 1943). The improved methods for estimating the basal failure caused by hydraulic uplift were then proposed since the traditional PBM ignores the soil strength and leads to conservative results (Milligan and Lo, 1970). Further modifications about the clay-wall interface strength or the cohesion of

aquitard inside excavation can be found in (Liu and Liu, 2011; Sun, 2016; Yang and Zheng, 2009).

A number of **experimental** and **numerical analyses** have also been conducted. Hong and Ng (2013) conducted centrifuge tests (shown in Fig. 1.12) and finite element analyses to analyse multi-propped excavations which are destabilized by hydraulic pressure from an underlying sand aquifer. The results indicate that the artesian pressure required to initiate uplift inside the excavation is about 1.2 times the overburden pressure of the clay; Ding et al. (2014) performed the finite element analysis to analyse the confined water head, length & width size of the pit effects on the inrushing plastic deformation failure of the pit; Hong et al. (2015b) investigated the initiation and failure mechanism of base instability of excavation in clay subjected to hydraulic uplift. The main pattern of damage was found to change from simple shear in narrow excavations to a combination of patterns in wide excavations; Koltuk et al. (2019) performed experimental and numerical investigations to clarify the seepage failure by heave in sheeted excavation pits; Chen et al. (2020) and Lai et al. (2022) employed the finite element limit analysis to investigate the base instability triggered by the hydraulic uplift of pit-in-pit braced excavations.

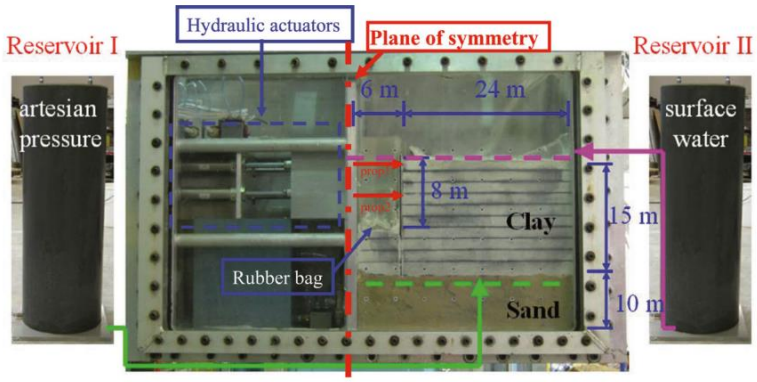

Fig. 1.12 Centrifuge model package for the excavation basal heave stability against hydraulic uplift.

The basal heave of excavations subjected to hydraulic uplift has been discussed extensively in previous works. However, most of the studies focused on rectangular excavations and there has been little discussion about the circular shaft failure induced by hydraulic uplift.

1.2.3.1 Permeability coefficient

Soil permeability is a fundamental soil property that is used to understand the water flow in soil and the relevant parameter is the permeability coefficient. It can be measured using field

measurements (Li et al., 2013; Nagy et al., 2013; Sahin, 2016; Yang et al., 2018) or laboratory-scale physical tests (Brault and Konrad, 2007; Chapuis, 2002; Daliri, 2011; Huang et al., 1998b; Leroueil et al., 2002). In addition, several analytical methods were also proposed for the permeability coefficient determination (Chapuis and Aubertin, 2003; Fredlund et al., 1994; Huang et al., 1998a).

The permeability coefficient in most studies (about the basal heave stability of excavations) was considered isotropic and uniform for simplicity, which means that the horizontal and vertical permeability coefficients (k_x and k_y respectively) are identical. However, in real projects, it has been noted that anisotropic permeabilities are common due to soil stratification, compaction, deposition and densification. Hong (2012) implemented the laboratory constant head tests for a Shanghai excavation and found that the permeability coefficients in horizontal and vertical directions are different for each layer. The horizontal permeability coefficient is varied from 1.1e-8 m/s to 6.0e-8 m/s whereas the vertical one is in the range of [2.2e-9 m/s, 7.7e-9 m/s]. The anisotropy permeability coefficient r_k ($r_k=k_x/k_y$) is varied with the values being respectively 2.69 (Medium-Soft Clay), 5.71 (Soft Silty Clay), 2.62 (Medium Clay) and 17.5 (Medium Silty Clay); Zhang et al. (2016) also provided different values of k_x and k_y in the analysis of braced excavation deformation affected by confined water in soft soil. Therefore, the anisotropy of permeability should be considered in the basal heave stability analysis of excavations.

The anisotropy discussions of hydraulic conductivities can be found in earth dams (Fell, 2005; Mouyeaux et al., 2019; Siacara et al., 2022), but are rarely discussed in excavations, which will be analysed in this study. Due to the inconvenient, costly, and time-consuming of field measurements or laboratory tests, discussions about permeability anisotropy on the excavation basal instability are difficult to be implemented. This study will perform numerical simulations to investigate the effects of r_k on excavation stability.

1.2.4 Soil-wall interaction

The interaction between soil and wall is a key issue in geotechnical engineering and can significantly affect excavation behaviour (Dong, 2014). A series of field investigations (Ng et al., 2012; Tedd et al., 1984) or experimental tests (Boulon, 1989; Lam, 2010; Lam et al., 2014; Richards and Powrie, 1998) were performed to investigate the soil-structure interaction effects. It is noted that using in-situ tests or laboratory experiments is difficult and costly, in contrast,

the numerical analysis makes it easier to study the soil-wall interaction effects on excavation stability.

Interface elements are used to study the interaction between soil and wall in numerical analyses. In the last few decades, several types of interface elements were developed, such as zero-thickness elements, slip elements, connecting elements and thin-layer elements (Desai et al., 1984; Dong, 2014; Gholampour and Johari, 2019; Herrmann, 1978).

Powrie and Li (1991) used slip elements, which have nearly zero stiffness in tension and a limited elastic shear modulus, to simulate the interface between soil and wall. The Coulomb friction criterion was used for the shear resistance of the soil-wall interface; Day and Potts (1998) developed a zero thickness interface element with a simple elastoplastic Mohr-Coulomb failure criterion. The results indicated that the predicted limiting active and passive pressure on the wall are related to the maximum wall friction angle; Hsi and Yu (2005) carried out the finite element analysis to analyse a 20 m-deep excavation stability in deep marine soft clays. The interface between soil and structural elements was modelled with a strength reduction factor of 0.5 for clay and 0.67 for sand materials; Zheng et al. (2014) constructed a soil-fluid coupled finite element model to study the mechanism of the dewatering-induced diaphragm wall deflections. A zero-thickness interface was used and a friction behaviour is governed by a limiting shear slip and friction coefficient with a value of 0.3; Dong (2014) used an extended Coulomb frictional contact model to describe the soil-wall interface. The influence of interface properties on the excavation behaviour was investigated using 5 cases, which include fully rough contact, fully smooth contact, and other three scenarios that lie between these two boundaries. The results show that the calculated wall deflections and ground movements are sensitive to the soil/wall interface properties; Sun (2016) discussed the excavations under the effects of confined aquifer pressures in soft soils. The interface element with zero thickness within the model was used to study the interaction between the soil and the retaining structure. The strength properties of the interface were linked to the strength properties of the soil layer with a reduction factor. A series of parametric analyses with the reduction factor being in a range of [0.4, 1.0] are conducted; Goh (2017a) implemented the finite element analyses to analyse the stability of excavations with jet grout slab. The interface between the jet grout slab and the wall is considered and the shear response of the interface element is controlled by an elastic-perfectly plastic Coulomb shear strength criterion. The results indicate that the interface friction is a key component contributing to the resistance of the excavation system; Goh et al. (2019b) investigated the excavation basal heave stability with different geometrical properties of the excavation, wall and soil properties.

A clay-wall adhesion factor is introduced for the interface strength determination; Lai et al. (2022) analysed the undrained excavations stability subjected to hydraulic uplift using the Finite Element Limit Analysis (FELA) method. The interface elements were used to model the soil-wall interactions. The corresponding strength was obtained by the product of the strength reduction factor and surrounding soils shear strength.

In general, the soil-wall interface strength is linked to the strength properties of the adjacent soil layer and is often reduced due to the disturbance caused by the wall construction. Its effects on the deep excavations (with depth being above 30 m) or circular shaft stability are rarely seen and will be discussed in this study.

1.3 Probabilistic analysis of supported excavations

Once the deterministic model is determined, the probabilistic analysis should be performed to take into account the soil variabilities. This section aims to provide some basic concepts and common methods of probabilistic analysis. An overview of the former probabilistic studies on excavations is then reviewed.

1.3.1 Reliability theory

In structural system analysis with uncertainty consideration, the structure can operate outside of its nominal range. In such cases, the system encounters a failure. A limit state should be defined for the classification of failure & safe domains.

The system response is related to a random vector ($\boldsymbol{x}$) which is composed of n random variables (x_1, x_2, …, x_n) and there exist two domains (safe domain and failure domain) in the input space defined by x. Taking n=2 as an example, a schematic illustration of the domains and Limit State Surface (LSS) is depicted in Fig. 1.13. $G(x)$ is called as a limit-state function or performance function, which is used to express the relationship between the limit state and the input variables. It can be observed that the estimations of function $G(x)$ are related to the system domain classification. The system is safe when the function $G(x)>0$ whereas the $G(x)<0$ corresponds to system failure. Correspondingly, the $G(x)$ is equal to 0 if the x is on the LSS.

The failure probability (P_f), which is defined as the probability of system response being in the failure domain, can be defined as

$$P_f = P(G(\boldsymbol{x}) \le 0) \tag{1.10}$$

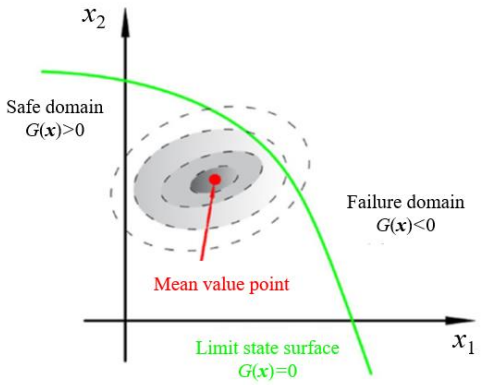

Fig. 1.13 Schematic illustration of the safe/failure region and LSS (Wang et al., 2021).

In a probabilistic setting, each uncertain parameter can be represented by a Probability Density Function (PDF) $X \sim f_X(x)$. Several input parameters, including their dependence structure, can be grouped in a random vector with a joint PDF $\boldsymbol{X} \sim f_{\boldsymbol{X}}(\boldsymbol{x})$. The P_f can then be determined by

$$P_f = \int_{G(\boldsymbol{x})\leq 0} f_X(\boldsymbol{x}) d\boldsymbol{x} \tag{1.11}$$

Considering the parameter distributions, the parametric distributions, which are defined by a set of parameters, are often used. Several commonly used parametric distributions (such as the Gaussian distribution, the lognormal or the uniform distributions) and the corresponding properties (e.g., PDF, cumulative distribution function (CDF), support and moments) are summarized in Table 1.2. The parametric distributions can be determined empirically or, when data sets are available that are relevant to the input parameters, the parameters of the estimated distribution are optimized to find the distribution that best matches the data.

Table 1.2 Commonly-used univariate probability distributions (Marelli and Sudret, 2014).

Distribution	Notation	Support	PDF	CDF	Moments
Uniform	$X \sim \mathcal{U}(a,b)$	$\mathcal{D}_X = [a,b]$	$f_X(x) = \begin{cases} \frac{1}{b-a} & \text{if } x \in [a,b] \\ 0 & \text{if } x \notin [a,b] \end{cases}$	$F_X(x) = \frac{x-a}{b-a}\mathbb{I}_{[a,b]}(x)$ $= \begin{cases} 0 & \text{if } x \leq a \\ \frac{x-a}{b-a} & \text{if } x \in [a,b] \\ 1 & \text{if } x \geq b \end{cases}$	$\mu_X = \frac{a+b}{2}$ $\sigma_X = \frac{b-a}{2\sqrt{3}}$
Gaussian (Normal)	$X \sim \mathcal{N}(\mu,\sigma)$	$\mathcal{D}_X = \mathbb{R}$	$f_X(x) = \frac{1}{\sigma\sqrt{2\pi}} e^{-\frac{(x-\mu)^2}{2\sigma^2}}$	$F_X(x) = \frac{1}{2}\left[1 + \text{erf}\left(\frac{x-\mu}{\sigma\sqrt{2}}\right)\right]$ $= \Phi\left(\frac{x-\mu}{\sigma}\right)$	$\mu_X = \mu$ $\sigma_X = \sigma$
Lognormal	$X \sim \mathcal{LN}(\lambda,\zeta)$	$\mathcal{D}_X = (0,+\infty)$	$f_X(x) = \frac{1}{\sqrt{2\pi}\zeta x} \exp\left(-\frac{(\ln x - \lambda)^2}{2\zeta^2}\right)$	$F_X(x) = \frac{1}{2} + \frac{1}{2}\text{erf}\left(\frac{\ln x - \lambda}{\sqrt{2}\zeta}\right)$ $= \Phi\left(\frac{\ln x - \lambda}{\zeta}\right)$	$\mu_X = e^{\lambda+\zeta^2/2}$ $\sigma_X = e^{\lambda+\zeta^2/2}\sqrt{e^{\zeta^2}}$
Exponential	$X \sim \mathcal{E}(\lambda)$	$\mathcal{D}_X = (0,+\infty)$	$f_X(x) = \lambda e^{-\lambda x}$	$F_X(x) = 1 - e^{-\lambda x}$	$\mu_X = 1/\lambda$ $\sigma_X = 1/\lambda$
Gamma	$X \sim \Gamma(\lambda,k)$	$\mathcal{D}_X = (0,+\infty)$	$f_X(x) = \frac{\lambda^k}{\Gamma(k)} x^{k-1} e^{-\lambda x}$	$F_X(x) = \frac{\gamma(k,\lambda x)}{\Gamma(k)}$	$\mu_X = \frac{k}{\lambda}$ $\sigma_X = \frac{\sqrt{k}}{\lambda}$

Conversely, the **non-parametric distribution** is a non-parametric method to infer a univariate distribution directly from data. Kernel Density Estimation (KDE), also known as kernel smoothing, is often used. It aims to approximate the true PDF of a variable by placing a "kernel" function at each data point, and then summing these functions to obtain an estimate of the PDF (Álvarez et al., 2011).

In addition, it is noted that a **truncated distribution** should be considered when the data is known to be limited to a certain range and the support of a probability distribution should be restricted (Tokmachev, 2018).

1.3.2 Characterization of the soil variability

The parameters uncertainties and randomness can be represented by random variables (RV) and random fields (RF) approaches as presented in Fig. 1.14. The RV approach assumes the soil as homogeneous for one simulation and is easy to generate different samples for a probabilistic analysis according to the given random variables' statistical information as summarized in Table 1.2. It is simple and was widely implemented in existing probabilistic analyses (Pan et al., 2020; T. Zhang et al., 2021b; Zhou et al., 2020).

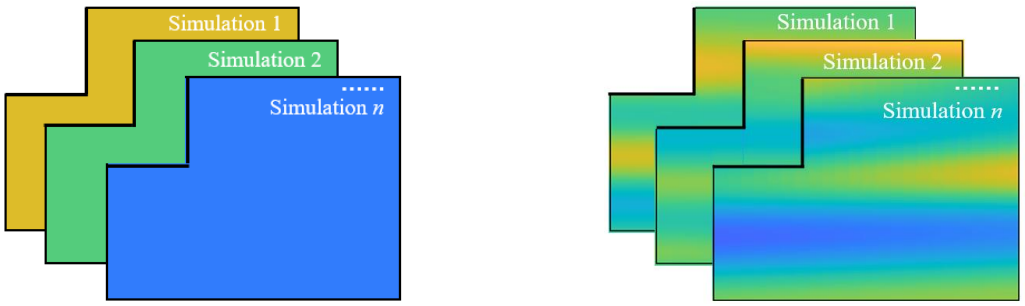

(a) RV (b) RF

Fig. 1.14 Comparison of RV and RF generation.

The RF approach, which can generate different values at different locations according to the given statistical properties and autocorrelation structures (autocorrelation function and autocorrelation lengths), can consider the soil spatial variability results from complex geological conditions (Xue et al., 2021). It is more reasonable to model the soil properties variation as it can give more consistent results when dealing with real projects. Several methods were developed for the discretization of random fields, including the point discretization methods (such as the midpoint and integration point), average discretization methods (such as the spatial average and weighted integral) and series expansion methods (such as the Karhunen-Loève expansion and expansion optimal linear estimation). Compared to the first two methods, which

are sensitive to the finite element mesh size and require a large number of random variables to obtain a good field approximation, the series expansion methods, are more efficient and will be used in this study. More details can be found in Chapter 6.

1.3.3 Reliability analysis methods

After the determination of the parameter uncertainties, a reliability analysis should be performed to deal with the quantitative assessment of the probability of failure occurrence. Three strategies are mainly used for the reliability analysis, including the approximation method, simulation method and active learning method. The corresponding introduction and methods used in this study are detailed below.

1.3.3.1 Approximation methods

Approximation methods approximate the limit-state function using linear or quadratic expansions at the design point $\boldsymbol{P}^*$ to estimate the system reliability. Two approximation methods are often used, including the First Order Reliability Method (FORM) and the Second Order Reliability Method (SORM).

The FORM includes an iterative gradient-based search for the design point and a local linear approximation of the limit-state function. The first step is to transform the input random vector X into a standard normal vector U using the iso-probabilistic transformation method as presented in Fig. 1.15 (Bourinet et al., 2018; Hamrouni et al., 2019; Wang et al., 2021).

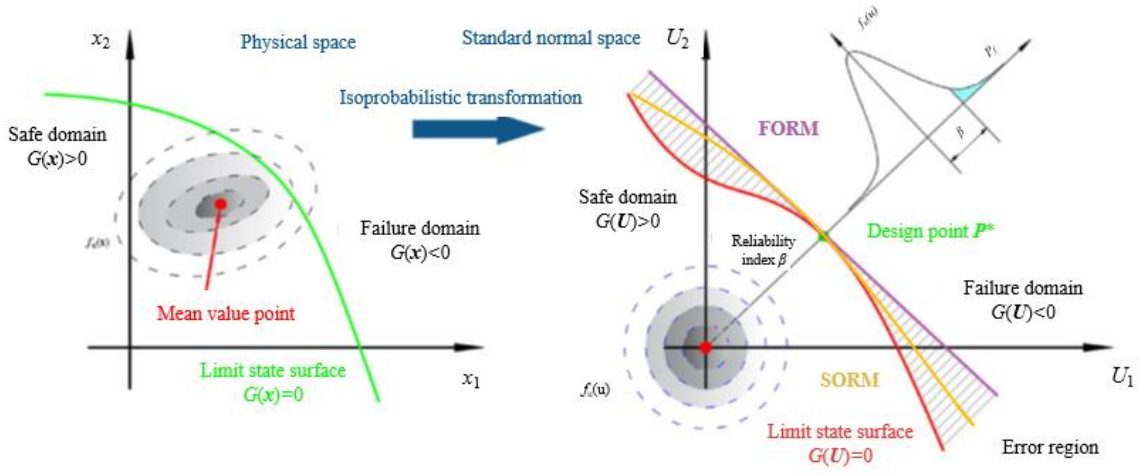

Fig. 1.15 Approximation of the LSS by FORM (Wang et al., 2021).

Then it aims at finding the point on the LSS that is closest to the origin in the standard normal space. This point is known as the design point in the reliability analysis and can be determined by

$$U^* = \arg\min\left\{\|u\|, G(u) \le 0\right\} \tag{1.12}$$

where $G(u)$ is the limit-state function evaluated in the standard normal space. Once the design point is found, the Hasofer-Lind reliability index β_{HL} can be determined as the norm of the design point, which can be expressed as

$$\beta_{HL} = \left\|U^*\right\| \tag{1.13}$$

It should be noted that the algorithm is iterated until some stopping criteria (about β, U and G) are satisfied as mentioned by Marelli and Sudret (Marelli and Sudret, 2014). The failure probability in the framework of FORM can be obtained by

$$P_f = \Phi(-\beta_{HL}) \tag{1.14}$$

where Φ denotes the standard normal cumulative distribution function.

Besides, the importance factor of each random variable can be defined as the fraction of the safety margin, whereas it is only effective for cases with independent input parameters (Marelli and Sudret, 2014).

The SORM is an extension of the FORM solution. It approximates the LSS by a tangent hyper-paraboloid at the design point identified by FORM as shown in Fig. 1.15. The probability of failure is finally computed from the curvatures of the parabola and the first-order reliability index (Hu et al., 2021). The commonly used SORM methods include Breitung's method (Breitung, 1984), Tvedt's method (Tvedt, 1990), Hohenbichler's method (Hohenbichler et al., 1987), etc. It is noted that the SORM can improve the results accuracy of FORM, while the computational costs associated with this refinement increase rapidly with the input random variables dimension (Marelli and Sudret, 2014).

The approximation methods are efficient since only a relatively small number of model evaluations are required for the determination of failure probability (or reliability index, design point, importance factor). They are popular due to the efficiency and the abundant analysis results which are useful in practical designs. However, the results tend to become unreliable for cases with a complex and highly non-linear LSS.

1.3.3.2 Sampling methods

Simulation methods provide more robust estimations compared to the approximation methods since this class of methods aim to draw samples randomly or intelligently from the joint PDF of input parameters, and the failure probability can be determined based on the corresponding system responses (Marelli and Sudret, 2014). The commonly used methods in the field of geotechnical reliability analysis encompass the Monte Carlo simulation (MCS), Subset Simulation (SS) (Au and Beck, 2001), Importance Sampling and Moment Methods. The MCS and SS used in this study are detailed.

The MCS is a simple sampling method that generates samples crudely as presented in Fig. 1.16(a) and evaluates the samples with a computational model to find an estimation of the failure probability P_f. It has been widely used in engineering and is often regarded as a standard reference to evaluate the accuracy of other probabilistic methods due to its simplicity and robustness. Besides, the MCS is independent of the LSS complexity and the problem dimension. P_f can be estimated by the fraction of samples that belong to the failure domain over the total number of samples, which can be expressed as

$$P_f = \frac{1}{N_{MCS}} \sum_{k=1}^{N_{MCS}} I_k \tag{1.15}$$

where N_{MCS} is the total number of samples, and the indicator function I_k is equal to 1 when the failure occurs, i.e. $I_k(G(x) < 0) = 1$, otherwise, the value of I_k is set to 0. It is noted that the calculated failure probability is biased when N_{MCS} is small, and on the contrary, a large number of samples can increase the computational effort. In order to balance the computational accuracy and efficiency, the coefficient of variation of P_f (COV_{P_f}) for MCS is given and can be defined by

$$COV_{P_f} = \sqrt{\frac{1 - P_f}{N_{MCS} P_f}} \tag{1.16}$$

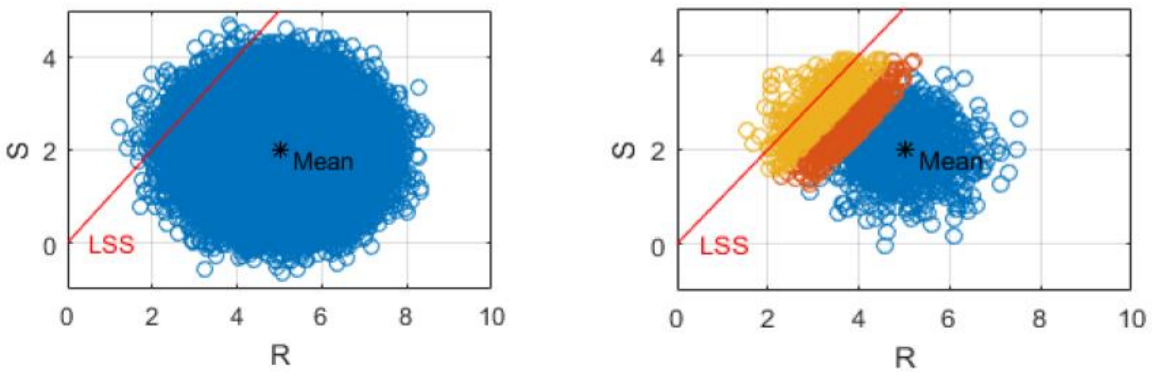

(a) MCS (b) SS

Fig. 1.16 Generated samples from MCS and SS (*R*-*S* problem) (Guo, 2020).

An improved sampling method, the Subset Simulation (denoted SS, also known as adaptive multilevel splitting), was then proposed by Au and Beck (Au and Beck, 2001) to reduce the variance of the MCS estimator with limited evaluations. It expresses a small failure probability as a product of larger conditional failure probabilities for some intermediate failure events. The probability of the failure can be expressed as

$$P_f = P(F_1)\prod_{i=2}^{m} P(F_i|F_{i-1}) \tag{1.17}$$

where m is the necessary number of levels to reach the real failure domain, $P(F_1)$ is the failure probability corresponding to the first level of SS which is often obtained by a direct MCS (blue samples presented in Fig. 1.16 (b)), $P(F_i|F_{i-1})$ is the intermediate conditional failure probability of the event $F_i|F_{i-1}$, and $F_i=\{G(x)<t_i\}$ $(i=1,2,...,m)$ is the intermediate failure domains defined by a failure threshold t_i. In practice, the value of t_i is selected to make the estimated results of $P(F_1)$ and $P(F_i|F_{i-1})$ are equal to a fixed value p_0 which is suggested as $0<p_0<0.5$, herein it is defined as a commonly specified value 0.1 (Marelli and Sudret, 2014). N deterministic slope stability analyses are required for the m levels of simulations (one direct MCS level and m-1 levels of conditional simulations):

$$N=N_l+(m-1)(1-p_0)N_l \tag{1.18}$$

where N_l is the number of samples at each level of SS, and the accuracy can be improved when the value of N_l is large enough, while it also makes the computation less efficient. This value is taken equal to 1000 based on the trade-off between computational accuracy and efficiency as recommended by Papaioannou et al. (2015).

1.3.3.3 Active learning methods

Active Learning Methods (ALM) is increasingly used for reliability analyses in recent years with the development of surrogate models as cheap proxies of computational models. The ALM aims to construct a surrogate model with an active learning method, which means that the experimental design of a surrogate model is sequentially enriched following a so-called learning function. The enrichment can then be stopped when the criteria are satisfied, otherwise, the new samples should be selected and enriched again. The reliability methods can then be performed based on the well-built surrogate models to provide the probabilistic results, such as the failure probability, reliability index, etc. The ALM consists of four main different models, which include:

(1) **Surrogate model**. It is a simplified or approximated model that is used to represent the behaviour of a more complex system since it is computationally less expensive to evaluate. They can be constructed using various techniques, such as polynomial regression, artificial neural networks, and kriging. The common surrogate models used for the probabilistic analysis include the Kriging (Guo and Dias, 2020; Schöbi et al., 2017; Zhou et al., 2020), Polynomial Chaos Expansions (PCE) (Guo et al., 2019a; Pan and Dias, 2017), Support Vector Machines (Kordjazi et al., 2014), etc.

(2) **Learning function**. It aims to find which new candidate enrichment points can bring the most useful information for the surrogate model construction (namely to reduce the surrogate model errors). It is often defined from the characteristics of the surrogate model, such as the variance or built-in errors. For instance, the local variance estimator of Kriging can be used for the learning process and the *U* learning function is developed by Echard et al. (2011). Besides, the Fraction of Bootstrap Replicates (FBR), which uses the bootstrap resampling technique, is also popular when the PCE metamodel is used (Marelli and Sudret, 2018).

(3) **Stopping criterion.** It is noted that too strict criteria can lead to more accurate results, whereas the enriched experimental design points and computational time will also increase. Conversely, overly loose stopping criteria can cause the results to converge prematurely. Therefore, the determination of the stopping criteria is an important part for the metamodel robustness and efficiency. The commonly used criteria include the stability-based criteria (which means that estimated failure probability or reliability index converges), and variance-based criteria, which are related to the surrogate-induced uncertainty in the estimates of the P_f or β (Marelli and Sudret, 2018).

(4) **Reliability estimation algorithm**. The commonly used approximation methods and sampling methods are introduced in Sections 1.3.3.1 and 1.3.3.2. All of them can be performed once the surrogate models are constructed well. Besides, the sensitivity analysis, which aims to quantify the input variables effects on the model response variability (more details can be found in Section 1.3.4), can also be performed benefiting from the high efficiency of surrogate models.

In this study, the active learning method which is based on the surrogate model construction, is mainly used. More detailed introduction and discussion can be found hereafter.

1.3.4 Sensitivity analysis methods

In a probabilistic analysis, it is also interesting to study how the input random variables affect the model response, which can be achieved by sensitivity analysis. It is often used to identify the most/less contributing inputs (or inputs that have the greatest/smallest impact on the output) or help the designers to reduce the dimension (model simplification) when the high-dimensional problem is discussed (Mishra, 2004). Numerous approaches are available (Marelli and Sudret, 2014). The local approach is the historical approach. It aims to study the impact of small input perturbations on the model output and the small perturbations tend to occur around nominal values (such as the mean of random variables). This approach involves estimating the partial derivatives of the model at a specific point or using the adjoint methods when there is an explicit adjoint formula (Iooss and Lemaître, 2015). However, this approach is not suitable to solve problems when a large number of input variables that are simultaneously varied on a wide domain or with non-linear behaviours.

To overcome the limitations of local methods (linearity and normality assumptions, local variations), the Global Sensitivity Analysis (GSA) is proposed to consider the entire space of all input variables and may refer to different features of the model output, such as variance or distribution. A variety of methods are available (Marelli and Sudret, 2014), for instance, the Sobol-based GSA (Sobol, 1993), ANCOVA method (Xu and Gertner, 2008), and Kucherenko method (Kucherenko et al., 2012). Sobol-based GSA is mainly used in this study since it receives much attention and can give accurate sensitivity indices among the GSA methods. Besides, it is efficiently post-processed on the PCE coefficients to estimate the Sobol indices without further deterministic calculation (Sudret, 2008).

The Sobol' indices are based on the variance decomposition of the model output and Sobol' decomposition can be expressed as

$$f(x_1, x_2, ...x_M) = f_0 + \sum_{i=1}^{M} f_i(x_i) + \sum_{i<j} f_{ij}(x_i, x_j) + ... + f_{1,2...M}(x_1, x_2, ...x_M) \quad (1.19)$$

where f () is the computational model, M is the input variables number, term f_0 is constant and equals to the expected value of $f(\boldsymbol{x})$, $f_i(x_i)$ is a function only related to x_i, $f_{ij}(x_{ij})$ is a function related to x_i, x_j, analogously, $f_{1,2...,M}(x_1, x_2, ...x_M)$ is a function of $\boldsymbol{x}$. The function of $f_i(x_i)$ represents the main effects, whereas the function with higher input dimension $f_{1,2...,M}(x_1, x_2, ...x_M)$ relates to interactions. Eq. (1.19) expands the model f () to a series of functions that are related to one or more variables and the expansions can be recursively computed by integrals as follows:

$$f_0 = \int f(\boldsymbol{x}) dx \quad (1.20)$$

$$f_i(x_i) = \int_0^1 ... \int_0^1 f(\boldsymbol{x}) d\,\boldsymbol{x}_{\sim i} - f_0 \quad (1.21)$$

$$f_{ij}(x_{ij}) = \int_0^1 ... \int_0^1 f(\boldsymbol{x}) d\,\boldsymbol{x}_{\sim ij} - f_0 - f_i(x_i) - f_j(x_j) \quad (1.22)$$

where notation ~ means that variables are excluded and the higher-order summands can then be constructed in an analogous way. The total variance can be defined as

$$V_t = \int f^2(\boldsymbol{x}) dx - f_0^2 \quad (1.23)$$

It can be further decomposed as

$$V_t = \sum_{i=1}^{M} V_i(Y) + \sum_{i<j}^{M} V_{ij}(Y) + ...V_{1,...M}(Y) \quad (1.24)$$

where Y is the model output, $V_i(Y)$ is the partial variance related to variable x_i which can be defined by $Var[E(Y \,||\, x_i)]$, where $E(Y \,||\, x_i)$ is the mean of Y with $\boldsymbol{x}_{\sim I}$ values and constant x_i, Var is the variance value. The first-order Sobol index, which represents the effect of x_i on the total variance, can then be expressed as

$$S_i = \frac{V_i}{V_t} \quad (1.25)$$

The higher-order Sobol index (such as S_{ij}) which considers the interaction effects among different variables, can also be determined analogously.

The total Sobol index of input variable x_i is the sum of all the Sobol index involving this variable (including the main and the interaction effects) and can be written as

$$S_t = S_i + \sum_{i \neq j} S_{ij} + ...S_{1...M} \quad (1.26)$$

It is noted that the input variables are supposed to be independent. For the cases with consideration of input variables dependency, the Kucherenko method is recommended (Kucherenko et al., 2012).

1.3.5 Previous studies about probabilistic analysis of supported excavations

This section aims to provide a literature review of the existing studies about the supported excavations stability in a probabilistic framework, which include: (1) probabilistic analysis of excavations considering the basal heave stability; (2) probabilistic serviceability assessment of excavations; (3) probabilistic analysis of excavations considering spatial variability.

1.3.5.1 Probabilistic basal heave stability analysis

Several works were done for the supported excavations basal heave stability analysis in probabilistic framework and the existing scientific studies are summarized in Table 1.3. It is seen the studies are related to the rectangular-shaped excavations and the deterministic analysis is often implemented by the analytical methods as presented in Section 1.2.1, such as the Terzaghi method, the Bjerrum & Eide method and the slip circle method. However, the probabilistic stability analysis of circular shafts is rarely discussed. Besides, the undrained case is often discussed and the undrained shear strength is considered as a random variable. The influence of hydraulic effects on the stability of circular shafts and the corresponding uncertainties are less discussed. In addition, concerning the probabilistic methods, the FORM and MCS are mainly carried out. In order to improve the calculation efficiency, the surrogate model-based methods are expected to be provided in this study. The corresponding studies will be presented in Chapters 2, 4 and 5.

Table 1.3 Summary of previous probabilistic basal heave stability analysis.

No.	Case	Deterministic method	Input random variables	Probabilistic method	Research findings
1	RE (Goh et al., 2008)	Terzaghi method, Bjerrum & Eide method	Undrained shear strength, unit weight, loading	FORM	Same factor of safety can have vastly different levels of risk, depending on the degree of uncertainty of the design parameters
2	RE (Tang and Kung, 2011)	Slip circle method	Undrained shear strength	MCS	Different design codes can lead different failure probabilities
3	RE (Wu et al., 2011)	Slip circle method,	Undrained shear strength	FORM	Modified Terzaghi's equation is the least biased with a reasonably small model variation

		Modified Terzaghi method, Bjerrum & Eide method			
4	RE (Tang and Kung, 2012)	Slip circle method	Undrained shear strength	MCS	Probability of basal heave safety factor being higher than 0.95 with respect to FS=1.2 when the COV is assumed to be in the range of 0-0.3
5	RE (Wu et al., 2014)	Terzaghi method, Bjerrum & Eide method, Slip circle method	Undrained shear strength	MCS	Required factor of safety depends on: (a) the target reliability index and (b) the *COV* of the calculated safety factor
6	RE (Chowdhury, 2017)	Slip circle method	Undrained shear strength, unit weight	FORM	Effects of undrained shear strength are more significant compared to the unit weight; Some design tables are provided (for different combination of the design parameters)
7	RE (Goh, 2017a)	Finite element analyses, Slip circle method, modified Terzaghi method	Undrained shear strength, unit weight, loading	FORM	Interface between the jet grout slab and the wall is a key component of the resistance of the excavation system to basal heave failure
8	RE (Zhou et al., 2018)	Slip circle method, Terzaghi method, Bjerrum & Eide method	Undrained shear strength, unit weight, loading	MCS	Slip circle method is more economical than the other two methods; Terzaghi method is more sensitive to the penetration depth of the wall than the other two methods

1.3.5.2 Probabilistic serviceability assessment

Concerning the probabilistic serviceability assessment of supported excavations, the maximum horizontal wall deflection or ground surface settlement is usually considered of primary importance. In order to consider the wall type, the location, the foundation systems and the existing condition of the structures, the numerical simulations are often implemented. Zhang et al. (2015b) presented a probabilistic assessment of serviceability limit state of diaphragm walls for braced excavations. A polynomial regression (PR) model considering the excavation width, excavation depth, soft clay thickness, soil unit weight and the system stiffness, is developed based on more than 1,000 FEM simulations using the hardening small strain (HSS) model. The FORM and MCS are then implemented to give probabilistic results. The effects of threshold values on the failure probability are presented in Fig. 1.17(a). It is seen that a small limiting value can lead to a higher failure probability, and the failure probability values decrease with the increase of thresholds. The threshold values can be determined by the target reliability index as presented in Fig. 1.17(b).

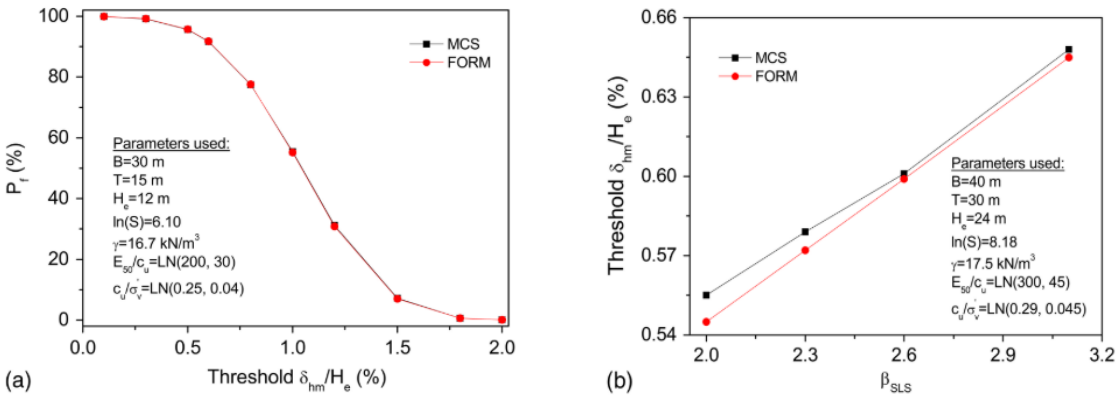

(a) Threshold influence on failure probability (b) Determination of threshold based on the target reliability index

Fig. 1.17 Influence of threshold values (Zhang et al., 2015b).

Tang (2011) analysed the probabilistic stability of Formosa excavation in Taiwan. The MCS was used for the probabilistic analysis and the results indicated that the acceptable number of simulations for the excavation-induced deformation analysis is 1000. The exceedance probability of wall deflection caused by excavation is estimated. Based on this case, Luo and Das (2015) considered the horizontal wall deflection and ground surface settlement in probabilistic stability analysis. The deterministic model is constructed by FEM and the normalized undrained shear strength and normalized initial tangent modulus are modelled by random variables. The relationship between the system failure probability and the limiting wall deflection & surface settlement can be observed in Fig. 1.18. It is seen that for a given level of ultimate wall deflection, the failure probability initially decreases as the ultimate ground settlement increases. Whereas a further increase in limiting ground settlement cannot result in any change in the failure probability of the system after the ultimate ground settlement exceeds a critical value.

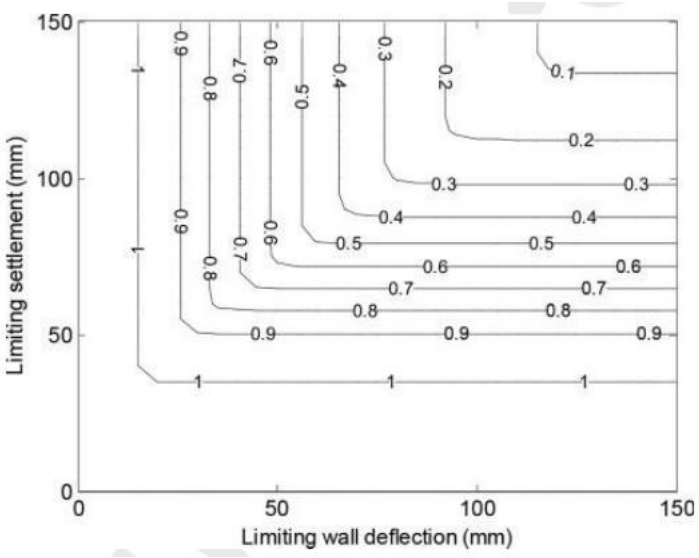

Fig. 1.18 System probability of serviceability failure contour at various combinations of limiting wall deflection and limiting ground surface settlement (Luo and Das, 2015).

The excavation depth of above-mentioned studies is in the range of [9 m, 24 m], whereas the supported excavations at large depths (above 30 m) are rarely discussed. This study will analyse the stability of a great-depth FIVC excavation (32 m) of the Grand Paris project in France and is expected to provide some practical suggestions for cases with similar conditions at least in a preliminary stage. The corresponding studies can be found in Chapter 3.

1.3.5.3 Probabilistic analysis with consideration of spatial variability

Due to complex geological processes (deposition, sedimentation, weathering and biological effects), the physical and mechanical soil properties can be significantly different from one location to another (T. Zhang et al., 2021a). Probabilistic analyses considering the soil spatial variability are becoming increasingly popular in excavation designs and permit to provide more accurate results. Some relevant studies have been done in terms of the basal heave stability analysis and serviceability assessment.

Table 1.4 gives a summary of the **probabilistic basal heave stability analysis** for supported excavations with consideration of the spatial variability. Similar to the random variable case, the existing studies are related to the rectangular-shaped excavations and the deterministic analysis is often implemented by the analytical methods. Most of them used the slip circle method since it can easily account for the soil spatial variability and the (normalized) undrained shear strength is modelled by the RF approach. Fig. 1.19 depicts a stationary lognormal RFs generated by the Cholesky decomposition method (Luo et al., 2012b). Besides, the FORM or

MCS are mainly used for the evaluation of the basal heave failures in spatially variable soils. All studies indicated that the neglect of spatial variability can make the basal heave stability design conservative.

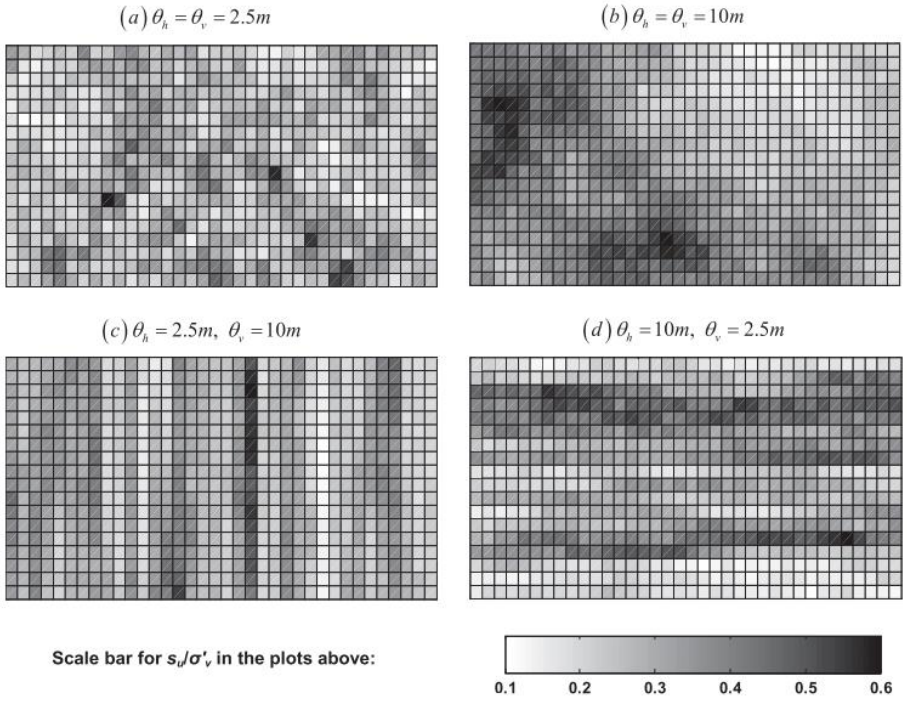

Fig. 1.19 RF realizations of Normalized undrained shear strength for different scales of fluctuation (Luo et al., 2012b).

Table 1.4 Summary of probabilistic basal heave analyses considering spatial variability.

No.	Case	Deterministic method	Input random variables	Random field consideration	Probabilistic method	Research findings
1	RE+undrained (Wu et al., 2012)	Slip circle method	Undrained shear strength	Vertical	MCS	Ignorance of spatial variability can make the calibrated required safety factor conservative
2	RE+undrained (Luo et al., 2012a)	Slip circle method	Normalized undrained shear strength	Vertical	FORM	Basal-heave stability design will be too conservative if the effect of spatial variability is ignored
3	RE+undrained (Luo et al., 2012b)	Slip circle method	Normalized undrained shear strength, unit weight, loading	Vertical + horizontal	MCS	Negligence of the model bias of the slip circle method leads to an overestimation of failure probability

4	RE+undrained (Luo et al., 2012c)	Slip circle method	Normalized undrained shear strength	Vertical + horizontal	MCS	Negligence of the 2D spatial random effect could yield a basal-heave design that is over-conservative
5	RE+undrained (Tang and Kung, 2014)	Slip circle method	Normalized undrained shear strength	Vertical	MCS	Probability of basal heave failure tends to be overestimated if the effect of spatial variability is neglected.
6	RE+undrained (Goh et al., 2019b)	Modified Terzaghi method	Undrained shear strength	-	FORM	Compared to the FEM, the predictions based on the Terzaghi method and the slip circle method are more conservative and the reliability index is significantly influenced by the spatial variability of the different soil layers

The studies of **probabilistic serviceability assessment** considering the spatial variability are summarized in Table 1.5. The Random Finite Element Method (RFEM), which combines the random field simulation with the finite element method, is often implemented. This is because RFEM accounts for the soil inherent randomness and variability, boundary conditions, complex geometrical and geological conditions and other parameters that affect the behavior of structures (Fenton and Griffiths, 2010). It has also been widely used in foundations (Li et al., 2016; Pieczyńska-Kozłowska and Vessia, 2022; Selmi et al., 2019), slopes (Burgess et al., 2019; Griffiths et al., 2009; Gu et al., 2023; Wijesinghe et al., 2022) and tunnels (Cheng et al., 2019; Pan and Lee, 2019).

Luo et al. (2011b) and Dang et al. (2014) adopted a spatial averaging technique to characterize the vertical spatial variations of soil properties. The spatial variability effects on the variability of excavation responses (wall deflection and ground settlement) are depicted in Fig. 1.20. It is seen that the excavation responses will be overestimated when the spatial variability is ignored. The Cholesky decomposition method was implemented by (Luo et al., 2018a, 2018b; Sert et al., 2016) and vertical random field of soil properties was modelled in these studies; Papaioannou and Straub (2012) performed the stochastic discretization of the non-Gaussian random fields to represent the spatial variability of the uncertain material parameters. Bayesian updating with equality information was applied to handle efficiently reliability problems with a large number of random variables; Gholampour and Johari (2019) generated the conditional random fields

using the sequential Gaussian simulation to analyse the excavation stability considering rough and perfectly smooth interfaces; Nguyen and Likitlersuang (2021) presented the reliability analysis of deep excavations using two-dimensional RFEM. The spatial variability of the undrained shear strength was simulated by Cholesky decomposition technique.

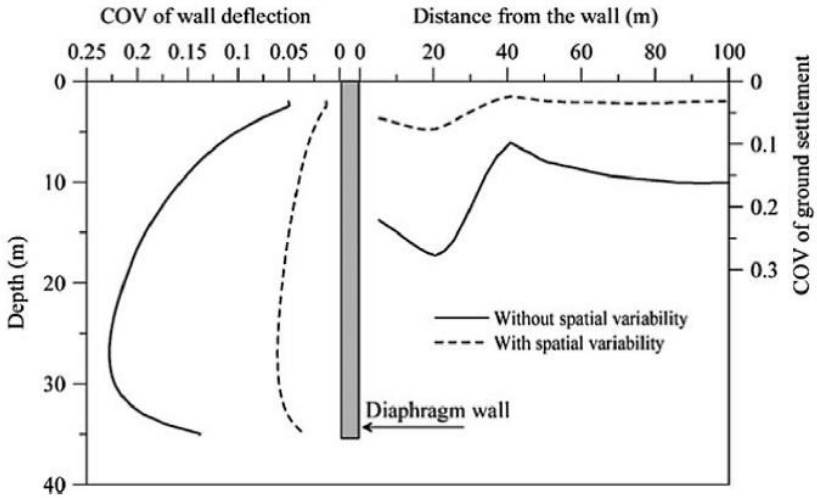

Fig. 1.20 Spatial variability effects on the variability of excavation responses (Dang et al., 2014).

Table 1.5 Summary of probabilistic serviceability assessment considering spatial variability.

No.	Case	Deterministic method	Input random variables	Random field consideration	Probabilistic method	Research findings
1	RE (Luo et al., 2011b)	FEM (PLAXIS)	Normalized undrained shear strength normalized initial tangent modulus	Vertical	MCS	Neglecting spatial variability of input soil parameters can lead to an overestimation of variation of wall and ground responses
2	RE (Papaioannou and Straub, 2012)	FEM (SOFiSTiK)	Weight, Young's modulus, friction angle	Vertical + horizontal	Bayesian updating with equality information	Consider different deformation measurement outcomes at an intermediate construction stage
3	RE (Dang et al., 2014)	FEM (PLAXIS)	Soil stiffness, undrained shear strength	Vertical	FORM	With consideration of the spatial variability, smaller variation and *COV* in the predicted responses are observed
4	RE (Sert et al., 2016)	FEM (PLAXIS)	Friction angle	Vertical	MCS	Neglecting spatial soil variability results in either overestimation or underestimation of the probability of serviceability failure

						depending on the chosen limiting values
5	RE (Luo et al., 2018b)	FEM (PLAXIS)	Standard penetration blow count (N1)60	Vertical	MCS	Spatial variability has a significant impact on multiple excavation-induced responses
6	RE (Luo et al., 2018a)	FEM (PLAXIS)	Normalized undrained shear strength, normalized secant modulus	Vertical	MCS	Spatial variability in soil properties is ignored, the failure probability can be either overestimated or under- estimated, depending on the specific limiting criteria
7	RE (Gholampour and Johari, 2019)	FEM	Bulk density, water content, fine-grained content, density, cohesion, friction angle	Vertical + horizontal	MCS	Suction has important effects on the excavation responses, and cannot be overlooked when conducting a reliability assessment of braced excavation in spatially varying unsaturated soils.
8	RE (Nguyen and Likitlersuang, 2021)	FEM (PLAXIS)	Undrained shear strength	Vertical + horizontal	MCS	Spatial variability of the undrained shear strength has a significant influence on simulated lateral wall movements and ground surface settlements.

These above-mentioned random field studies improve the excavation stability analysis considering soil spatial variability, however there are still aspects that should be addressed. The major concern is the probabilistic methods, the existing studies mainly used the MCS, which lacks computational efficiency, and FORM, which may fail to give accurate estimates for non-linear limit state surface cases. The active learning methods are necessary for the efficiency improvement of probabilistic analyses. The other one is the lack of research on the selection of input parameters that are simulated by the random field approach. A sensitivity analysis is preferred for the parameters importance determination to select the important parameters that have a significant impact on the model response. For the basal heave stability analysis, the probabilistic stability analysis of circular shafts considering the spatial variability can be found in Chapter 7. For the serviceability assessment, a real case study with great depth will be discussed in Chapter 6.

1.4 Machine learning-based excavation analyses

In recent years, with rapid development of scientific computing software, Machine learning (ML) has received much attention in geotechnical engineering due to its high efficiency, flexibility and predictive capacity. It can be used to find solutions, recognize patterns, classify data or predict future events (Gordan et al., 2016; Sasmal and Behera, 2021). It has been extensively used in different geotechnical works, such as the slopes (Mahmoodzadeh et al., 2022), tunnels (He et al., 2023; Qu et al., 2023), underground mines (Li et al., 2021a), footings (Zhang et al., 2022) and embankments (Kłosowski and Rymarczyk, 2022).

ML has also been introduced for the excavation performance assessment and Table 1.6 gives a summary of the machine learning methods application on the supported excavations. It can be observed that numerous machine learning methods have been developed in existing literatures to analyse the excavation stability. Among the methods, the ANN is one of the most popular ML methods due to the simplicity and efficiency. Besides, most of the studies are related to the predictions of the retaining wall deflections and ground surface settlements for the rectangular-shaped excavations. However, the circular shafts (axis-symmetrical conditions) stability assessments are rarely discussed.

Table 1.6 Application of the machine learning methods on the supported excavations.

No.	Case	Input Parameters	Predictions	Analysis method	Number of cases
1	RF (Goh et al., 1995)	Excavation width, depth, soil stiffness, shear strength, unit weight	Horizontal wall deflection	ANN	253
2	RF (Jan et al., 2002)	Wall thickness, excavation depth, excavation stages	Horizontal wall deflection	ANN	1767
3	RF (Leu and Lo, 2004)	Construction method, excavation depth	Ground surface settlement	ANN	146
4	RF (Chua and Goh, 2005)	Soil strength, the soil modulus, the in-situ stress condition, the wall and support stiffness, the depth and width of excavation	Horizontal wall deflection	EBBP	3844
5	RF (Hsiao et al., 2006)	Soil shear strength, initial stiffness, wall thickness and excavation width	Horizontal wall deflection	ANN	720
6	RF (Kung et al., 2007b)	Excavation depth, system stiffness, excavation width, shear strength, Young's modulus	Horizontal wall deflection	ANN	3486
7	RF (Jun et al., 2009)	Cohesion, internal friction angle, natural gravity, foundation pit's length, foundation pit's width, foundation pit's depth,	Ground surface settlement	ANN	23

		groundwater level, permeability coefficient, piles diameter, and buried depth			
8	RF (Cheng and Wu, 2009)	Wall thickness, excavation depth	Horizontal wall deflection	SVM	1083
9	RF (Zhang, 2017)	Excavation depth, width, system stiffness, unit weight, undrained shear strength	Horizontal wall deflection	MARS	-
10	RF (Zhang et al., 2017)	Excavation width; excavation depth; soft clay thickness; soil unit weight; system stiffness	Inverse analysis of soil and wall properties	MARS	1032
11	RF (Zhang et al., 2019)	Soil type, wall stiffness, excavation length, excavation depth	Horizontal wall deflection	MARS	90
12	RF (R. Zhang et al., 2021)	Excavation width, wall stiffness, wall penetration, soil parameters, shear modulus over active shear strength	Horizontal wall deflection	XGBoost RFR DTR MLPR MARS	1778
13	RF (Zhao et al., 2021)	Field measurement for different construction procedure	Horizontal wall deflection	ANN LSTM GRU	7728

Note: ANN: Artificial Neural Network; EBBP: Bayesian back-propagation neural network; SVM: Support Vector Machine; MARS: Multivariate Adaptive Regression Spline; RFR: Random Forest Regression; DTR: Decision Tree Regression; MLPR: Multilayer Perceptron Regression; LSTM: Long Short-Term Memory; GRU: Gated Recurrent Unit.

The machine learning techniques have also been applied for the probabilistic analyses with consideration of the soil variabilities. The ML methods are used for the surrogate model construction, the probabilistic methods are then performed to provide probabilistic results. Goh and Kulhawy (2005) used an integrated neural network-reliability method to assess the risk of serviceability failure through the calculation of the reliability index. Performing a series of parametric studies using the finite element method to discuss the probability of exceeding the limiting lateral wall deflection for sheet pile wall; Huang and Wang (2007) analysed the excavation stability using the ANN-based FORM and ANN-based MCS, and found the probabilistic methods based on the ANN are superior to direct reliability methods, since the ANN provides a surrogate model to predict the model response in a fast way; Li et al. (2021b) build the surrogates models for the hard rock pillar strength predictions based on the SVM and BPNN methods, the MCS is then conducted to complete the stochastic assessment; Qu et al. (2023) assessed the twin tunnels stability considering the fluid-solid coupling in deterministic and probabilistic frameworks. The physics-guided machine learning method is used for the metamodel construction based on 1000 groups of input combinations generated by the finite element method. The MCS is then performed to assess the probabilistic tunnel stability.

Most probabilistic studies often determined the deterministic evaluations samples for the ML-based surrogate model construction in advance and thousands of simulations are often considered to ensure the model accuracy. It cannot reduce significantly the probabilistic computational effort. In order to overcome this limitation, the iterative probabilistic procedures based on ANN models are proposed. Cho (2009) considered the slope stability problems with uncertain quantities through a practical procedure that combined a commercial numerical analysis code and artificial neural networks into the probabilistic analysis of slope stability. An ANN technique was adopted to establish a model for the approximation of the limit state function. Training and test data sets for the model were obtained from numerical calculations. The samples are enriched to the datasets until the probabilistic results are stable. Probabilistic stability assessments for a hypothetical two-layer slope as well as for the Cannon Dam in Missouri, USA were performed to verify the application potential of the proposed method; Lü et al. (2012) proposed an efficient approach for probabilistic ground-support interaction analysis of deep rock excavation using the ANN-based response surface and uniform design. The uniform design table is used to prepare the sampling points for training the ANN and for determining the parameters of the network via an iterative procedure. The iterations will be stopped when the probabilistic results start to converge and the flowchart is given in Fig. 1.21. The efficiency of this proposed procedure is then validated by comparing the results of the FORM/SORM based on the generated ANN response surface with the MCS and polynomial response surface method.

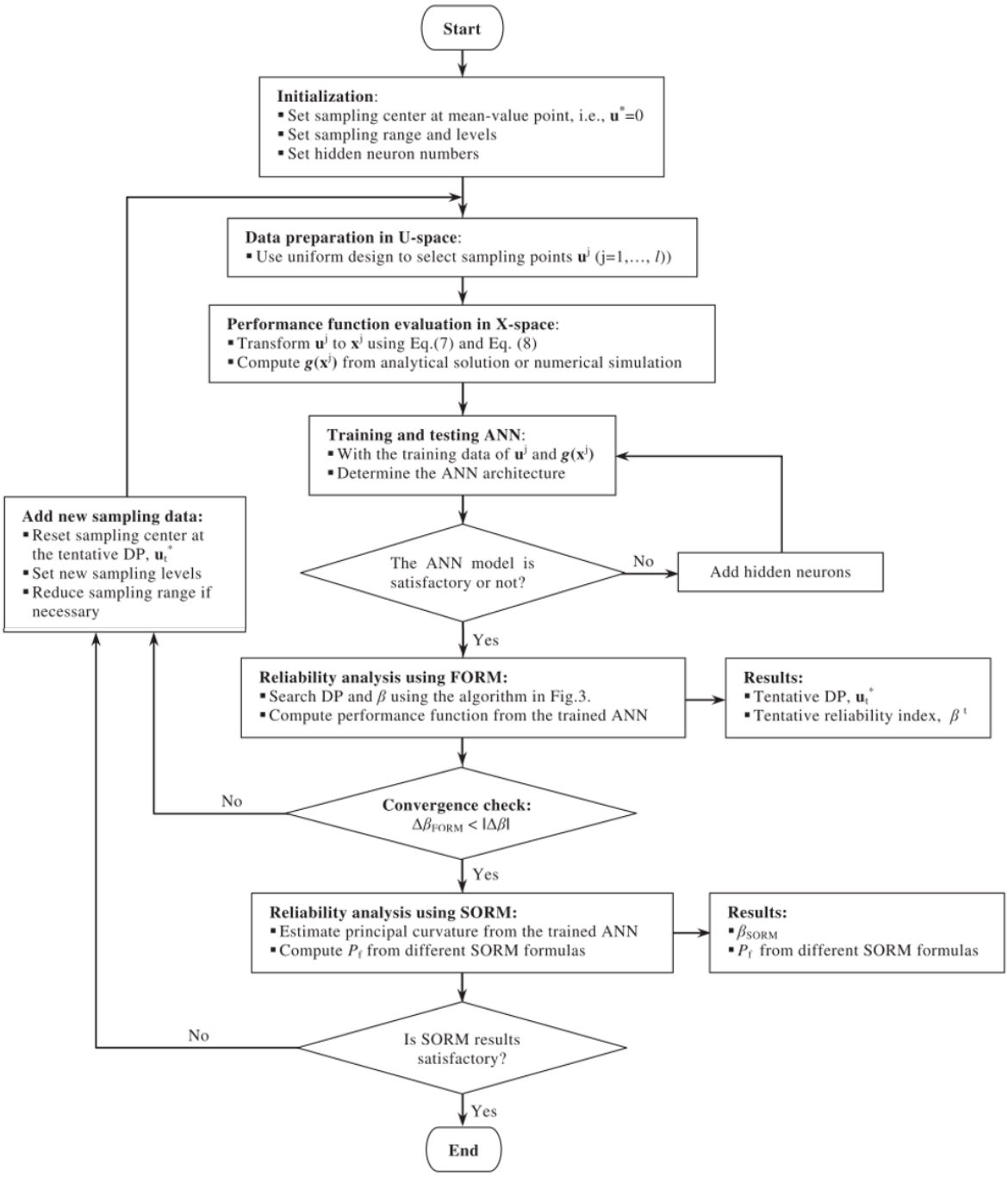

Fig. 1.21 The procedure presented in (Lü et al., 2012).

The adaptive probabilistic methods can provide probabilistic results with minimal deterministic simulations and guaranteed accuracy, which improve the efficiency of ANN applications in geotechnical engineering. However, there are still two aspects that could be further improved, which include: (1) the procedure can only be considered in low-dimensional cases (random variables number < 20) and is limited for high-dimensional problems (such as the random field case). This is because the ANN model was used to approximate the real limit state surface and the approximation methods were then performed to determine the reliability index. It is noted

that for high-dimensional problems, the approximation methods tend to become unreliable due to the presence of complex non-linear limit-state surfaces (Marelli and Sudret, 2014). To avoid dimensional restraints, the combination of the ANN and the crude MCS is performed in this study; (2) the existing studies often use single basic machine learning methods. With the development of computer science, novel hybrid methods can be applied to improve calculation efficiency and stability. Atom Search Optimization (ASO)-ANN method will be introduced and implemented in this study, which exhibits better adaptive convergence and efficiency in optimizing neuron network parameters (W. G. Zhao et al., 2019). The improvements can be found in Chapter 7.

1.5 Conclusion

Supported excavation analyses (rectangular excavation and circular shaft) in deterministic and probabilistic frameworks are presented. The field observations, laboratory-scale physical tests, analytical/empirical methods and numerical simulations are used for the deterministic analyses. The probabilistic methods, which include the reliability methods (approximation method, simulation method and active learning method) and sensitivity analysis methods, are then introduced. Some previous probabilistic studies of supported excavations are reviewed and the advantages/limitations are discussed. In order to address the existing studies limitations and to better understand the supported excavations stability under different conditions, the supported excavation stability analyses in deterministic and probabilistic frameworks are presented in the following chapters.

Chapter 2

Stability analysis of rectangular excavations in undrained conditions

Contents

2.1 Introduction 74

2.2 Development of limit analysis model 74

2.2.1 Improved limit analysis 74

2.2.2 Deterministic model comparison 78

2.3 Proposed probabilistic analysis framework 84

2.3.1 Polynomial Chaos Kriging 84

2.3.2 Probabilistic analysis framework 86

2.3.3 Comparison and discussion of the probabilistic results 88

2.4 Parametric study 91

2.5 Conclusion 93

2.1 Introduction

This chapter presents deterministic and probabilistic methods for the supported excavation stability analysis considering a two-dimensional plane-strain configuration. An improved limit analysis mechanism (ILA) is proposed first based on the existing limit analysis mechanism to assess their basal heave safety factor under undrained conditions. A comparative study with numerical simulation and three limit equilibrium methods, including the modified Terzaghi method, the modified Bjerrum & Eide method and the slip circle method, is carried out to validate the proposed ILA effectiveness.

In the probabilistic framework, an active learning method based on the Polynomial Chaos Kriging model is introduced to improve the efficiency of the probabilistic results estimation. Academic cases are then conducted to get some insights into the efficiency and accuracy of the probabilistic framework compared with the direct probabilistic methods, such as the direct Monte Carlo Simulation. Benefiting from the high efficiency, the effects of the wall embedment depth, shear strength coefficient of variation, and soil-wall interface on the excavation stability are then discussed.

2.2 Development of limit analysis model

2.2.1 Improved limit analysis

Chang (2000) and Cai et al. (2018) discussed the basal heave stability using the limit analysis method based on the failure mechanism illustrated in Fig. 2.1(a). H and B are respectively the excavation depth and width. B_1 refers to the distance from the wall to the vertical failure surface *fi*. D is the wall embedment depth, and T is the depth from the wall bottom tip to the hard stratum. The wall is assumed to be fully rigid and the lateral resistance afforded by the wall is not considered, which means that the wall moves along the vertical direction while it is motionless in the horizontal direction (Faheem et al., 2003; Huang et al., 2018).

The existing limit analysis (ELA) mechanism consists of a 90^o circular arc (*jkh*) sandwiched between two 45^o isosceles wedges (*ijk* and *gjh*), soil columns *efij* and *mljg*. v is the velocity of plastic flow and the safety factor can be determined by the ratio of the internal energy dissipation E and the external work rate W. The safety factor $F_{s\text{-ELA}}$ can be calculated using Eq.

(1.9). B_1 is set to B when a hard stratum is present at a depth of $T \geq T_c$, otherwise, $B_1 = \sqrt{2}T$ ($T < T_c$), T_c is the critical hard stratum depth from the wall bottom tip and is equal to $B/\sqrt{2}$.

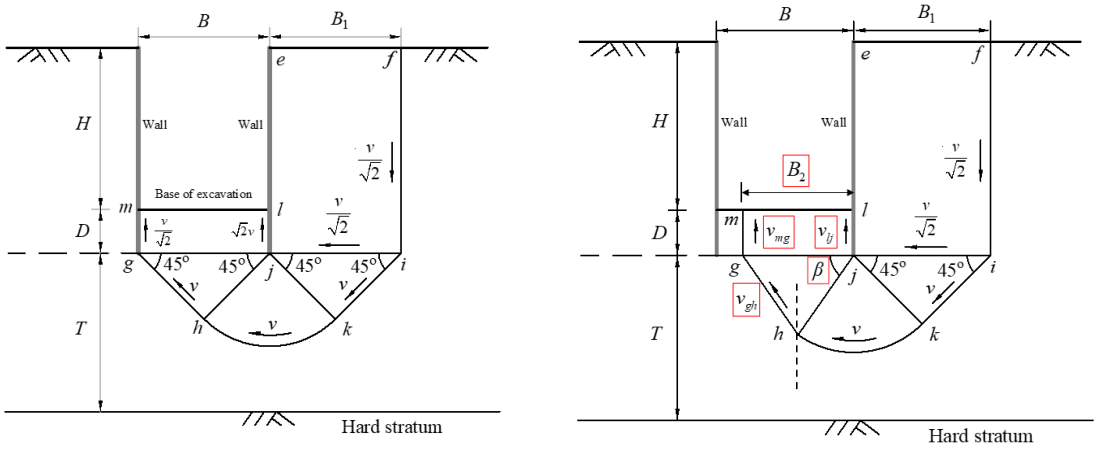

(a) Existing (ELA) (b) Improved (ILA)

Fig. 2.1 Limit analysis failure mechanism.

It should be noted that the triangular wedges *ijk* and *gjh* of the existing failure mechanism are defined by a constant angle of 45°. However, this mechanism may change in different excavations with different geometry or soil parameters. In order to assess excavation stability more accurately, the improvements to the failure mechanism are necessary.

This study proposed a failure mechanism as depicted in Fig. 2.1(b). It can be found that the isosceles triangle *gjh* is determined by a variable angle β varying in the range (0, π/2) and the circular arc angle (*hjk*) is then equal to $3\pi/4-\beta$. The value of B_2 can then be defined as

$$B_2 = \sqrt{2}B_1 \cos\beta \tag{2.1}$$

B_1 is equal to B in the existing failure mechanism when $T \geq T_c$. However, the plastic area behind the wall is often larger than B (Huang et al., 2011) since it is also related to the wall penetration depth and the value of B_1 is normally increased as the penetration depth increases. It is more reasonable to consider the corresponding effects and set it to be $B+0.5D$ in this improved failure mechanism.

The value of β under different cases (different undrained shear strength, excavation depth, width and wall embedment depth) can be optimized by the work rate balance equation of upper bound limit analysis. It states that the external work rate W is no more than the energy dissipation E. Otherwise, the failure occurs due to the excessive external work rate (Hou et al., 2019). Therefore, the values of W and E should be evaluated.

Herein, the external work rate is provided by the blocks weight (*efij*, *ijk*, *jkh*, *gjh* and *mljg*) respectively denoted by dW_i ($i \in [1, 5]$) and can be expressed as

$$efij: dW_1 = \gamma(H+\mathrm{D})B_1 \frac{v}{\sqrt{2}} \tag{2.2}$$

$$ijk: dW_2 = \gamma \cdot \frac{1}{2} \cdot (\frac{B_1}{\sqrt{2}})^2 \cdot \frac{v}{\sqrt{2}} = \frac{1}{4\sqrt{2}} \gamma B_1^2 v \tag{2.3}$$

$$jkh: dW_3 = \int_{\frac{\pi}{4}}^{\pi-\beta} \gamma \cdot \frac{1}{2} \cdot (\frac{B_1}{\sqrt{2}})^2 \cdot v \cos\theta d\theta = \frac{1}{4} \gamma B_1^2 v \int_{\frac{\pi}{4}}^{\pi-\beta} \cos\theta d\theta \tag{2.4}$$

$$gjh: dW_4 = -\gamma \cdot \frac{1}{2} \cdot B_2 \cdot \frac{B_2}{2} \cdot \tan\beta \cdot v_{gh} \sin\beta = -\frac{1}{4} \gamma B_2^2 v_{gh} \sin\beta \tan\beta \tag{2.5}$$

$$mljg: dW_5 = -\gamma D B_2 v_{mg} \tag{2.6}$$

where γ is the unit weight of the soil (kN/m^3). The total external work rate can be obtained by the work rate summation of these 5 blocks

$$W = \sum_{i=1}^{5} dW_i \tag{2.7}$$

The internal energy dissipation E is deduced from the sliding along *fi*, *ij*, *ik*, *hg*, *mg*, *lj* and the arc *kh* combined with the radial shear sliding (radial shear zone *jkh*), which are denoted by dE_j ($j \in [1, 8]$) and expressed as follows

$$fi: dE_1 = \frac{1}{\sqrt{2}} (H + D) S_u v \tag{2.8}$$

$$ij: dE_2 = \frac{1}{\sqrt{2}} B_1 S_u v \tag{2.9}$$

$$ik: dE_3 = \frac{1}{\sqrt{2}} B_1 S_u v \tag{2.10}$$

$$hg: dE_4 = \frac{1}{2\cos\beta} B_2 S_u v_{gh} \tag{2.11}$$

$$mg: dE_5 = r_i D S_u v_{mg} \tag{2.12}$$

$$lj: dE_6 = r_i D S_u v_{lj} \tag{2.13}$$

$$kh: dE_7 = \int_{\frac{\pi}{4}}^{\pi-\beta} \frac{B_1}{\sqrt{2}} \cdot Su \cdot v d\theta \tag{2.14}$$

$$jkh: dE_8 = \int_{\frac{\pi}{4}}^{\pi-\beta} \int_{H+D}^{H+D+\frac{B_1 \sin\theta}{\sqrt{2}}} Su \cdot v \cdot \frac{1}{\sin\theta} dz d\theta \tag{2.15}$$

where S_u is the undrained shear strength (kPa) and r_i is the soil-wall adhesion coefficient. It is introduced since the soil-wall interface strength is reduced due to the wall construction disturbance and is often considered to be proportional to the adjacent soil strength, i.e. $r_i S_u$. The velocity along *gh*, *mg* and *lj* can be respectively determined by

$$v_{gh} = \frac{v}{\sin(\pi - 2\beta)} \tag{2.16}$$

$$v_{gm} = \frac{v}{\sin(\pi - 2\beta)} \sin\beta \tag{2.17}$$

$$v_{lj} = (\frac{1}{\sin(\pi - 2\beta)} \sin\beta + \frac{1}{\sqrt{2}}) v \tag{2.18}$$

Like the external work rate calculation, the energy dissipation can also be obtained by the summation of the elementary work rate dE_j. The total energy dissipation finally writes

$$E = \sum_{j=1}^{8} dE_j \tag{2.19}$$

The safety factor can then be obtained by performing an optimization work with respect to the variable (i.e. β) and expressed as

$$F_{s\text{-ILA}} = \frac{E}{W} = f(\beta) \tag{2.20}$$

The strength reduction method and a bisection approach (Hou *et al*., 2019) are employed to find the critical F_s value. The flowchart can be found in Fig. 2.2.

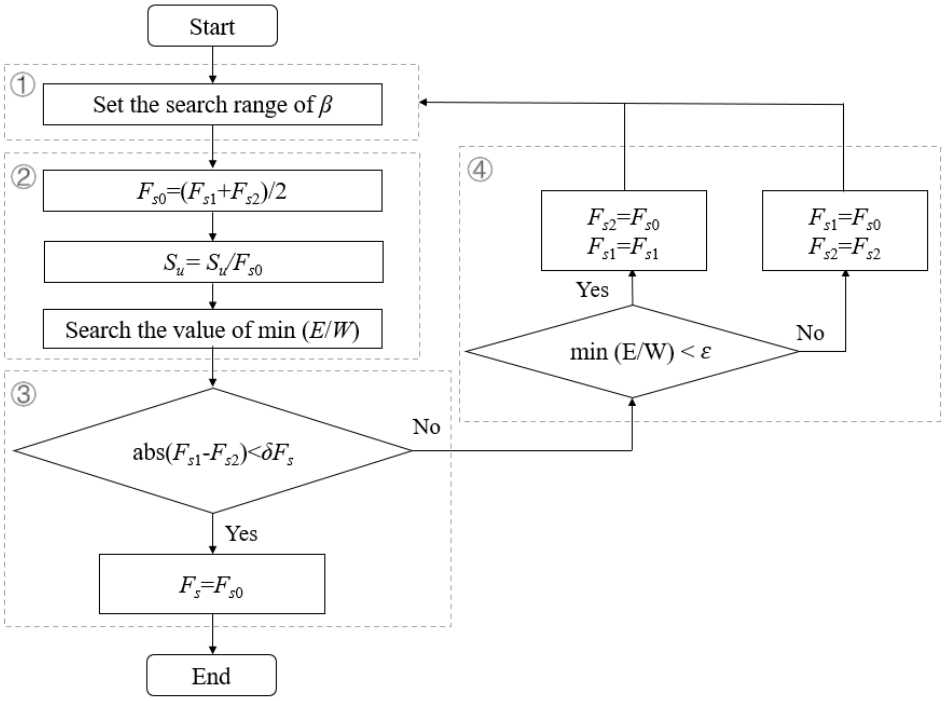

Fig. 2.2 Flowchart of the safety factor optimization.

It is noted that the value of β is in the range of $[45^{\circ}, 90^{\circ})$, and the limitation of $B_2 \leq B$ should be satisfied to ensure the failure mechanism is within the excavation.

2.2.2 Deterministic model comparison

This section aims to present the comparison of safety factors assessed by the improved limit analysis, numerical simulations (NS) and the existing analytical methods presented in Section 1.2.1.2, including the modified Terzaghi method (MT, see Eq. (1.5)), the modified Bjerrum & Eide method (MBE, see Eq. (1.7)), the slip circle method (SC, see Eq. (1.8)) and the existing limit analysis method (ELA, see Eq. (1.9)).

A Finite Element Limit Analysis (FELA) is performed for the NS evaluations (Krabbenhoft et al., 2015). A plane-strain model is used and half of the cross-section is considered due to the excavation symmetry. The horizontal distance between the wall and the outer model boundary and the vertical distance from the excavation base to the outer boundary are respectively larger than 2B and 5H in order to minimize the boundary effects. Besides, the displacements are fully fixed at the bottom boundary while only vertical displacements are allowed for the lateral boundaries. The soil is modelled as a linear elastic-plastic Tresca material and the wall is assumed to be rigid. The interface elements are introduced to consider the soil-wall interface roughness.

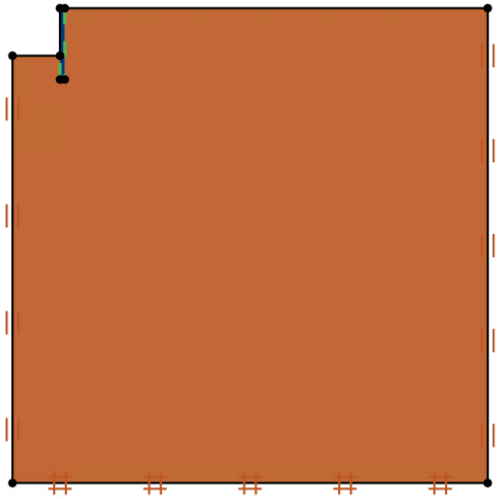

Fig. 2.3 A FELA model for D=5 m, H=10 m, B=20 m, S_u=40 kPa, and r_i=1.

In order to account for the applicability of each basal heave stability method, several cases with different excavation depths, widths, wall embedment depths and soil-wall interfaces are implemented and presented in Fig. 2.4 to Fig. 2.7.

A discussion of the effects on excavation depths is depicted in Fig. 2.4. 14 cases with different excavation depths from 10 m to 40 m with an interval of 5 m under S_u=20kPa and 40kPa are performed. The excavation width is supposed to be constant and equal to 20 m and the wall embedment depth to 5 m. It is seen that the safety factor decreases with the increase of H/B (i.e. increase of H) and the decrease is significant for small values of H/B. The safety factor of ILA is the closest to the FELA among the 5 analytical methods and the maximum difference is found to be lower than 2%. $F_{s-\mathrm{ELA}}$ is always larger than $F_{s-\mathrm{NS}}$ by the fact that the ELA assumes the failure mechanism to be deterministic as shown in Fig. 2.1(a) and cannot obtain the critical safety factor with accuracy. It can also be concluded that the $F_{s-\mathrm{MT}}$ is consistent with the $F_{s-\mathrm{NS}}$ when the H/B is small, however, the difference is increasing with the increase of H/B. For example, when H/B=0.5 and S_u=20kPa, the $F_{s-\mathrm{MT}}$ and $F_{s-\mathrm{NS}}$ are respectively equal to 1.58 and 1.63, with a difference of 3.0%. While this value can be up to 9.0% when H/B=2. Conversely, the difference of $F_{s-\mathrm{MBE}}$ and $F_{s-\mathrm{NS}}$ becomes lower as H/B increases. This finding is consistent with the existing remarks considering that the Terzaghi method is valid for wide excavations whereas the Bjerrum & Eide method is more suitable for deep excavations (Goh et al., 2008). The slip circle method gives the most conservative results and the differences can be up to 36%.

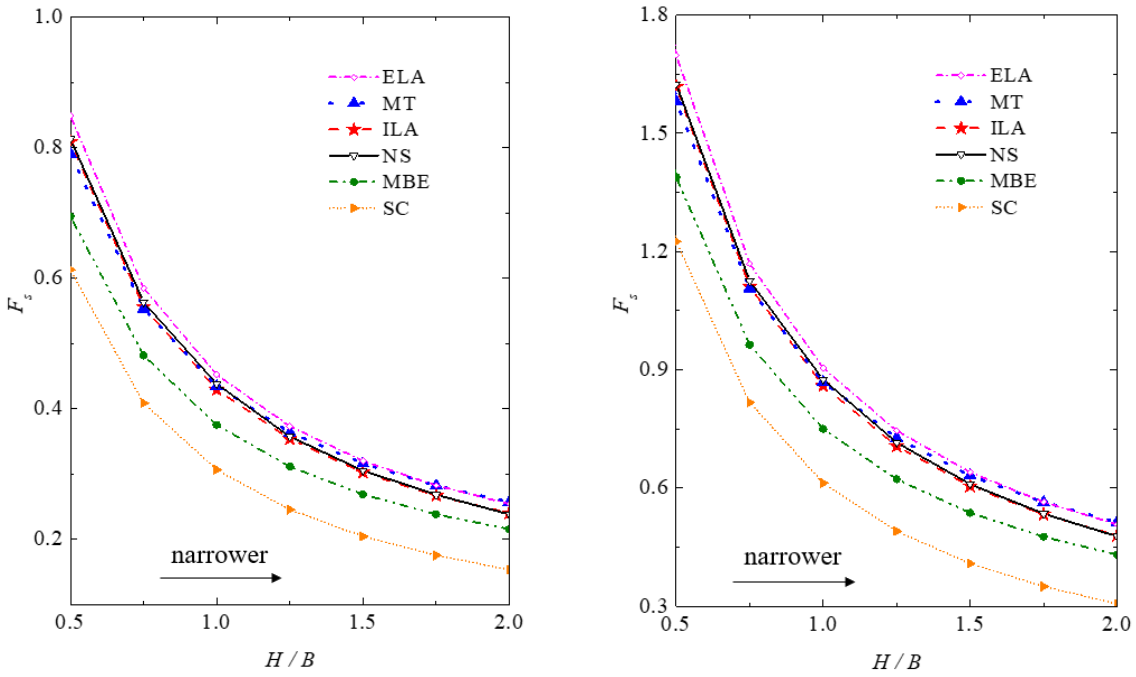

(a) S_u=20 kPa (b) S_u=40 kPa

Fig. 2.4 Safety factors comparison for different values of H/B with B=20 m, D=5 m.

The excavation width influence is discussed for different cases with B/H (0.5~2.0) and S_u (20 kPa and 40 kPa). The results are shown in Fig. 2.5. The safety factors increase with the H/B (i.e. with the decrease of B) except for the slip circle method, which is independent of the excavation width. It can also be seen that the SC method is suitable for wide excavations by the fact that the difference between $F_{s-\mathrm{SC}}$ and $F_{s-\mathrm{NS}}$ becomes smaller with the decrease of H/B. Similarly to the results presented in Fig. 2.4, as H/B increases, the difference of $F_{s-\mathrm{MT}}$ and $F_{s-\mathrm{NS}}$ becomes significant while $F_{s-\mathrm{MBE}}$ is closer to $F_{s-\mathrm{NS}}$. The existing limit analysis mechanism still overestimates the basal heave stability and the improved ones are consistent with the numerical results in both wide and narrow excavations.

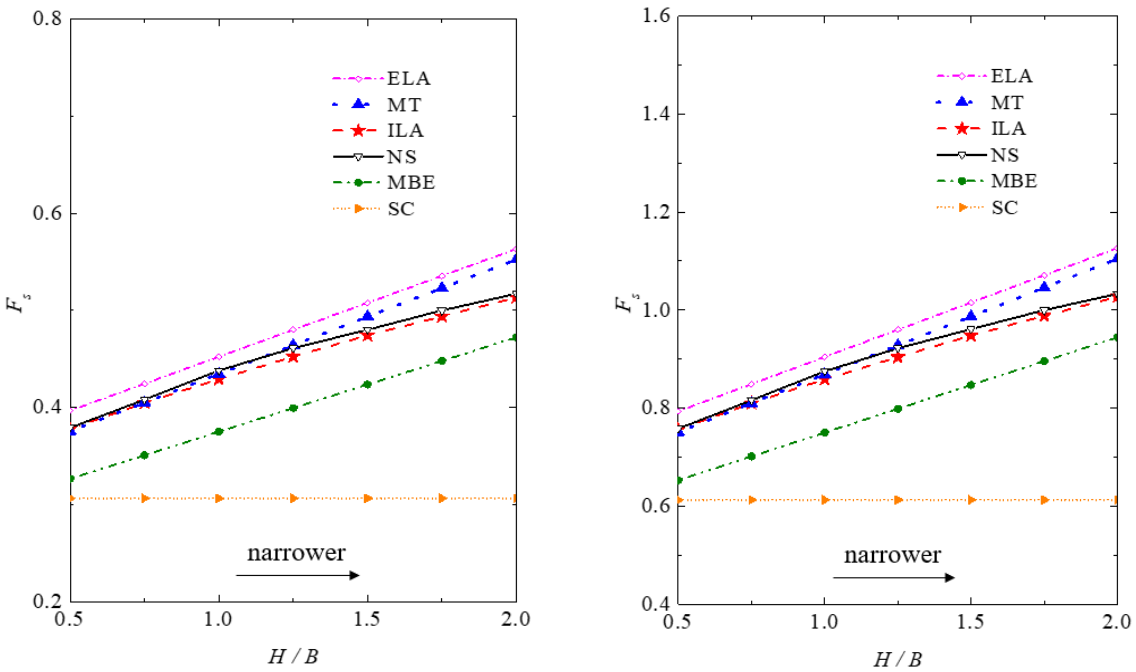

(a) S_u=20 kPa (b) S_u=40 kPa

Fig. 2.5 Safety factors comparison for different values of H/B with H=20 m, D=5 m.

Fig. 2.6 illustrates the wall embedment depth influence ($D/H \in [0, 2]$) on the basal heave stability. The excavation depth and soil undrained shear strength are respectively equal to 20 m and 40 kPa. Two kinds of excavation width are considered, including B=10 m (narrow excavation) and B=30 m (wide excavation). As expected, the longer embedment depth increases the safety factor. However, it should be noted that the slip circle method cannot give reasonable results and underestimates significantly the excavations stability when the embedment depth equals 0. This is because when D=0, the slip circle radius is the distance from the lowest strut level to the final excavation level. It means that the failure surface terminates at the intersection point of the excavation base and wall (point l as depicted in Fig. 2.1(a)), which will significantly underestimate the resisting moment M_r. Besides, it is seen that the existing limit analysis method gives more biased results with the increase of the wall penetration depth, and the difference can be up to 36%. In addition, for the narrow excavation, the safety factor differences between the MT and NS are increased with the wall embedment depth, in contrast to the wide case where the results are consistent. MBE can give reasonable results for the narrow excavation whereas underestimates the basal heave stability for the wide excavation. The results obtained by the proposed limit analysis method can give accurate results for all the cases with different excavation widths and wall penetration depths.

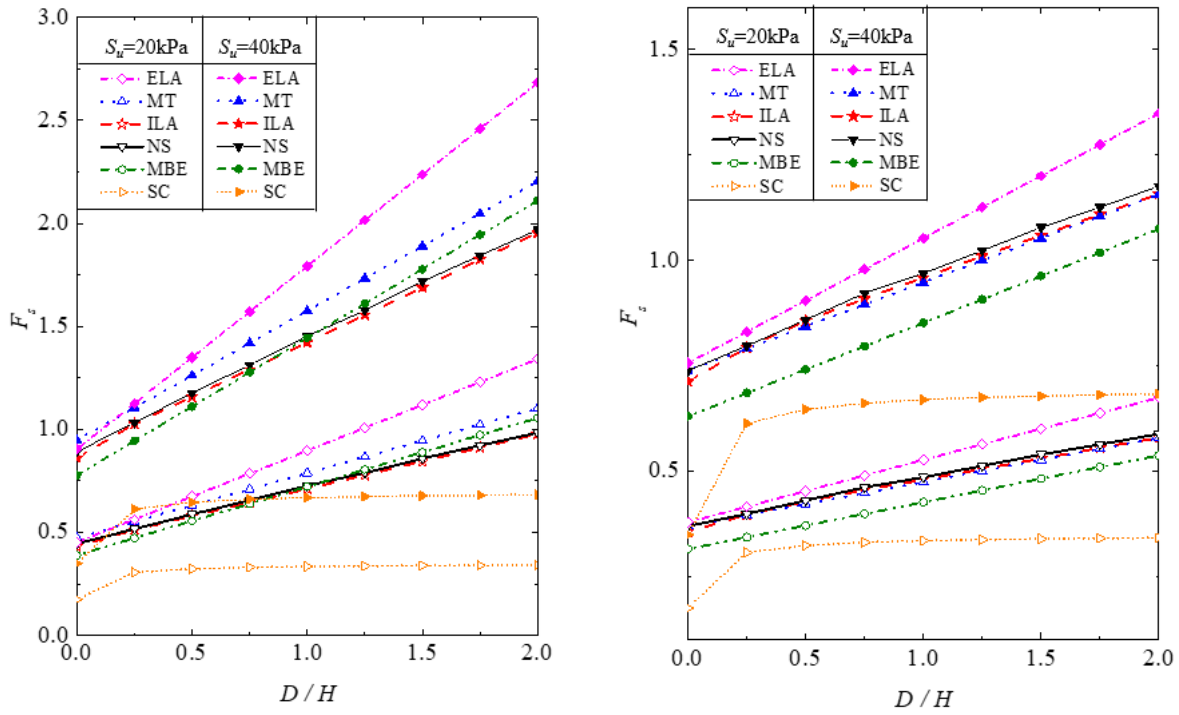

(a) B=10 m (b) B=30 m

Fig. 2.6 Safety factors comparison for different values of D with H=20 m.

The soil wall interface effects on the excavation basal heave stability are also discussed. It is noted that the soil-wall interface coefficient is considered to vary in the range of [0, 1] (Day and Potts, 1998). In the existing analytical methods, the MT, MBE and the present ILA methods are able to consider the soil-wall interface influence and will be performed in this discussion. The results are depicted in Fig. 2.7. These results allow to discuss of the soil-wall interface effects with the excavation depth and undrained shear strength being respectively equal to 20 m and 40 kPa. Six subfigures are depicted for different cases considering two excavation widths (10 m and 30 m) and wall embedment depths varying from 5 m to 15 m (interval of 5 m).

The safety factor increases with the increase of r_i. The effects of r_i are more essential for the cases with larger D values. Taking B=30 m as an example, the safety factors are respectively equal to 0.85 (r_i=0) and 1.03 (r_i=1) when D=5 m, whereas the values are 0.90 (r_i=0) and 1.31 (r_i=1) with a difference being up to 46.7%. It can be explained by Eqs. (2.12) and (2.13), the effects of r_i increase with the increase of D, which can lead to a higher influence on the excavation stability. It is seen that the safety factor may be lower or higher than 1 with the variation of the soil-wall interface, which can be defined as a failure or safe state in the analysis. The determination should be done with attention.

Besides, it can be observed that the MT can provide better results when the soil-wall interface strength is higher, while the MBE is more suitable for most cases with small soil-wall interface

strength. The proposed ILA can give results that are consistent with the NS for different soil-wall interface coefficients. In addition, similar to the above discussions, the MT and MBE are respectively suitable for wide and narrow excavations.

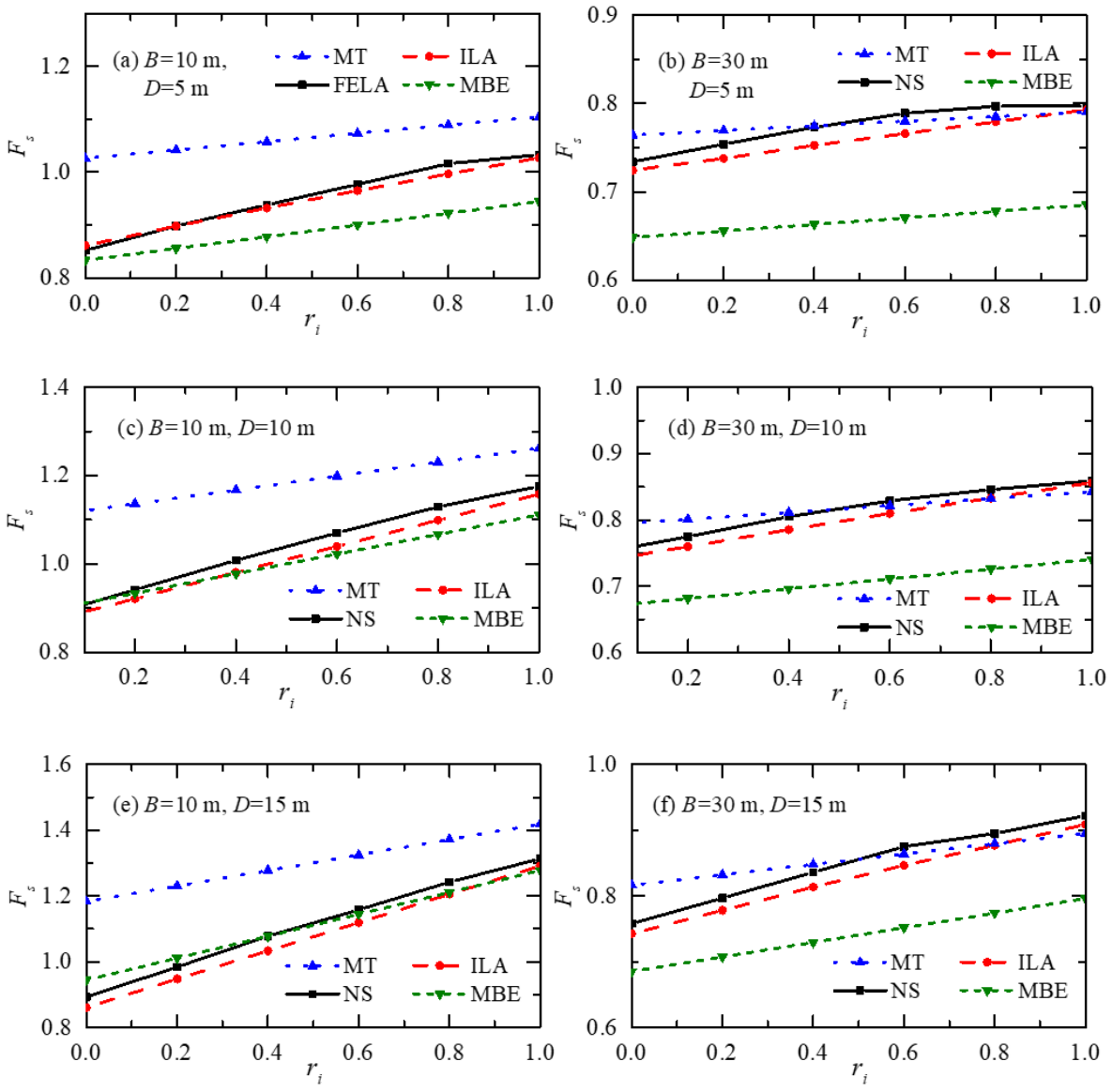

Fig. 2.7 Safety factors comparison for different values of r_i with H=20 m and S_u=40 kPa.

In general, the safety factors increase with the decrease of the excavation depth, width as well as the increase of embedment depth and soil-wall adhesion factor. The ELA method overestimates the safety factors, in contrast, the MBE and SC provide smaller ones for most of cases. Compared to the limit analysis with the well-known failure mechanism, the proposed ILA method can provide more consistent results within less than one second (around 0.15 s) when compared with the time-consuming numerical ones (around 40 s) and can significantly alleviate the computational burden. Besides, the MT method can lead to reasonable results for wide

excavations whereas the MBE is more suitable for narrow ones. The MT and MBE methods are also restrained to account for the soil non-homogeneity. The SC gives the most conservative results among the analytical methods. It cannot explain the excavation width effect and gives unrealistic results for the case without wall embedment. Therefore, the proposed ILA is preferable and has the potential to be an effective tool to analyse the stability of the supported excavations under undrained conditions in an efficient way.

2.3 Proposed probabilistic analysis framework

Once the deterministic model is determined, a probabilistic analysis should be performed to reflect the impact of the soil parameters uncertainties. The active learning method (LAM) is carried out in this study. This section aims to introduce the probabilistic methods employed and the flowchart of the proposed probabilistic framework.

2.3.1 Polynomial Chaos Kriging

The commonly used surrogate models used for the probabilistic analysis include the Kriging (Guo and Dias, 2020; Schöbi et al., 2017; Zhou et al., 2020), Polynomial Chaos Expansions (PCE) (Guo et al., 2019a; Pan and Dias, 2017), Support Vector Machines (Kordjazi et al., 2014), etc. This study introduces an advanced metamodeling technique, the Polynomial Chaos Kriging (PCK), which integrates the advantages of PCE and Kriging. It uses a sparse set of orthonormal polynomials to approximate the global behavior of the computational model and the Kriging to manage the local variability of the model output (Schöbi et al., 2015). It permits to build a more efficient and accurate metamodel compared to PCE and Kriging separately (Schöbi et al., 2017).

More specifically, PCK is defined as a universal Kriging model, whose trend is modelled by a sparse set of orthogonal polynomials instead of a constant value within the ordinary Kriging. The basic function of the PCK theory is expressed as

$$Y \approx M^{PCK}(\boldsymbol{x}) = \sum_{i \in A} \alpha_i \Phi_i(\boldsymbol{x}) + \sigma^2 Z(\boldsymbol{x}) \tag{2.21}$$

where $\boldsymbol{x}$ is a vector with input random variables, $M^{PCK}(\boldsymbol{x})$ is the model output approximation using PCK and A is the index set of polynomials. $\sum_{i \in A} \alpha_i \Phi_i(\boldsymbol{x})$ is the sum of orthonormal polynomials, which is used to describe the trend within the universal Kriging formula. It is required to truncate to a finite number of terms for the sake of practical applications. Using the

standard truncation method can be inefficient particularly for the high dimensional problems and then an improved hyperbolic truncation scheme is proposed by Blatman and Sudret (2011), which is used in this study. The model construction includes the determination of multivariate polynomial basis $\Phi_i(\boldsymbol{x})$, which is the tensor product of univariate orthonormal polynomials, and the corresponding unknown coefficients α_i, which is estimated by the least-square minimization method (Pan et al., 2020). Several families for the univariate orthonormal polynomials are proposed and the Hermite polynomials which correspond to the standard normal random variables are considered in this study (Pan and Dias, 2017). Besides, the sparse PCE (SPCE) is considered by implementing the Least Angle Regression (LAR) algorithm to determine and select the important candidate polynomial basis. The insignificant PCE coefficients are then ignored and the polynomial number can be reduced.

σ^2 and $Z(\boldsymbol{x})$ denote respectively the variance and the zero mean, unit variance stationary Gaussian process defined by an autocorrelation function between two sample points $R(|x-x'|;\theta)$, where θ is the hyper-parameter to be estimated. Several autocorrelation functions have been proposed, i.e. linear, exponential, Gaussian and Matern functions. The Matern-5/2 model is adopted as the autocorrelation function in this study (Marelli and Sudret, 2014)

$$R = R(x,x';\theta,v=5/2) = (1+\sqrt{5}\frac{|x-x'|}{\theta}+\frac{5}{3}(\frac{|x-x'|}{\theta})^2)\exp\left[-\sqrt{5}\frac{|x-x'|}{\theta}\right] \tag{2.22}$$

The construction of the PCK model can be divided into two parts, which consist of the sets of polynomials determination in the trend and the calibration of the Kriging model. Optimal PCK, which defines the metamodel iteratively, is performed. The sparse set of polynomials obtained by the LAR algorithm are ranked in decreasing order according to their correlation to the model response. Each polynomial is then added individually to the trend of a PCK. In each iteration, a new PCK model (coefficients of trend and parameters of autocorrelation function) is calibrated, and the optimal PCK metamodel corresponds to the model with minimal value of the leave-one-out error (Err_{LOO}) as defined by

$$Err_{LOO} = \frac{1}{N}\left[\frac{\sum_{i=1}^{N}(Y^{(i)}-\mu_{y,(-i)}(x^{(i)}))^2}{\mathrm{Var}(Y)}\right] \tag{2.23}$$

where $\mu_{y,(-i)}(x^{(i)})$ is the prediction values based on the PCK metamodel using all the experimental design points except $x^{(i)}$, $Y^{(i)}$ is the exact model response, and Var(Y) is the corresponding estimated variance. The corresponding flowchart of the PCK metamodel construction can be found in Fig. 2.8. More details of the PCK can be found in Marelli and Sudret (2014).

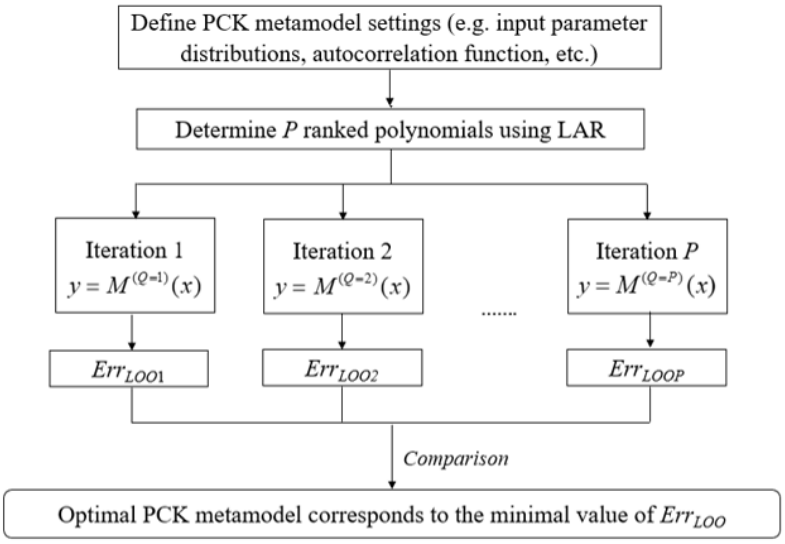

Fig. 2.8 Optimal PCK metamodel construction.

2.3.2 Probabilistic analysis framework

This study proposed the PCK metamodel-based probabilistic analysis (PCK-PA) and this section aims to present the detailed procedure. To improve the efficiency and facilitate the automatic calculations, MATLAB is used for the pre- and post-processing of the probabilistic analyses. A flowchart of the PCK-PA is depicted in Fig. 2.9 and the details are described below:

Step 1: Preparation. Determine the geometrical and geotechnical parameters and construct the deterministic model as shown in Section 2.2; Determine the input parameters statistics (i.e., the distribution, mean value and coefficient of variation) and an initial Experimental Design (ED) based on the Latin Hypercube Sampling (LHS) can be generated. The ED initial size corresponds to the max [10, 2N], where N is the considered random variables number.

Step 2: Input-output sets determination. Compile the batch commands and map the generated samples on the deterministic model. The model response (such as the basal heave safety factor) is then exported and saved automatically.

Step 3: Metamodel determination. Construct an initial PCK metamodel based on the initial input-output sets and check the PCK metamodel accuracy. Two criteria, which correlate to the Leave-One-Out error (*LOO*) Err_{LOO} and failure probability convergence error Err_{P_f}, are considered for the metamodel accuracy improvement.

$$\begin{cases} Err_{LOO} = \dfrac{1}{N}\left[\dfrac{\sum_{i=1}^{N}(Y^{(i)} - \mu_{Y,(-i)}(x^{(i)}))^2}{\sigma^2_{Y,(-i)}(x^{(i)})}\right] \le Err_{LOO\_tg} \\ Err_{P_f}(i) = \max\left\{\left|\dfrac{P_f(i) - P_f(i-1)}{P_f(i-1)}\right|,\ i \in [N_{en} - N_{tg} + 1,\ N_{en}]\right\} \le Err_{P_f\_tg} \end{cases} \tag{2.24}$$

where $Y^{(i)}$ is the result from the FEM model, $\mu_{Y,(-i)}(x^{(i)})$ is the prediction from PCK metamodel using all the ED points except $x^{(i)}$, $\sigma^2_{Y,(-i)}(x^{(i)})$ is the estimated variance, $P_f(i-1)$ and $P_f(i)$ are respectively the (i-1)$^{\text{th}}$ and i^{th} failure probabilities, N_{en} is the enrichment samples number, N_{tg} is the number of failure probability needs to be compared, Err_{LOO_tg} and $Err_{P_f\_tg}$ are the threshold values for both criteria.

Err_{LOO_tg}, $Err_{P_f\_tg}$ and N_{tg} are respectively set to 0.01, 0.01 and 10 in this study (Pan and Dias, 2017). Once the Err_{LOO} and Err_{P_f} are smaller than the values of Err_{LOO_tg} and $Err_{P_f\_tg}$, the procedure enters the next step. Otherwise, ED enrichment for the PCK metamodel construction is necessary. The *U*-function is performed in this study (Moustapha et al., 2022), which is expressed by

$$U(x) = \frac{|\mu(x)|}{\sigma(x)} \tag{2.25}$$

The newly added sample is chosen by minimizing Eq. (2.25), i.e., $S_n = \arg\min U(x)$, which permits finding the point which has the highest probability of being misjudged as failure or safety.

Step 4: Probabilistic analysis. Determine the limit state function and perform the existing probabilistic methods based on the PCK metamodel and export results, which include ① Monte-Carlo Simulations (MCS): failure probability, model response distributions and statistical moments of the system response (mean value and standard deviation (std.)); ② First Order Reliability Method (FORM): reliability index, design point (DP) and importance factor;

③ Global Sensitivity Analysis (GSA): first-order sensitivity index and total effect sensitivity index. It should be noted that not only the mentioned probabilistic methods but also others, such as the Subset Simulation (SS), can be performed after the PCK construction. The calculations are performed on a computer with an Intel (R) Core (TM) i7-8700K 3.70GHz CPU.

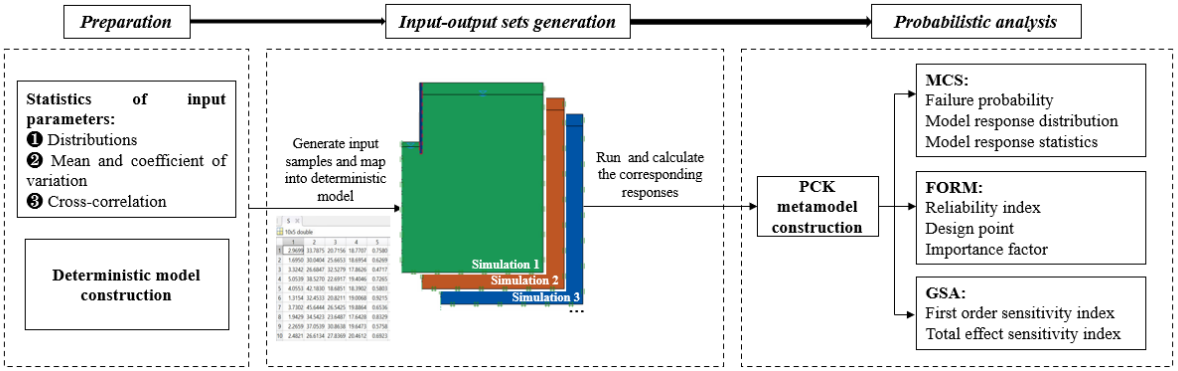

(a) Framework of the proposed PCK-PA

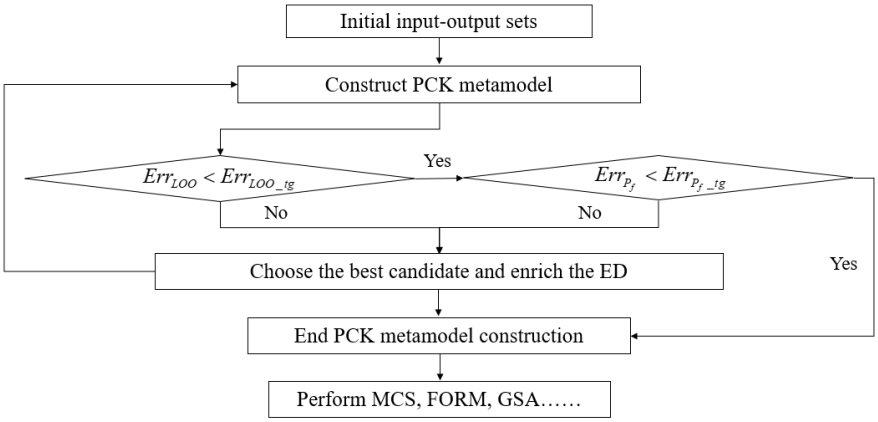

(b) An active learning process for the PCK metamodel construction

Fig. 2.9 Flowchart of the proposed metamodel-based stochastic analysis procedure PCK-PA.

2.3.3 Comparison and discussion of the probabilistic results

This section carries out the above-mentioned probabilistic analysis procedure and the improved limit analysis method to analyse the basal heave stability of supported excavations in a probabilistic framework. The undrained shear strength S_u and the unit weight γ are considered as random variables and the others are constant. To avoid negative values, a lognormal distribution is adopted and the statistical properties (mean value and coefficient of variation (*COV*)) details are summarized in Table 2.1. Other parameters of the reference case include D=5 m, H=10 m, B=20 m, S_u=40 kPa, and r_i=1. These values will be used if there is no specific statement. Besides, it should be noted that in the deterministic framework, the excavation is

considered a failure when the safety factor is smaller than 1, leading to the limit-state function in a probabilistic analysis as $G(x) = F_s - 1$.

Table 2.1 Statistical properties of input random variables.

Parameters	Notation	Statistics of parameters		
		Mean	*COV*	Distribution
Undrained shear strength	S_u (kPa)	40	0.2	Lognormal
Unit weight	γ (kN/m^3)	18	0.05	Lognormal

The PCK metamodel is constructed first. 10 input samples are initially generated by the LHS for the metamodel construction. An iterative procedure is then followed to satisfy the criteria presented in Eq. (2.24). Fig. 2.9 depicts the numerical convergence of the leave-one-out error Err_{LOO} and of the failure probability error Err_{P_f}. The criterion for *LOO* is always satisfied. Err_{P_f} satisfies the requirement after 2 sample enrichments, and the error becomes smaller than 0.01. A total of 22 evaluations, including 10 initial EDs and 12 enrichments, are used for the PCK metamodel construction.

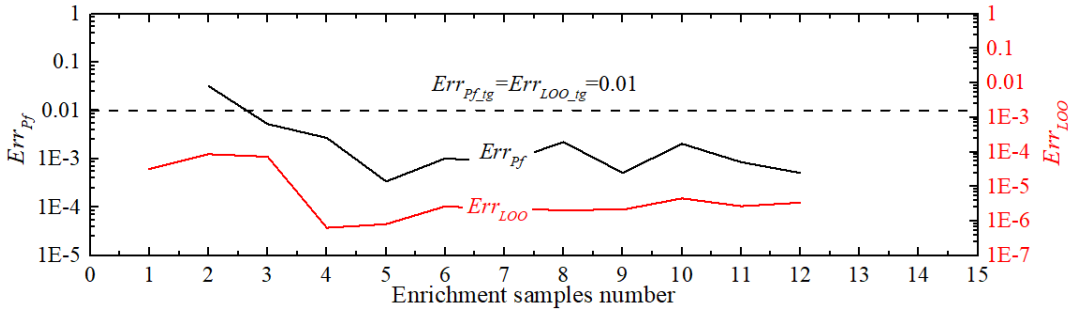

Fig. 2.10 PCK metamodel construction process with the enrichment samples increase.

The probabilistic methods are calculated after the metamodel construction and the probabilistic results can be found in Table 2.2. The results obtained by the direct probabilistic methods are also given for comparison and validation. The failure probabilities, reliability index, design point and sensitivity index which are calculated by the PCK-MCS, PCK-SS, PCK-FORM, PCK-GSA and the direct MCS, SS, FORM and GSA, are very consistent. The PDFs of 40000 safety factors calculated by the direct MCS and PCK-MCS are also given and can be found in Fig. 2.11. It can be observed that the results of PCK-MCS are in good agreement with the ones of the direct MCS. This allows validating the accuracy of the PCK-based probabilistic analysis.

Table 2.2 Comparison of probabilistic results.

Method		P_f	β	DP		Sensitivity index		Number of evaluations
				S_u	γ	S_u	γ	
PCK-MCS		1.15e-2	-	-	-	-	-	
PCK-SS		1.13e-2	-	-	-	-	-	
PCK-FORM		1.17e-2	2.266	25.4	18.5	0.938	0.062	22
PCK-GSA	Total	-	-	-	-	0.930	0.070	
	First					0.929	0.066	
MCS		1.13e-2	-	-	-	-	-	40000
SS		1.12e-2	-	-	-	-	-	1841
FORM		1.19e-2	2.256	25.5	18.5	0.937	0.063	26
GSA	Total	-	-	-	-	0.939	0.061	4000
	First					0.938	0.052	

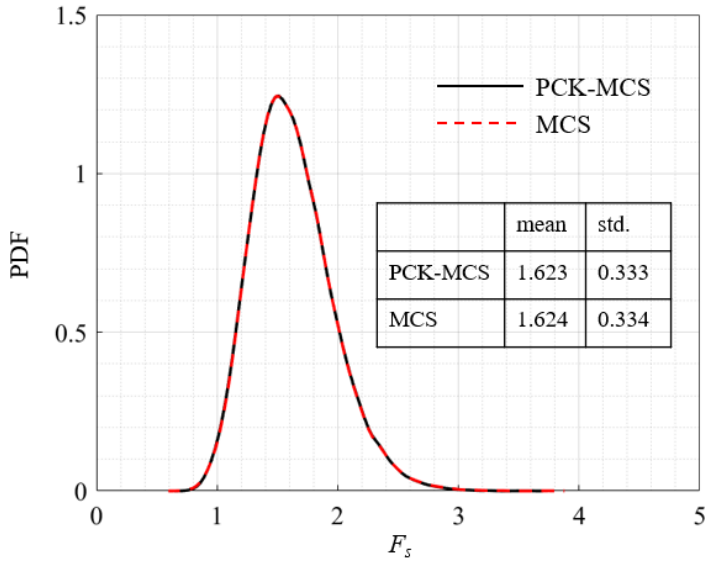

Fig. 2.11 PDFs of safety factor obtained by the PCK-based MCS and the direct MCS.

Concerning the computational effort, it is noted that the computation time of the PCK-based probabilistic analysis consists of 2 parts, the construction of the PCK model and the performance of the probabilistic methods. The surrogate model is fast-evaluated compared to the computational model (Marelli and Sudret, 2014), the computation time of the MCS, SS, FORM and GSA based on the PCK model can thus be negligible. The direct comparison of the deterministic evaluation number is reasonable. It can be observed that the PCK-based probabilistic analysis only needs 22 deterministic evaluations. However, a total of 40000 evaluations are required for the direct MCS, and the improved sampling technique SS increases the calculation efficiency, however, it still needs 1841. The sensitivity index determination also requires further 4000 evaluations. The FORM although only needs 26, which is close to that of

PCK. However, it should be noted that the FORM may fail to give accurate estimates for complex or non-linear limit state surface cases. In general, the proposed PCK-metamodel probabilistic analysis procedure is efficient in terms of the results accuracy and the computational effort, particularly for the cases with small failure probability. For example, when the direct MCS is implemented, around 10e6 runs are required with a P_f of 10e-4 in order to ensure the failure probability accuracy and the calculation time can be up to 41.67 h, which is time-consuming. In addition, the PCK-based probabilistic method is also effective and interesting when the deterministic model is constructed by numerical simulations, which will also be discussed in the following chapters.

2.4 Parametric study

Fig. 2.12 depicts the influence of COV_{Su} on the failure probability. It can be observed that for the same safety factor, the value of P_f is different with the COV_{Su} values change. The failure probability increases with COV_{Su} increases. The effect of COV_{Su} is more significant for the case with larger F_s values. For example, when the mean safety factor is equal to 1.0, the failure probabilities are respectively equal to 0.52 and 0.59 for COV_{Su} =0.2 and COV_{Su} =0.5, while the failure probability varies from 4.5e-4 (COV_{Su} =0.2) to 1.1e-1 (COV_{Su} =0.5) when the safety factor is equal to 2.0. It represents a difference of 3 orders of magnitude.

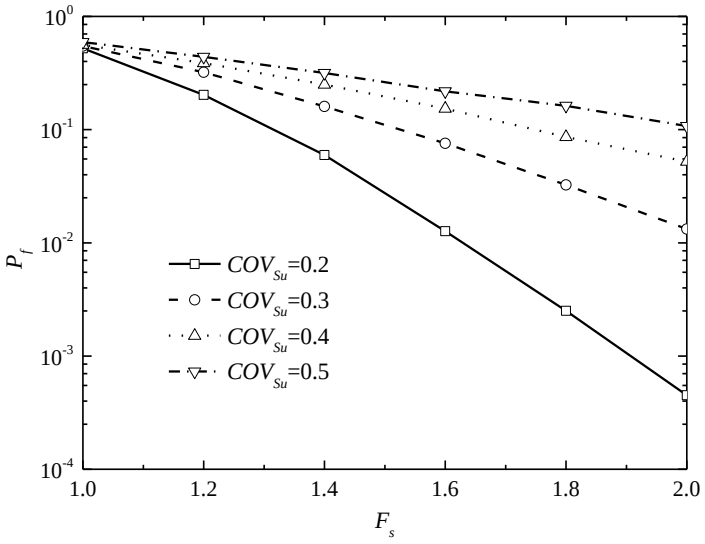

Fig. 2.12 Effect of the COV_{Su} on the failure probability.

Fig. 2.13 gives some information about how the soil-wall adhesion coefficient influences the failure probability. It can be seen that for larger values of r_i, the failure probability is smaller as expected. This is because the $r_i S_u$ values increase leads to more resistance between the soil and

wall, which is beneficial to the excavation stability. Besides, the influence of r_i is significant with the S_u increase. It can be explained by the fact that for larger undrained shear strengths, the value of r_iS_u is larger and can have more influence on the basal heave stability. For example, the failure probability ranges from 0.51 (r_i=1) to 0.69 (r_i=0) when S_u=20 kPa, while for the case with S_u=50 kPa, the difference can be up to 87% (3.0e-3 and 4.0e-4 for r_i =0 and r_i=1, respectively). Therefore, the soil-wall adhesion coefficient should be chosen with caution in excavation probabilistic analyses, particularly for the large undrained shear strength value cases.

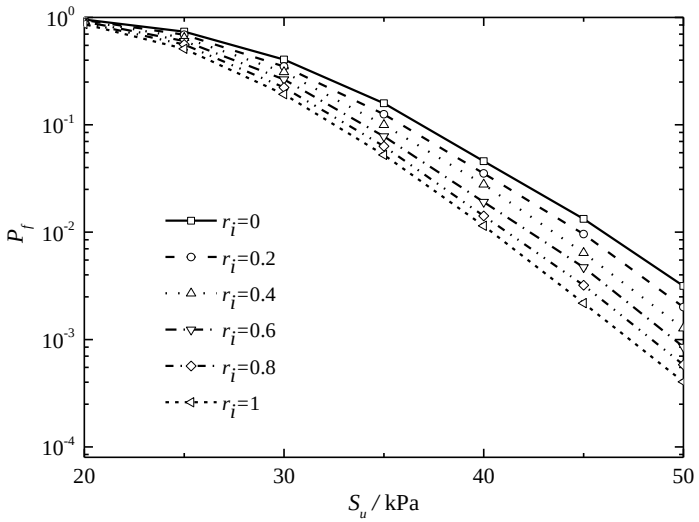

Fig. 2.13 Effect of the soil-wall adhesion coefficient on the failure probability.

The wall embedment depth effect on the failure probability is shown in Fig. 2.14. The failure probability decreases with the embedment depth increase. Its influence is more significant for the cases of large soil-wall adhesion coefficient values, i.e. the failure probability of r_i=1 changes rapidly compared with the case of r_i=0.1 for different embedment depths. For example, the failure probabilities are respectively equal to 6.5e-2 and 1.7e-2 when the wall embedment depth increases from 0 to 20 m with r_i=0.1 and S_u=40 kPa. However, this probability decreases to 2.01e-4 for the case of r_i=1 and D=20 m. The explanation is similar to the one of Fig. 2.7, i.e. the effects of D can be enlarged with the increase of r_i values. It clarifies the important soil-wall adhesion coefficient role, particularly for excavations with larger wall embedment depth. Besides, the wall embedment depth can have a significant effect on the failure probability for large undrained shear strength values.

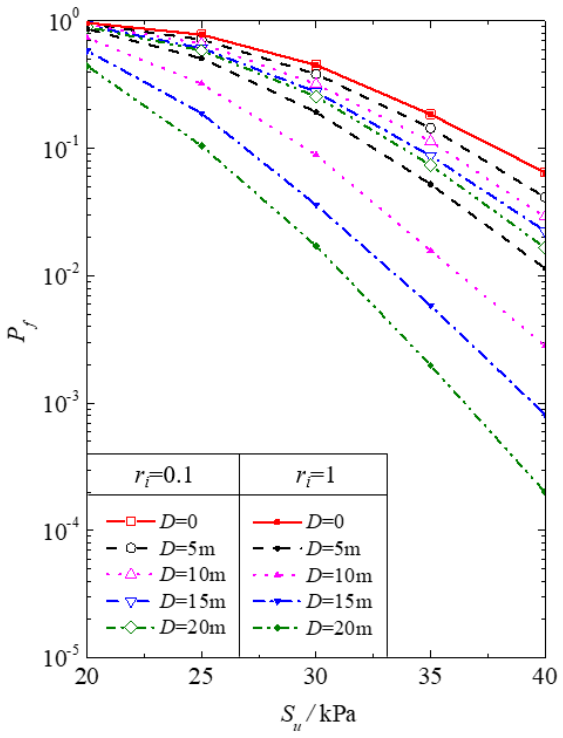

Fig. 2.14 Effect of the embedment depth *D* on the failure probability.

2.5 Conclusion

This chapter has presented deterministic and probabilistic analyses of the basal stability analysis of supported excavations in undrained clays. An improved limit analysis (ILA) mechanism is proposed to estimate the basal heave safety factor of supported excavations under undrained conditions. Compared with other existing analytical methods, including the modified Terzaghi method (MT), the modified Bjerrum & Eide method (MBE), the slip circle method (SC) and the existing limit analysis method (ELA), the ILA determines the safety factor and failure mechanism through an optimization process, which can lead to more consistent results with the numerical simulation (NS) ones in an affordable calculation time. Besides, the advantages of ILA are enhanced by its low time calculation and results accuracy compared with the NS, which may be preferable and has the potential to be an effective tool to analyse the excavation stability.

The comparison results indicate that the ELA method overestimates the safety factors and the safety factor differences are increased with the wall penetration depth increase and the wall width decrease. The MT and MBE methods are not suitable for respectively narrow and wide excavations stability analyses. Besides, they are restrained to account for the soil non-

homogeneity. The SC method gives the most conservative results, ignores the excavation width effect and may be unreasonable for cases without wall embedment depth.

The Polynomial Chaos Kriging-based probabilistic analysis (PCK-PA) is then proposed. The involved metamodel construction, adaptive procedure, criteria, and probabilistic methods implementation are introduced via a flowchart. A variety of probabilistic results can be obtained, including failure probability, model response distributions and statistical moments of the system response (from Monte-Carlo Simulations); reliability index, design point and importance factor (from First Order Reliability Method); first-order sensitivity index and total effect sensitivity index (from Global Sensitivity Analysis). A comparative study of the probabilistic results obtained by the PCK-based probabilistic methods and the direct ones is then carried out. The results indicate the proposed probabilistic procedure PCK-PA helps to improve the computational efficiency of probabilistic analyses, particularly for cases with small failure probabilities.

By benefiting from the high computational efficiency of the proposed method, a parametric study is also performed. The results show that the excavation stability is increased with the decrease of the excavation depth, width and the increase of embedment depth and soil-wall adhesion factor. The coefficient of variation of undrained shear strength effect is important on the failure probability, and its value should be chosen with caution. The soil-wall adhesion coefficient significantly influences the failure probability estimation and its influence is important for large values of undrained shear strength and embedment depths.

The ILA and PCK-PA allow for the effective assessment of the excavation stability and are recommended for practical design and construction. The proposed PCK-PA will also be used in the probabilistic analyses of the following chapters due to its high efficiency.

Chapter 3

Stability analysis of rectangular excavations with great depth

Contents

3.1 Introduction 96

3.2 Presentation of the FIVC excavation 97

3.3 Deterministic analysis 99

3.3.1 Finite Element Modelling 99

3.3.2 Comparison and discussion 101

3.4 Probabilistic analysis 105

3.4.1 Definition of the limit state function and statistical parameters 105

3.4.2 Probabilistic results 106

3.4.3 Probabilistic distributions of the wall deflection and ground surface settlement 112

3.4.4 Relation between the maximum wall deflection and ground surface settlement 119

3.4.5 Probabilistic serviceability assessment 121

3.4.6 Soil-wall interaction effects 123

3.5 Conclusion 124

3.1 Introduction

Existing rectangular-shaped excavations mainly focus on small-depth excavations from 6 m to 20 m, whereas studies on excavations at large depths (greater than 30 m) are rarely discussed as shown in Chapter 1. This chapter aims to discuss the stability of a supported excavation at great depth based on a real case study: the Fort d'Issy-Vanves-Clamart excavation (FIVC) of the Grand Paris Express project. The FIVC excavation is located at the southwest of Paris and is the first metro station of the subway line 15. The excavation reaches a depth of 32 m, and Fig. 3.1 shows its location and aerial photo. It is seen that the FIVC metro station is surrounded by adjacent buildings and a rail traffic system. It is important to control the construction activities influences.

(a) Location

(b) Aerial photo

Fig. 3.1 Location and aerial photo of the FIVC excavation.

The introduction for the FIVC excavation is presented, which is followed by the numerical simulations using the Finite Element Method (FEM). The hardening soil constitutive model is used to simulate the soils behaviour during the excavation phases. The comparison between the numerical results with field measurements and the discussions in terms of wall deflections and ground surface settlements are presented. Then the probabilistic analysis based on the proposed PCK-PA of Chapter 2 is carried out. A series of studies are implemented to discuss the: (1)

probabilistic distributions of the wall deflections and ground surface settlements, (2) correlation between the maximum horizontal wall deflections and maximum ground surface settlements, (3) probabilistic serviceability assessment with different limiting criteria, (4) sensitivity analysis for the considered parameters, and (5) soil-wall interaction effects on the excavation stability.

3.2 Presentation of the FIVC excavation

The Fort d'Issy-Vanves-Clamart excavation, located in the suburbs of Paris, is the study case adopted. Fig. 3.2(a) depicts the top view, which is about 110 m long and 22 m wide. To prevent damage to adjacent buildings and to the existing transportation system, this excavation is supported by a 40 m deep and 1.2 m thick diaphragm wall, a cover slab, three-floor levels (N1, N2, N3), four strut levels (B1, B2, B3 and B4) and a raft. Struts B1, B2 and B3 are used in western and eastern zones, while B4 is for the whole excavation between the lowest floor level N3 and the raft. Fig. 3.2(b) shows the cross-section of the supporting system and seven excavation levels (E1~E7). A top-down construction method is adopted in the central zone, whereas the bottom-up method is adopted for the western and eastern zones.

The FIVC station is located in the Parisian sedimentary basin and there are five strata below 77 m from the ground surface. It mainly consists of a 11 m-thick layer of Backfill (BF), a 10 m-thick layer of Hard Limestone (HL), a 8 m-thick layer of Ypresian Plastic Clay (PC), a 8~10 m-thick layer of Meudon Marls (MM) and the wall bottom is embedded into Chalk (CK) (Khadija et al., 2021).

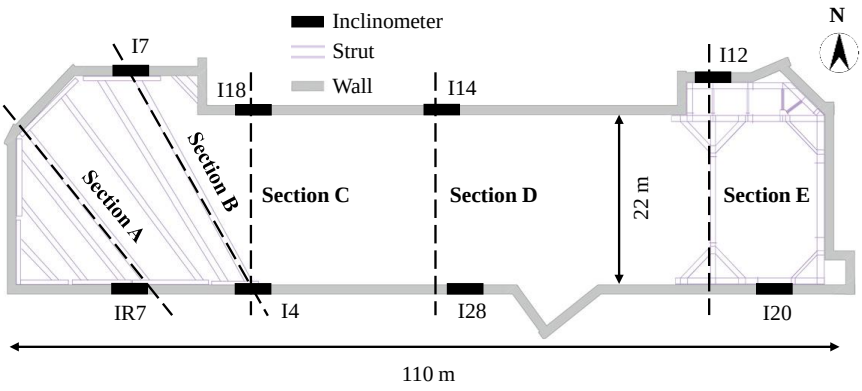

(a) Top view

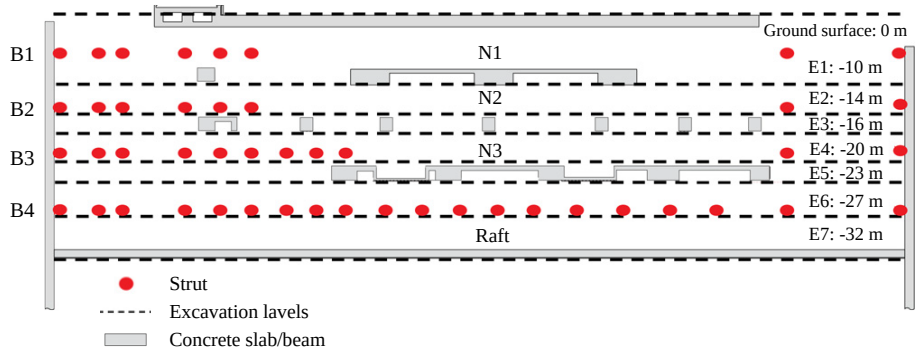

(b) Supporting system

Fig. 3.2 Top view and supporting system of the FIVC excavation.

This study discusses the FIVC excavation stability based on the central section D using a two-dimensional plane-strain model. The other sections in the western and eastern zones are closer to corners and three-dimensional effects in these zones can be important. Fig. 3.3 depicts the rectangular cross-section of Section D, with the excavation width *B* and final excavation depth *H* being 22 m and 32 m, respectively. The retaining wall is embedded into MM and CK layers and the embedment depth *D* is 8 m. Table 3.1 summarizes the top-down construction sequence of Section D and the excavation activities are mainly divided into 7 parts. The cover slab, floor levels N1, N2, N3, strut B4 and raft will then be installed respectively at stages I, III, V, VI and VII. The detailed excavation process and strut locations can be found in Fig. 3.2(b), Fig. 3.3 and Table 3.1.

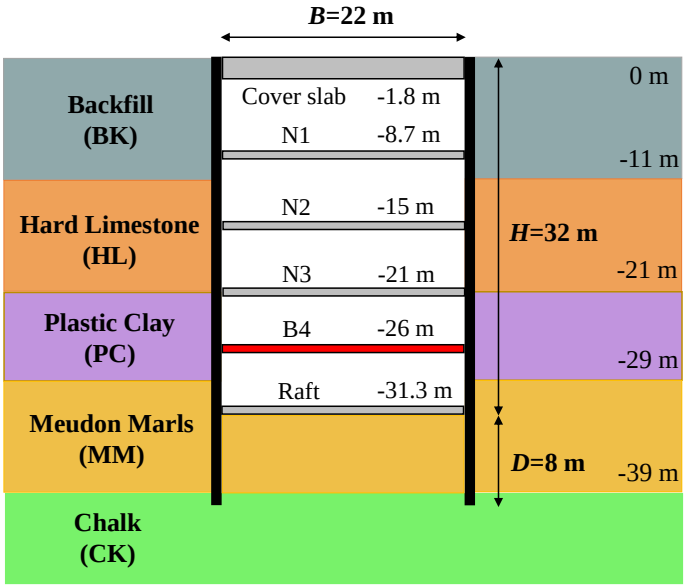

Fig. 3.3 Section D layout.

Table 3.1 Excavation stages.

Stage	Construction activity
I	Excavation to -10 m and install the cover slab and N1
II	Excavation to -14 m
III	Excavation to -16 m and installation of N2
IV	Excavation to -20 m
V	Excavation to -23 m and installation of N3
VI	Excavation to -27 m and installation of B4
VII	Excavation to -32 m and installation of raft

3.3 Deterministic analysis

3.3.1 Finite Element Modelling

A two-dimensional Finite Element software, PLAXIS 2D, is adopted to analyse the excavation stability. One-half of the cross-section is modeled due to symmetry and the plane-strain numerical model is presented in Fig. 3.4. The horizontal and vertical lengths are respectively set equal to 100 m and 80 m to minimize the geometry influence. Displacements are fixed at the model bottom in horizontal and vertical directions, while only the horizontal direction is constrained for the lateral sides. Due to the existing rail traffic system and several buildings effects, a homogenized load of -30 kN/m/m is chosen conservatively and applied uniformly on the ground surface. The total number of elements and nodes of the numerical model are respectively equal to 3448 and 28178.

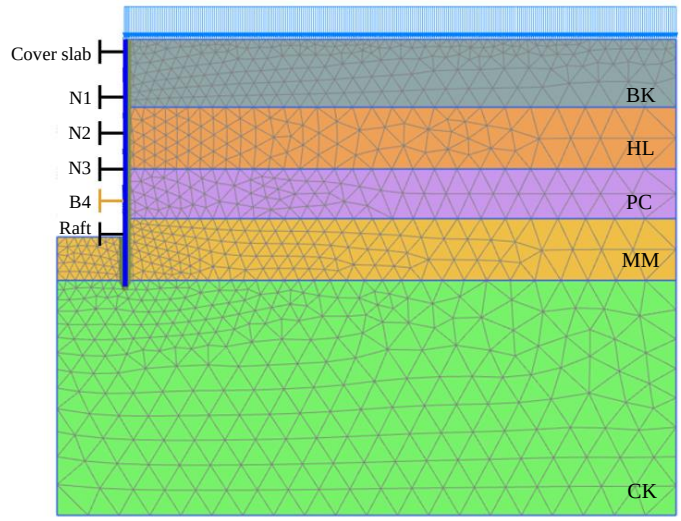

Fig. 3.4 FEM model of the FIVC excavation.

The hardening soil model (HS), which is an elastoplastic model and able to simulate the soil non-linearity and failure using the Mohr-Coulomb failure criterion, is used to simulate the soils behaviour during the excavation phases. Table 3.2 summarizes the detailed soil parameters based on the site tests (pressure-meter, cross hole and cone penetration tests), laboratory tests (the oedometric and triaxial tests) and the numerical back analyses presented by Khadija et al. (2021). It should be noted that the Ypresian plastic clay is over-consolidated by the fact that it was loaded by more than 120 m of sedimentary soils after the Ypresian age. Therefore, its initial earth pressure coefficient at rest k_0 is affected by both the friction angle and the Over Consolidation Ratio (OCR). The wall installation also influences the soil stress and the k_0 value is set equal to 0.85 (Khadija et al., 2021; Paul W and Fred H, 1982).

Table 3.2 Soil parameters of each layer (Nejjar and Dias, 2019).

Parameter	Notation (Unit)	Value				
		BK	HL	PC	MM	CK
Material model	-	HS	HS	HS	HS	HS
Unsaturated unit weight	γ_{dry} (kN/m^3)	19	21	19	19.5	19.5
Saturated unit weight	γ_{sat} (kN/m^3)	20	22	20	20.5	20.5
Secant stiffness	E_{50}^{ref} (MN/m^2)	48	200	150	600	1,360
Tangent oedometer stiffness	E_{oed}^{ref} (MN/m^2)	48	200	150	600	1,360
Unloading/reloading stiffness	E_{ur}^{ref} (MN/m^2)	144	600	450	1,800	4,080
Cohesion	c (kPa)	0	20	20	30	40
Friction angle	φ (°)	29	35	18	25	35
Poisson's ratio	υ_{ur}	0.2	0.2	0.2	0.2	0.2
Over consolidation ratio	OCR	1	1	2.2	1	1
Initial earth pressure coefficient at rest	k_0	0.52	0.43	0.85	0.58	0.43

Vertical diaphragm walls were installed with a cover slab, floor levels N1, N2, N3, strut B4 and raft to ensure the excavation stability. The supports are modeled by plates considering a linear-elastic constitutive model and the corresponding parameters are presented in Table 3.3. Quasi-permanent loads are considered and applied on the cover slab, floor levels N1, N2, N3 and raft.

Table 3.3 Properties of the structural support elements (Nejjar and Dias, 2019).

Parameter	Notation (Unit)	Value						
		Wall	Cover slab	N1	N2	N3	B4	Raft
Normal stiffness	EA (kN)	2.9e7	3.2e7	2.2e7	1.8e6	5.5e6	2.8e6	2.3e7
Flexural stiffness	EI (kN·m^2)	3.5e6	-	-	-	-	-	-
Loading	F_y (kN)	-	-1370	-361	-59	-381	-	-70

3.3.2 Comparison and discussion

During the FIVC excavation construction, a comprehensive monitoring system (such as wall inclinometers and optical fiber), was implemented to assess the excavation performance. More detailed descriptions can be found in Nejjar and Dias (2019).

Fig. 3.5(a) depicts the measured and simulated excavation-induced wall deflection profiles of section D at Stages IV, V and VI. It can be seen that the trend and magnitude of the simulated horizontal wall deflections are generally in good agreement with the measured ones. It allows to validate the numerical model effectiveness. Besides, the maximum horizontal wall deflection is increased by about 6 mm from stage IV to stage V, which is larger than the increment from stage V to stage VI (2 mm). This is because the horizontal wall deflection is strongly related to the soil behaviour behind the retaining wall. The soil stiffness difference between layers HL, PC and MM causes the wall to deflect more easily at layer PC. N3 floor was installed at stage V and it is located at the junction between layers HL and PC. Conversely, at stage VI, strut B4 is installed in the layer PC middle, which can resist effectively the wall deformation. In addition, no toe movements occurred since the diaphragm wall is embedded into the layers MM and CK with high stiffness.

Fig. 3.5(b) presents a comparison of the observed and computed ground surface settlements at Stages IV and VI. The ground surface settlement trends are similar, while the FEM simulation overestimates the settlement magnitudes. The possible explanation is that the railway tracks above the excavation were still in operation during the FIVC station construction and the loads applied on the ground surface may vary in time. In this numerical model, a static uniform load of -30 kN/m^2 is assumed to be distributed on the ground surface for the sake of simplicity and the load variations are not considered. Besides, compared with the wall deflection measurements, the surface settlement data is relatively scattered and cannot totally be used to identify the surface settlement contours.

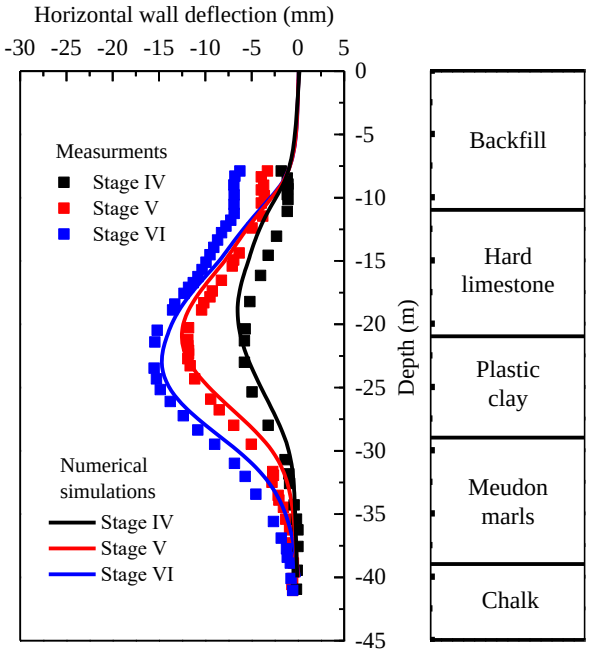

(a) Horizontal wall deflection

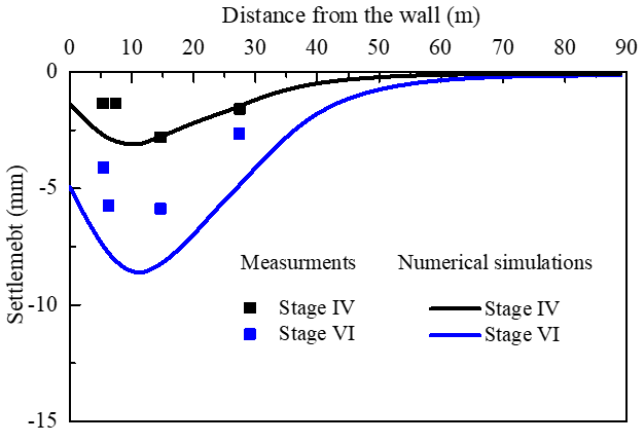

(b) Ground surface settlement

Fig. 3.5 Comparison between measured and predicted excavation responses.

The deterministic FEM model implemented in this study is able to reflect reasonably the excavation phases and will be used in the following discussions.

Fig. 3.6(a) depicts the development of the maximum horizontal wall deflection δ_{hm} during construction. It can be observed that the ratio R_d, which denotes the relationship between δ_{hm} and the excavation depth H, ranges from 0.05‰ to 0.2‰ when H is smaller than 16 m. δ_{hm} varies almost linearly with the excavation depth when H lies between 23 m and 32 m, and the corresponding R_d value is close to 0.58‰. The R_d value increase lies in the fact that the plastic clay is involved in excavation activities with H being larger than 21 m, and the stiffness decrease of layer PC can increase the wall deflection.

Some existing empirical relationships are also provided for comparison. It can be seen that the wall deflection is significantly smaller than the reported ones, which include 0.2%H~1%H in soft clays (Peck, 1969), 0.22%H~0.5%H in stiff clays (Clough and O'Rourke, 1990) and 0.3%H~0.6%H in soft-medium clays (Kung et al., 2007c). Tan and Wei (2012) provide a R_d range of 0.2‰H~0.23%H in Shanghai soft clays and the lower bound 0.2‰H is relatively close to the present study one, whereas the excavation depth is limited to 18 m. One documented deep excavation (38m) is also given, and the δ_{hm} value is around 0.14%H (Liu et al., 2011).

The relationship between the maximum ground surface settlement δ_{vm} and excavation depth H can be found in Fig. 3.6(b). R_s is the ratio between δ_{vm} and H. It is seen that the results are consistent with the wall deflection ones, and the surface settlements of Stages I, II and III are very small with R_s (around 0.03‰). The magnitude of δ_{vm} increases with H within an upper bound of R_d = 0.45‰. The settlement values in this study are also smaller than those of the documented excavations: 0.15%H~0.5%H in stiff clay (Clough and O'Rourke, 1990), 0.3‰H~0.18%H of Shanghai soft clay (Tan and Wei, 2012) and 0.45‰ for a 38 m deep excavation (Liu et al., 2011).

The small values of δ_{hm} and δ_{vm} can be explained by the fact that a considerable thickness of hard layers (HL, MM and CK) is present along the excavation and the diaphragm wall is also embedded into the layers MM and CK. It can effectively prevent excavation deformations. The installation of several supports, which include the diaphragm wall, cover slab, raft and struts, can also increase the excavation stability.

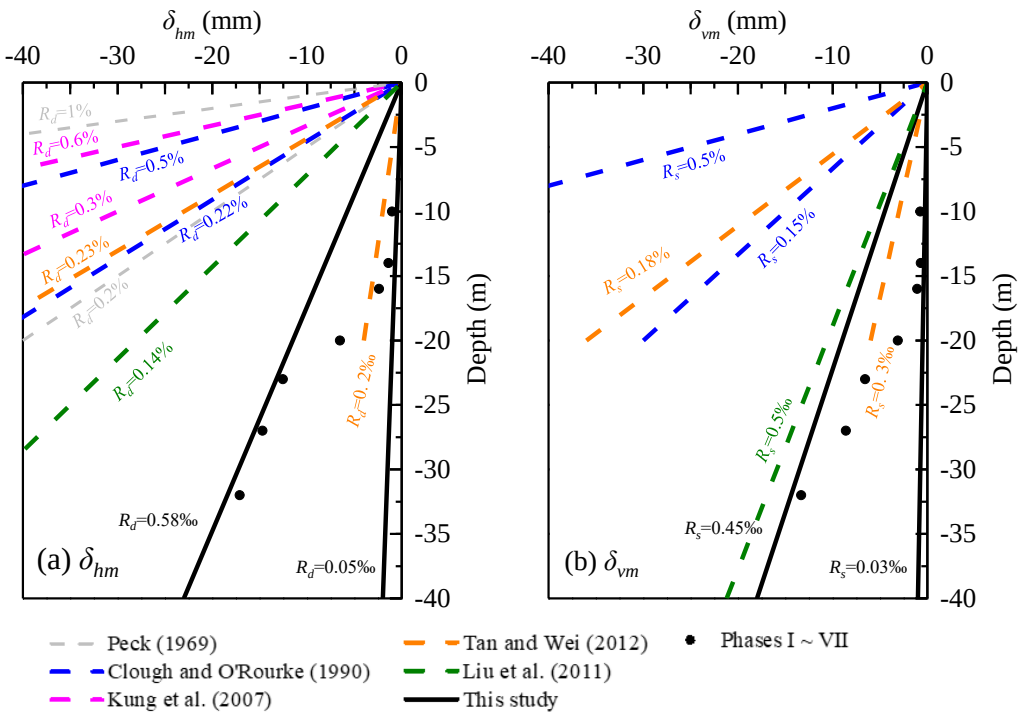

Fig. 3.6 Relationships between the excavation depth and maximum horizontal wall deflection, and maximum ground surface settlement.

Fig. 3.7 gives the locations where the maximum wall deflection and maximum ground surface settlement occur with the excavation depth increase. There is no doubt that the location of δ_{hm} moves downward with the H increase. For stages I, II and III, δ_{hm} is approximately located 3 m above the excavation bottom. When H approaches 20 m, the location is close to the excavation bottom. For the rest of the excavation phases (stages V, VI and VII), the maximum wall deflection falls within the layer PC due to its relatively small stiffness contrast with the adjacent layers (HL and MM). The maximum surface settlement is located at 4~7 m from the retaining wall for stages I, II and III. The location changes slightly when H is larger than 20 m and is mainly distributed around 10 m from the wall. Construction at these locations should be particularly careful and strengthening measurements need to be implemented to prevent uneven settlements and potential damages.

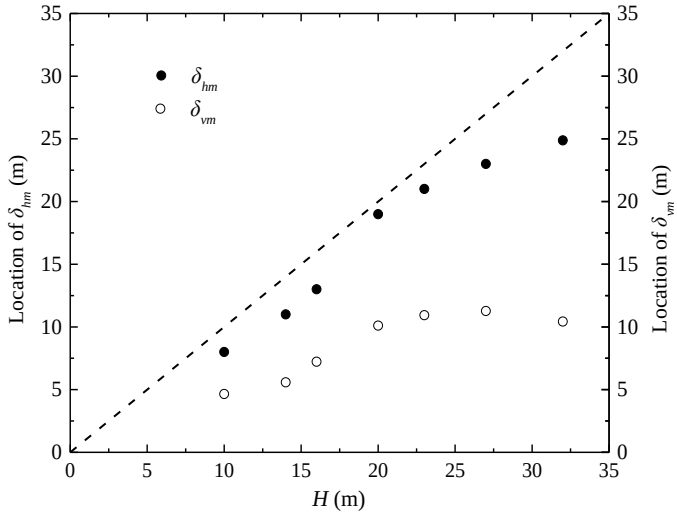

Fig. 3.7 Locations of maximum wall deflection and maximum ground surface settlement with excavation depth increase.

3.4 Probabilistic analysis

This section aims to investigate the (1) uncertainties consideration effects on the wall deflection and surface settlement distributions, (2) relationship between the maximum wall deflection and maximum surface settlement, (3) probabilistic serviceability assessment with different limiting values, (4) soil-wall interaction effects on the excavation stability.

3.4.1 Definition of the limit state function and statistical parameters

The excavation design and construction need to satisfy the horizontal wall deflection and ground surface settlement requirements at the serviceability limit state, i.e., the values of δ_{hm} and δ_{vm} should be smaller than the defined limiting values. In this study, the probabilistic analysis related to the wall deflection is considered (the explanations are detailed in Section 5.3) and the limit state function is defined by

$$g(X)=\delta_{hm}-\delta_{hm\_lim} \tag{3.1}$$

where X denotes the considered random variables, and $g(X)$ is the limit state function regarding the maximum wall deflection. δ_{hm_lim} is the limiting maximum wall deflection and is set equal to 28 mm in this study (Philipponnat and Hubert, 2016). The excavation is considered as safe when $g(x) \leq 0$, and failure occurs when $g(x) > 0$.

Parameter uncertainties of layers HL, PC and MM are considered since the excavation is done through these three layers. The uncertainty of layer BK is neglected due to its insignificant contribution to the horizontal wall deflection as presented in Fig. 3.5(a). Seven random variables, which include the friction angle and secant stiffness of layers HL, PC and MM, and the initial earth pressure coefficient at the rest of layer PC, are discussed. The input uncertain parameters are considered statistically independent and a lognormal distribution is taken into account to model the samples distribution. The detailed statistical information determined by the existing studies (Phoon and Kulhawy, 1999; Zhou et al., 2020), is summarized in Table 3.4.

Table 3.4 Statistical properties of input random variables.

Layer	Parameters	Notation (Unit)	Statistics of parameters	
			Mean	Coefficient of variation (*COV*)
HL	Friction angle	φ_{HL} (°)	35	0.1
	Secant-stiffness	$E_{50}^{ref}{}_{HL}$ (kN/m^2)	2.0e5	0.15
PC	Friction angle	φ_{PC} (°)	18	0.1
	Secant-stiffness	$E_{50}^{ref}{}_{PC}$ (kN/m^2)	1.5e5	0.15
	Initial earth pressure coefficient at rest	k_{0PC}	0.85	0.15
MM	Friction angle	φ_{MM} (°)	25	0.1
	Secant-stiffness	$E_{50}^{ref}{}_{MM}$ (kN/m^2)	6.0e5	0.15

3.4.2 Probabilistic results

The proposed PCK-PA presented in Chapter 2 is implemented. Fig. 3.8 depicts the numerical convergence of the leave-one-out error Err_{LOO} and of the failure probability error Err_{P_f}. The criterion for *LOO* is satisfied when 8 samples are added. P_f values vary considerably for the former 100 sample enrichments, start to converge after 131 and Err_{P_f} satisfies the requirement after 141 sample enrichments. A total of 155 evaluations, including 14 initial experimental design points, are used for the PCK metamodel construction.

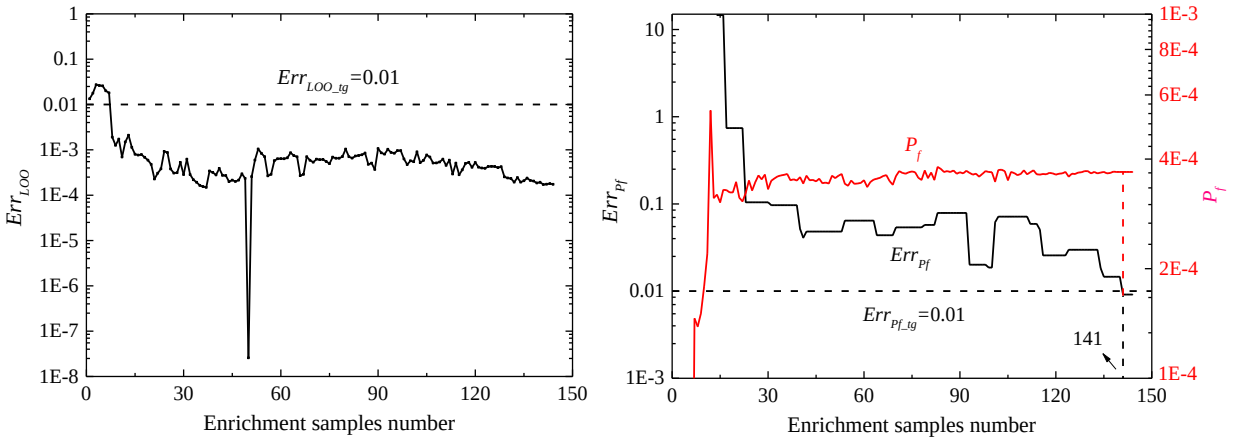

(a) Err_{LOO} (b) Err_{Pf}

Fig. 3.8 PCK metamodel construction process with the enrichment samples increase.

The metamodel accuracy can be checked in Fig. 3.9. It is noted that the accuracy of the PCK-based probabilistic analysis should be investigated by comparing the results obtained by a direct MCS and GSA. However, around 1.0e6 model evaluations are essential to meet the requirements of COV_{Pf} with a P_f of 3.6e-4. It requires 1736 days at least to calculate the failure probability, which is unaffordable. Therefore, the proposed procedure accuracy is discussed by the validation of the metamodel evaluations. If the maximum wall deflections obtained from the PCK metamodel are accurate enough, the subsequent probabilistic methods can perform in a good manner. Fig. 3.9 that the points are distributed on a line at 45° and the R^2 value can be up to 0.994, which means that the PCK metamodel can provide similar δ_{hm} as the numerical simulations. The effective PCK predictions can then ensure the accuracy of the following probabilistic discussions.

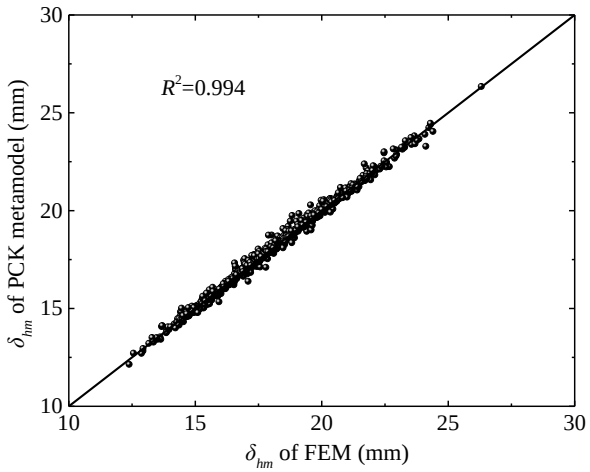

Fig. 3.9 Maximum horizontal wall deflection comparison using FEM and PCK methods.

The PCK-based MCS provides a failure probability of 3.6e-4. In order to satisfy the COV_{Pf} requirement (5%), a total of 1.11 million simulations are performed after a numerical convergence study. The corresponding maximum wall deflection distribution is depicted in Fig. 3.10. It is found that δ_{hm} is mainly distributed in the range of [12.5 mm, 25 mm], and there is a probability of 3.6‰ exceeding the limiting wall deflection value (28 mm). The statistical moments of the system response are respectively the mean value and standard deviation of 17.9 mm and 2.2 mm.

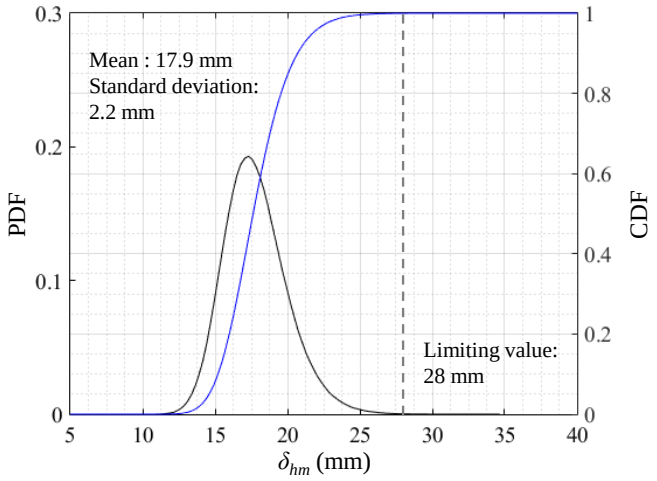

Fig. 3.10 PDF and CDF of maximum wall deflections of PCK-MCS.

Fig. 3.11 depicts the PCK-based GSA analysis results. Although there are small differences in the magnitudes of the first-order and total-effects Sobol indices, they can give a consistent ranking order. Besides, the friction angle plays a dominant role in the wall deflection variation within the current probabilistic input configuration, and the one of layer MM contributes the most, followed by layers PC and HL. A possible explanation can be found in Fig. 3.12, which depicts 4 plastic zone distributions with different friction angles of layers MM and PC. The corresponding magnitudes are determined considering the mean ± 3×standard deviations.

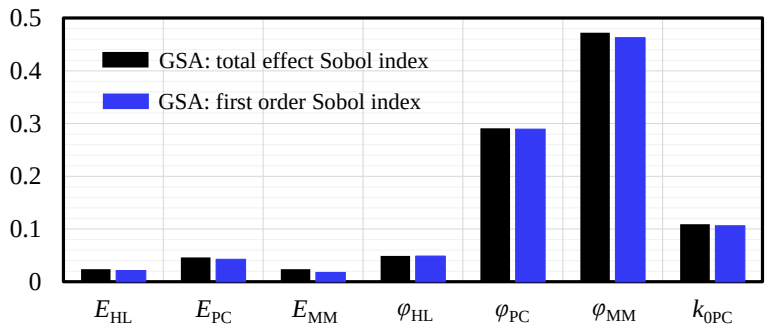

Fig. 3.11 Sensitivity analysis results of PCK-GSA.

It can be observed that when the friction angle of layer MM is large, the failure points are mainly distributed at the soil-wall interface, and the intersection of the wall and the excavation base is found to have a direction being around 45° as shown in Fig. 3.12(a). However, when its friction angle value decreases, the failure points move to the retaining wall back and the failure surface is through layer MM. It even reaches the wall toe due to the reduced shear strength. Soil deformations in layer MM increase the active earth pressure on the wall and subsequently induce significant wall deflections due to the deformation compatibility (Zheng et al., 2014). Besides, the connection of the shear failure surface and the wall toe may lead to wall toe deformations and decreases greatly the excavation stability.

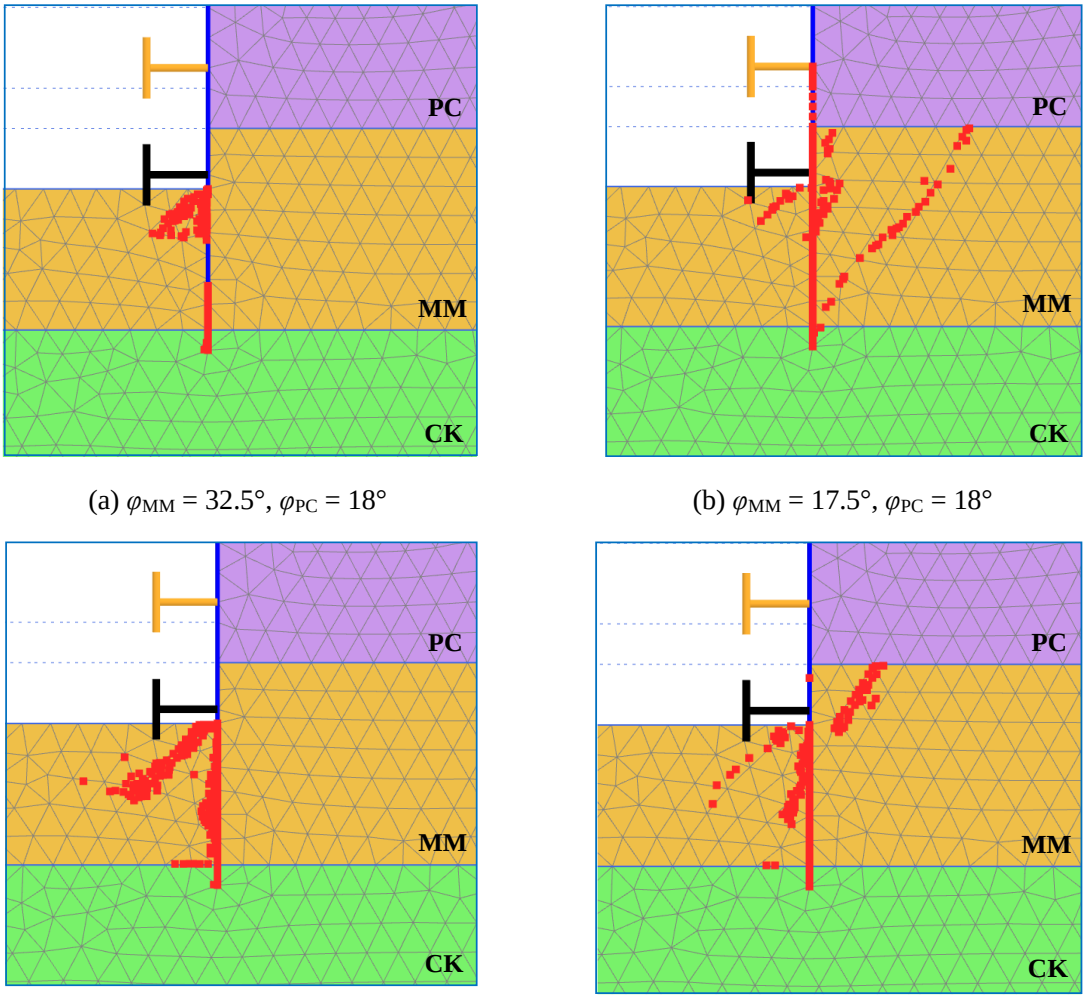

(a) φ_{MM} = 32.5°, φ_{PC} = 18°

(b) φ_{MM} = 17.5°, φ_{PC} = 18°

(c) φ_{MM} = 25°, φ_{PC} = 23.4°

(d) φ_{MM} = 25°, φ_{PC} = 12.6°

Fig. 3.12 Influences of layers MM and PC friction angles on the plastic zone distributions.

Comparatively, the effects of the PC layer friction angle on the plastic zone distributions are presented in Fig. 3.12(c) and (d). Similar results are achieved. The friction angle decrease can make the failure points move behind the wall. However, it can only affect the excavation phases

depth range, i.e., the upper MM layer part. Correspondingly, the friction angle influence on the horizontal wall deflection is small.

In addition, the bending moment and wall deflection profiles are also presented in Fig. 3.13 to provide a quantitative interpretation. It is seen that the MM friction angle decrease leads to the increase of the bending moment at layer MM (2114 kN·m/m) and subsequently induces an increase of the horizontal wall deflection. The δ_{hm} value is up to 26 mm with an increase of 76.4% compared to the case of φ_{MM}= 32.5° (14.8 mm) and the maximum wall deflection location is lowered to the intersection of layers MM and PC. Conversely, the bending moment and wall deflection variations with the PC friction angle decrease are less significant. The maximum wall deflection difference is around 50.7% and occurs mainly in the middle of layer PC. In summary, the layer MM friction angle has an essential effect on the excavation stability and its value should be determined with caution in designs and constructions.

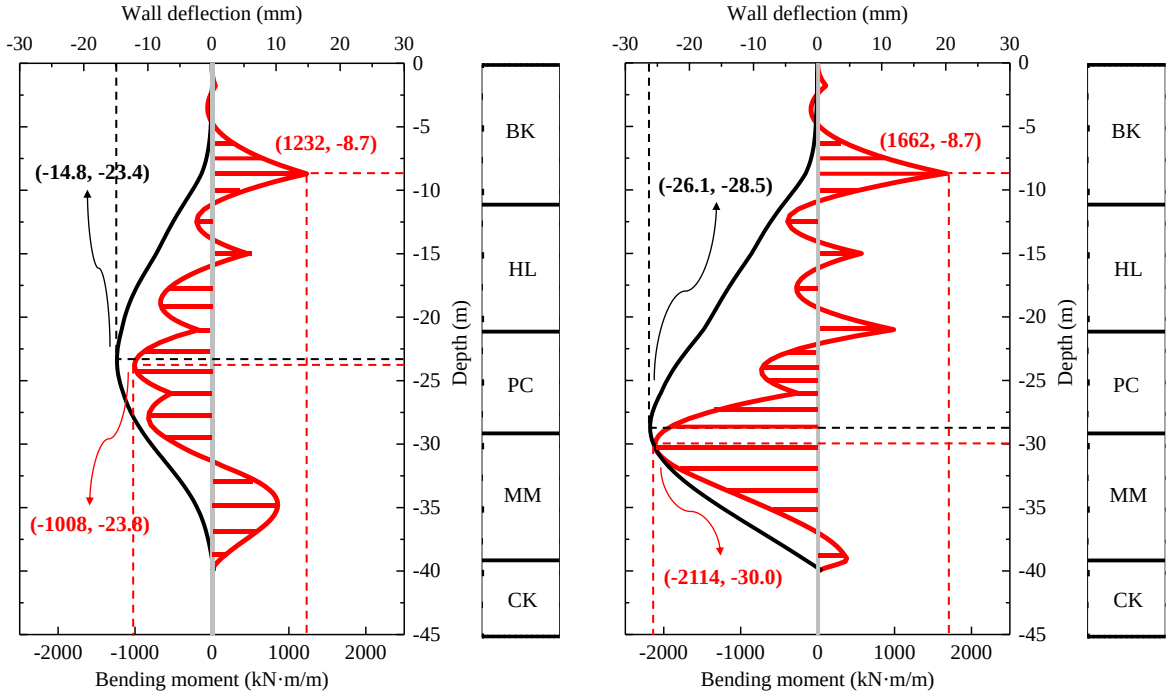

(a) φ_{MM} = 32.5°, φ_{PC} = 18°

(b) φ_{MM} = 17.5°, φ_{PC} = 18°

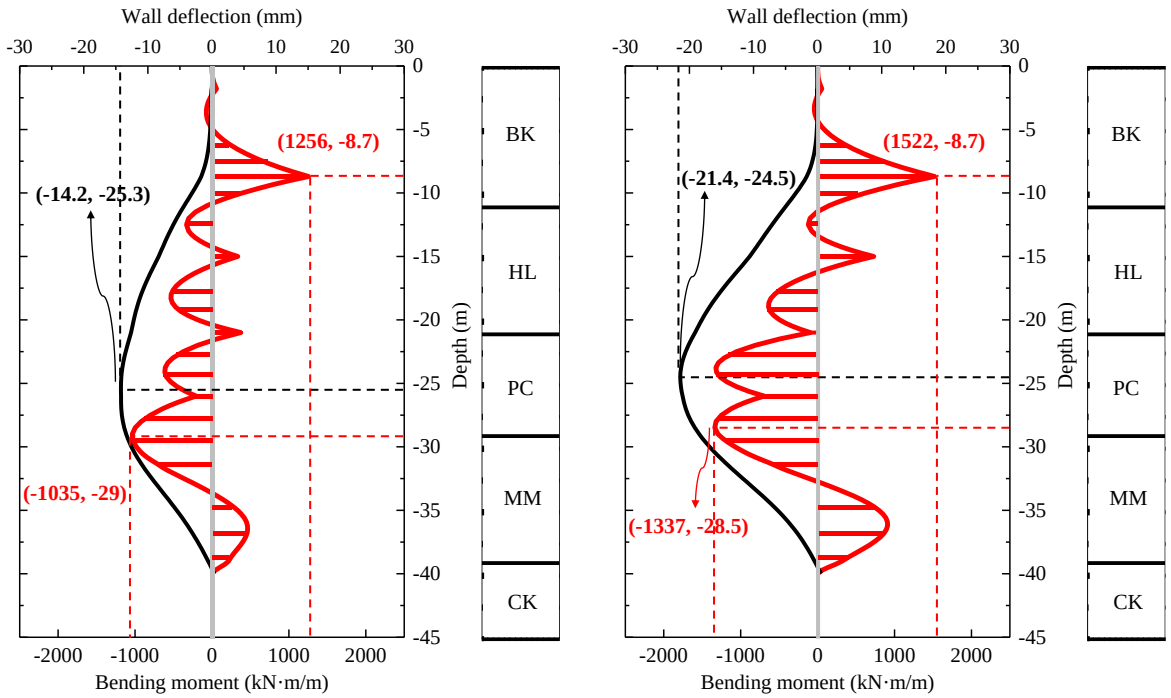

(c) φ_{MM} = 25°, φ_{PC} = 23.4° (d) φ_{MM} = 25°, φ_{PC} = 12.6°

Fig. 3.13 Influences of MM and PC friction angles on the wall bending moment and horizontal deflection.

The sensitivity index of the initial earth pressure coefficient at the rest of layer PC follows with being around 0.1. Its importance can be explained by the stiffness difference between the PC and adjacent layers (HL and MM), which may lead to the maximum wall deflection more likely to occur at layer PC as presented in Fig. 3.7. The k_{0PC} affects the lateral stress magnitudes, and the wall deflection will be directly affected. For the secant stiffness, layer PC contributes the most among the considered layers. It can also be explained by the fact that the maximum wall deflection is more prone to occur in layer PC and the corresponding stiffness is more sensitive to the wall deflection.

Moreover, it should be noted that at least 1.11 million samples are necessary for the MCS calculation. It requires about 3855 days using the direct crude MCS, which is unaffordable in practice. However, for the analysis based on the PCK metamodel, 155 samples can ensure the surrogate model accuracy and the calculation time is around 13 h. It is able to decrease greatly the computational effort. In summary, this proposed PCK-PA makes the probabilistic analysis affordable with accurate results.

3.4.3 Probabilistic distributions of the wall deflection and ground surface settlement

4 cases with different combinations of *COV* for 7 random variables are considered and details are given in Table 3.5. Case A is the reference case, and the *COV* values of secant stiffness, friction angle and initial earth pressure coefficient at rest are respectively increased by 0.1 for cases B, C and D, while the other parameters are kept constant. 500 realizations (samples are generated using LHS) are simulated for each case to investigate the uncertainty effects on the wall deflections and ground surface settlements.

Table 3.5 Four cases for probabilistic analysis.

Cases	COV_{E50ref}	COV_{φ}	COV_{k0}
A	0.15	0.1	0.15
B	0.25	0.1	0.15
C	0.15	0.2	0.15
D	0.15	0.1	0.25

The mean values of the maximum wall deflection and ground surface settlement are respectively given in Fig. 3.14(a) and (b). The deterministic FEM analysis results are also presented for comparison. The mean values are larger than the deterministic ones, and the magnitude is increased with the uncertainty level. Therefore, the excavation stability will be overestimated when the uncertainty is neglected or the uncertainty level is underestimated. It is also observed that there is a significant increase in cases C and D compared to case A, while case B is relatively close to case A.

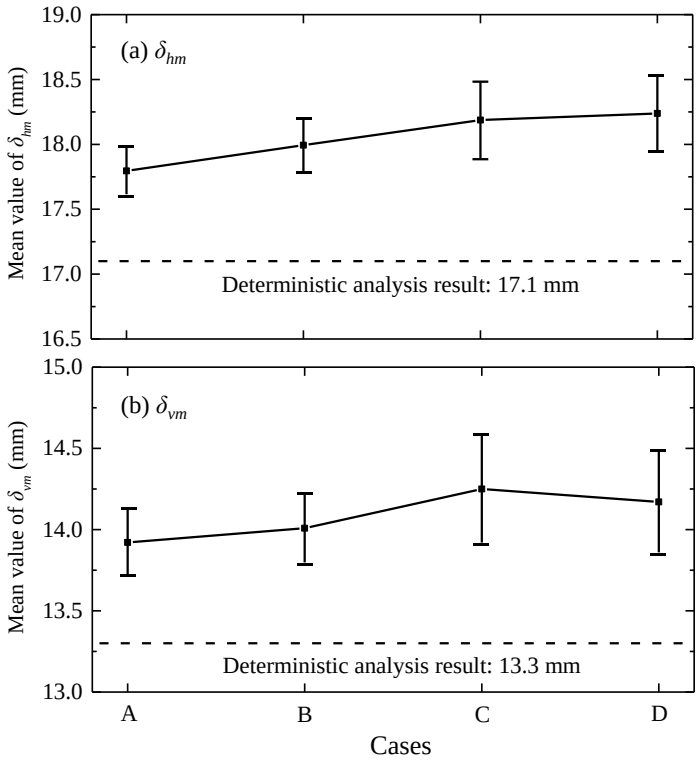

Fig. 3.14 Mean values of the maximum wall deflection and maximum ground surface settlement under different cases.

A confidence interval at 95% level for the mean values is also presented to discuss the parameters variability and the results accuracy. It is observed that the confidence bound width is affected by the input parameters' uncertainty level. Case A has the narrowest confidence interval due to the smallest *COV*s combinations. The confidence intervals of case C are the largest. They are followed by cases D and B. It demonstrates that the friction angle *COV* increase leads to more varied wall deflections and ground surface settlements whereas the secant stiffness is the least sensitive one. It is consistent with the sensitivity analysis results presented in Fig. 3.11. Besides, the confidence intervals for ground surface settlement are greater than the wall deflection ones, which is similar to the results of Nguyen and Likitlersuang (2021).

It is noted that the confidence interval is also affected by the considered simulations number, i.e., a large simulations number can reduce the interval and improve the analysis results accuracy. However, there is no significant improvement in the analysis results when the simulation number is greater than a certain value, whereas the computational efforts are increased. A simulation number sensitivity analysis is necessary to balance the accuracy and computational burden. Fig. 3.15 displays the numerical convergence of the estimates of mean values and standard deviation (Std.) for δ_{hm} and δ_{vm}. It can be observed that case A with small *COV* values is more prone to converge and there is no prominent change for cases B, C and D after 300 simulations. It

confirms the accuracy and rationality of the results based on 500 simulations for each case in this study.

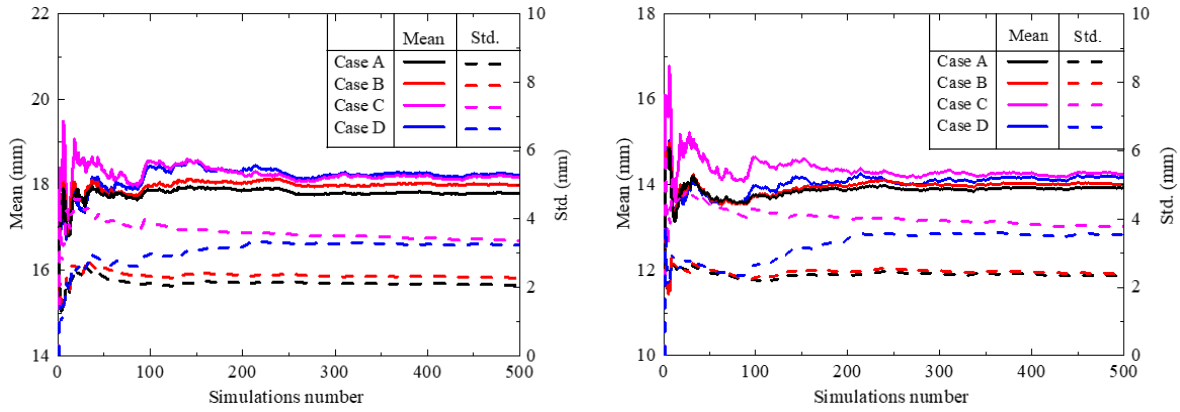

(a) δ_{hm} (b) δ_{vm}

Fig. 3.15 Numerical convergence of mean values of maximum wall horizontal deflection and surface settlement.

The distributions of the wall deflection and ground surface settlement are plotted respectively in Fig. 3.16 and Fig. 3.17. The deterministic analysis (DA) contour is also shown for comparison. It is seen that the wall deflection and ground surface settlement obtained by the deterministic analysis are included in the probabilistic analysis (PA) distribution range, while the probabilistic analysis gives further possible cases compared to the deterministic one. It allows providing more references for the excavation design and construction. Besides, case A gives the narrowest wall deflection and ground surface settlement distribution and the ranges are greater as the *COV* value increases. Case C has the most significant variation, which is followed by cases D and B (taking the wall deflection as an example, the ranges are respectively [-13 mm, -26.5 m], [-10.4 mm, -28.6 m] and [-11 mm, -28.5 m] for cases B, C and D). It indicates again that the friction angle is more sensitive to the horizontal wall deflections and ground surface settlements compared with other parameters (secant stiffness and initial earth pressure coefficient at rest).

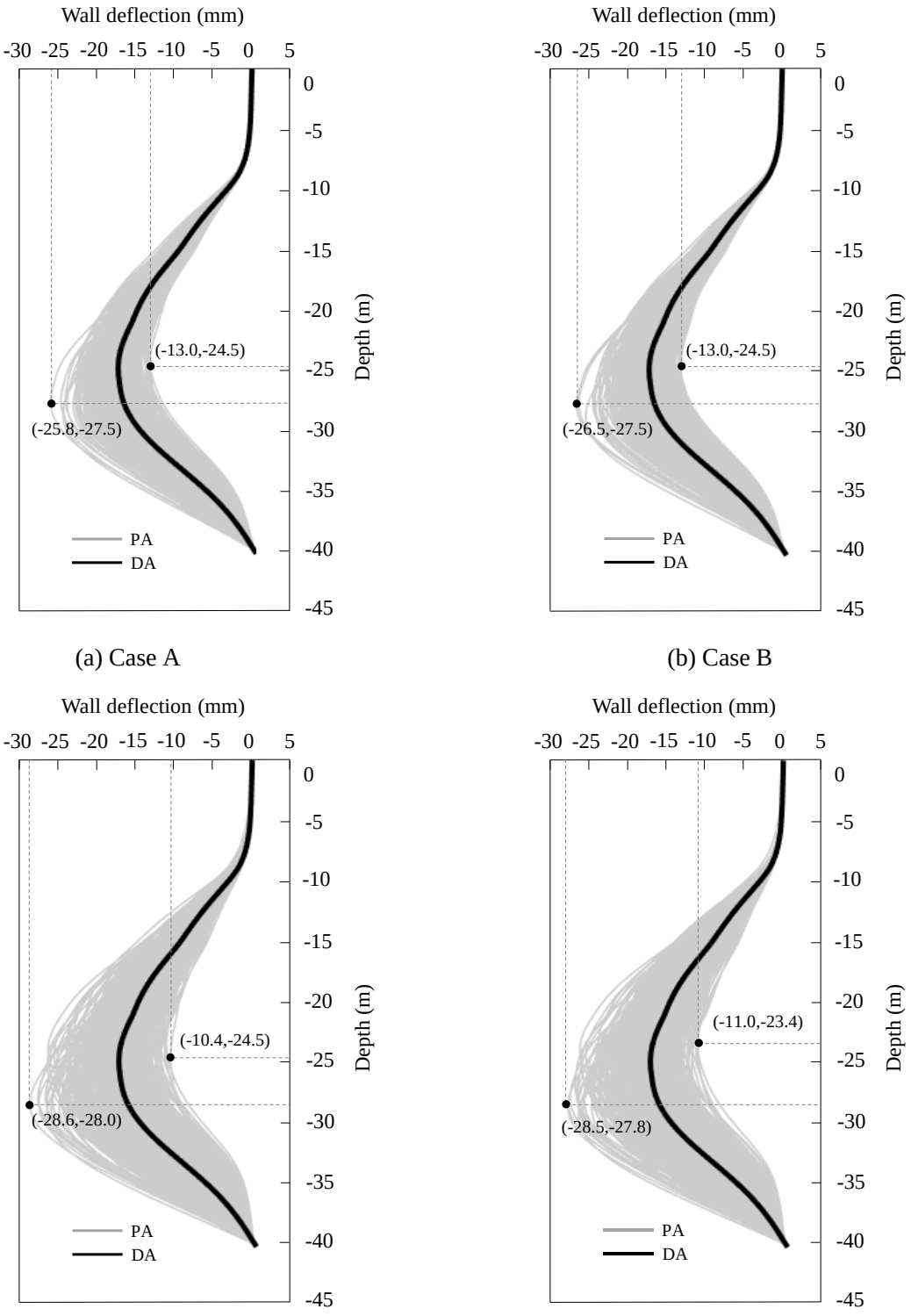

Fig. 3.16 Wall deflection contours using deterministic and probabilistic analyses.

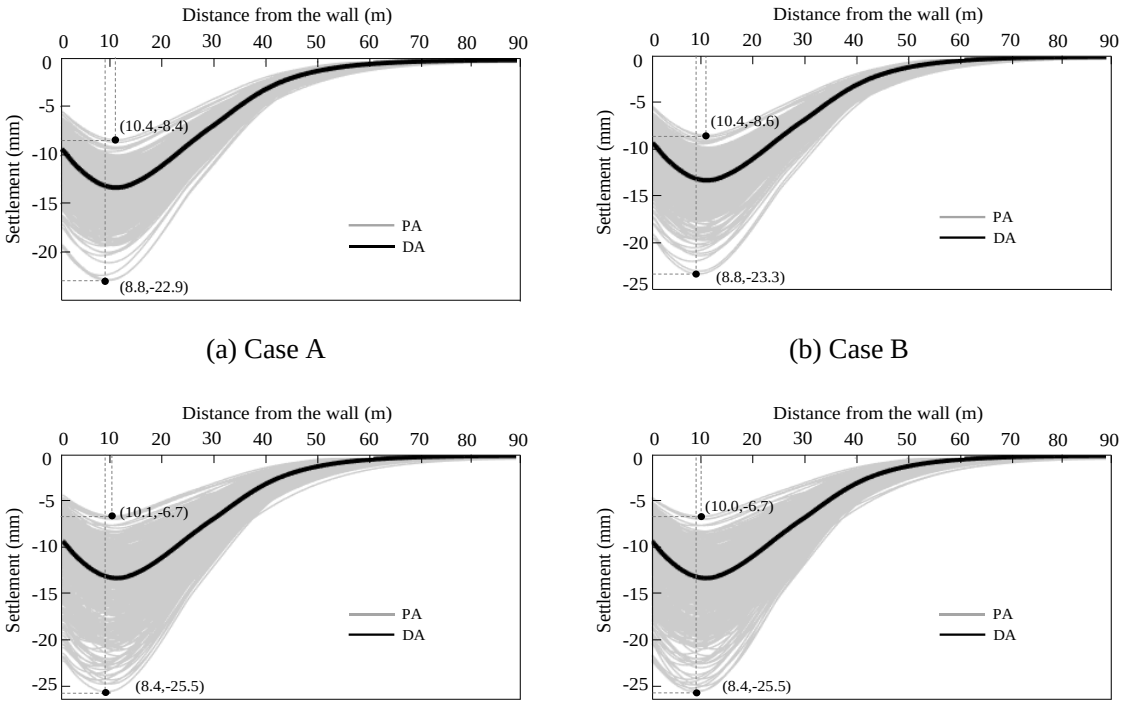

Fig. 3.17 Ground surface settlement contours using deterministic and probabilistic analyses.

In order to specify the probability of overestimation and underestimation for the wall deflection and ground surface settlement, the PDF and CDF of δ_{hm} and δ_{vm} based on 500 realizations are presented in Fig. 3.18. For the maximum wall deflections, about 36~42% of the probabilistic simulations are smaller than the deterministic one, while the percentage range is 42~48% for the ground surface settlements. In addition, the overestimation probability of case C is the smallest. It is followed by cases D, A and B. It can be explained by Fig. 3.16 and Fig. 3.17, the wall deflection and surface settlement distribution ranges are wider for case C and more cases with small magnitudes are generated.

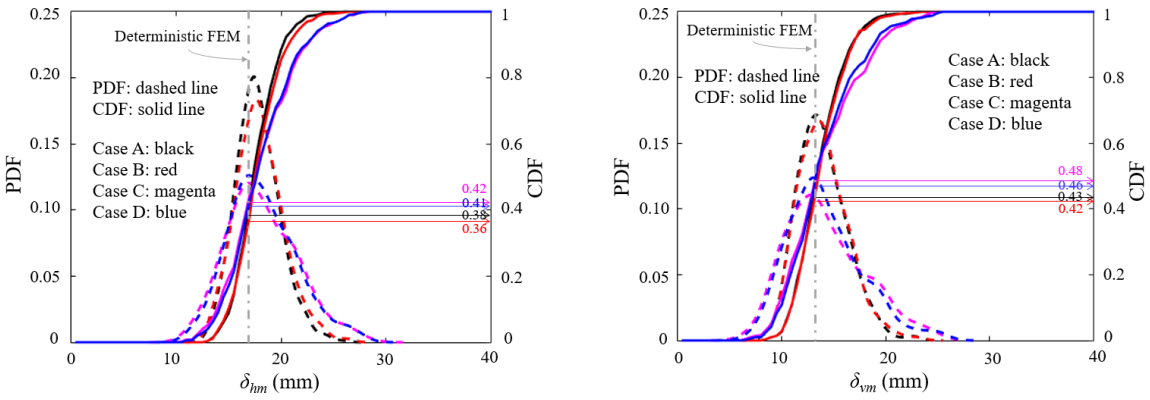

Fig. 3.18 PDF and CDF of maximum wall deflections and ground surface settlements.

The location determination where the maximum wall deflection and maximum ground surface settlement occur is important for the structural assessment of diaphragm walls and the adjacent buildings construction. Fig. 3.19 depicts the depth frequency at which the maximum wall deflection occurs for different cases. It is observed that the δ_{hm} locations are distributed widely as the *COV* value increases ([22 m, 30 m] for cases A and B; [18 m, 30m] for cases C and D). However, the depths are mainly located between 24 m and 26 m below the ground surface (case A: 62%, case B: 59%, case C: 36% and case D: 41%) due to the stiffness difference between layers HL, PC and MM.

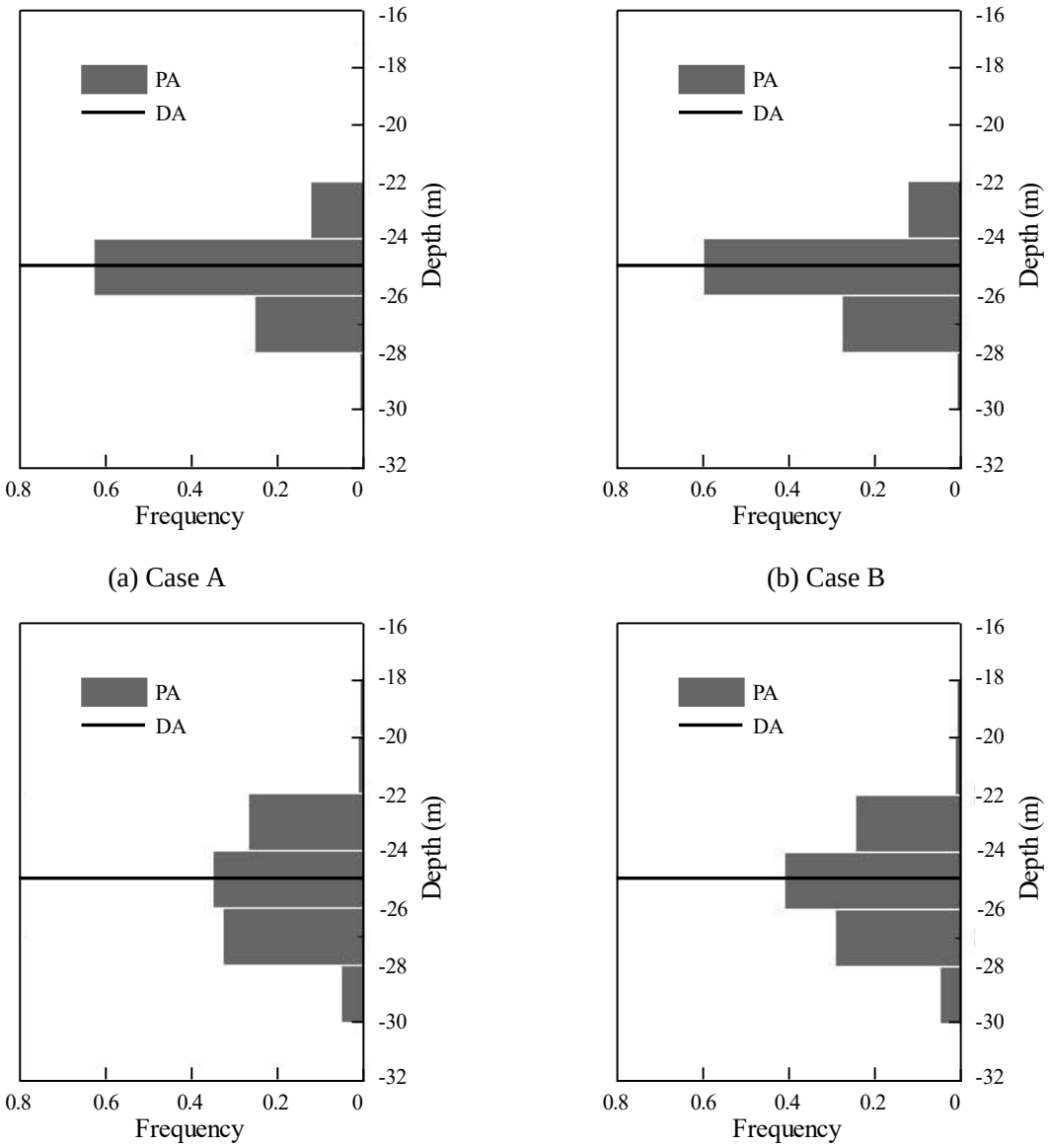

(a) Case A

(b) Case B

(c) Case C

(d) Case D

Fig. 3.19 Frequency of the maximum horizontal wall deflection location.

Fig. 3.20 gives the distance from the diaphragm wall distributions where the maximum ground surface settlement occurs. The δ_{hm} is located between 6 m and 12 m from the diaphragm wall for cases A and B, and the range increases to [4 m, 14 m] for cases C and D. Whereas the maximum surface settlements mainly occur in the range of 10 m to 12 m from the wall. Therefore, the construction activities should be considered and monitored in the ground surface settlement influence zone (80 m, approximately 2.5 times the excavation depth as shown in Fig. 3.17), particularly in the range of [10 m, 12 m], where most of the maximum surface settlements outcomes are observed.

In addition, similar results are achieved for the wall deflections and ground surface settlements that the deterministic results lie in the highest frequency range of the probabilistic analysis.

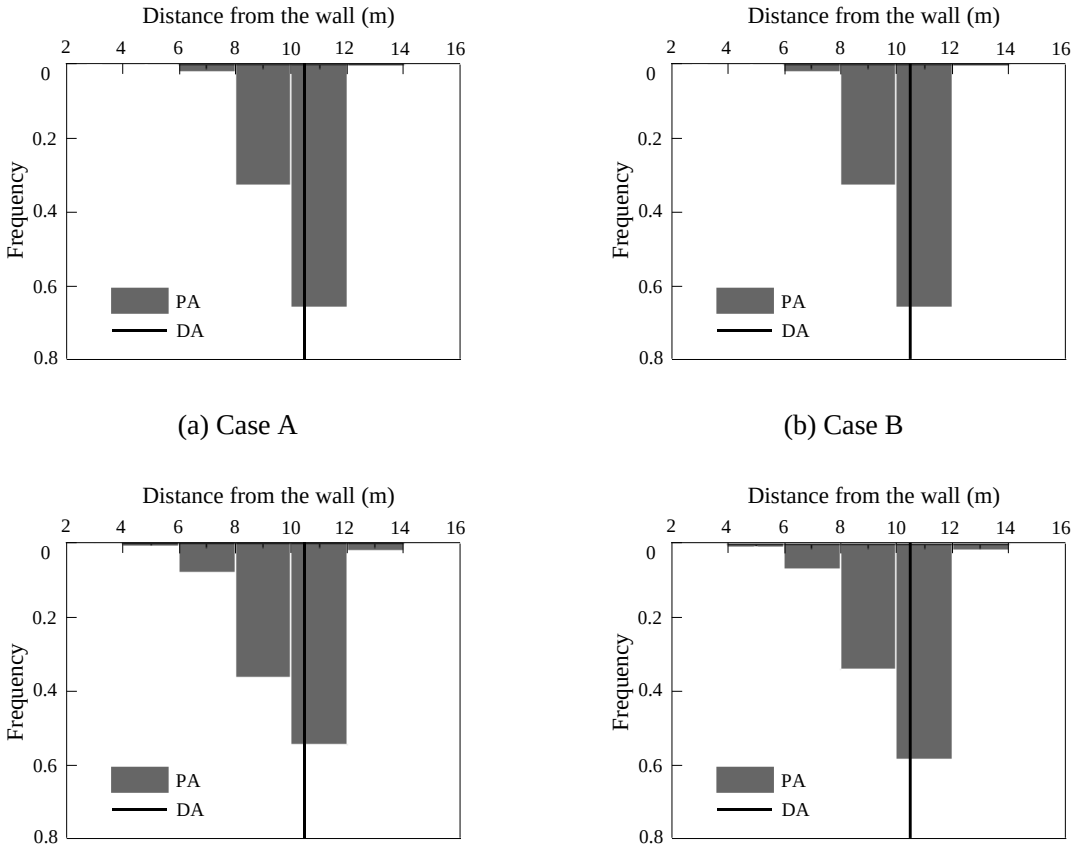

Fig. 3.20 Frequency of the maximum ground surface settlement location.

3.4.4 Relation between the maximum wall deflection and ground surface settlement

This section investigates the relation between the maximum wall deflection and maximum ground surface settlement under 4 cases presented in Table 3.5. Fig. 3.21 plots the δ_{hm} distributions versus the ratio between δ_{vm} and δ_{hm}. As expected, with the *COV* level increase, the points are more dispersed. However, the ratio δ_{vm}/δ_{hm} is generally within the range of [0.5, 1], which is similar to the existing studies (Kung et al., 2007c; Tan and Wei, 2012). It means that the maximum ground surface settlements are smaller than the maximum wall deflections and there is a positive linear relation between δ_{vm} and δ_{hm}. The ratio histogram distributions are presented in the upper part of each subfigure and it is observed that most of the ratios fall between 0.7 to 0.8 regardless of the uncertainty effect.

In addition, there is a trend between the ratio and the maximum wall deflections from the scatter figures. The ratio distributions within 4 deflection ranges ([10 mm, 15 mm), [15 mm, 20 mm), [20 mm, 25 mm), [25 mm, 30 mm]) are discussed and the results can be found in the right part of each subfigure. It can be observed that the ratio tends to be greater for cases with large δ_{hm} values. Taking case C as an example, when the δ_{hm} falls between 10 to 15 mm, the ratio varies from 0.5 to 0.9 and most of the cases are within the range of [0.7, 0.8]. However, the ratios are mainly located between 0.8 to 0.9 when the δ_{hm} is larger than 20 mm. Therefore, it is more rational and conservative to consider larger δ_{vm}/δ_{hm} ratios for cases with larger values of δ_{hm}.

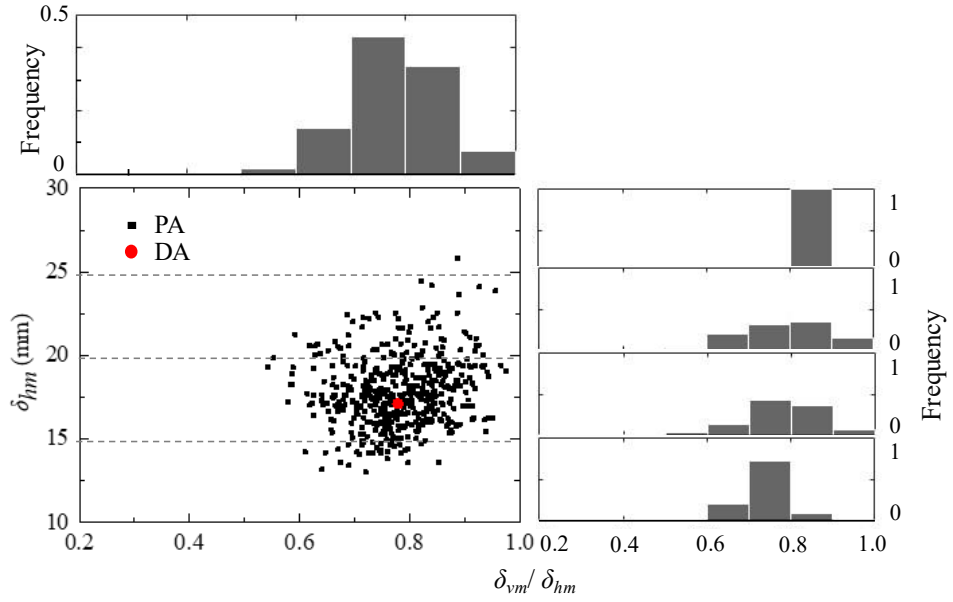

(a) Case A

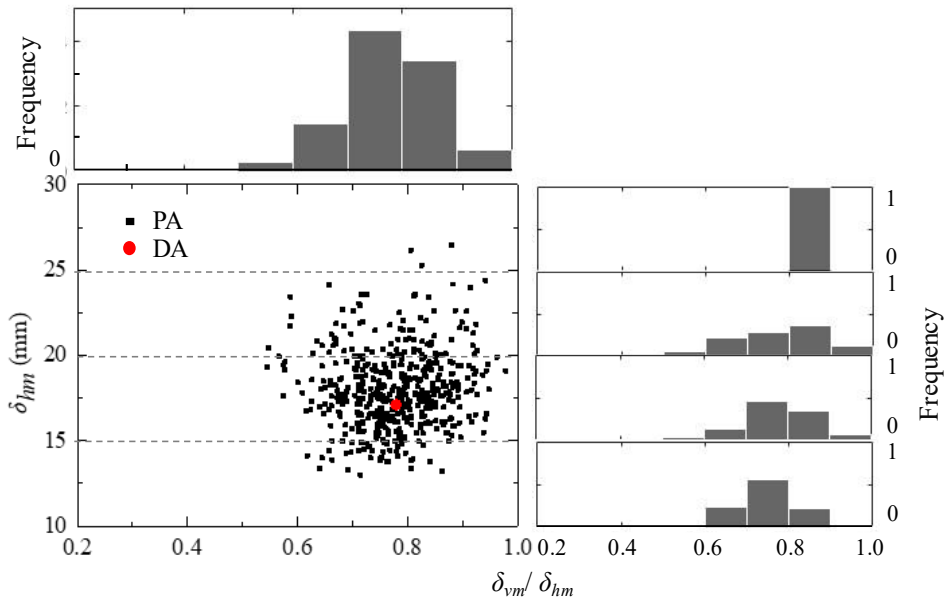

(b) Case B

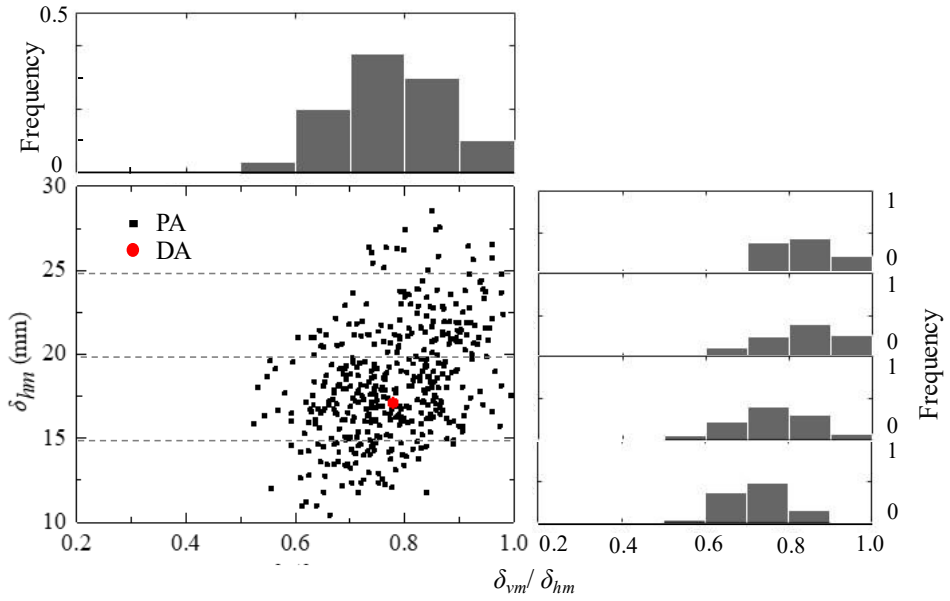

(c) Case C

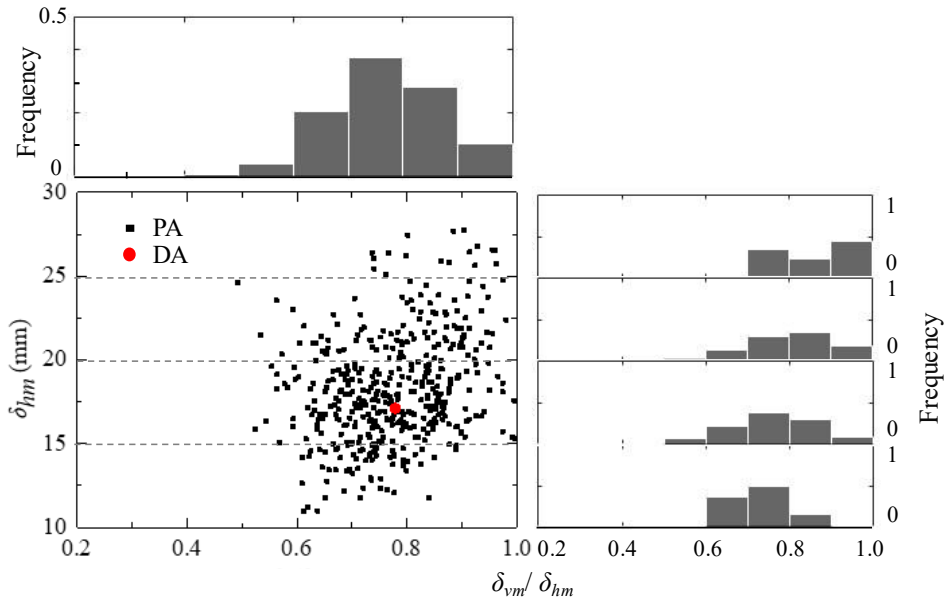

(d) Case D

Fig. 3.21 Relationship between the maximum wall deflection and maximum ground surface settlement under different cases.

3.4.5 Probabilistic serviceability assessment

It should be noted that the allowable thresholds in one probabilistic analysis depend on several factors, such as the soil types, supporting system and the construction safety level requirement (Zhang et al., 2015c). This section assesses the probability of serviceability limit state failure considering different limiting values. The failure mode associated with the wall deflection instead of the ground surface settlement is considered by the fact that: (1) the maximum wall defection is larger than the maximum ground surface settlement values as discussed in section 3.4.4. It is thus more critical to consider that; (2) the wall deflection is relatively easier to predict accurately than the ground surface settlement (Kung et al., 2007a); (3) the horizontal wall deflection-induced excavation failure mode is important in the SLS assessment (Johari and Kalantari, 2021; Luo et al., 2018b; Zhang et al., 2015c).

Fig. 3.22 depicts the P_f value variation with the maximum horizontal wall deflection exceeding different limiting values (12 mm to 30 mm). With the increase of the limiting wall deflection, the failure probability is decreasing since higher thresholds are not easily exceeded. The P_f value variation is large for small *COV* value cases with a difference of 5 orders of magnitude. Besides, the friction angle *COV* increase can increase considerably the failure probability, which is followed by the effects of k_0 and E_{50}^{ref}. Taking the limiting wall deflection of 30 mm as an example, the P_f value varies from 1.3e-5 to 6.9e-4 in the COV_{E50ref} range of [0.15, 0.35], while

the P_f can be up to 0.091 with the COV_φ increase. It highlights again the importance of the friction angle.

Besides, it is seen that when the limiting wall deflection is larger than about 17 mm, the P_f value is increased as the uncertainty increases. Conversely, the P_f is decreased. This is because the deterministic maximum horizontal wall deflection is 17.1 mm for the reference case and the peak value of wall deflection PDF corresponds to about 17 mm as shown in Fig. 3.10. Therefore, when the limiting value is smaller than 17 mm, the probability of exceeding the limiting value decreases with the *COV* value increase due to the wide distributions of maximum horizontal wall deflection, and subsequently induce a smaller failure probability.

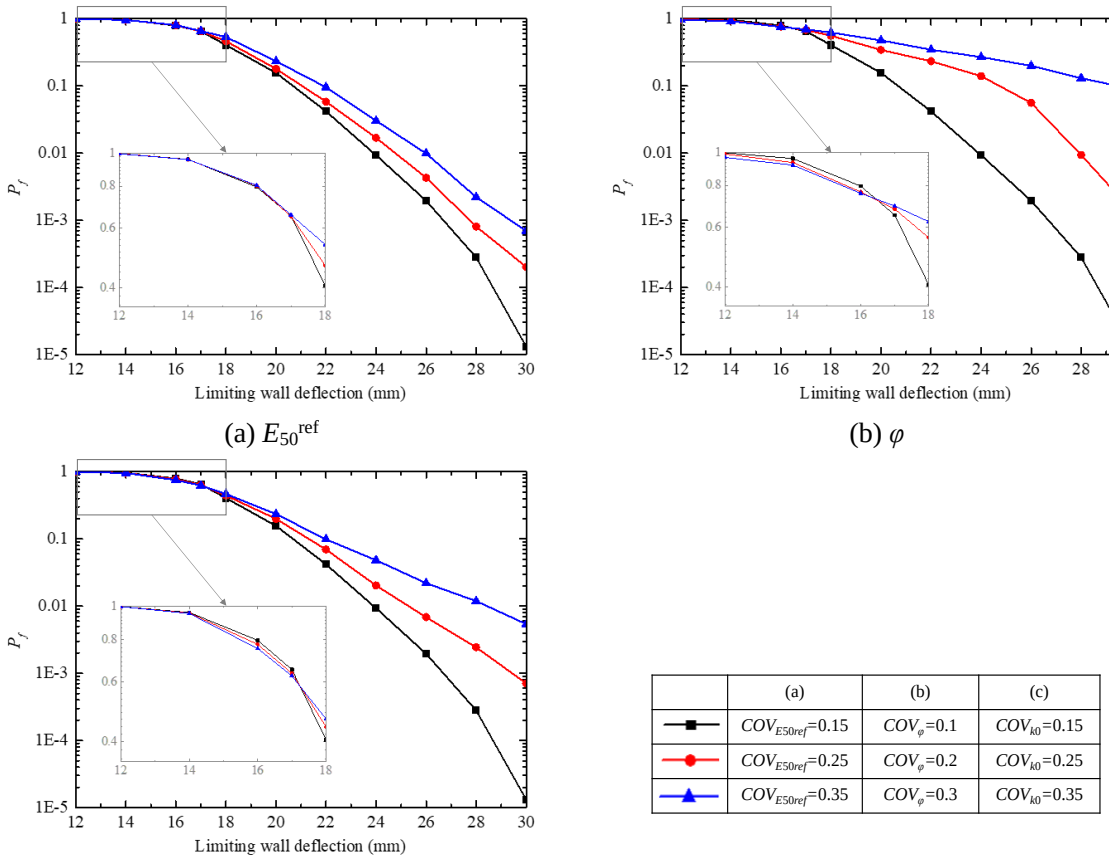

Fig. 3.22 Effect of parameters uncertainties on the probability of exceeding specified limiting wall deflection.

The sensitivity analysis is also implemented for different uncertainty levels and the results can be found in Fig. 3.23. It is observed that with the *COV* increase, the corresponding sensitivity indices also increase. For example, the secant stiffness of layer PC has a great influence on the wall deflections and the index can be up to 0.2 when the *COV* value is equal to 0.35. Therefore, the determination of the uncertainty level should be accurately done.

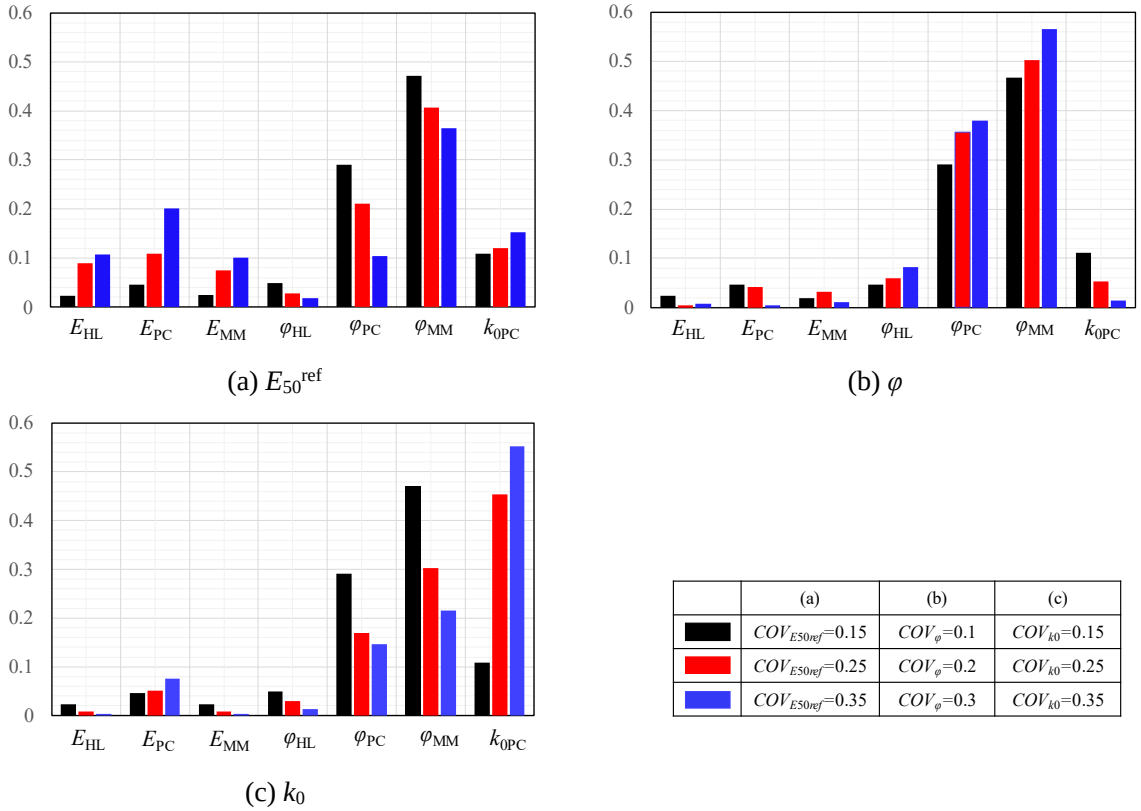

Fig. 3.23 Effect of parameters uncertainties on the sensitivity indices.

This section indicates that the choices of the limiting wall deflection and parameters uncertainty level play a significant role in the failure probability calculation. Some references for the determination of the limiting wall deflection considering the related parameter uncertainties and the target serviceability failure probability are provided.

3.4.6 Soil-wall interaction effects

Fig. 3.12 shows that the plastic points are mainly distributed on the soil-wall interface, which means that the interface plays an important role in the excavation deformation. The above discussions consider the interface coefficient r_i equals to 1, while retaining wall installation or excavation construction may influence the interface strength and the horizontal wall deflection may be further affected. Therefore, the soil-wall interface strength reduction effects on the serviceability failure probability are necessary. The shear strength is reduced by the interface coefficient and can be determined by

$$\begin{cases} c_i = r_i c \\ \varphi_i = \arctan(r_i \tan\varphi) \end{cases} \tag{3.2}$$

where c_i and φ_i are respectively the cohesion and friction angle of the soil-wall interface and r_i is the reduction factor.

A range of [0.5, 1] is considered in this real case study, which is suggested by the design manuals (Canadian, 2006; Taylor and Wang, 2013) and the results are presented in Fig. 3.24. It can be found that with the r_i increase, the failure probability is decreasing and the P_f varies considerably for cases with small *COV* values. For example, the P_f decreases respectively about 99.9% and 68.2% for cases of COV_φ =0.1 and COV_φ =0.3. Besides, the parameters uncertainty level determination is more significant with the soil-wall interface coefficient increase.

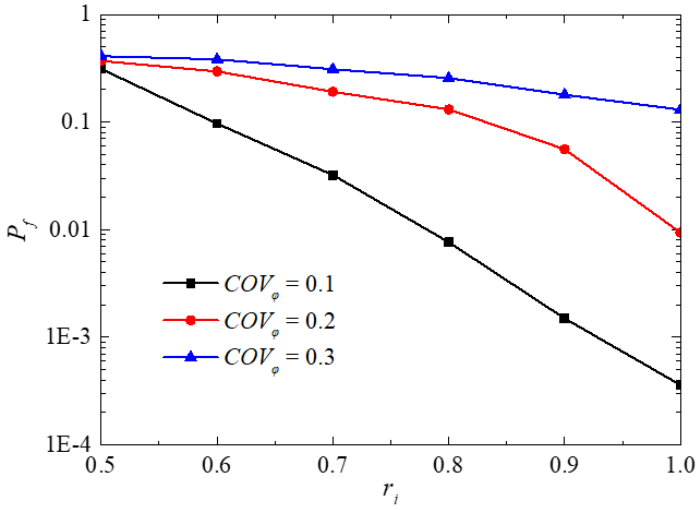

Fig. 3.24 Effects of the soil-wall interface on failure probability.

3.5 Conclusion

This study investigated the deterministic and probabilistic stability of deep excavations based on a real case: the Fort d'Issy-Vanves-Clamart excavation (FIVC). The Finite Element Method (FEM) is adopted to predict the wall horizontal deflections and ground surface settlements. The comparison with the field measurements and the existing studies is carried out. The results indicate that the horizontal wall deflections and ground surface settlements of the FIVC excavation are smaller than the former studies since ① the FIVC station is located in a site with a considerable thickness of hard layers (Hard Limestone, Meudon Marls and Chalk); ② the diaphragm wall is embedded into layers Meudon Marls and Chalk; ③ a multi-strutted support system is implemented.

The proposed PCK-PA is then implemented for the excavation serviceability assessment in a probabilistic framework. The distributions of the wall deflections and ground surface settlements are wider as the *COV* value increases. The corresponding ranges for locations where the maximum wall deflection (δ_{hm}) and ground surface settlement (δ_{vm}) occur are also increased. The δ_{hm} mainly occurs from 24 m to 26 m below the ground surface, and δ_{vm} is mainly distributed at the range of [10 m, 12 m] behind the retaining wall for the FIVC excavation. Besides, the maximum ground surface settlement is linearly distributed with the maximum horizontal wall deflection and the δ_{vm}/δ_{hm} ratio is generally in the range of [0.5, 1]. It is more rational to use a larger δ_{vm}/δ_{hm} ratio to determine the δ_{vm} value for cases with larger δ_{hm}.

The sensitivity analysis indicates that the friction angle for the excavation bottom layer (MM) contributes the most to the model response variation by the fact that the soil deformation behind the wall is significant due to the reduced shear strength and the slip surface even reaches the wall toe. Parameters related to layer PC are also important by the fact that the maximum wall deflection is more likely to occur in the PC layer. The corresponding parameters are sensitive to the wall deflection variations. The parameter uncertainty level also influences the sensitivity indices. It should then be determined carefully.

Benefitting from the high efficiency of the PCK-PA, the probabilistic serviceability assessment is implemented. The results show that the serviceability failure probability depends on the adopted limit wall deflection and on the parameters uncertainty level. The failure probability P_f increases with the *COV* value when the limiting wall deflection is larger than the deterministic wall deflection. The P_f decreases as the *COV* increases when the limiting wall deflection becomes smaller than the deterministic one. Some references for the limiting wall deflection determination are also provided. The soil-wall interface influences on the excavation stability are discussed and the results found that the interface influence greatly the excavation stability, particularly for cases with small *COV* values.

Chapter 4

Undrained stability analysis of circular shafts in non-homogeneous clayey soils

Contents

4.1 Introduction 127

4.2 Problem statement 127

4.2.1 Circular shaft 127

4.2.2 Uncertainty consideration 130

4.3 Model of non-homogeneity and comparison 130

4.3.1 Deterministic computational model 130

4.3.2 Deterministic FELA model verification 132

4.4 Probabilistic discussions 134

4.4.1 Probabilistic results of the reference case 135

4.4.2 Importance of the uncertainty consideration 136

4.4.3 Influence of the soil-wall adhesion 138

4.4.4 Influence of the soil non-homogeneity 140

4.5 Conclusion 142

4.1 Introduction

This chapter aims to perform probabilistic basal heave stability analyses of supported circular shafts in undrained non-homogeneous soils. After a brief explanation of the studied problem, the deterministic model construction and analysis using the Finite Element Limit Analysis is detailed. The probabilistic analysis based on the proposed PCK-PA is then implemented to discuss the circular shaft stability. Some comparisons and discussions considering the soil non-homogeneity and uncertainties consideration, and the soil-wall interaction of the circular shafts are provided. The major contributions of this work compared to the previous studies about the circular shaft stability are the following ones: (1) the basal-heave stability for supported circular shafts is discussed in a probabilistic framework, and the soil undrained shear strength parameter uncertainties and its increasing gradient (i.e. non-homogeneity coefficient), unit weight and soil-wall interface strength, are considered; (2) the effects of parameter uncertainties, soil-wall interface and soil non-homogeneity on the circular shaft stability are discussed, and the sensitivity indices are estimated to rank the uncertain parameters importance, which is useful for the design and construction in practice.

(***Disclaimer***: The content of this chapter was published in the following journal paper: Tingting Zhang, Julien Baroth and Daniel Dias. (2021). Probabilistic basal heave stability analyses of supported circular shafts in non-homogeneous clayey soils. Computers and Geotechnics, 140, 104457)

4.2 Problem statement

4.2.1 Circular shaft

The supported circular shaft is illustrated in Fig. 4.1 using 3D and 2D representations. H and R_c are respectively the depth and diameter of the circular shaft. D is the wall embedment depth, and T is the depth from the excavation base to the hard stratum.

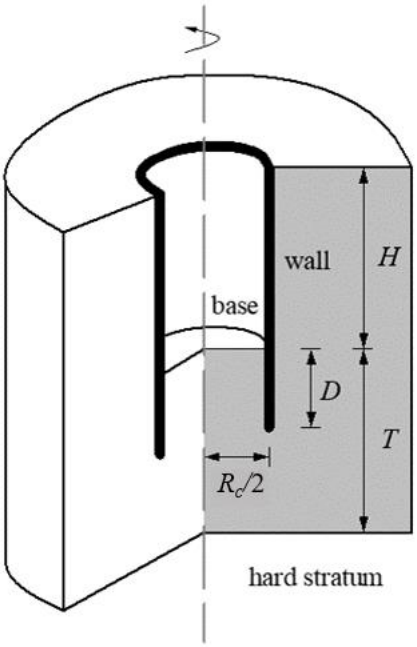

(a) 3D view

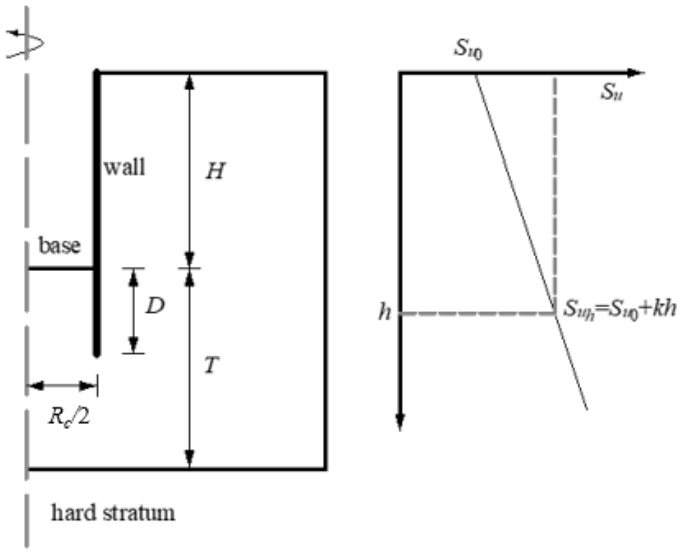

(b) 2D view

Fig. 4.1 Introduction of the supported circular shaft of the geometry and evolution of the undrained shear strength with depth.

The soil is supposed to follow a linear elastic-perfectly plastic model based on the Tresca criterion, which is characterized by the undrained shear strength (S_u), Young's modulus (E_u) and Poisson's ratio (υ_{soil}). The soil profile is non-homogeneous and the undrained shear strength is considered to vary linearly with depth as shown in Fig. 4.1(b), where S_{u0} is the undrained shear strength at the ground surface, and the undrained shear strength value at any depth h below the ground surface can be expressed by

$$S_{uh} = S_{u0} + kh \tag{4.1}$$

where k is the gradient that defines the rate at which the undrained shear strength increases linearly with depth h, its value varies from 0 to 3.5 kN/m^3 (Zhu et al., 2017).

The wall is assumed to behave as a linear elastic material and is embedded to improve the shaft stability. The wall thickness is set equal to 1.0 m in this study by the fact that its value slightly influences the shaft stability. The safety factors difference is lower than 0.5% for the wall thicknesses in the range from 0.6 m to 1.2 m (Goh et al., 2019). The interface between the soil and wall is specified by the Tresca material and its strength is modified using the soil-wall interface r_i, which can be expressed by $S_{u-interface} = r_i S_{u-soil}$. The value of r_i is considered to vary from 0.1 to 1 for this circular shaft (Cai et al., 2002; Dong, 2014; Faheem et al., 2003; Goh, 2017a; Goh et al., 2019b; Zhao et al., 2020). Table 4.1 presents the input parameters of the deterministic reference case used in this study.

Table 4.1 Summary of soil, wall and geometric input parameters of the reference case.

Parameters	Notation	Value
Soil		
Undrained shear strength at ground surface	S_{u0} (kPa)	10[a]
Undrained shear strength increase gradient	k (KN/m^3)	1[b]
Soil wall adhesion factor	r_i	0.5[a]
Unit weight	γ_s (KN/m^3)	16[a]
Soil undrained stiffness ratio	Eu / S_u	300[a]
Poisson's ratio	υ_{soil}	0.495[a]
Wall		
Unit weight	γ_w (Kn/m^3)	25
Young's modulus	Eu (kPa)	2.0e7
Poisson's ratio	υ_{wall}	0.25
Geometry		
Circular shaft depth	H (m)	16[a]
Circular shaft diameter	R_c (m)	15[a]
Wall embedment depth	D (m)	10[a]
Thickness to hard stratum	T (m)	84[a]

Note :

[a] Based on values given by Goh (2017b).

[b] Griffiths and Yu (2015).

4.2.2 Uncertainty consideration

Four input parameters are considered as random variables in the probabilistic analysis, which include the undrained shear strength at the ground surface S_{u0}, undrained shear strength increase gradient k, soil-wall adhesion factor r_i and unit weight γ. Other parameters can be controlled during construction and are considered deterministic parameters. A lognormal distribution is adopted to model the parameter variability to avoid negative values, and the input parameters are considered independent. The summary of the parameters' statistics and corresponding limits, which cover a range of extremes, is summarized in Table 4.2.

Table 4.2 Statistical properties of input random variables.

Parameters	Notation	Statistics of parameters			
		Mean	*COV*	Distribution	Range
Undrained shear strength at ground surface	S_{u0} (kPa)	10	0.2[a]	Lognormal	0~100
Undrained shear strength increase gradient	k (kN/m^3)	1	0.1	Lognormal	0~3.5[b]
Soil wall adhesion factor	r_i	0.5	0.2[a]	Lognormal	0.1~1
Unit weight	γ (kN/m^3)	16	0.05[c]	Lognormal	-

Note:
[a] Based on values given by Goh et al. (2019b).
[b] Zhu et al. (2017).
[c] Luo et al. (2012a).

4.3 Model of non-homogeneity and comparison

This section aims to present the deterministic computational model and the comparison with the existing studies to validate the model effectiveness.

4.3.1 Deterministic computational model

A Finite Element Limit Analysis (FELA) software (Krabbenhoft et al., 2016) is used to analyse the circular shaft deterministic stability. It combines the powerful capabilities of the finite elements discretization with plastic bound theorems to bracket the exact solutions by the upper bound (UB) and lower bound (LB) analysis (Keawsawasvong and Ukritchon, 2017). It has been extensively used in other kind of geotechnical works, such as tunnels (Wu et al., 2021), strip footings (Raj et al., 2018) and slopes (T. Zhang et al., 2021b).

In UB FELA analysis, the problem is formulated into a second-order conic programming (SOCP), that satisfies the kinematically admissible velocity constraints. In LB FELA analysis, the problem is formulated into a SOCP which satisfies the statically admissible stress constraints including equilibrium equations, stress boundary conditions and yield criterion (Keawsawasvong and Ukritchon, 2017; Krabbenhoft et al., 2016).

The supported circular shaft numerical model is presented in Fig. 4.2. An axisymmetric model is used because of the circular shape and a slice of the cross-section is considered due to the excavation symmetry. Displacements are fixed at the lateral sides in the horizontal directions and are free in the vertical boundary, while they are fully fixed at the model bottom. Besides, the model boundaries are assumed to be at least 5B and 3(H+D) in respectively the horizontal and vertical directions to avoid boundary effects.

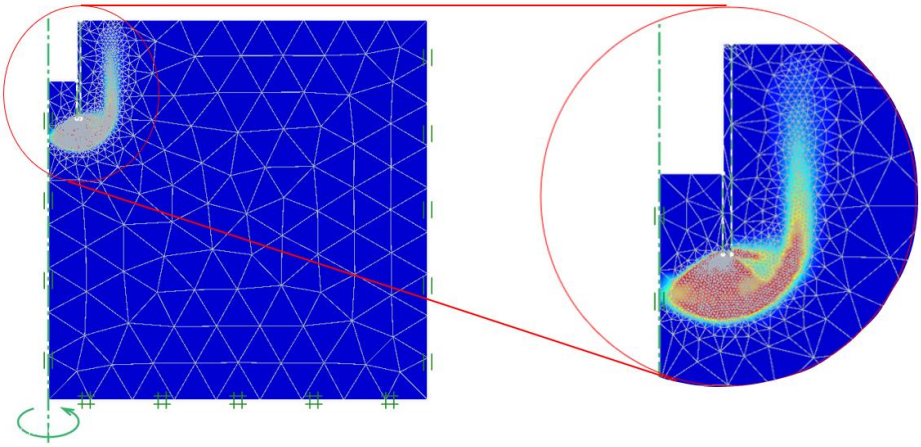

Fig. 4.2 FELA model of the reference circular shaft with adaptive mesh refinement.

The soil is discretized using 3-noded triangular elements. The shear strength value increases linearly with depth from the ground surface considering the k gradient. The contact interface between wall and surrounding soil is specified by means of a shear joint element. Its strength corresponds to the surrounding soil shear strength using the soil-wall adhesion factor r_i.

A powerful feature of Optum G2 is the automatically adaptive mesh refinement according to the distribution of shear dissipation, total dissipation, strain or plastic multiplier. Shear dissipation is considered the adaptivity control parameter in this study since it is generally the most efficient and reliable one for limit analysis (Krabbenhoft et al., 2016). The shear dissipation distribution with mesh is shown in Fig. 4.2. It can be observed that the very fine mesh in the failure region is a consequence of the adaptive mesh refinement.

In order to determine the optimal mesh combining better accuracy and computation effort, a mesh sensitivity analysis was conducted. Non-adaptive mesh refinement cases were also considered for the sake of comparison. Taking the LB FELA analysis as an example, the calculated safety factor (*Fs*) and corresponding computational time are depicted in Fig. 4.3. The elements number (*Ne*) affects greatly the *Fs* and computational time. For the adaptive mesh refinement cases, the values of *Fs* increase quickly when *Ne* is lower than 1000 and tend to a stable value with *Ne* increasing. It allows giving precise results when *Ne* is larger, whereas the computational burden is also simultaneously increasing. For example, *Fs* values are almost the same (1.506 and 1.510 respectively) when the elements number are 3000 and 4000, the calculation time differs considerably (60 s and 83 s respectively). *Fs* using non-adaptive mesh refinement is irregular when *Ne* is small and converges to a value of 1.445 as *Ne* increases, which is conservative compared to the adaptive mesh case. As a result, an adaptive mesh refinement in combination with an element number of 3000 is selected to be used in the following calculations as it provides an optimal results compromise between accuracy and computational burden.

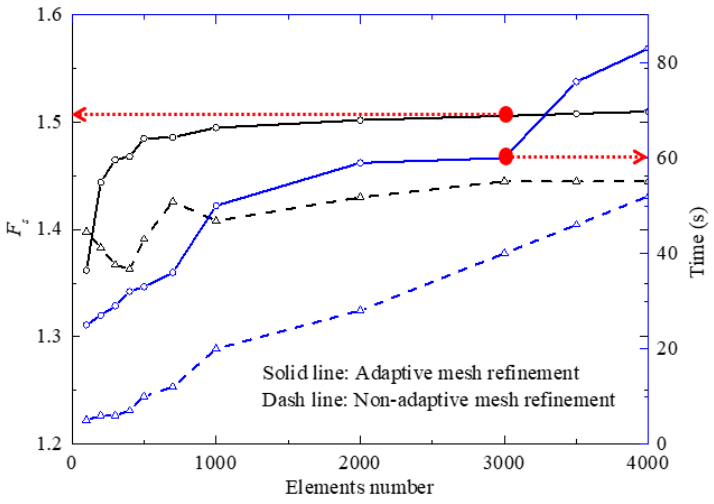

Fig. 4.3 Comparison of the safety factors (left vertical axis, black curves) and computational time (right vertical axis, blue curves) considering the cases with and without adaptive mesh refinement.

4.3.2 Deterministic FELA model verification

Fig. 4.4 shows the safety factor comparison under different combinations of wall embedment depth *D* and *B/H* for homogeneous cases. The safety factors evaluated by the FELA-UB and FELA-LB present the same trends with FEM results as shown in Goh (2017b). It can be observed that the results of FEM are in the range of FELA-LB and FELA-UB. Besides, the non-homogeneity effects are also considered and the comparison is summarized in Table 4.3. The

results are consistent under different cases with different excavation widths, depths, wall embedment depths, undrained shear strengths and non-homogeneity coefficients. All the comparisons can validate the effectiveness the numerical model presented in this study.

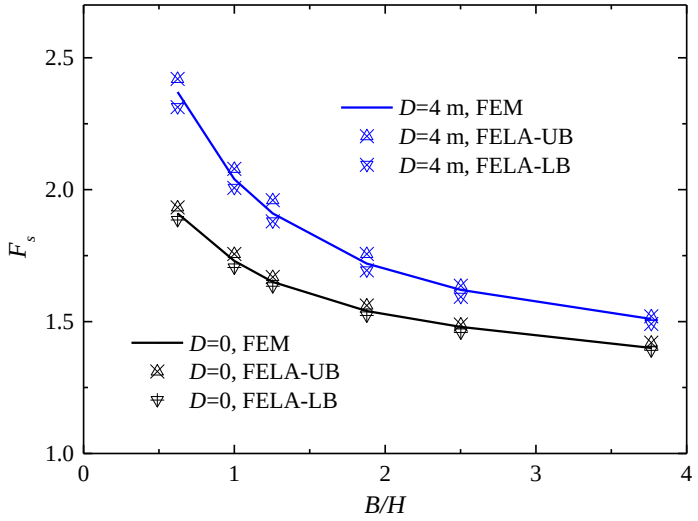

Fig. 4.4 Comparison of the safety factors for homogeneous circular shafts.

Table 4.3 Comparison of the safety factors for non-homogeneous circular shafts.

Case	γ (kN/m^3)	B(m)	T(m)	H(m)	D(m)	S_{u0}(kPa)	k (kN/m^3)	Average method (Goh, 2017b)	FEM (Goh, 2017b)	FELA -LB	FELA -LB
1	16	40	60	16	4	5	1.5	1.287	1.288	1.268	1.306
2	16	40	60	16	4	10	1.5	1.450	1.473	1.440	1.504
3	16	40	60	16	4	20	1.5	1.776	1.813	1.783	1.839
4	16	40	60	16	10	10	1.5	1.952	1.923	1.889	1.95
5	16	40	72	24	4	10	1.5	1.291	1.285	1.266	1.3
6	16	40	80	24	12	10	1.5	1.785	1.748	1.721	1.769
7	16	100	120	24	24	10	1.5	2.180	2.192	2.152	2.23
8	16	20	60	16	10	10	1.5	2.300	2.177	2.133	2.223
9	16	20	60	16	4	10	1.5	1.610	1.544	1.521	1.577
10	16	30	60	16	4	10	1.5	1.498	1.479	1.454	1.509
11	16	40	60	16	4	20	1.2	1.551	1.584	1.557	1.621
12	16	40	60	16	4	10	1.2	1.225	1.246	1.226	1.276
13	16	40	60	16	10	10	1.2	1.634	1.617	1.585	1.651

In order to validate the soil-wall interface application of the present FELA model, the results are obtained with conditions similar to the ones in Goh et al. (2019b), i.e. under plane-strain conditions. Fig. 4.5 shows the *Fs* comparison with different values of soil-wall interface adhesion factor. It is found that the results evaluated by this study and Goh et al. (2019) are consistent.

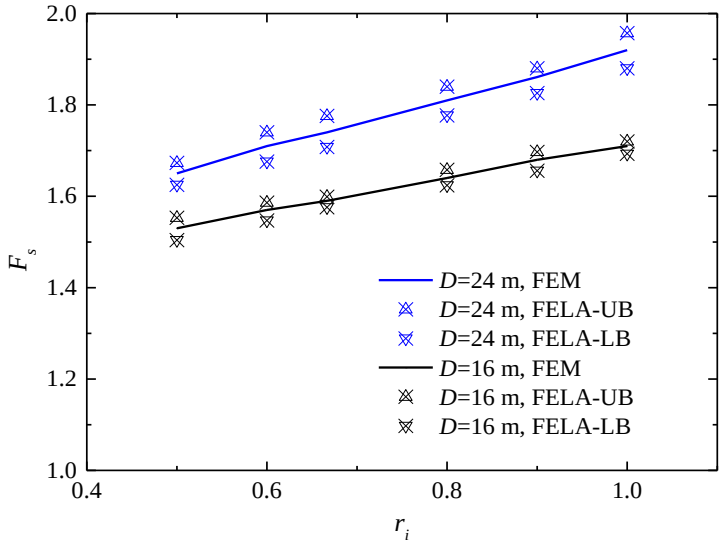

Fig. 4.5 Comparison of the safety factors for different values of soil-wall adhesion factor *m*.

As the comparisons in terms of homogeneous, non-homogeneous soils and soil-wall interface effects are in good agreement, the implemented deterministic FELA model is validated and will be used for the subsequent probabilistic analyses.

4.4 Probabilistic discussions

The probabilistic analysis results are presented first. The discussions of the circular shaft stability under undrained conditions are given, which include (1) importance of parameter uncertainties; (2) soil-wall adhesion effects; (3) soil non-homogeneity. Some recommendations are then provided based on these discussions. It should be noted that the parameters are the same as the reference case presented in Table 4.1 and Table 4.2 if there is no more description. The excavation state is respectively considered as failure and safe when the safety factor is smaller or larger than 1 in the present study. The limit-state function can thus be determined by $Y=Fs-1$. The LB FELA analysis, which can provide safer solutions, is employed in the subsequent probabilistic analysis.

4.4.1 Probabilistic results of the reference case

The reference circular shaft presented in Section 4.2 is analysed based on the above-mentioned probabilistic analysis procedure PCK-PA, and the main results are plotted in Fig. 4.6 and Fig. 4.7. 2.0e5 samples are set for the failure probability calculation, and P_f is found to be 2.2e-3 with a COV_{Pf} being 4.8%, which can ensure the P_f value accuracy. For the statistical moments, the mean value and standard deviation are respectively 1.47 and 0.17. Fig. 4.6 shows the PDF and CDF for the safety factor estimations based on the PCK-MCS. It can be observed from the PDF that the safety factor distribution is approximately symmetric and the *Fs* values mainly vary from 1.0 to 2.0. The CDF allows providing the probability that *Fs* is lower than or equal to one specific value. For example, it can be observed that 59% of the safety factors are smaller than 1.5.

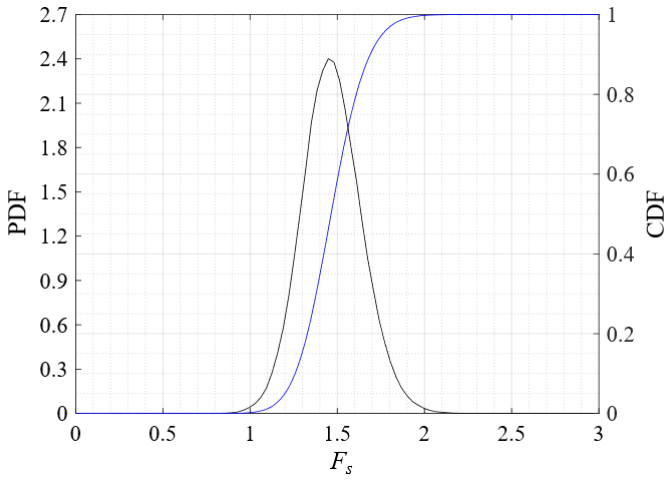

Fig. 4.6 PDF and CDF of the obtained safety factor F_s.

Fig. 4.7 shows the total effect Sobol' indices of the 4 input random variables. It is found that the undrained shear strength increase gradient *k* has the highest sensitivity index with a value of 0.341. It reveals that *k* contributes the most to the model response variation. The soil-wall adhesion factor r_i sensitivity index is slightly smaller than the one of *k*, however, it still influences more the results than the undrained shear strength at the ground surface S_{u0} (0.329 and 0.304 respectively). The least one is the unit weight γ with a Sobol' index being lower than 0.08. This sensitivity discussion demonstrates the importance of the soil non-homogeneity and the soil-wall interface.

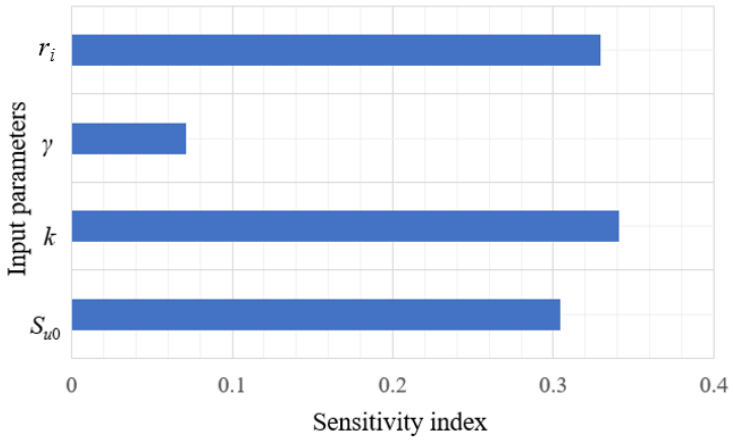

Fig. 4.7 Sensitivity analysis results: undrained shear strength at the ground surface S_{u0}, strength gradient k, unit weight γ and soil-wall adhesion factor r_i.

The metamodel accuracy validation can be found in Fig. 4.8. 1000 input samples are firstly generated based on the LHS, and then the PCK metamodel and numerical model are used to estimate the safety factors. It is observed that the points are distributed around a 45° line and in a range limited by the lines considering a 5% of error. The good consistency of the safety factors indicates that the PCK metamodel can give accurate model evaluations. Besides, it is noted that the PCK-PA only requires 99 calls (10 for the initial ED and 89 for the iterative procedure) to construct the metamodel and then perform the probabilistic methods in a few seconds, which is far below the calculation time of direct probabilistic analysis.

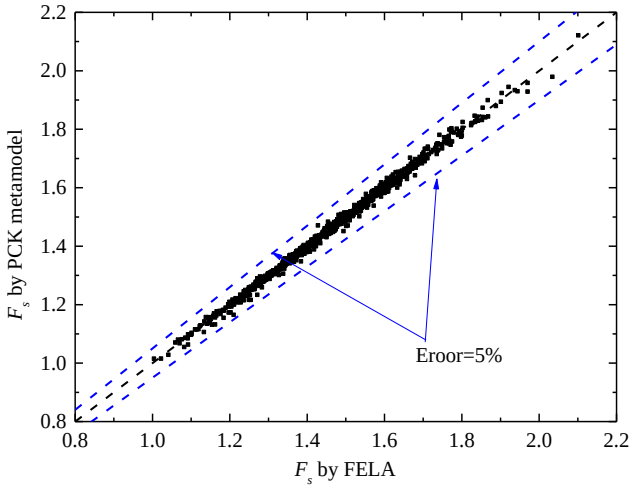

Fig. 4.8 Comparison of the safety factors estimated by FELA and PCK metamodel.

4.4.2 Importance of the uncertainty consideration

Fig. 4.9 depicts the influence of four input variables' coefficient of variation (COV_{Su}, COV_{ri}, COV_k, COV_γ) on the failure probability. 4 cases with different safety factors (Fs=1.06, 1.26, 1.51,

1.77) corresponding to embedment depths (D=3, 6, 10, 14 m) are respectively considered. It is shown that P_f varies with the *COV* values change although the deterministic *Fs* is the same. The larger the *COV* values, the greater the failure probabilities. The *COV* influences are more pronounced for shafts with larger safety factors. Besides, the failure probability is more sensitive when the coefficient of variation value is small. For example, the P_f values are respectively 4.6e-1 (*Fs*=1.06) and 4.7e-3 (*Fs*=1.77) with COV_k being equal to 0.25, whereas the P_f value can be lower to 7.8e-5 (*Fs*=1.77) from 3.6e-1 (*Fs*=1.06) when the COV_k is equal to 0.05. The results reveal that different *COV* values can lead to totally different failure probabilities when varying from 6.0e-1 (hazardous) to 1.0e-5 (good-high level) even for the case with the same safety factors, which point out the important role of the uncertainties consideration for the circular shaft stability analyses.

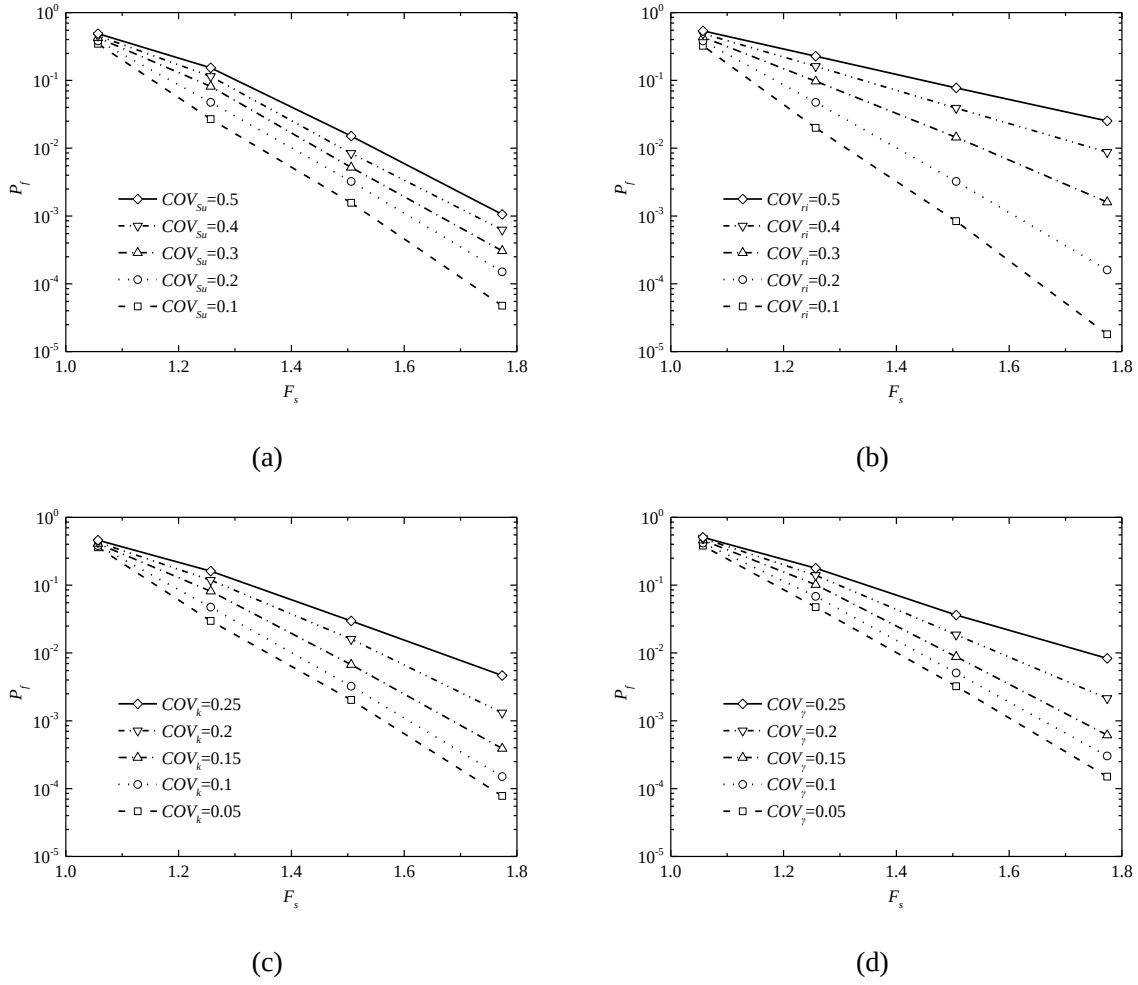

Fig. 4.9 Coefficient of variation of (a) S_u (b) r_i (c) k (d) γ effects on the failure probability

4.4.3 Influence of the soil-wall adhesion

The soil-wall adhesion factor r_i influence on the supported circular shafts stability under different S_{u0} values is discussed and the results are plotted in Fig. 4.10. As shown in this figure, the increase of r_i leads to smaller failure probabilities as expected and its influence is more significant for larger S_{u0} values. For example, the failure probability is in the range from 8.4e-1 (r_i=0.3) to 1.0e-2 (r_i=1) when S_{u0}=2.5 kPa, while for the case with S_{u0}=10 kPa, the values are respectively 1.3e-1 and 1.0e-6 with a difference of 5 orders of magnitude. This is because for larger values of undrained shear strengths, the interface adhesion can be more significant, which is beneficial to the shaft stability. The soil-wall adhesion should thus be considered in the circular shafts analysis, particularly for large undrained shear strength cases which can result in a great P_f decrease.

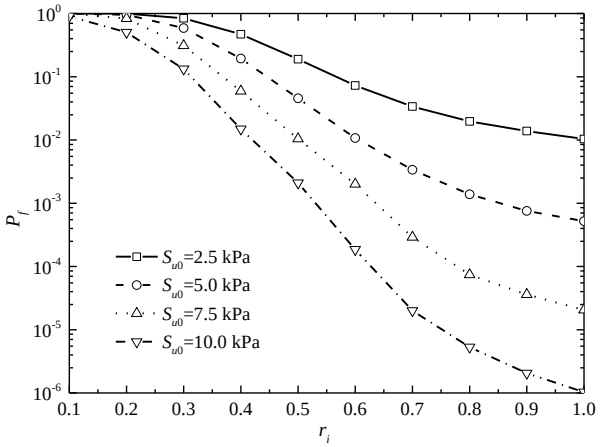

Fig. 4.10 Soil-wall adhesion factor effects under different undrained shear strengths.

Besides, the P_f values change rapidly when r_i is in the range from 0.3 to 0.7. It can be explained by Fig. 4.11, which presents the sensitivity index variations of 4 input variables with r_i by performing GSA based on PCK metamodel. As illustrated in this figure, the r_i sensitivity index increases firstly and reaches a peak (around 0.55) when r_i equals 0.3, then the importance of r_i on the model response decreases with its value increase. The sensitivity indices are more pronounced when the soil-wall adhesion coefficient varies from 0.3 to 0.7 compared with the cases when r_i=0.1, 0.7~1.0 (with a sensitivity index being smaller than 0.14), which can cause less change for the failure probability. Therefore, the soil-wall adhesion coefficient should be determined with caution in shaft probabilistic analyses.

In addition, it can also be found from Fig. 4.11 that the sensitivity indices of the undrained shear strength at the ground surface S_{u0}, non-homogeneity coefficient k and unit weight γ decrease firstly and then increase as r_i increases, which is opposite to the r_i sensitivity index variations.

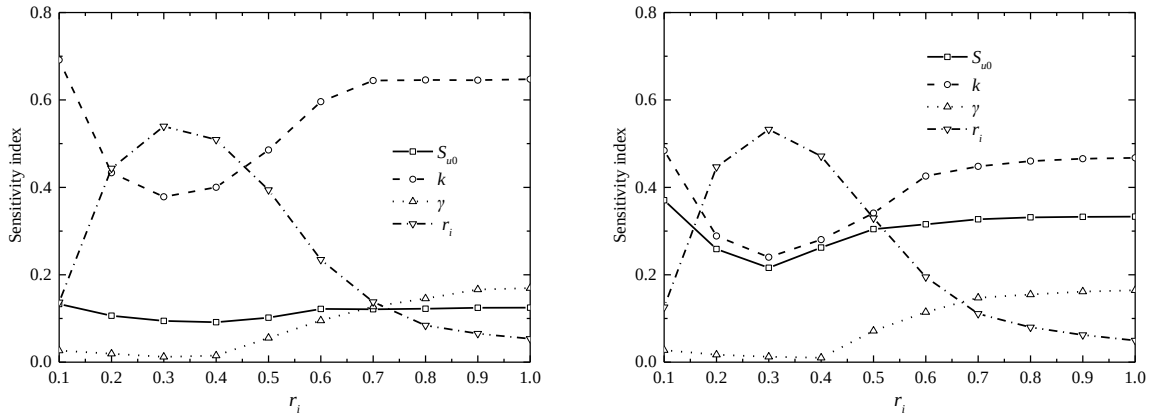

(a) S_{u0}=5 kPa (b) S_{u0}=10 kPa

Fig. 4.11 Sensitivity analysis for different soil-wall adhesion coefficients.

The soil-wall adhesion coefficient effect with different wall embedment depths (D=2.5, 5, 7.5, 10.0 m) is also discussed and the results are depicted in Fig. 4.12. As expected, the failure probability decreases with the embedment depth increase. The influence of r_i variations on the failure probability becomes slight when its value is larger than 0.7. In addition, r_i affects greatly the shaft stability for cases with large embedment depths, i.e. the P_f value for case of D=10.0 m changes more compared with the case of D=2.5 m. This is because larger values of D lead to stronger contacts between the soil and wall, the soil-wall interface coefficient can thus make more influence on the failure probability. It can also be illustrated by Fig. 4.13, which shows the Sobol' index of the input parameters under different embedment depths. With the increase of D, the sensitivity indices of r_i increase simultaneously, which can lead to a remarkable impact. The sensitivity indices of the non-homogeneity coefficient k are also improving with the embedment depth increase; however, its variation is not significant compared to the r_i ones (difference of respectively 0.05 and 0.10). The undrained shear strength sensitivity index changes most when its value varies from 0.44 to 0.30.

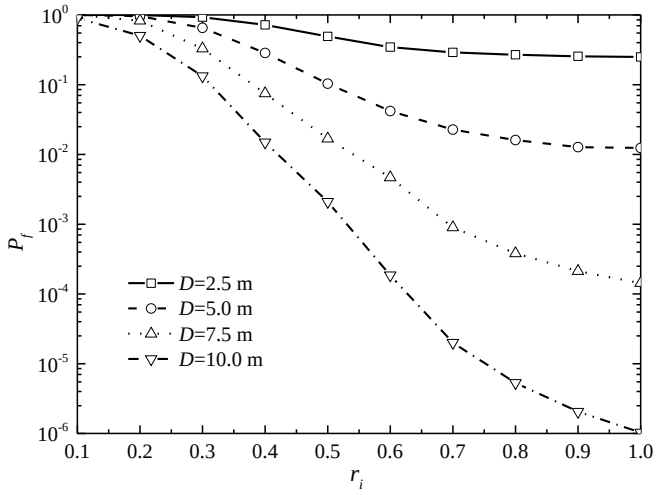

Fig. 4.12 Soil-wall adhesion factor effects under different embedment depths.

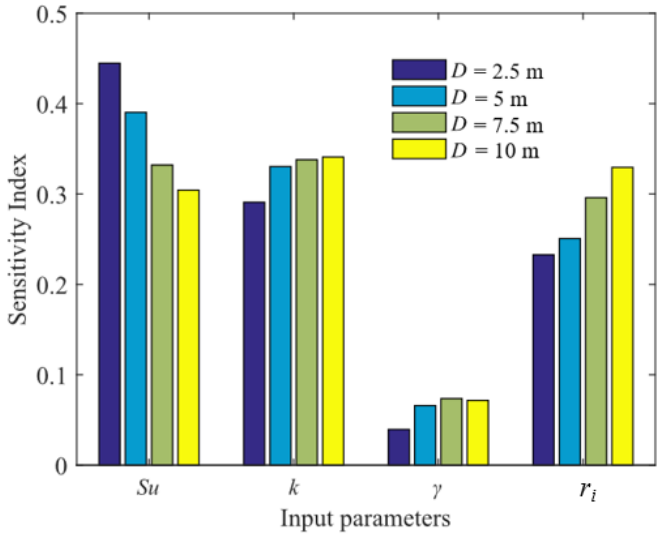

Fig. 4.13 Sensitivity indices under different embedment depths.

In summary, the soil-wall adhesion coefficient plays an essential role in the shaft stability analysis, particularly for cases with larger values of undrained shear strengths and embedment depths. The r_i influence is more pronounced when its value is in the range from 0.3 to 0.7, which means that even small changes can result in different failure probabilities. Therefore, it should be paid attention to in practice.

4.4.4 Influence of the soil non-homogeneity

The effects of the strength gradient k which corresponds to the soil non-homogeneity on the failure probability under different undrained shear strengths S_{u0} (10, 15 and 20 kPa) are also considered, and the results are plotted in Fig. 4.14. It can be found that k considerably influences the failure probability, and its effects are more prominent for cases with larger undrained shear

strength values. For example, the failure probability can be reduced to 3.4e-5 (k=1) from 9.0e-1 (k=0) when the undrained shear strength at the ground surface is equal to 20 kPa. The significant difference points out the importance of the soil non-homogeneity. Considering a homogeneous case (k=0) may lead to a failure probability which can underestimate the shaft stability.

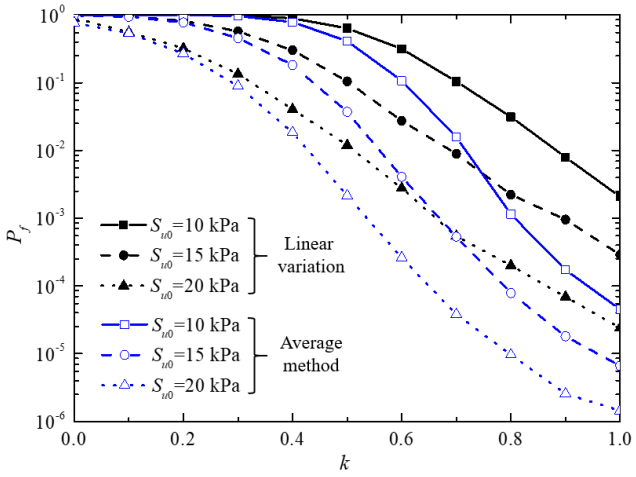

Fig. 4.14 Soil non-homogeneity effects under different undrained shear strengths.

Non-homogeneous cases can also be transformed into homogeneous ones by taking an average of the shear strengths profile (Qin and Chian, 2018) for the sake of simplicity. Goh (2017b) gave a simplified method that can be achieved by considering the average S_u between a depth of (H+D) and (H+D+0.15B) as the constant undrained shear strength of a homogeneous one. The average method is discussed in a probabilistic framework and the results are also plotted in Fig. 4.15 for direct comparisons with the non-homogeneous cases. It can be observed that the simplified method overestimates greatly the shaft stability and gives smaller failure probabilities. The possible explanation is that the undrained shear strength of the simplified average method is related to the excavation depth, width and wall embedment depth. As shown in Table 4.3, the average method (Goh, 2017b) can lead to larger safety factors when H+D is larger (compared Case 4 to Case 1) or the embedment depth is smaller (compared Cases 9, 10 to Case 1). Fig. 4.14 plots the comparison based on the circular shaft with B=15m, H=16m and D=10m (a relatively small B and large H+D), which may lead to larger safety factors and be followed by smaller failure probabilities. Therefore, the average method is limited to the application for some special cases, and should be used with caution in practical engineering.

The sensitivity indices of the 4 input parameters versus the non-homogeneity coefficients k are also discussed and the results are presented in Fig. 4.15. For large values of the non-homogeneity coefficients, the sensitivity index of r_i is also greater as expected whereas the undrained shear

strength one is decreasing. Besides, the soil-wall adhesion factor can influence more the model response with the k increase. The results highlight again the significance of the soil non-homogeneity and soil-wall adhesion.

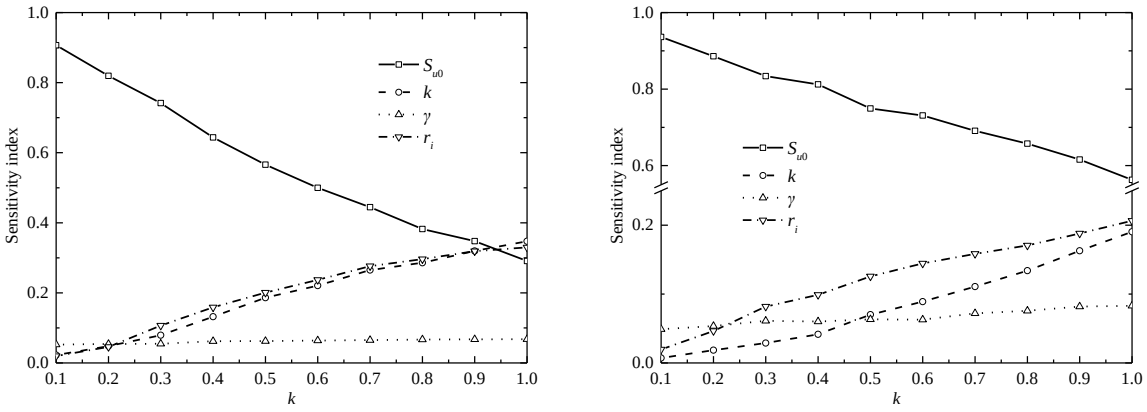

(a) S_{u0}=10 kPa (b) S_{u0}=20 kPa

Fig. 4.15 Sensitivity analysis for different non-homogeneity coefficients.

4.5 Conclusion

This study discusses the deterministic and probabilistic basal heave stability of circular shafts with the consideration of the soil-wall interface in undrained and non-homogeneous clayey soils. The coupling of the finite element limit analysis and of the proposed procedure PCK-PA makes the circular shaft probabilistic analyses possible. The results are validated by comparing them with former studies in deterministic and probabilistic frameworks.

The effects of the input variables uncertainties, soil-wall interface and soil non-homogeneity on the shaft stability are discussed. The failure probability increases with the coefficient of variation increase and the decrease of the soil-wall adhesion coefficient r_i, undrained shear strength at the ground surface S_{u0}, soil non-homogeneity coefficient k and wall embedment depth D.

Concerning the soil uncertainties, the results show that the probabilistic analyses are necessary for the circular shaft stability and the coefficient of variation effect is more pronounced for cases with larger safety factors. The soil-wall interaction influences on the shaft stability are then discussed. It is seen that r_i affects considerably the shaft failure probability, and its influence is more significant with the increase of the undrained shear strength and of the embedment depth. The r_i influences greatly the model response when its value is in the range from 0.3 to 0.7. The choice of this parameter should then be carefully done or based on experimental tests. In addition, the soil non-homogeneity influences are investigated. It indicates that there is a remarkable

effect on the failure probability, and the simplified average method may give biased results, which should be used carefully when considering probabilistic analyses. The sensitivity indices of k and r_i are increasing as k increases, whereas the importance of S_{u0} decreases.

This study provides a good insight into the probabilistic basal heave stability analyses of supported circular shafts, and highlights the importance of the soil-wall adhesion, soil non-homogeneity and uncertainties consideration.

Chapter 5

Stability analysis of circular shaft against an hydraulic uplift

Contents

5.1 Introduction 145

5.2 Problem statement 145

5.2.1 Circular shaft against an hydraulic uplift 145

5.2.2 Uncertainty consideration 147

5.3 Deterministic analysis 148

5.3.1 Numerical model construction 148

5.3.2 Influence of the permeability anisotropy 149

5.3.3 Influence of soil-wall interaction 153

5.4 Probabilistic analysis 155

5.4.1 Probabilistic results for the reference case 155

5.4.2 Influence of permeability anisotropy 158

5.4.3 Influence of soil-wall interaction 161

5.5 Conclusion 162

5.1 Introduction

Underground water is commonly encountered in practical engineering, which can make shafts more prone to hydraulic heaves and significant amounts of soil uplift rebound that could cause serious accidents. Therefore, the hydraulic effects on shaft stability under drained conditions should be discussed. A brief explanation of the studied problem is given first, the deterministic and probabilistic analyses are then detailed, followed by comparisons and discussions. The permeability anisotropy coefficient, soil-wall interaction, and soil tension cut-off on the shaft basal heave stability against hydraulic effects are discussed in deterministic and probabilistic frameworks.

(***Disclaimer***: The content of this chapter was published in the following journal paper: Tingting Zhang, Julien Baroth and Daniel Dias. (2022). Deterministic and probabilistic basal heave stability analysis of circular shafts against hydraulic uplift. Computers and Geotechnics, 150, 104922)

5.2 Problem statement

5.2.1 Circular shaft against an hydraulic uplift

Fig. 5.1 shows the reference supported circular shaft after excavation. H and R_c are respectively the depth and radius of the circular shaft. t_w is the wall thickness and D is its corresponding embedment depth. The groundwater level is located at h_w_1 below the ground surface. For the excavation side, the water is lowered to the level h_w_2 from the excavation base to facilitate practical works (dry excavation).

The soil is supposed to follow a linear elastic-perfectly plastic model with the Mohr-Coulomb failure criterion, which is characterized by the friction angle (φ), cohesion (c), Young's modulus (E_u) and Poisson's ratio (υ).

The soil tensile strength is generally assumed to be insignificant compared to the shear strength of soils. Its small value may lead to tensile cracks development and can further affect the structures stability, particularly when underground water is considered. This is because the generated cracks may create preferential flow paths in soil, which can influence the soil hydraulic conductivity and shaft stability (Lv et al., 2020). The soil tensile strength is considered in this shaft stability analysis and can be expressed by

$$f_{tc} = r_t \cdot f_t \tag{5.1}$$

where f_t and f_{tc} are respectively the soil tensile strength before and after cut-off, and r_t is the corresponding tensile strength cut-off coefficient within the range of [0, 1] (Hou et al., 2019).

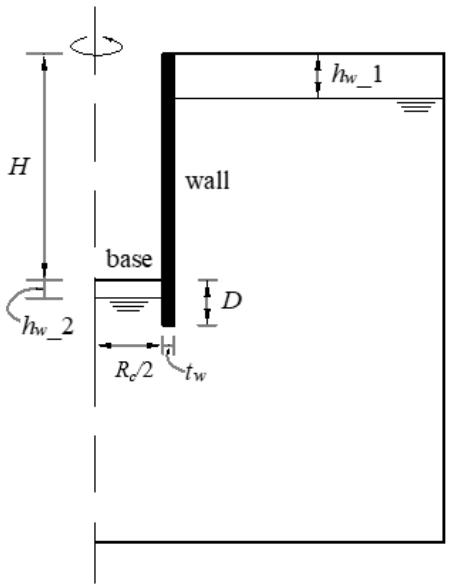

Fig. 5.1 Cross-section of the circular shaft.

Due to the stratification, deposition and densification, the soil develops an anisotropic permeability, and the permeability anisotropy coefficient r_k can be considered as

$$r_k = \frac{k_x}{k_y} \tag{5.2}$$

where k_x and k_y are respectively the horizontal and vertical permeability coefficients. In general, the value of r_k is often considered to be larger than 1 because the soils are usually vertically compacted by layers (Mouyeaux et al., 2019). The value of k_y is set as a constant while the k_x value varies accordingly with the considered r_k values in the following discussions.

The Linear-Elastic model is adopted for the retaining wall, and the wall is assumed to be impervious. The soil-wall interface strength is linked to the strength properties of the adjacent soil layer and its strength can be determined by Eq. (3.2).

Table 5.1 presents the input parameters of the reference case used in this study.

Table 5.1 Parameters summary of the reference case.

Parameters	**Notation**	**Value**	
Circular shaft depth	H (m)	25	
Circular shaft radius	R_c (m)	15	
Wall embedment depth	D (m)	5	
Wall thickness	t_w (m)	1.2	
Water level from ground surface	h_w_1 (m)	5	
Water level from excavation base	h_w_2 (m)	2	
		Soil	**Wall**
Material model	-	Mohr-Coulomb	Linear-Elastic
Unsaturated unit weight	γ_{dry} (kN/m^3)	19	25
Saturated unit weight	γ_{sat} (kN/m^3)	20	25
Friction angle	φ (°)	25	-
Cohesion	c (kPa)	35	-
Young's modulus	E (kN/m^2)	5.0e5	2.0e7
Poisson's ratio	υ	0.25	0.2
Vertical permeability coefficient	k_y (m/d)	0.864 [a]	8.64e-5 [c]
Permeability anisotropy coefficient	r_k	3 (1~50) [b]	1
Tension cut-off coefficient	r_t	0.5 (0~1) [d]	-
Soil-wall interface coefficient	r_i	0.7 (0.1~1) [e]	

Note:
[a] Based on values given by Goh et al. (2019a).
[b] Mouyeaux et al. (2019).
[c] Shen et al. (2017).
[d] Hou et al. (2019).
[e] Sun (2016).

5.2.2 Uncertainty consideration

Four input parameters are considered random variables in the probabilistic analyses, which include the permeability anisotropy coefficient, the soil cohesion and friction angle, and the soil-wall interface coefficient. The soil unit weight uncertainties are ignored as its variation makes an insignificant influence on the shaft stability as shown in Fig. 4.7. Lognormal random variables are arbitrarily chosen to model input uncertain parameters, and the input parameters are considered independent. Table 5.2 summarizes the parameters' statistics and corresponding limits.

Table 5.2 Statistical properties of input random variables.

Parameters	Notation	Statistics of parameters			
		Mean	*COV*	Distribution	Range

Permeability anisotropy coefficient	r_k	3	0.5 [a]	Truncated Lognormal	1~50
Cohesion	c (kPa)	35	0.2	Lognormal	-
Friction angle	φ (^{o})	25	0.2	Lognormal	-
Soil-wall interface coefficient	r_i	0.7	0.3	Truncated Lognormal	0.1~1

Note:
[a] Based on values given by (Cho, 2012).

5.3 Deterministic analysis

The circular shaft model is constructed first. The influences of the permeability anisotropy coefficient, soil-wall interface coefficient and soil tension cut-off coefficient in the deterministic framework are then discussed. It should be noted that the parameters are the same as the reference case if there is no more discussion about these parameters.

5.3.1 Numerical model construction

The finite element limit analysis presented in Chapter 4 is used to analyse the circular shaft deterministic stability subjected to hydraulic effects. Fig. 5.2 illustrates the numerical model configuration of the supported circular shaft against the hydraulic effects based on the data summarized in Table 5.1. An axisymmetric model is used because of the circular shape. Displacements are fixed at the lateral sides in the horizontal directions and are free in the vertical boundary, while they are fully restrained at the model bottom. The lateral and bottom boundaries are impermeable.

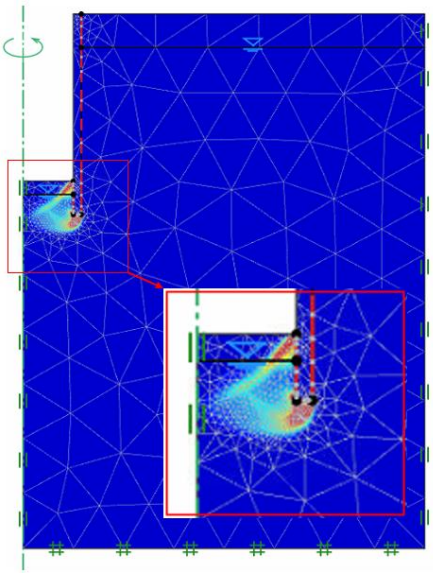

Fig. 5.2 Deterministic FELA model with adaptive mesh refinement.

The full tensile strength is calculated by (Krabbenhoft et al., 2015)

$$f_t = \frac{c}{\tan\varphi} \tag{5.3}$$

The reduced tensile strength is then determined by Eq. (5.1).

The contact interface between the wall and surrounding soil is specified by means of a shear joint element to consider the soil/wall interaction. Its strength corresponds to the surrounding soil shear strength and can be defined by Eq. (3.2).

5.3.2 Influence of the permeability anisotropy

Fig. 5.3 shows the permeability anisotropy coefficient influence on the circular shaft safety factor (F_s) for 4 different r_t values. The safety factor decreases as r_k increases, and it varies significantly when r_k is in the range of [1, 10] with a difference being up to 42.2% (r_t=0). However, when r_k is larger than 10, the anisotropy has less effect on the shaft stability. The safety factor is also varied with the tensile strength value variations and the difference is around 20%. Besides, when the tensile strength is equal to 0 (r_t=0), the safety factor values are below 1.0 for cases where r_k>10, while the correlated full tensile strength cases' (r_t =1) safety factors are larger than 1. It could be respectively considered as "failure" and "safe" zones in deterministic analyses. The tensile strength determination at the design stage is thus important.

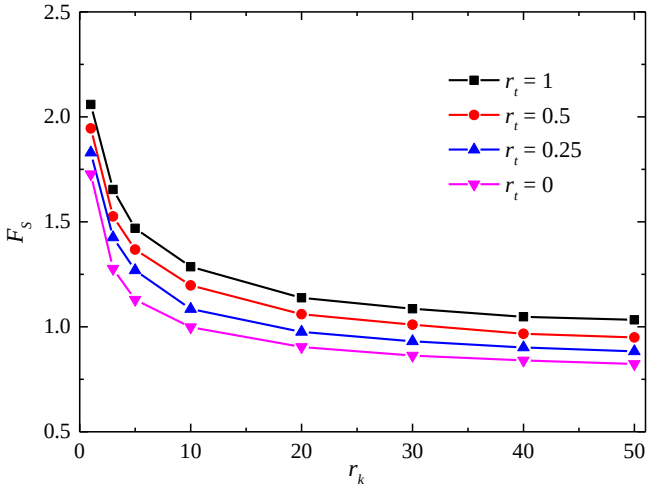

Fig. 5.3 Effects of r_k and r_t on F_s.

Fig. 5.4 shows the seepage velocity vectors around the circular shaft for different permeability anisotropy coefficients (3, 10, 30 and 50). It can be observed that the water flows bypass the

retaining wall toe and move towards the excavation side. This is because the retaining wall can block the groundwater seepage and lengthen the seepage path benefiting from its low hydraulic permeability coefficient. Besides, with the permeability anisotropy increases, the water flow around the retaining wall toe (Region 1) is almost parallel to the horizontal direction, and the flow direction close to the shaft center (Region 2) is modified with an anticlockwise rotation and tends to be more horizontal. The reason is that the horizontal permeability coefficient k_x is increasing with the increase of r_k. It leads to strong correlated hydraulic conductivities in the horizontal direction, and the horizontal water flow is accordingly prominent. Moreover, on the excavation side, the flow vectors are bigger and denser when they are closer to the soil-wall interface.

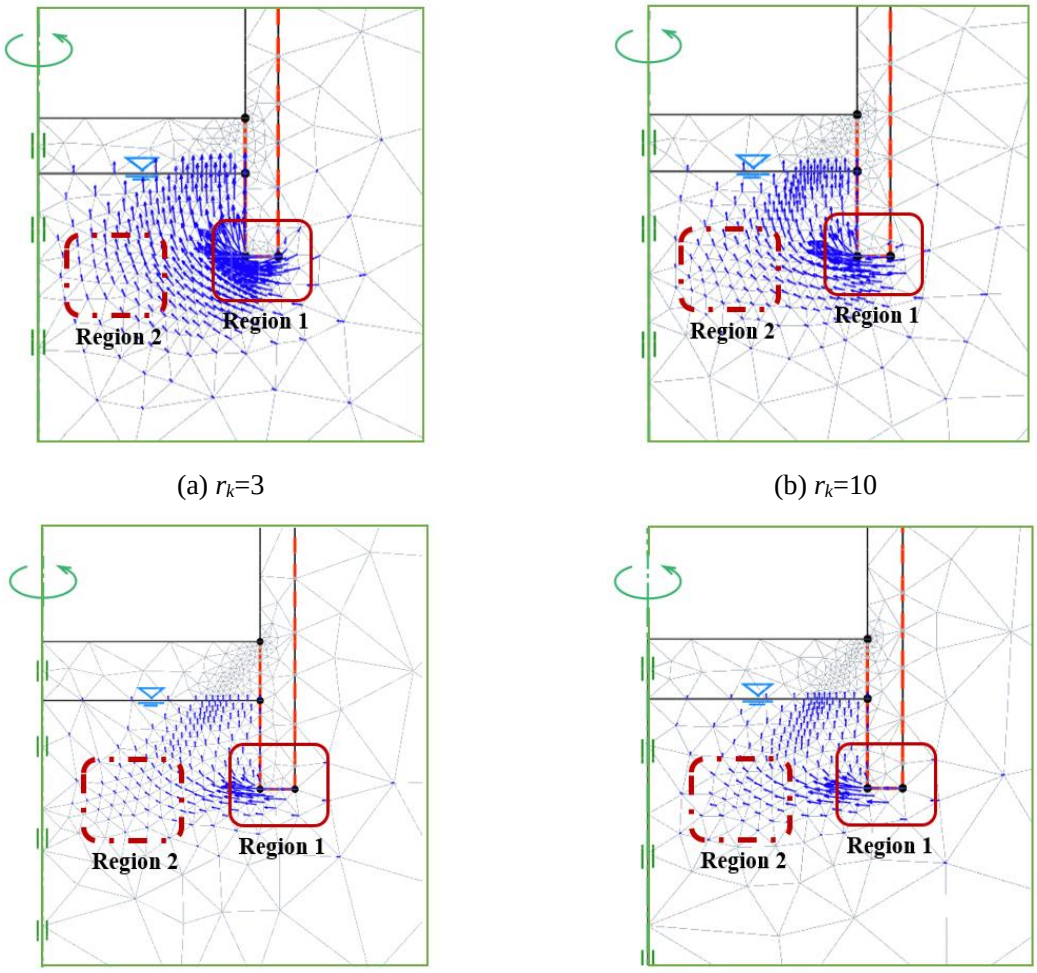

(a) r_k=3 (b) r_k=10

(c) r_k=30 (d) r_k=50

Fig. 5.4 Flow vectors for different r_k values.

Fig. 5.5 presents the correlated water pressure distribution, and only two points on the excavation side are given for the sake of simplicity. It can be noted that the water pressure distribution around the retaining wall toe is more horizontal with the increase of r_k. It shows similar trends

with the flow vector ones. Besides, the water pressure around the retaining wall increases on the excavation side as r_k increases. It indicates the flow volume is greater when the permeability coefficient is more anisotropic.

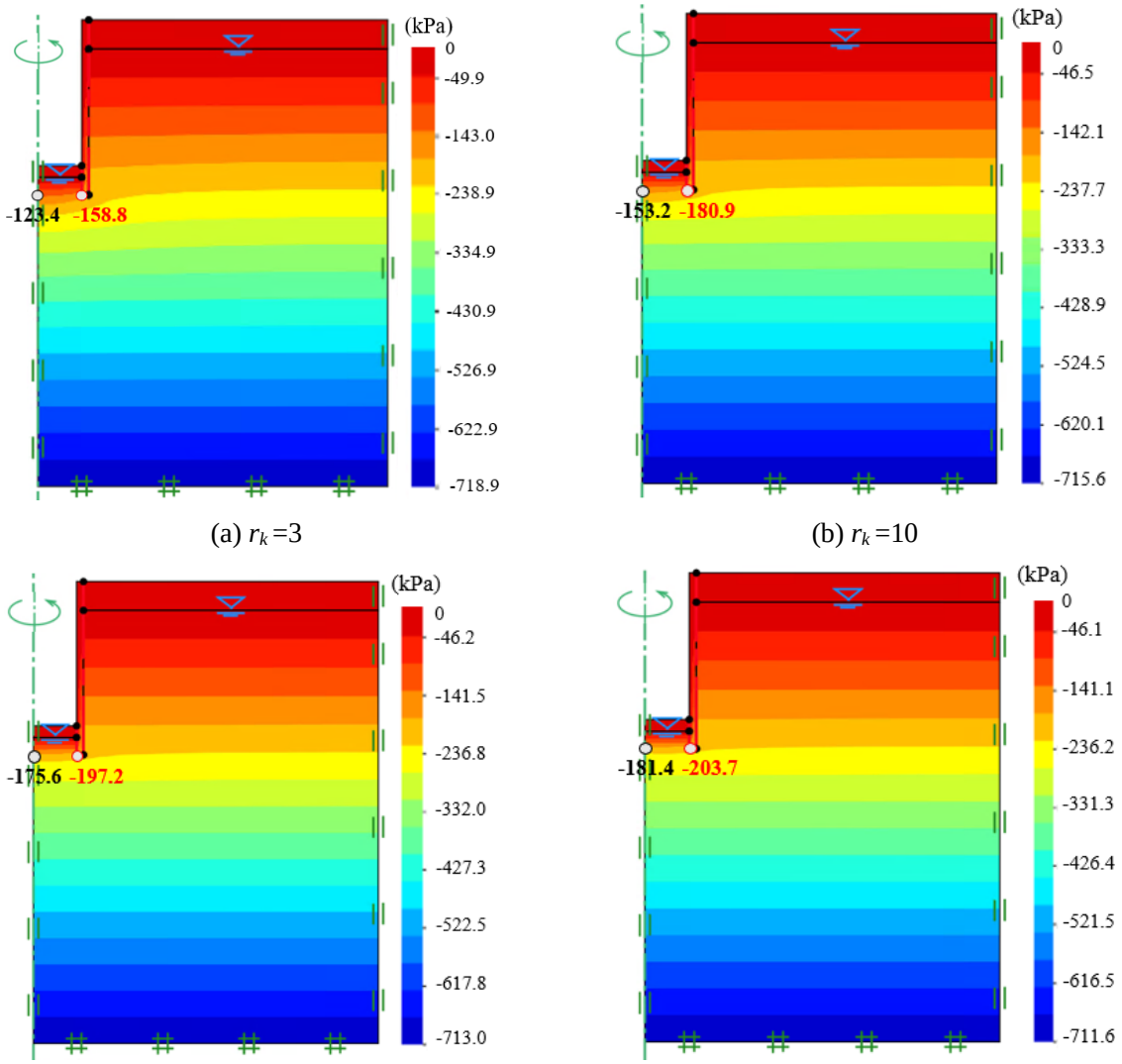

(a) r_k =3 (b) r_k =10

(c) r_k =30 (d) r_k =50

Fig. 5.5 Water pressure distributions for different r_k values.

The water head distributions with different levels of permeability anisotropy are also given in Fig. 5.6. The water head decreases along with the water flow by the fact that the groundwater flow is impacted by friction with the soil grains. It leads to mechanical energy consumption and a head loss. Besides, for cases with larger r_k values, the hydraulic head contours are also more horizontal and denser on the excavation side. It indicates that a higher hydraulic gradient is developed, which can increase the soil uplift potential.

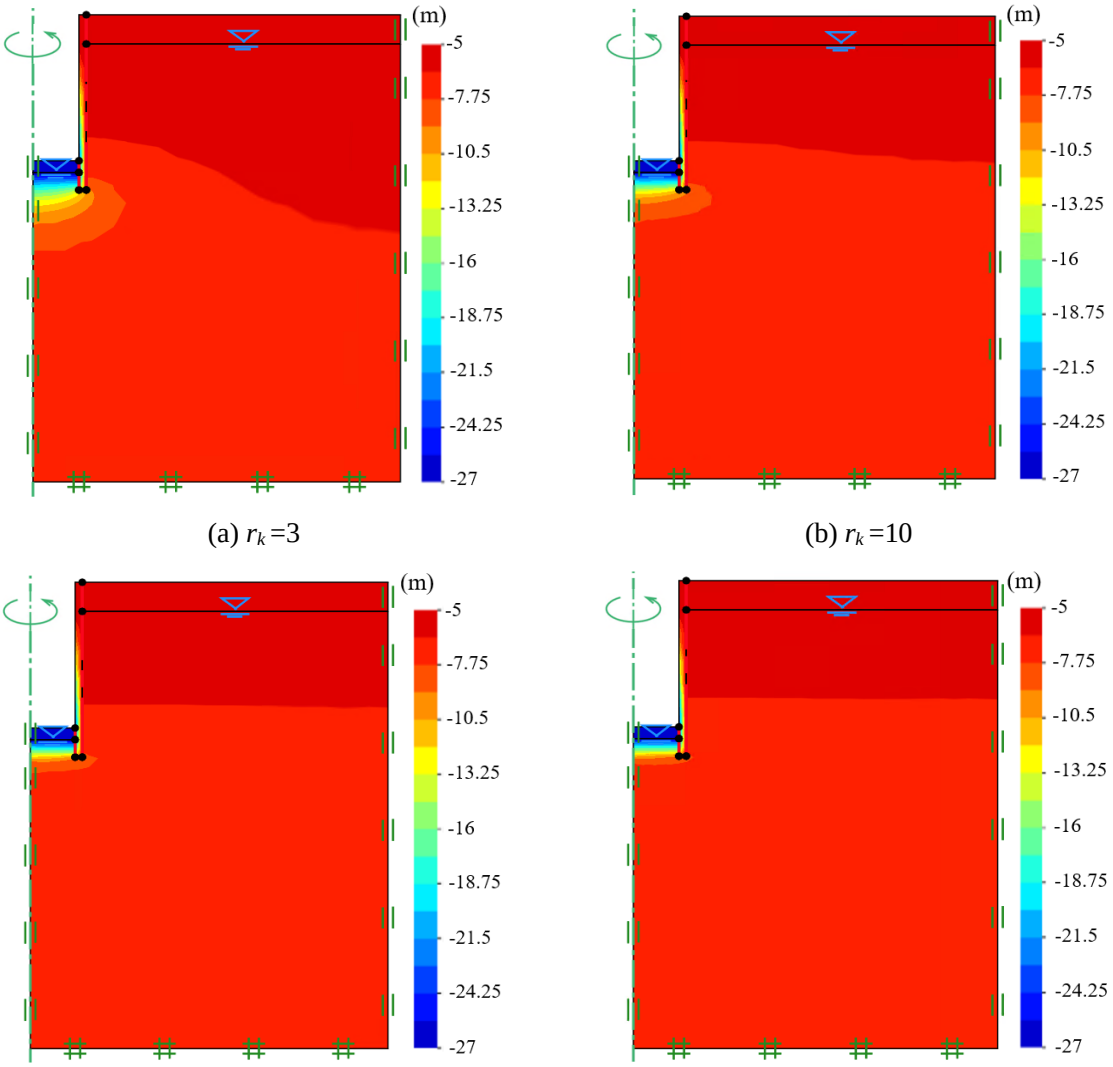

(a) r_k =3 (b) r_k =10

(c) r_k =30 (d) r_k =50

Fig. 5.6 Water head distributions for different r_k values.

As a result, ignoring the anisotropy of the permeability coefficient and tensile strength reduction will overestimate the shaft stability. The corresponding values should be determined with attention, particularly when r_k is in the range of [1, 10]. Larger r_k values induce a prominent horizontal water flow, which leads to horizontal water pressure distributions and a hydraulic head around the wall toe. Greater water pressure and hydraulic gradients will also be developed. In such a case, the excavation will be more prone to hydraulic heave accidents.

5.3.3 Influence of soil-wall interaction

Fig. 5.7 depicts the soil-wall interface effects on the shaft stability for different tensile strengths. The safety factor increases as r_i increases by the fact that it attributes more resistance between the soil and wall. The tensile strength also plays an important role in the stability analysis, and its difference is more significant when r_i is small. For example, the safety factors are respectively 1.127 and 0.567 when r_i =0.1, with a difference being 49.6%. This difference is larger than 20.9% for the case of r_i =1.

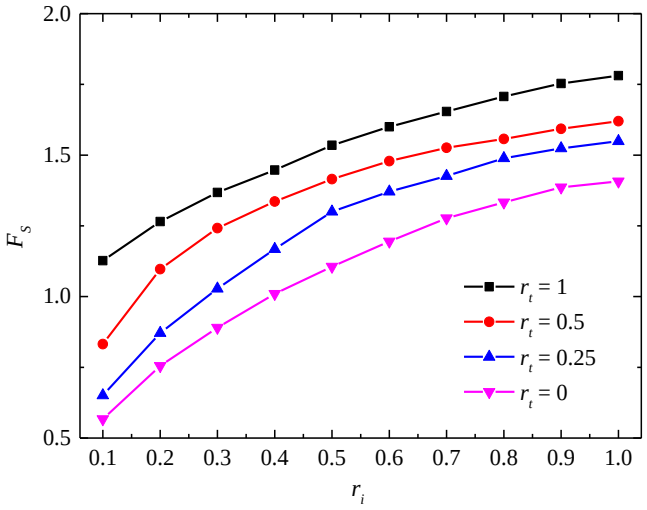

Fig. 5.7 Effects of r_i and r_t on F_s.

The interface strength effect under different permeability anisotropy coefficients is also discussed and the results are presented in Fig. 5.8. It is noted that the influence of r_i is less significant as r_k increases. For example, the safety factor differences are 0.79 and 0.53 when r_k equals respectively to 3 and 50.

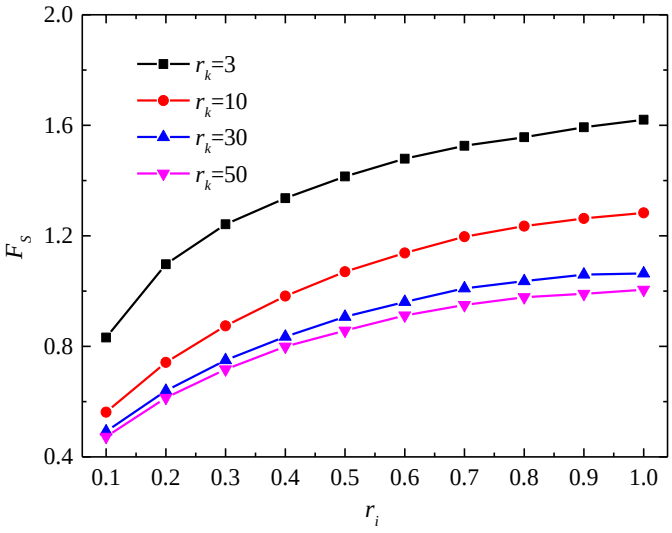

Fig. 5.8 Effects of r_i and r_k on F_s.

Fig. 5.9 gives the possible explanations. It can be observed that when r_k is small, the shear dissipation on the excavation side is mainly distributed on the soil-wall interface upper part due to the property diversity between soil and wall. Resisting to the hydraulic uplifts mainly depends on the soil-wall interface shear strength. Conversely, with the increase of r_k (Fig. 5.9(b)), the failure surface is developed away from the soil-wall interface and in the shaft center direction. The failure surface is around 30^o in relation to the vertical direction and tends to be horizontal when it is close to the retaining wall depth (-30 m). This is because with the r_k increases, the seepage in Region 2 tends to be horizontal as shown in Fig. 5.4(d) and the correlated hydraulic head distribution is almost horizontal (Fig. 5.6(d)). It induces hydrostatic water and no flow occurs. It places the soil in this area in a suspension state, which is more prone to cause the excavation uplift and destabilize the circular shaft.

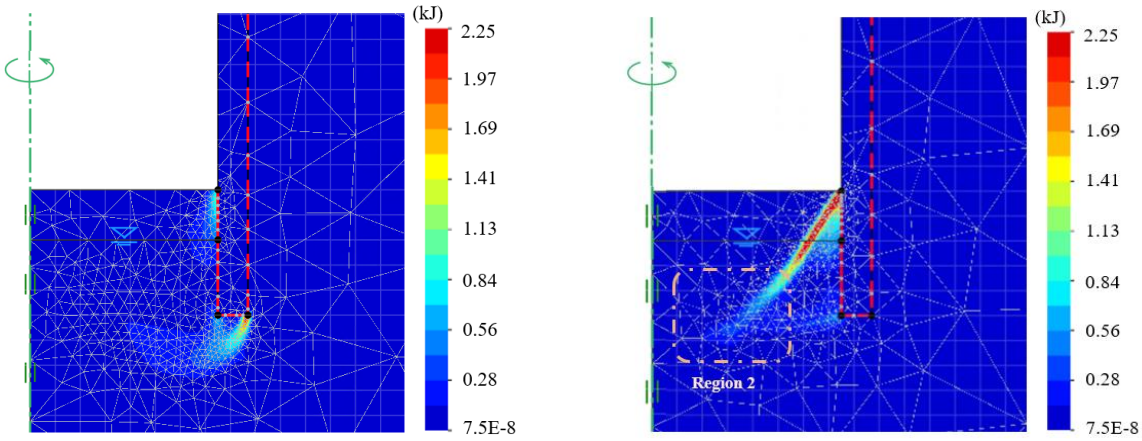

(a) r_k =1 (b) r_k =50

Fig. 5.9 Shear dissipation distribution for different r_k values (r_i =1).

In summary, the soil-wall interface influences greatly the shafts stability and is more correlated to the shaft stability when the permeability coefficient is less anisotropic.

5.4 Probabilistic analysis

The section aims to investigate the effects of the permeability anisotropy coefficient, the soil-wall interface coefficient and the soil tensile strength in a probabilistic framework. The sensitivity analysis is also performed to rank the importance of the considered random variables. The total effect Sobol's indices are given.

5.4.1 Probabilistic results for the reference case

It should be noted that two solutions can be provided in the limit analysis framework, i.e. lower and upper bounds (LB and UB). The lower one aims to provide a lower bound of the solution based on a statically admissible stress field, while the upper one gives an upper bound according to the kinematically admissible velocity field (Wu et al., 2020). A precise solution is enclosed in the interval between the UB and LB solutions. It is often approximated by the average of UB and LB solutions by the fact that the average value is relatively stable with the elements number increases and is closer to the results obtained by 15-node Gaussian element type as shown in the upper part of Fig. 5.10. However, the computational time of 15-node Gauss results is far longer and varies significantly with the increase of elements number compared to the average values as depicted in the lower part of Fig. 5.10. In view of this, the average of UB and LB results will be considered as the model response and 3000 element numbers will be used in the subsequent probabilistic analyses in combination with the calculation results efficiency and accuracy. One deterministic simulation needs around 180 s.

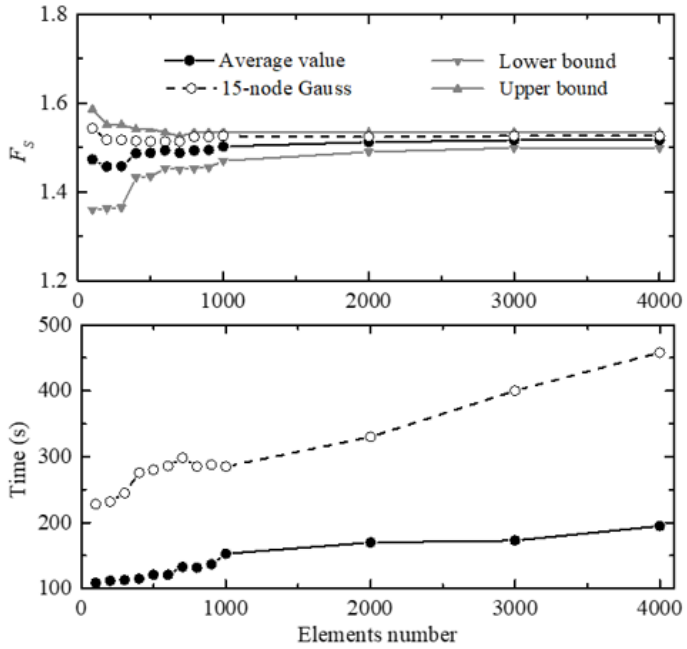

Fig. 5.10 Comparison between average and 15-node Gauss solutions.

The reference circular shaft is analysed based on the above-mentioned PCK-PA. 80 simulations (10 for the initial ED and 70 for the iterative procedure) are necessary to construct the PCK metamodel. The main probabilistic results are plotted in Table 5.3, Table 5.4, Fig. 5.11 and Fig. 5.12. 3.0e4 samples are set for the failure probability calculation using the MCS. The P_f is found to be 0.018 with a COV_{Pf} being 4.3%, which can ensure the P_f value accuracy. For the statistical moments, the mean value and standard deviation are respectively 1.53 and 0.28. Fig. 5.11 shows the PDF and CDF for the safety factor estimations based on the procedure.

Table 5.3 Results for the reference case.

		P_f	β	U^*	Sensitivity-index	Number of evaluations
PCK-PA	MCS	0.018	—	—	—	30000
	GSA	—	—	—	Fig. 5.12	6000
	FORM	-	1.975	Table 5.4	Fig. 5.12	102

Table 5.4 Design points for the reference case.

Parameters	r_k	c	φ	r_i
DP	4.38	26.0	21.9	0.53

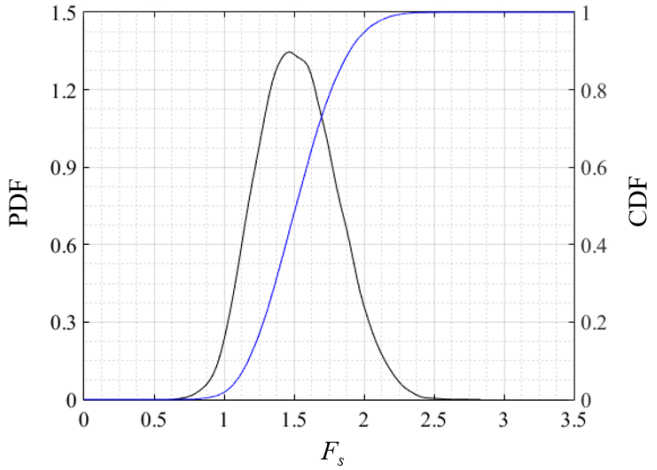

Fig. 5.11 PDF and CDF of F_s.

Fig. 5.12 shows the sensitivity indices obtained by GSA and FORM of the 4 input random variables. The cohesion contributes the most to the model response variation, with a sensitivity index being more than 0.5. The permeability anisotropy coefficient r_k follows. It reveals that the permeability anisotropy coefficient also plays a significant role in the basal heave stability analysis. The sensitivity index of the soil-wall interface coefficient r_i is slightly larger than the friction angle one. It indicates the importance of the soil-wall interface consideration. Although the values of the sensitivity index obtained by FORM and GSA are not totally the same, they can give consistent results with the same ranking orders, which can validate the results accuracy.

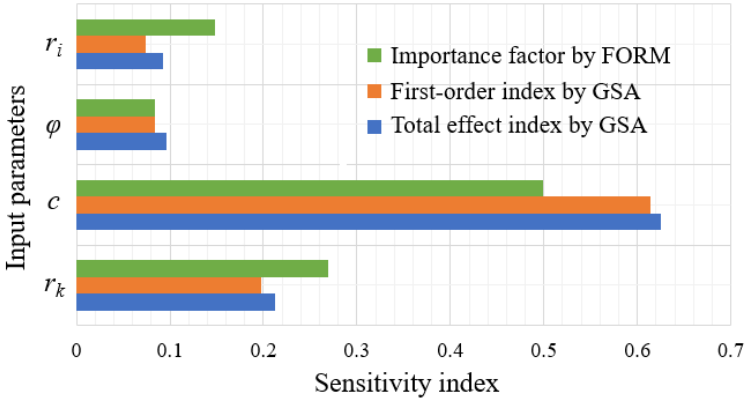

Fig. 5.12 Sensitivity analysis results based on the FORM and GSA.

The metamodel is validated by Fig. 5.13, which depicts the safety factor comparison and 900 sets of samples generated by the LHS are considered. The R^2 value is 98.4% and nearly all of the scatter points are within ±5% of the 45° line, which represents the results based on the PCK metamodel are approximately equal to the ones obtained by the numerical model. It allows validating the metamodel accuracy and the original mechanical model can then be substituted by the PCK metamodel.

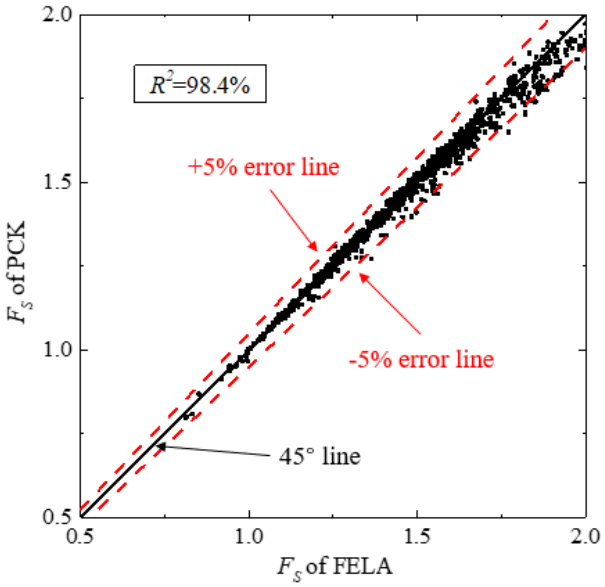

Fig. 5.13 F_s comparison obtained by FELA and PCK models.

5.4.2 Influence of permeability anisotropy

The permeability anisotropy coefficient effects on the failure probability and sensitivity indices under different r_t cases are depicted in Fig. 5.14. The failure probability increases with the r_k increases and its variation is significant with a difference of 3 orders of magnitude when r_k varies from 1 to 50. The corresponding expected performance levels are respectively “above average” and “hazardous” (Sivakumar Babu and Murthy, 2005). It points out again the permeability anisotropy coefficient importance.

The failure probability exhibits similar variations with Fig. 5.3. It shows that in the range of [1, 10], the result variation is more pronounced. It can be explained by Fig. 5.14(b), which presents the sensitivity index of r_k for different cases. The value of S_{rk} initially increases and reaches a peak when its value is around 5. Then the importance of r_k on the model response decreases as r_k increases.

It can also be seen that the tensile strength also influences significantly the failure probabilities, and the difference can be respectively up to 97.8%, 94.2%, 89.4%, 80.6%, 62.9% and 57.5% for cases with r_k being 1, 3, 5, 10, 30 and 50.

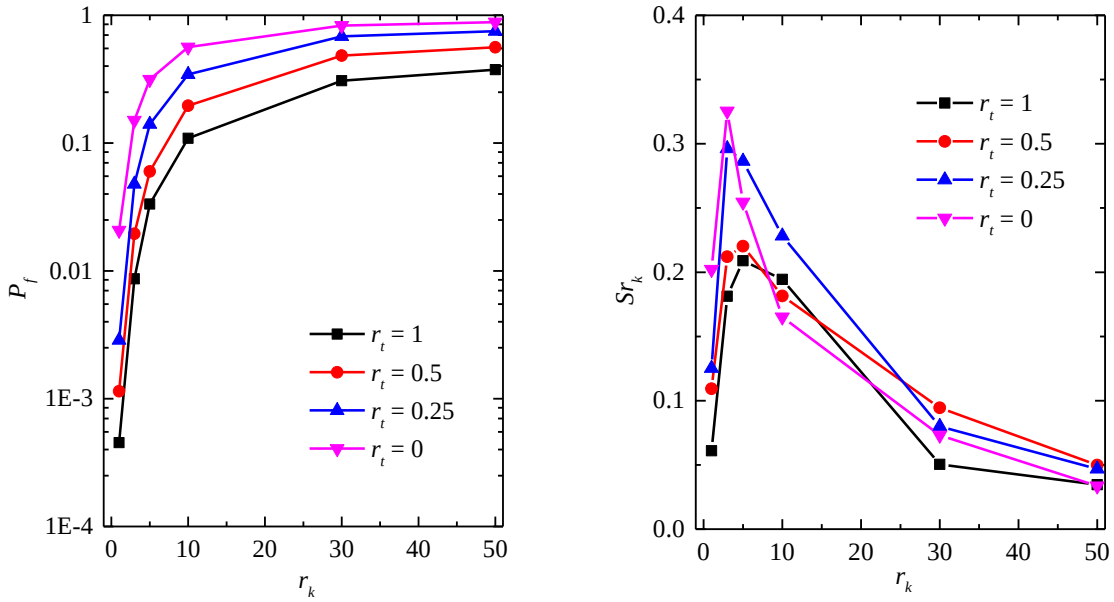

(a) Failure probability (b) Sensitivity index of r_k

Fig. 5.14 Effects of r_k and r_t on probabilistic analysis results.

Fig. 5.15 presents the permeability anisotropy coefficient effects on the failure probability and sensitivity indices. There is no doubt that the sensitivity index of r_k increases as the COV_{rk} increases by the fact that a higher coefficient of variation can lead to more variable samples, and make more significant influences on the response. The sensitivity indices of r_k = 30, 50 are smaller than the cases of r_k = 1, 3, 5, 10. It is consistent with the results shown in Fig. 5.14(b). However, the failure probability shows different variation trends with the increase of COV_{rk}. P_f is increasing when r_k is 1, 3, 5, while for the cases with r_k being 10, 30 and 50, the failure probability is decreasing.

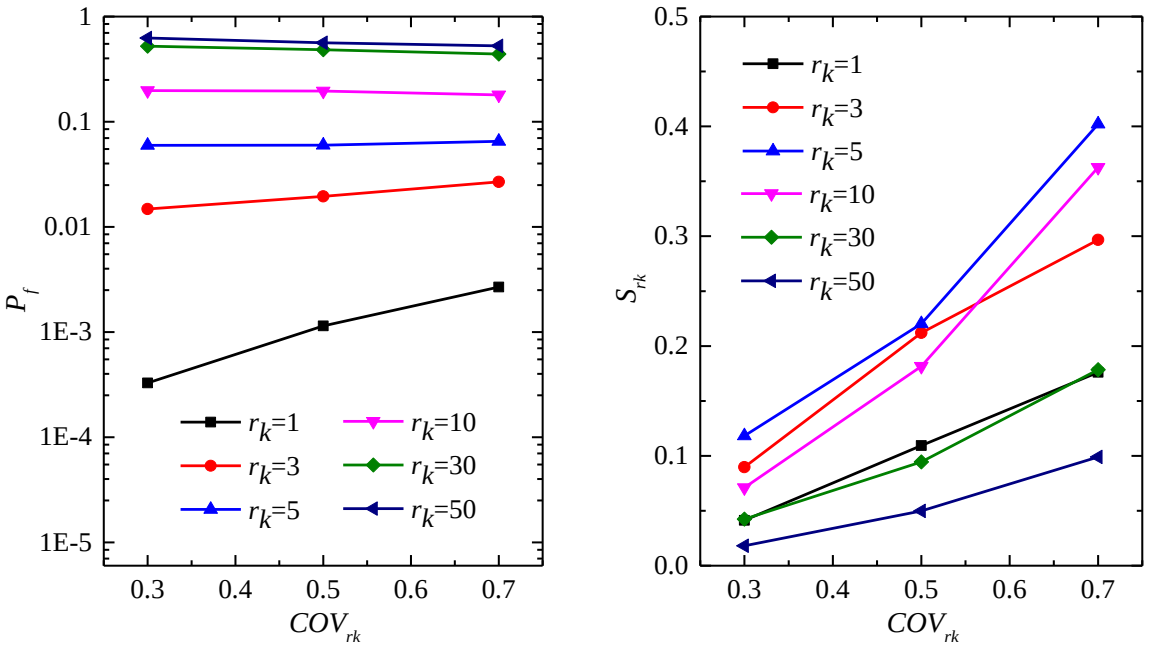

(a) Failure probability (b) Sensitivity index of r_k

Fig. 5.15 Effects of COV_{rk} on probabilistic analysis results.

It can be clarified by Fig. 5.16, which presents the r_k distribution with μ_{rk}=5, 30 and COV_{rk}=0.3, 0.5, 0.7. 100000 samples are generated for each case. The critical permeability anisotropy coefficient is around 34 for the reference case, which means that the safety factor with r_k=34 is equal to 1 when other parameters are set to the average values. It is noted that for the case with μ_{rk}=5 as shown in Fig. 5.16(a), the amount of r_k>34 can be up to 37 for a COV_{rk}=0.7 by its wide distribution. It is larger than the other two cases (COV_{rk}=0.3, 0.5). In such a case, the failure probability increases as the COV_{rk} increases. Conversely, the opposite trend is given when μ_{rk} is equal to 30 as shown in Fig. 5.16(b). There are respectively 26142, 23650 and 19926 samples greater than r_k=34 with COV_{rk} equal to 0.3, 0.5 and 0.7, it is followed by the failure probability decrease.

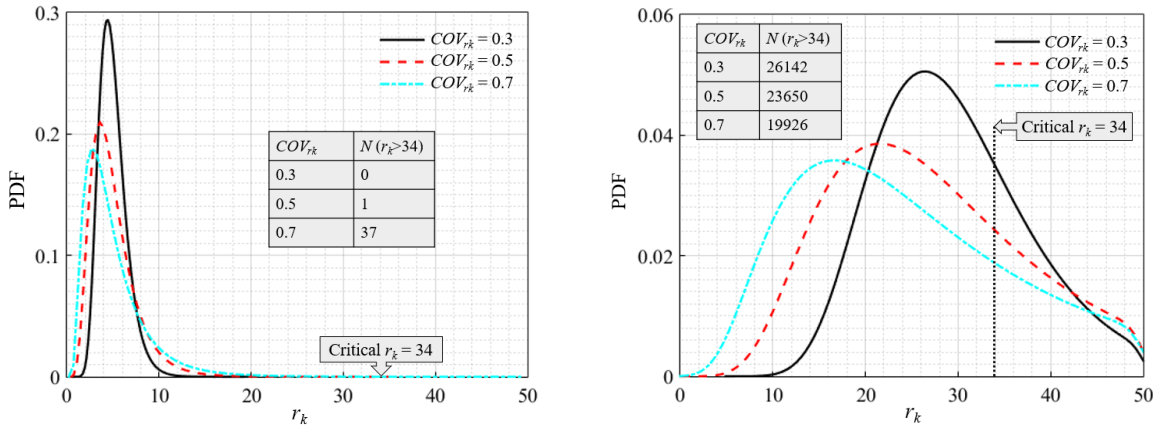

(a) μ_{rk} = 5 (b) μ_{rk} = 30

Fig. 5.16 PDF of r_k for different cases.

To sum up, the failure probability increases with r_k increases, whereas the effects of COV_{rk} on the P_f values are different for cases with different r_k values. Besides, the sensitivity indices are increasing with the COV_{rk}. r_k influences significantly the results when its value is in the range of [1, 10]. Therefore, the statistical properties determination should be done with attention in practice.

5.4.3 Influence of soil-wall interaction

The soil-wall interface coefficient influences on the circular shafts stability are discussed and the results are plotted in Fig. 5.17. As shown in Fig. 5.17(a), the failure probability decreases with the increase of r_i as expected. Its variation is more significant when r_i varies from 0.2 to 0.8. It is consistent with the results given by Fig. 5.17(b), the sensitivity index increases firstly and then decreases, and its value is relatively small when r_i is out of the range [0.2, 0.8]. It means r_i variation causes less change of the failure probability.

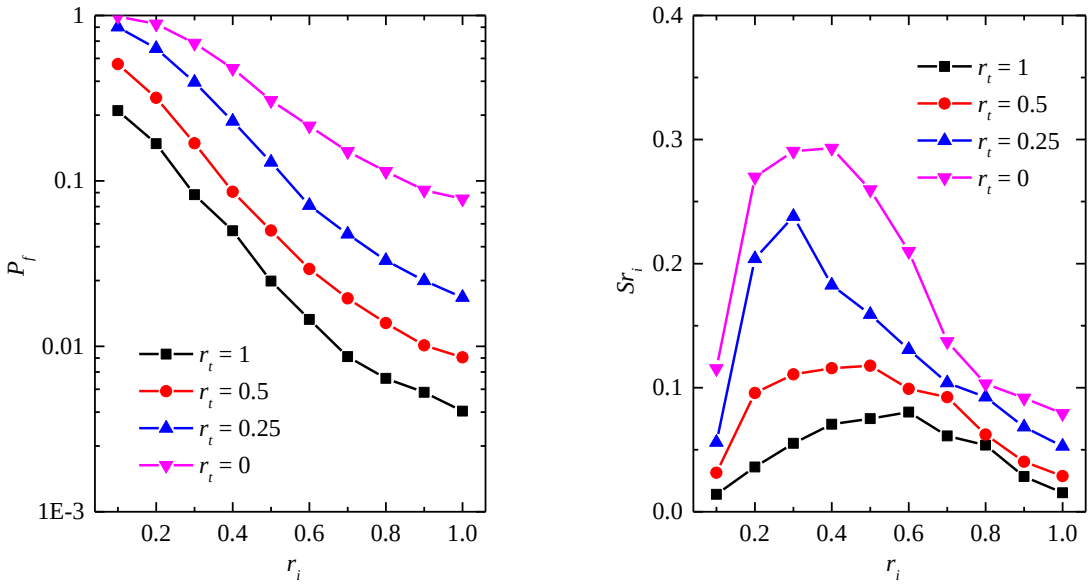

(a) Failure probability (b) Sensitivity index of r_i

Fig. 5.17 Effects of r_i and r_t on probabilistic analysis results.

The probabilistic effects of soil-wall interface strength with different permeability anisotropy coefficients are also discussed and the results are depicted in Fig. 5.18. The r_i influence on the failure probability becomes more important when the permeability anisotropy coefficient decreases. The difference is up to 97.9% when r_i=0.9. It shows similar trends with Fig. 5.8.

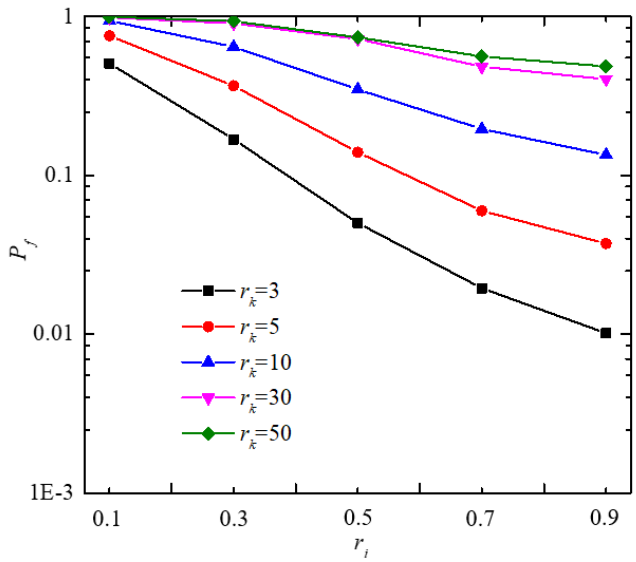

Fig. 5.18 Effects of r_i and r_k on P_f.

5.5 Conclusion

Deterministic and probabilistic analyses are conducted to analyse the stability of circular shafts subjected to hydraulic uplifts. The effects of the permeability anisotropy coefficient (r_k), soil-wall interface coefficient (r_i) and soil tension cut-off coefficient (r_t) are discussed. The results show that the safety factor increases with the increase of r_i and r_t, and with the decrease of r_k. Besides, when r_k increases, the horizontal water flow is prominent. The flow vectors, water pressures and water heads are then more horizontally distributed. The water pressures and hydraulic gradients on the excavation side are increased. The failure surface is developed from the shaft center, which is more prone to result in hydraulic heave accidents. Conversely, the shear failure occurs along the soil-wall interface when the soil permeability is less anisotropic. The effect of r_i is more pronounced with the r_k decreases.

The magnitudes of shaft stability results are not linearly proportional to the values of r_k and r_i. The permeability anisotropy coefficient sensitivity index is higher when r_k varies from 1 to 10 and the soil-wall interface coefficient influences significantly the shaft stability when it is in the range of [0.2, 0.8]. This is similar to the soil-wall interface discussions presented in Chapter 4 ([0.3, 0.7]). Even small changes can result in different stability results. The tensile strength can also make a significant influence on the circular shaft stability, and the difference can be up to 97.8%. Therefore, the corresponding values determination should be done with attention for the design of such structures.

A probabilistic analysis based on the PCK metamodel is then performed. The probabilistic results show that as COV_{rk} increases, the sensitivity index of r_k increases. However, the failure probability variation depends on the r_k mean values. When the permeability anisotropy coefficient is small (e.g., r_k<10), the failure probability is increased as the coefficient of variation. Conversely, the failure probability is decreased for the case with large permeability anisotropy coefficient. Therefore, one should take advantage to better characterize the variability of the inputs considered as uncertain parameters.

Chapter 6

Stability analysis of rectangular excavations at great depth considering the spatial variability

Contents

6.1 Introduction 165

6.2 Random finite element analysis 165

6.2.1 Random field generation 165

6.2.2 *b*SPCE method 167

6.2.3 Procedure 168

6.3 Results and discussions 170

6.3.1 Results and comparison 170

6.3.2 Probabilistic distributions of the wall deflection with consideration of the soil spatial variability 173

6.3.3 Probabilistic serviceability assessment 176

6.3.4 Influence of the autocorrelation lengths 177

6.4 Conclusion 177

6.1 Introduction

In Chapters 2-5, soil uncertainties are modelled only using random variables. However, soil spatial variability, which means that the mechanical soil properties are significantly different from one location to another, always exists due to the complex geological processes (deposition, sedimentation, weathering and biological effects) (T. Zhang et al., 2021a). Probabilistic analyses considering the soil spatial variability are more representative and permit to provide more complementary results.

This chapter improves the probabilistic analysis of the supported excavation at great depth in Chapter 3 by introducing random fields (RF) to consider the spatial variability. A random finite-element method is implemented to study the effect of two-dimensional spatial variability on the predicted wall responses of the FIVC excavation. The Karhunen-Loève (K-L) expansion is used to generate a discretized random field. An active learning method based on the bootstrap Sparse Polynomial Chaos Expansions (*b*SPCE) is then implemented to analyse the spatial variability effects on the excavation stability (in terms of failure probability and wall deflection). The Monte Carlo simulations are then coupled with *b*SPCE models for the serviceability assessment of the supported excavations.

6.2 Random finite element analysis

This section aims to present the random finite element analysis for the supported excavations. The random field generation is introduced first, which is followed by the probabilistic methods. A flowchart is then given for the probabilistic analysis of the supported excavations with consideration of the spatial variability.

6.2.1 Random field generation

A random field can describe the spatial correlation of soil properties at different locations and represent nonhomogeneous features. Among the random field discretization methods (i.e., the point discretization methods, the average discretization methods and the series expansion methods), the series expansion methods which are less sensitive to the finite element mesh size, will be implemented in this chapter (Sudret and Kiureghian, 2000).

The series expansion methods result in a Gaussian field represented by a series of random variables and deterministic spatial functions. The accuracy of the field depends on the number of terms used in the series expansion and the expansion method employed. The K-L expansion is used in this study since it requires the least random variables for a given accuracy and is independent of the finite element discretization (Cho, 2010; Sudret and Kiureghian, 2000).

Spatial correlation

A Gaussian random field can be described by its constant mean $\mu(x)$, variance $\sigma(x)$ and an autocorrelation function ρ, which is used to describe the spatial correlation of soil properties. In this study, a squared exponential autocorrelation function is used and reads as follows

$$\rho(x,y)=\exp\left[-\pi\left(\frac{|x-x'|^2}{l_h^{\,2}}+\frac{|y-y'|^2}{l_v^{\,2}}\right)\right] \tag{6.1}$$

where l_h and l_v are respectively the autocorrelation lengths in the horizontal and vertical directions, (x, y) and (x', y') are the coordinates of two arbitrary points. The autocorrelation length is used to describe the distance for the soil properties with correlation. A large autocorrelation length value implies that the soil property is highly correlated over a large spatial extent, resulting in a smooth variation within the soil profile (T. Zhang et al., 2021a).

K-L expansion

The Karhunen-Loève (K-L) expansion is based on the spectral decomposition of its autocovariance function, which is the product of the autocorrelation function and the random field variance. The realization of a stationary Gaussian random field, denoted $H(x,\xi)$, can be defined by (Cho, 2010; Liao and Ji, 2021)

$$H(x,\xi)=\mu+\sigma\sum_{i=1}^{\infty}\sqrt{\lambda_i}\theta_i(x)\xi_i\cong\mu+\sigma\sum_{i=1}^{S}\sqrt{\lambda_i}\theta_i(x)\xi_i \tag{6.2}$$

where μ and σ are respectively the mean value and standard deviation of the random field, λ_i and θ_i are respectively the eigenvalues and eigenfunctions of the autocovariance function, ξ_i is a set of uncorrelated random variables and S is the size of the truncated series expansion. It should be noted that S depends on the target accuracy, autocorrelation length and the random field dimension. It is noted that the higher the value of S, the higher the accuracy of the random field. However, a large amount of S can also increase the computational burden. The determination of the minimal random variables number with the accuracy guarantee is necessary.

The ratio of expected energy R_e is introduced and the approximation is considered good enough when the value is larger than a given threshold δ_{Re}, which can be expressed as (Jiang et al., 2014)

$$R_e = \sum_{i=1}^{S} \lambda_i / \sum_{i=1}^{\infty} \lambda_i \geq \delta_{R_e} \tag{6.3}$$

A log-normal random field can then be expressed as

$$H(x,\xi) = \exp\left[\mu_{\ln} + \sigma_{\ln} \sum_{i=1}^{S} \sqrt{\lambda_i} \theta_i(x) \xi_i \right] = \exp\left[\mu_{\ln} + \sigma_{\ln} G(x,\xi) \right] \tag{6.4}$$

where $G(x,\xi)$ is a standard normally distributed random field with S terms, $\mu_{\ln}$ and $\sigma_{\ln}$ are respectively mean value and standard deviation of the log-normal random field, which can be defined by

$$\sigma_{\ln} = \sqrt{\ln(1 + COV^2)} \tag{6.5}$$

$$\mu_{\ln} = \ln \mu - 0.5\sigma_{\ln}^{\ 2} \tag{6.6}$$

where COV is the coefficient of variation.

6.2.2 *b*SPCE method

The probabilistic analysis from Chapter 2 to Chapter 5 is based on the PCK-based probabilistic methods, and the optimal PCK is performed to find the metamodel with minimal value of the leave-one-out error. This metamodel includes the determination of the orthogonal polynomials and corresponding coefficients in sparse polynomial chaos expansions, and parameters of autocorrelation function in Kriging. It is recommended for the low-dimensional (random variable dimensionality is smaller than 20) problems.

It is noted that the probabilistic analysis becomes a high-dimensional problem due to the random field discretization. The increased random variables number can significantly increase the computational effort for the determination of the optimal PCK. The Polynomial Chaos Expansions (PCE) metamodel is recommended in terms of computational efficiency and accuracy, which is used in this probabilistic analysis with consideration of spatial variability (Moustapha et al., 2022). The PCE is a mathematical technique for quantifying the uncertainty in a system by representing it as a polynomial function of random variables, and the basic formula of PCE is defined as

$$Y \approx M^{PCE}(\boldsymbol{x}) = \sum_{i \in A} \alpha_i \Phi_i(\boldsymbol{x}) \tag{6.7}$$

The detailed definitions can be found in Section 2.3.1. The hyperbolic truncation scheme is used to truncate the PCE formula for the sake of practical applications and the least-square minimization regression strategy to calculate the coefficients.

The metamodel performance can then be assessed by the leave-one-out error, which represents the global error of the PCE metamodel. The smaller the error, the more accurate the model. In order to consider the local error estimate of PCE metamodel and can further employ the active learning method to enrich the model evaluations close to the limit state, the *b*PCE method is proposed by (Marelli and Sudret, 2018) by implementing the bootstrap resampling technique into PCE.

The rationale of the *b*PCE is: an initial experimental design (N_{ED}) is generated from the input space, and the corresponding model response (Y) can be determined by the deterministic models. A bootstrap resampling technique is then implemented to generate b new EDs by randomly assembling b N_{ED} realizations. Accordingly, b different PCE surrogate models are constructed based on the new EDs. Therefore, b possible predictions can be observed at each point. The local error bounds can then be determined by employing the empirical quantiles. A *b*SPCE (also known as the fast *b*PCE) approach is further proposed since performing b sparse-least square analysis is time-consuming. The sparse polynomial basis identified by the N_{ED} is performed only once and assumed effective for all the new Eds. The bootstrap is only applicable to the unknown coefficient estimation of the sparse basis which is based on a classic ordinary least-square regression. More detailed information about the *b*SPCE performance can be found in Fig. 6.1.

6.2.3 Procedure

This section aims to describe the procedure of the random finite element analysis based on the FEM code in PLAXIS software and the probabilistic analysis using the surrogate models *b*SPCE. Fig. 6.1 gives a detailed flowchart and can be described as follows,

Step 1: Preparation. Construct an RFEM model for the excavations. Generate an initial experimental design N_{ED} and a large of samples S_{Pf} used for the failure probability P_f calculation;

Step 2: Input-output sets determination. Compile the batch commands of MATLAB and map the generated samples on the RFEM model. After the evaluation, the model response (such as the horizontal wall deflection) is then exported and saved automatically;

Step 3: SPCE model construction. Construct a SPCE metamodel based on the N_{ED} and the corresponding model response. The failure probability can then be evaluated based on the metamodel and S_{Pf};

Step 4: *b*SPCE model construction. Generate *b* sets of new EDs based on the bootstrap resampling technique and construct *b* different SPCE surrogate models. A set of failure probabilities can then be evaluated;

Step 5: Accuracy control. Two stopping criteria are satisfied. The first one is related to the failure probability estimation as presented by

$$\frac{P_f^{+} - P_f^{-}}{P_f} \leq \varepsilon P_f \tag{6.8}$$

where P_f^{+} and P_f^{-} are respectively the maximum and minimum failure probability estimated by the *b* different SPCE models, and εP_f is the target accuracy with a range of [0.05, 0.15] and 0.05 is considered in this study (Marelli and Sudret, 2018).

If Eq. (6.8) is not satisfied, the informative samples from the S_{Pf} needs to be elected to enrich the experimental designs for the metamodel construction. The learning function for the *b*SPCE is the Fraction of bootstrap replicates (FBR) based on the probability of misclassification of a candidate sample. The FBR can be defined as

$$U_{\mathrm{FBR}}(x) = \frac{\left| B_s(x) - B_f(x) \right|}{B} \tag{6.9}$$

where $B_s(x)$ and $B_f(x)$ are respectively the number of safe and failed bootstrap replicate predictions at the point *x*. The newly added sample is chosen by minimizing Eq. (6.9), i.e., $S_n = \arg\min U_{\mathrm{FBR}}(x)$, which permits finding the point whose prediction is uncertain tend to have close values of $B_s(x)$ and $B_f(x)$.

The second criterion is related to the coefficient of variation of P_f as presented in Eq. (1.16), if it is smaller than 5%, the procedure enters the next step, otherwise, the enrichment of the S_{Pf} is necessary and enters Step 3;

Step 6: **Post-processing of MCS results.** The statistical moments of the model response and the PDF/CDF can be obtained.

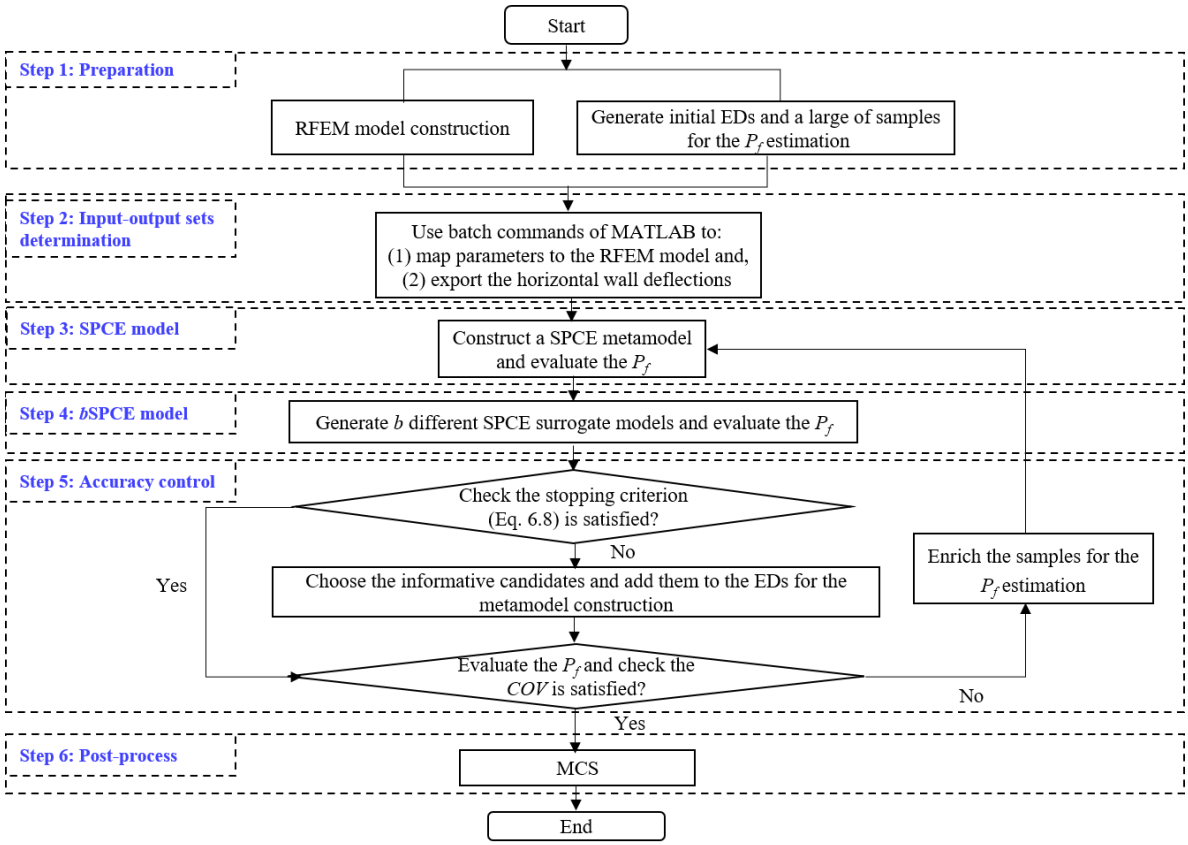

Fig. 6.1 Flowchart of the probabilistic analysis with consideration of the spatial variability

6.3 Results and discussions

This section aims to investigate the influence of the soil spatial variability on the stability of the supported excavation with great depth (Fort d'Issy-Vanves-Clamart excavation: FIVC) as presented in Chapter 3. The probabilistic analysis is validated first, which is followed by the discussion of the spatial variability effects on the maximum wall deflections and the failure probability of supported excavations.

6.3.1 Results and comparison

The sensitivity analysis presented in Fig. 3.11 shows that the friction angles of layers Meudon Marls (MM) and Ypresian Plastic Clay (PC), and the initial earth pressure coefficient at the rest of layer PC are the parameters contribute the model most, whose sensitivity indices exceed 0.1.

Therefore, the three key parameters (φ_{PC}, φ_{MM} and k_{0PC}) will be modelled using random fields and the other four parameters (E_{HL}, E_{PC}, E_{MM} and φ_{HL}) are modelled random variables. The random fields of layers MM and CP are considered and can be defined by subdividing the layers into square-shaped subdomains (Nguyen and Likitlersuang, 2021) as presented in Fig. 6.2. If the element sizes are too small, the computational effort increases significantly. In this study, the soil profile was subdivided into 360 elements, including 160 elements for the PC layer and 200 for the MM layer, each one in a block shape of 5 × 1 m^2.

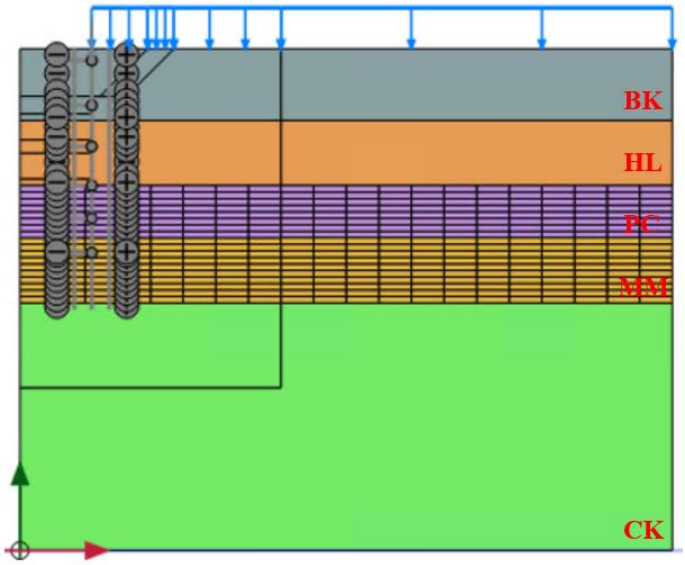

Fig. 6.2 FEM model of the FIVC excavation considering the spatial variability

The horizontal and vertical autocorrelation lengths are respectively 40 m and 3 m for the reference case and more statistical properties refer to Table 3.4. A total of 36 input variables will be considered in this probabilistic analysis, which includes 20 standard normal variables for the PC layer (φ_{PC} and k_{0PC}), 10 standard normal variables for the MM layer (φ_{MM}) and 4 random variables (E_{HL}, E_{PC}, E_{MM} and φ_{HL}). The random fields of φ_{PC}, φ_{MM} and k_{0PC} can be realized using Eq. (6.1) to Eq. (6.6) and the corresponding information can then be automatically imported to the numerical model via batch command codes. After the calculation, the horizontal wall deflection can be automatically exported and saved.

The probabilistic analysis presented in Section 6.2 is implemented. Initial EDs with 360 samples are generated first (Guo et al., 2019b). The input-output can then be determined and the adaptive metamodel *b*SPCE is constructed. The MCS is implemented to provide the failure probability, the distributions of the maximum wall deflection, and the corresponding statistical moments. Considering the limiting wall deflection, 28 mm is used for the reference case in Chapter 3.

However, the failure probability with consideration of the spatial variability is very small using 28 mm and is hard to calculate the corresponding failure probability (will be presented in Section 6.3.3). This section takes 20 mm as an example to discuss the accuracy of the probabilistic analysis procedure (Philipponnat and Hubert, 2016). A total of 589 samples are used for the metamodel construction and the MCS gives a failure probability of 1.9e-3 with a COV_{Pf} being 4.6%, which can ensure the P_f value accuracy. For the statistical moments, the mean value and standard deviation are respectively 16.50 mm and 1.11 mm. Fig. 6.3 shows the PDF and CDF for the maximum wall deflection estimations based on the procedure.

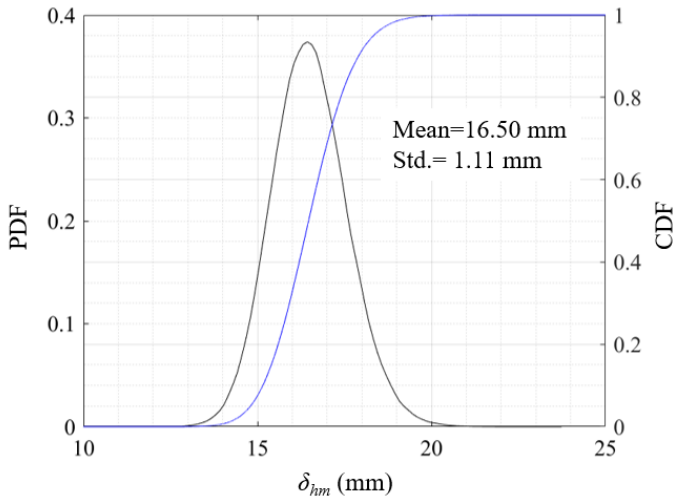

Fig. 6.3 PDF and CDF of δ_{hm}

The metamodel is validated by Fig. 6.4, which depicts the comparison of the maximum wall deflection with the numerical simulations. 300 sets of samples generated by the LHS are considered. It is seen that almost all the scatter points are within ±5% of the 45^o line, which represents that the results based on the metamodel are approximately equal to those obtained by the numerical simulations. It allows verifying the accuracy of the SPCE surrogate model.

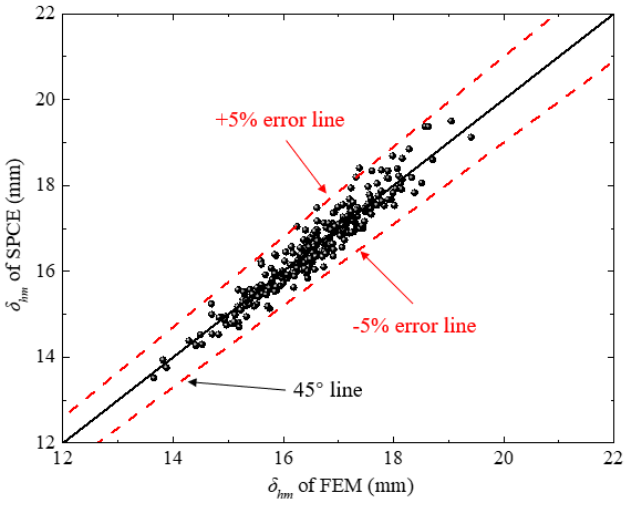

Fig. 6.4 δ_{hm} comparison obtained by FEM and SPCE models.

6.3.2 Probabilistic distributions of the wall deflection with consideration of the soil spatial variability

4 cases with different combinations of horizontal and vertical autocorrelation lengths, including l_h=∞ & l_v=∞, l_h=40 m & l_v=3 m, l_h=10 m & l_v=3 m and l_h=40 m & l_v=1 m, are considered (Phoon et al., 2022). The autocorrelation lengths for three key parameters are set the same. Similar to Chapter 3, 500 samples generated by the LHS, are simulated for each case to investigate the spatial variability consideration effects on the wall deflection distributions. The infinite value of the autocorrelation length in Fig. 6.5(a) is related to the random variable case and the variation of the horizontal wall deflection is the most significant. With the decrease of the autocorrelation lengths in horizontal and vertical directions, the distributions are less varied as presented in Fig. 6.5(b~d). This is because a higher autocorrelation length indicates a stronger correlation of the soil strength, which may lead to a relatively low variability. As a result, the global average of the strength parameters varies considerably from one realization to another, which results in higher variability of the obtained maximum wall deflections. Conversely, small autocorrelation lengths lead to more non-homogeneous zones, and smaller variations in the system response.

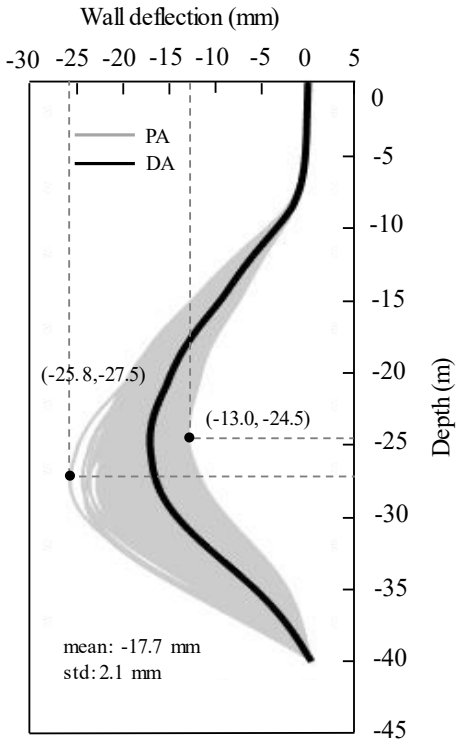

(a) l_h=∞, l_v=∞

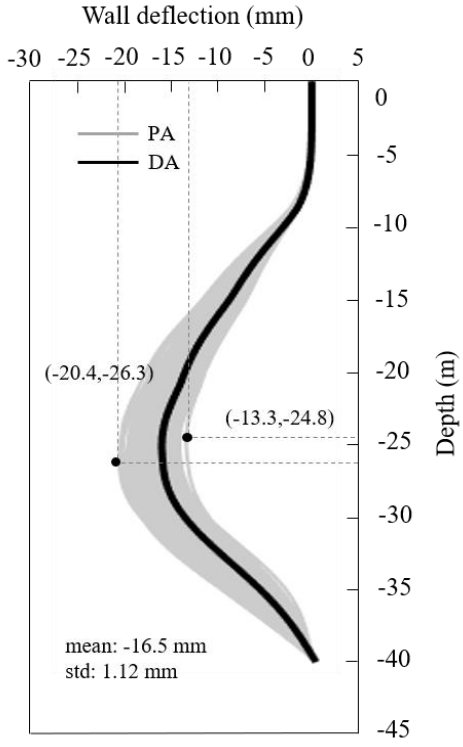

(b) l_h=40 m, l_v=3 m

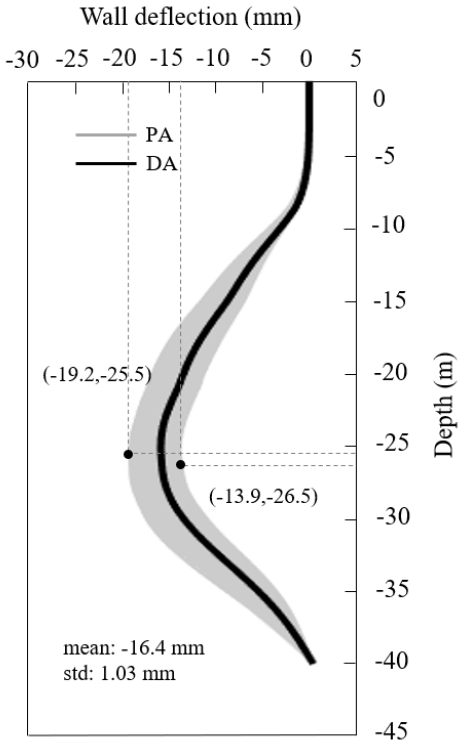

(c) l_h=10 m, l_v=3 m

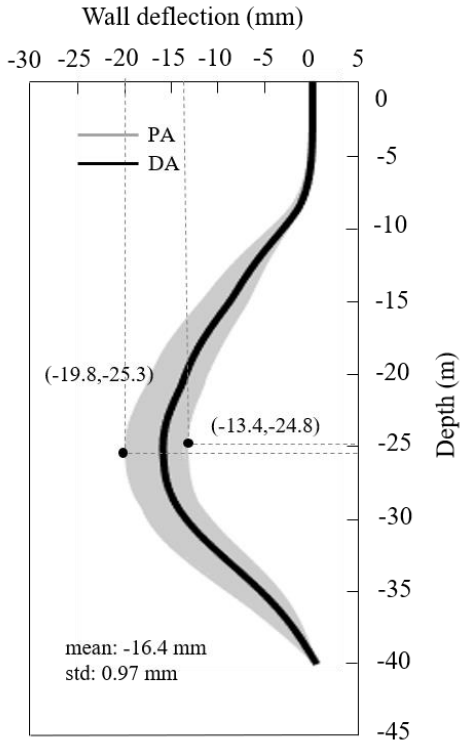

(d) l_h=40 m, l_v=1 m

Fig. 6.5 Wall deflection contours with consideration of the spatial variability.

Determining the corresponding locations where the maximum wall deflection occurs is also important for the structural evaluation of underground diaphragm walls. Fig. 6.6 depicts the depth frequencies at which the maximum deflection of the wall occurs for different cases. It is observed that the δ_{hm} locations are distributed narrower with the decrease of the autocorrelation lengths. The depths are mainly located between 24 m and 26 m below the ground surface due to the stiffness difference between layers HL, PC and MM. More attention should be paid in practice in these areas.

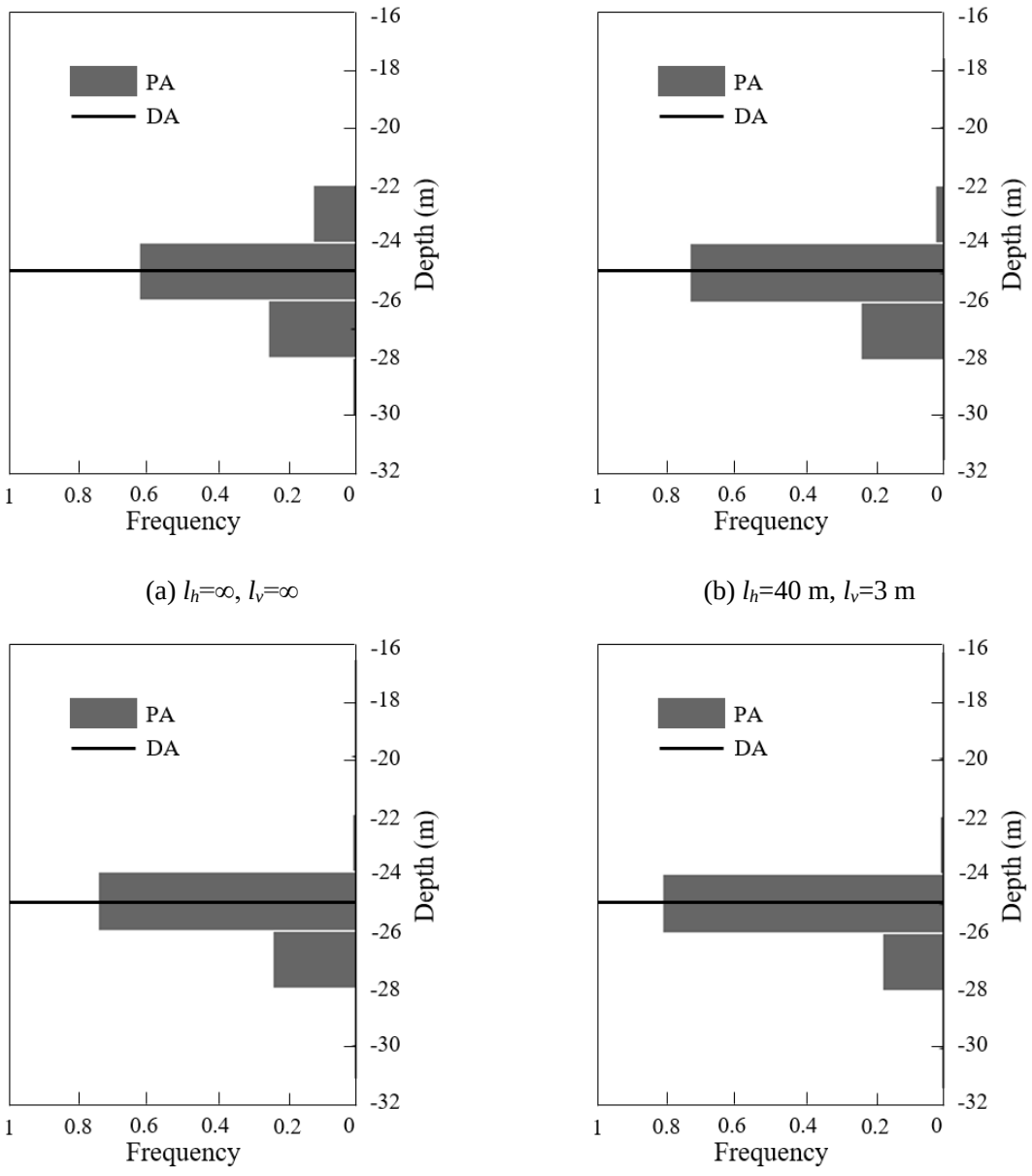

(a) l_h=∞, l_v=∞

(b) l_h=40 m, l_v=3 m

(c) l_h=10 m, l_v=3 m

(d) l_h=40 m, l_v=1 m

Fig. 6.6 Frequency of the maximum horizontal wall deflection location.

6.3.3 Probabilistic serviceability assessment

The limiting wall deflection effects on the probability of serviceability limit state are discussed in this section. Different soil autocorrelation lengths and coefficient of variations are considered and the limiting maximum horizontal wall deflection is varied from 12 mm to 30 mm. It is seen that with the increase of the limiting wall deflection, there is no doubt that the failure probability is decreasing since higher thresholds are not easily exceeded. With the decrease of the autocorrelation lengths, the P_f value is increased when the limiting wall deflection is smaller than about 16 mm. The failure probability is decreased with the increase of the limiting wall deflection after the limiting wall deflection is larger than 18 mm. This phenomenon is similar to Section 3.4.5 and the same explanation can be given since with the increase of the autocorrelation lengths, the maximum wall deflection distributions are also wider. The failure probability is decreased with the increase of the distributions when the limiting value is smaller than the mean horizontal wall deflection of about 17 mm. Besides, compared to Fig. 6.7 (a) and (b), the increase of the COV_φ of Fig. 6.7(c) makes more influence on the failure probability, which can highlight the importance of the friction angles.

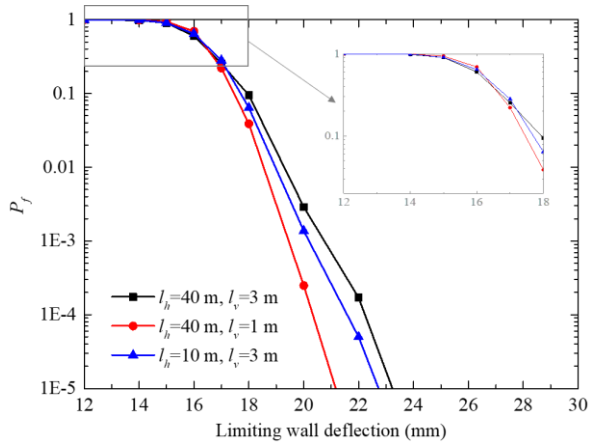

(a) COV_{E50ref}=0.15, COV_φ=0.1, COV_{k0}=0.15

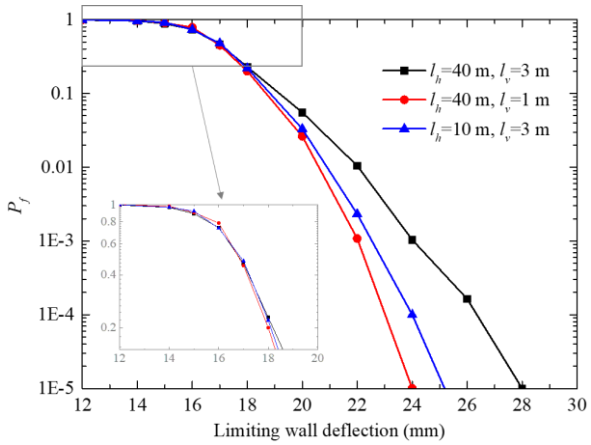

(b) COV_{E50ref}=0.15, COV_φ=0.1, COV_{k0}=0.35

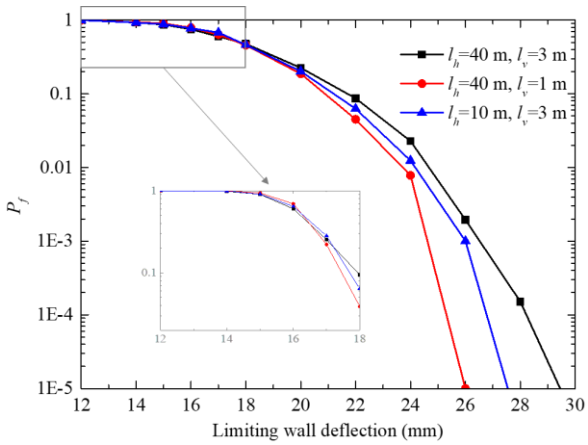

(c) COV_{E50ref}=0.15, COV_{φ}=0.3, COV_{k0}=0.15

Fig. 6.7 Effect of autocorrelation lengths on the probability of exceeding specified limiting wall deflection

6.3.4 Influence of the autocorrelation lengths

This section aims to discuss the effects of autocorrelation lengths on excavation stability. For the horizontal autocorrelation length l_h, it varies from 10 m to 40 m, and the vertical one l_y is in the range of [1 m, 4 m]. The limiting wall deflection is set to 20 mm and after the metamodel construction, 100000 input samples (generated by the LHS) are considered for the PDF and statistical moments discussions in each case. Table 6.1 gives an overview of the probabilistic analysis results with different autocorrelation lengths and Fig. 6.8 depicts the corresponding PDF curves. It can be seen that as the autocorrelation length increases, the failure probability is increased as expected. It can also be interpreted by the standard deviation variation in Table 6.1 and the PDF in Fig. 6.8. It is observed that with the decrease of the autocorrelation lengths, the standard deviation is smaller and the PDF curve is narrower, which shows a smaller variability.

Besides, Fig. 6.8(a) and Fig. 6.8(b) depict respectively the horizontal and vertical autocorrelation lengths on the excavation stability. The results indicate the excavation stability is more sensitive to the vertical autocorrelation length by the fact that the failure probability is increased from 2.49e-4 (l_v=1 m) to 2.79e-3 (l_v=4 m) when l_h=40 m, whereas the failure probability P_f changes less with the increase of the horizontal autocorrelation length. All of the cases are smaller than the random variable case with a failure probability of 0.234 as presented in Fig. 3.22 and the differences are significant. Therefore, ignoring the soil spatial variability may provide biased excavation stability.

Table 6.1 Probabilistic analysis with consideration of the spatial variability.

Autocorrelation lengths		P_f	Mean (mm)	Std. (mm)
l_h=40 m	l_v=1 m	2.49e-4	16.44	0.92
	l_v=2 m	1.2e-3	16.48	0.99
	l_v=3 m	1.88e-3	16.50	1.11
	l_v=4 m	2.79e-3	16.52	1.13
l_v=3 m	l_h=10 m	1.37e-3	16.44	1.02
	l_h=20 m	1.52e-3	16.46	1.05
	l_h=30 m	1.58e-3	16.48	1.07
	l_h=40 m	1.88e-3	16.50	1.11

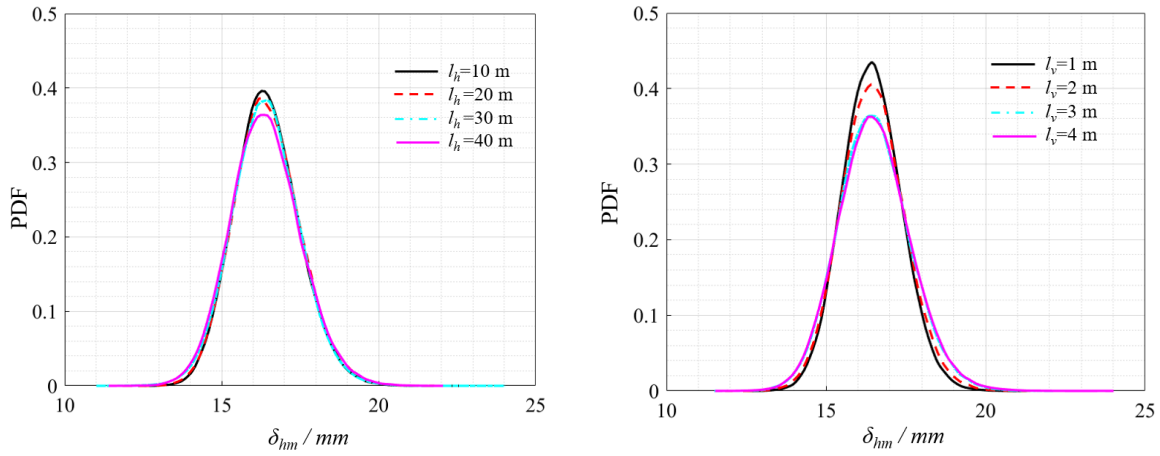

(a) l_v=3 m (b) l_h=40 m

Fig. 6.8 PDFs for different autocorrelation lengths

6.4 Conclusion

This chapter presents a probabilistic analysis of supported excavations at great depth considering the spatial variability. A random finite element model is constructed for the computation of the horizontal wall deflection. The Karhunen-Loève (K-L) expansion is used for the random field discretization and three parameters, which include the friction angles of the Meudon Marls (MM) and Plastic Clay (PC) layers, and the initial earth pressure coefficient at rest k_0 of the PC layer, are modelled by the random field approach since they contribute significantly to the model response as discussed in Chapter 3. An active bootstrap-sparse polynomial chaos expansion (*b*SPCE) is then implemented to replace the time-consuming deterministic models and allow to alleviate the computational effort. Finally, the Monte-Carlo Simulation is carried out to determine the probabilistic results.

The wall deflection distributions are discussed and the results show that the spatial variability highly affects the lateral wall deflection distributions. With the decrease of the autocorrelation lengths, the distributions are narrower since a small autocorrelation length leads to more non-homogeneous zones, and smaller variations in the system response. The maximum wall deflection occurs in the layer PC (from 22 m to 28 m below the ground surface) and with the decrease of the autocorrelation lengths, it is mainly distributed in the range of [-24 m, -26 m]. The probabilistic serviceability assessment considering the spatial variability is implemented. The results showed that the serviceability failure probability strongly depends on the limiting wall deflection and parameter uncertainties (autocorrelation lengths and coefficient of variation). Their determination should be done with attention. The failure probability P_f increases with the autocorrelation length value when the limiting wall deflection is larger than the deterministic wall deflection. Conversely, the failure probability is decreased. The autocorrelation lengths on the probability density functions of the maximum wall deflection and on the failure probabilities, are also discussed. The results show that ignoring the soil spatial variability can provide a biased estimation of the excavation stability, particularly the spatial variability in the vertical direction.

Chapter 7

Sample-wised probabilistic analysis using the Atom Search Optimization-based Artificial Neural Network

---

Contents

7.1 Introduction 181

7.2 Proposed hybrid SPAA approach 181

7.2.1 ASO-ANN method 181

7.2.2 Data preparation 185

7.2.3 SPAA procedure 186

7.3 Example and application 189

7.3.1 Case 1: drained circular shaft stability against hydraulic uplift 189

7.3.2 Case 2: undrained circular shaft stability in non-homogeneous soils 194

7.3.3 Case 3: circular shaft stability considering soil spatial variability 198

7.4 Discussion 200

7.4.1 Accuracy and efficiency survey 200

7.4.2 Initial samples determination 202

7.5 Conclusion 202

7.1 Introduction

It is noted that in the previous five chapters, the Polynomial Chaos Kriging and Sparse Polynomial Chaos Expansion methods were used to provide the probabilistic results, which can improve significantly the probabilistic analysis efficiency. With the rapid development of scientific computing software, machine learning approaches can make predictions based on regression analysis and received attention in geotechnical engineering due to their high efficiency and flexibility. This chapter proposes a Sample-wised Probabilistic Approach based on the Artificial Neural Network (ANN) (SPAA) to analyse the supported excavations stability. An adaptive Atom Search Optimization (ASO)-ANN model is introduced to replace the time-consuming numerical simulations. The existing reliability methods (such as the Monte Carlo Simulation (MCS) and the First Order Reliability Method (FORM)) are then implemented to provide the stability results. The Global Sensitivity Analysis (GSA) is also performed to provide information about the importance of the considered parameters. Then, based on the proposed SPAA, the circular shafts examples presented in Chapters 4 and 5 are used for the validation and comparisons with other methods (including Subset Simulation (SS), Polynomial Chaos Kriging (PCK)-MCS, PCK-FORM and Sparse Polynomial Chaos Expansion (SPCE)-MCS).

7.2 Proposed hybrid SPAA approach

This section introduces the proposed sample-wised probabilistic analysis approach SPAA via a flowchart. The principle of the ASO-ANN method and the determination of initial data are detailed.

7.2.1 ASO-ANN method

Artificial neural networks inspired by biological neural networks can be trained to find solutions, recognize patterns, classify data and forecast future events (Gordan et al., 2016; Sasmal and Behera, 2021). ANN was used for figures and speech recognition and also have been applied to data science in engineering field more recently (Li et al., 2021a; Salazar et al., 2017).

The multilayer perceptron (MLP) is one of the most popular supervised algorithms, and it can be easily built with open-source packages in Python (Rosenblatt, 1958). In MLP, information is transferred from the input layer to the output layer through hidden layers, as shown in Fig. 7.1. d is the target output dataset. n_{ij} is the neuron in the hidden layer and its value could be calculated

by

$$n_{ij} = f\left(\sum_{i=1}^{n}(w_{ij}\theta_i + b_j)\right) \tag{7.1}$$

where f is the activation function, including logistic sigmoid function, hyperbolic tangent function and some other non-linear functions (Wei et al., 2021). w_{ij} and b_j are respectively the weight and bias of the neural network. The network is trained by adapting $\boldsymbol{w}$ and $\boldsymbol{b}$ to minimize the errors between the predicted and target values. It is noted that inappropriate initial values of $\boldsymbol{w}$ and $\boldsymbol{b}$ can not only increase the training convergence steps, but also lead the model to fall into a local optimum solution (Gharehchopogh et al., 2022). Therefore, the initial values determination of $\boldsymbol{w}$ and $\boldsymbol{b}$ is important, which can be found by the optimization method. A recently proposed optimization algorithm, Atom Search Optimization (ASO) is applied to explore efficiently the appropriate initial values.

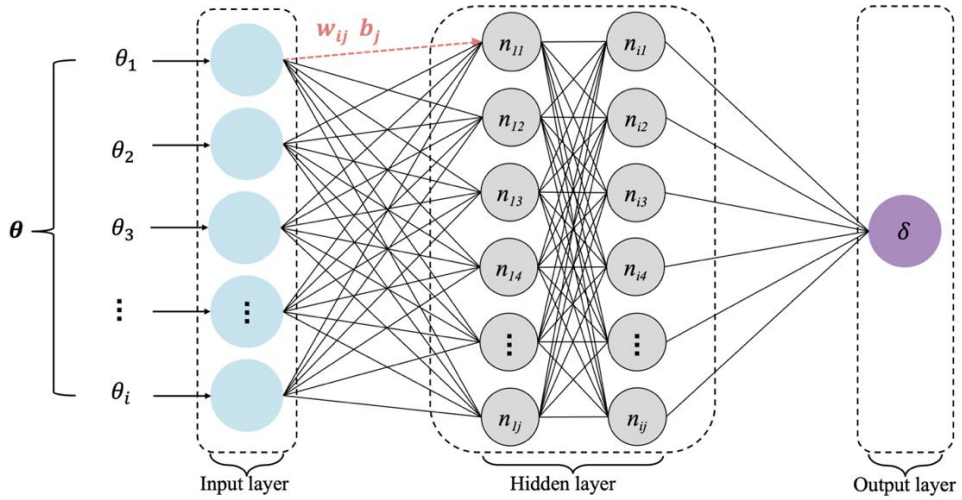

Fig. 7.1 The architecture of artificial neural networks.

ASO was inspired by basic molecular dynamics (Alder and Wainwright, 1959) and was first proposed in the theoretical physics field. It was then developed to address a set of optimization problems by Zhao et al. (2019). This optimization method shows strong competitiveness for multimodal functions and it can adeptly balance the explorative and exploitative search in dealing with hybrid and composition functions. It has been tested on a series of benchmark functions and its effectiveness was verified qualitatively and quantitatively by comparing with other classic and popular optimization methods, such as the Particle Swarm Optimization (Li et al., 2022b), Genetic Algorithm (GA) (Whitley, 1994) and Wind Driven Optimization (W. G. Zhao et al., 2019), which is not further discussed in this study.

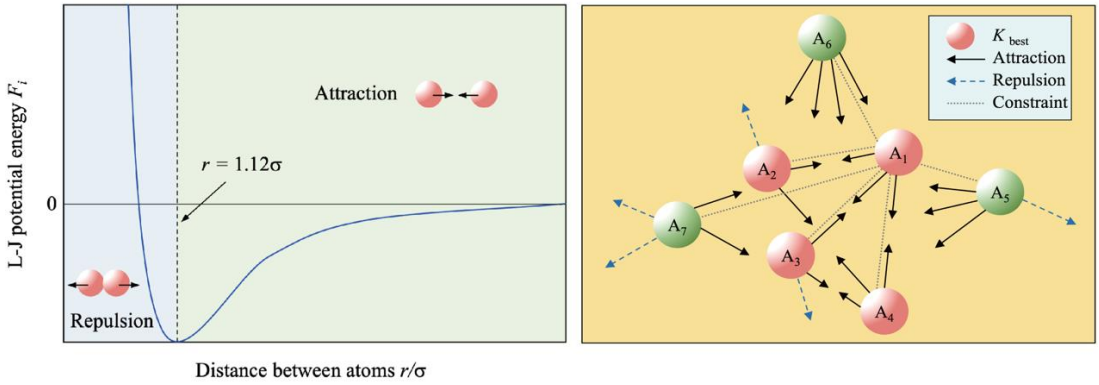

(a) L-J potential curve with attraction and repulsion (b) forces of an atom system with K_{best}.

Fig. 7.2 Atomic motion theory model.

ASO starts the optimization by generating a set of random solutions. It mathematically models and mimics the atomic motion model in nature that follows the classical Newton second law for updating their positions and velocities in each iteration, where atoms interact through interaction forces F_i resulting from the Lennard-Jones potential and constraint forces G_i resulting from the bond-length potential. L-J potential including attraction and repulsion regions shown in Fig. 7.2(a), in the attractive zone, the attraction force gradually decreases to zero as the distance r between the atoms increases. In the repulsive zone, the repulsive force rapidly increases as the distance decreases. When the distance between two atoms is 1.12 times the atomic diameter σ, the L-J potential energy is equal to zero. Therefore, the acceleration a_i of the atom could be calculated by

$$a_i = \frac{F_i + G_i}{m_i} \tag{7.2}$$

where the m_i is the mass of i^{th} atom. Fig. 7.2(b) depicts the forces of an atom population, where the first four atoms with the best fitness values are considered the K_{best}. The K_{best} is made up of A1, A2, A3, and A4, as seen in the diagram. Each atom in the K_{best} attracts or repels A5, A6, and A7, and A1, A2, A3, and A4 attract or repel each other. Except for A1 every atom in the population is constrained by the best atom A1. A more detailed mathematical introduction was descripted in Ghosh et al. (2020).

Among them, the total interaction force working on the i^{th} atom from all other atoms is the weighted sum of components of the forces in d^{th} dimension can be formulated by

$$F_i^d(t) = \sum_{j \in K_{best}} \text{random}_j F_{ij}^d(t) \tag{7.3}$$

where random$_j$ is a random number in [0, 1] and j is the number of K_{best}. In ASO, an atom is assumed to have a covalent bond with the best atom, so each atom is acted upon by a constraint force by the best atom (W. G. Zhao et al., 2019). This constraint force acting on the i^{th} atom in the d^{th} dimension is defined by the position of atom $x_i^d(t)$ and the optimum atom $x_{\text{best}}^d(t)$ as below

$$G_i^d = \beta e^{-\frac{20t}{T_n}} \left(x_{\text{best}}^d(t) - x_i^d(t)\right) \tag{7.4}$$

where β is the multiplier weight and T_n is the maximum number of iterations. The acceleration aid can then be calculated. And the new position of the atom is updated from the time t position

$$v_i^d(t+1) = \text{random}_i^d v_i^d(t) + a_i^d(t) \tag{7.5}$$

$$x_i^d(t+1) = x_i^d(t) + v_i^d(t+1) \tag{7.6}$$

where random_i^d is a random number in [0, 1]. v_i^d and x_i^d are the atom velocity and the position of the i^{th} atom in d^{th} dimension, respectively.

To improve the exploration in the first iteration of the ASO algorithm, each atom must interact with many atoms with higher fitness values as its K neighbors. To improve exploitation in the final iteration stage, the atoms should interact with as few atoms with higher fitness values as possible as their K neighbors. Therefore, as a function of time, K gradually decreases with the lapse of iterations. K can be calculated as

$$K(t) = N - (N-2) \times \sqrt{\frac{t}{T_n}} \tag{7.7}$$

where N is the initial population size. Initially, the positions of the four atoms in the search space are generated at random. Each iteration also updates the position of the best atom located. All updating and calculations are developing progressively until the stop criterion is reached. With the passing of time, all of the atoms apply the mathematical motion mode to approach the target and form a swarm. Finally, as an approximation to the global optimum, the position and fitness value of the best atom (***w*** and ***b***) are restored. Based on the optimized values of ***w*** and ***b***, the ANN model can then be efficiently determined.

7.2.2 Data preparation

A large number of samples are necessary for the P_f determination using the MCS to ensure the probabilistic results accuracy. Latin Hypercube Sampling (LHS) is widely used for the sample generation by the fact that it combines the advantages of random sampling and stratified sampling. The run number required for an accurate probabilistic analysis can thus be reduced significantly compared to using the random and stratified sampling methods respectively (Helton and Davis, 2003). It is known for decades that about 10^{k+2} deterministic simulations are usually required for a failure probability of 10^{-k} with a coefficient of variation of 10% (Guo, 2020). The computational burden is strong using the direct MCS, particularly for cases with time-consuming deterministic simulations (Yoo et al., 2022). An accurate surrogate model (ASO-ANN) can then be constructed to replace the time-consuming evaluations and assess the large samples safety factor. The main task is to select the sampling points for the model construction that can represent large samples used for P_f calculations. It is no doubt that a large amount of initial sampling data can build a sufficiently accurate surrogate model. However, the required deterministic evaluations increase along with a heavier computational burden. Finding the most representative points, which means using few sampling points to build an accurate surrogate model, is necessary.

The uniform design is often carried out for the initial sampling generation in the existing studies about the ANN-based adaptive probabilistic analysis (Cho, 2009; Lü et al., 2012). The possible explanation can be found in Fig. 7.3, which depicts the generated sample distributions. R_1 and R_2 are two considered lognormal random variables and are modelled by the lognormal distributions. It is observed that a uniform method guarantees the sampling points being scattered uniformly (30 black solid points) to make sure of the ANN model effectiveness. However, the large samples used for the P_f calculation (1000 blue hollow points) are mainly distributed in a range of [0.7, 1.3], and only 4 uniform samples are spread in the densest domain (green box).

Conversely, most of the LHS initial samples (30 red solid points) are located around the blue points. That is to say, the distributions of LHS initial samples and P_f calculation samples are similar. It is observed that about 23 samples are in the green box, which confirms that sampling points generated by the LHS are more effective for the surrogate model construction compared to the uniform one. Besides, the boundary points, composing of limit values, are also added to the initial samples to cover the samples domain.

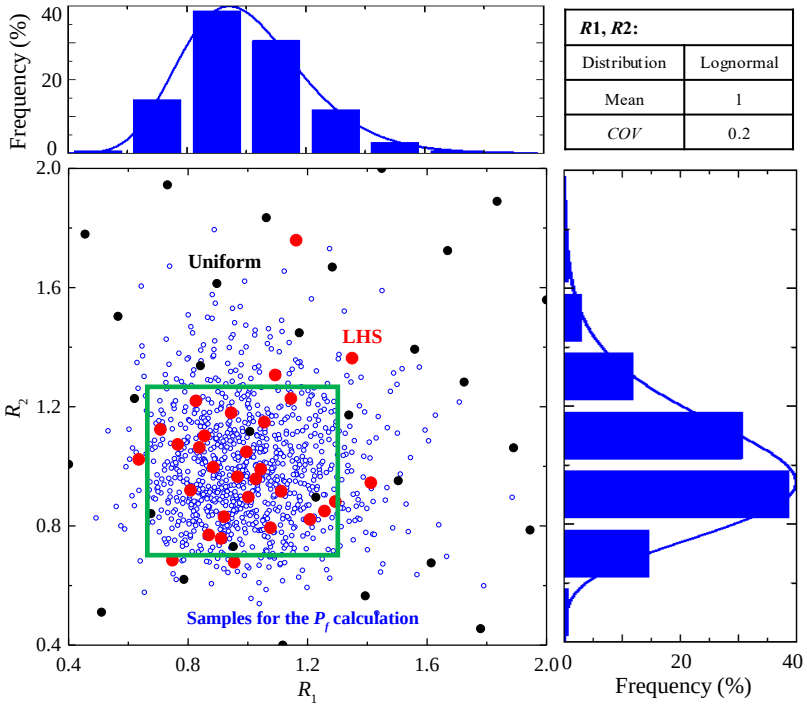

Fig. 7.3 Comparison of samples generated by the LHS and uniform methods.

7.2.3 SPAA procedure

This study considers the SPAA for excavations probabilistic analyses and this section aims to present the detailed procedure. Fig. 7.4 depicts a detailed description of the SPAA and the main steps are described below:

Step 1: Preparation. Determine the input variables statistics information and build a deterministic numerical model. For the random variable case, the variables distribution, mean value, coefficient of variation and cross-correlation coefficient should be determined. The autocorrelation function and autocorrelation lengths are also provided when the soil spatial variation is considered.

Step 2: Input-output sets determination. Map the generated input samples to deterministic models. The responses are evaluated and exported for the post-process.

Step 3: ASO-ANN model determination. It is noted that the input-output dataset is divided into 70% and 30% for training and testing, respectively. Besides, the datasets are normalized to −1 and 1 by the MinMax scaling method to reduce all characteristics to a common dimension without distorting differences in the range of values (Li et al., 2022a). The ASO-ANN model is then constructed by adjusting the hidden layer neurons of ANN, the population size of ASO, and

enriching the datasets. It is noted that the points that are most likely to be misjudged as failures or safe should be enriched and can be determined by

$$A_d(x) = \arg\min(|P_d(x) - 1|) \tag{7.8}$$

where $P_d(x)$ is the predictions based on the ASO-ANN model.

Step 4: Perform the MCS and GSA based on the ASO-ANN model and several probabilistic results can be provided. The MCS and GSA are employed within the uncertainty quantification toolbox UQLab (Marelli and Sudret, 2014) and the ASO-ANN model construction is implemented with Python. The calculations were carried out on a computer equipped with an Intel(R) Core (TM) i7-8700K 3.70GHz CPU.

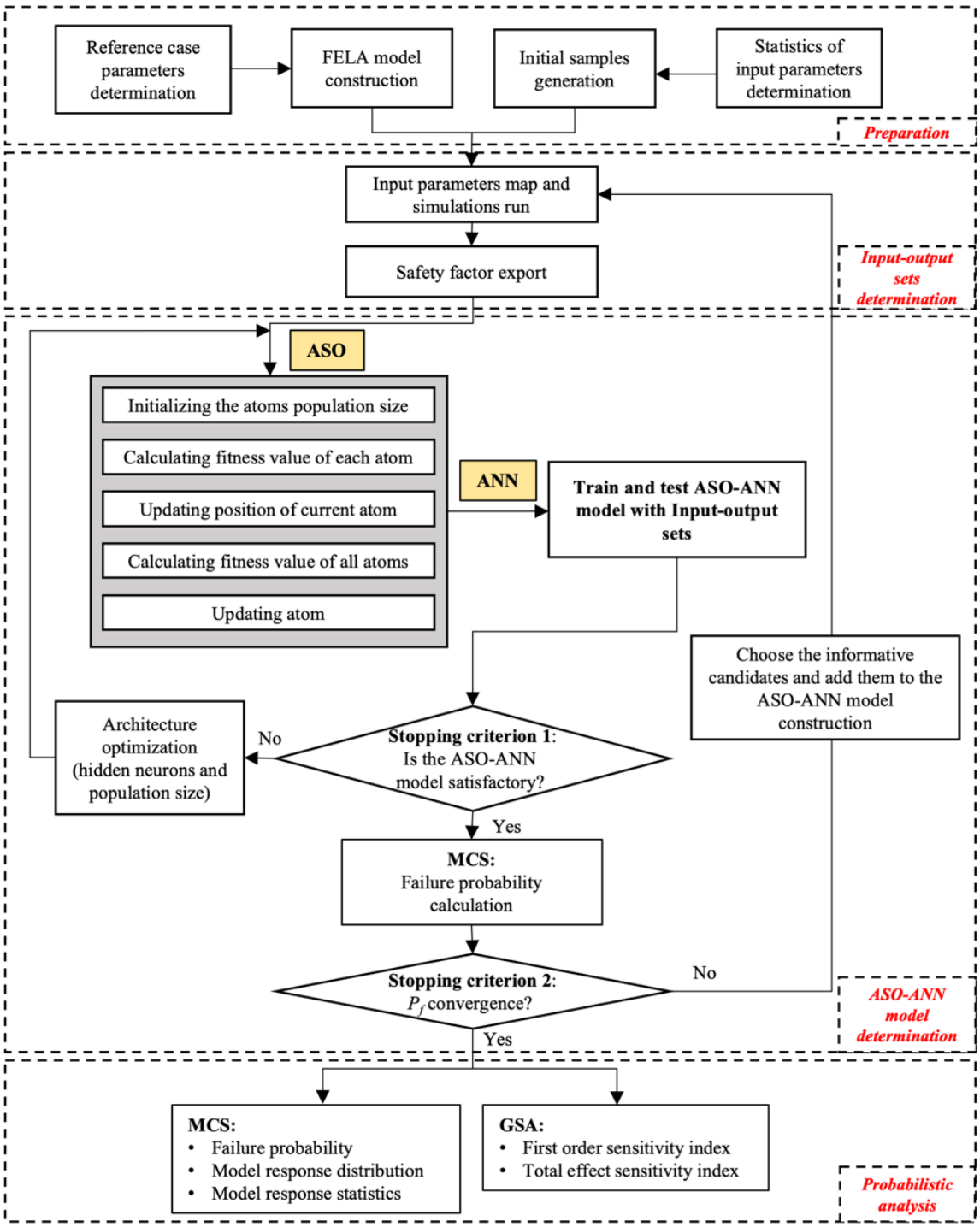

Note*: *Stopping criterion 1: evaluation metrics of ASO-ANN model with test datasets mean square error (MSE)). The model needs to meet one of the criteria: the epochs amount achieves 1000 or the MSE≤1.0e-5.

Stopping criterion 2: failure probability convergence. $Err_{P_f}(i)=\left|[P_f(i)-P_f(i-1)]/P_f(i-1)\right|$, where $P_f(i-1)$ and $P_f(i)$ are the failure probabilities of (i-1)th and i^{th} iteration, N_{en} is the sample enrichment iteration number, N_{tg} is the number of failure probabilities which are required to be compared, and i is in the range of $[N_{en}-N_{tg}+1, N_{en}]$. When the Err_{P_f} value is smaller than the threshold value, i.e., $Err_{P_f} < Err_{P_f\_tg}$, the procedure can enter Step 4. In this study, $Err_{P_f\_tg}$ and N_{tg} are respectively set to 0.02 and 2.

Fig. 7.4 Flowchart of the proposed SPAA.

7.3 Example and application

In this section, the probabilistic analyses are performed using the proposed SPAA approach. Two low-dimensional random variable cases with respect to 1) drained circular shaft stability against hydraulic uplift; 2) undrained circular shaft stability in non-homogeneous soils; and a high-dimensional random field problem 3) circular shaft stability considering soil spatial variability, are considered and discussed. The results are discussed and compared with the previous results to validate the effectiveness of the proposed SPAA approach.

7.3.1 Case 1: drained circular shaft stability against hydraulic uplift

The circular shaft considering the hydraulic effects as presented in Chapter 5 is firstly considered. The geometrical, soil and water levels information are referred to Section 5.2. Four input parameters are considered random variables, including the permeability anisotropy coefficient (r_k), the soil cohesion (c), friction angle (φ) and the soil-wall interface coefficient (r_i). Lognormal random variables are implemented to model input uncertain parameters, and the statistical properties can be found in Table 5.2.

32 input samples are initially generated by LHS according to the statistical information and the corresponding outputs are evaluated by the FELA. The ASO-ANN model can be constructed based on the datasets and an iterative procedure is then followed to satisfy the criteria presented in Section 7.2.3. It is noted that 5 informative sampling points are selected for each iteration and a new ASO-ANN model can be built based on the updated input-output datasets. Table 7.1 summarizes the iterative results and the ones using uniform sampling method are also provided for comparison.

It can be observed that the final ASO-ANN model is constructed based on a total of 47 sampling points: 32 points from the first iteration (30 points from LHS sampling and 2 points of the boundary points), and 15 points from the subsequent three iterations. The number of samples is far less than the results of the uniform sampling method which needs around 17 iterations and 112 simulations.

Table 7.1 Probabilistic analysis iterative results of case 1.

Iteration	P_f		Number of evaluations	Iteration	P_f		Number of evaluations
	LHS	Uniform			LHS	Uniform	
1	0.029	0.059	32	10	-	0.017	77
2	0.018	0.013	37	11	-	0.015	82
3	0.018	0.004	42	12	-	0.017	87
4	**0.018**	0.020	**47**	13	-	0.018	92
5	-	0.024	52	14	-	0.019	97
6	-	0.017	57	15	-	0.020	102
7	-	0.020	62	16	-	0.019	107
8	-	0.019	65	17		**0.019**	**112**
9	-	0.008	72				

*The bold is the converged result.

The Pearson correlation coefficients are computed and demonstrated in Fig. 7.5. The cloud graphs depict the density of every two sets of related parameters: the denser the circle, the more concentrated the data. The height of the yellow histogram and the curve above it denote the density of data for different input parameters. It can be concluded that most of the adding sensitive samples are distributed around the limit F_s (=1) and the corresponding input variables are located near specific values, for example, the enriched cohesions are generally in the range of [20 kPa, 30 kPa]. Besides, one interesting finding is that the scatter points can be regressed as a curve after the enrichment, which indicates that there is a correlation for the enriched samples (coefficient is marked above the regression line) between the two parameters corresponding to the horizontal and vertical coordinates. In addition, the correlation between the considered parameters and the basal heave safety factor of circular shafts is also given. It is seen that the parameters are significantly correlated with the model responses with a correlation coefficients being larger than 0.1 and the cohesion has a higher correlation compared with other parameters.

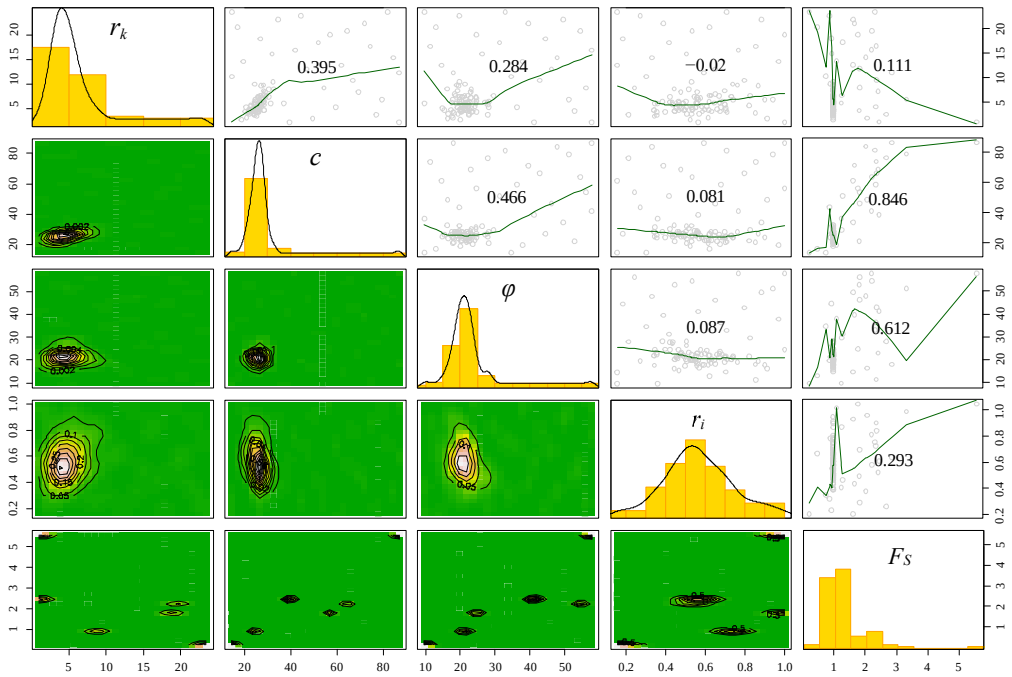

Fig. 7.5 Pearson correlation coefficients between the influential factors (r_k: permeability anisotropy coefficient, c: the soil cohesion, φ: friction angle, r_i: the soil-wall interface coefficient).

Fig. 7.6 presents the comparison between the predictions from ASO-ANN and the results computed from the numerical simulations sampled by LHS and uniform. A good consistency is observed for both train (R^2_LHS=0.9998) and test (R^2_LHS=0.9957) datasets, which can validate the effectiveness of the proposed SPAA approach. Besides, although the points sampled by uniform are relatively scattered (Fig. 7.6(b)) compared to the LHS one (Fig. 7.6a), the performance of LHS and uniform sampling methods can give reasonable results by the fact that the prediction errors are mainly distributed in the range of [10^{-4}, 10^{-2}] as presented in Fig. 7.7. In addition, it is also observed that the output sets of enrichment samples are around 1.

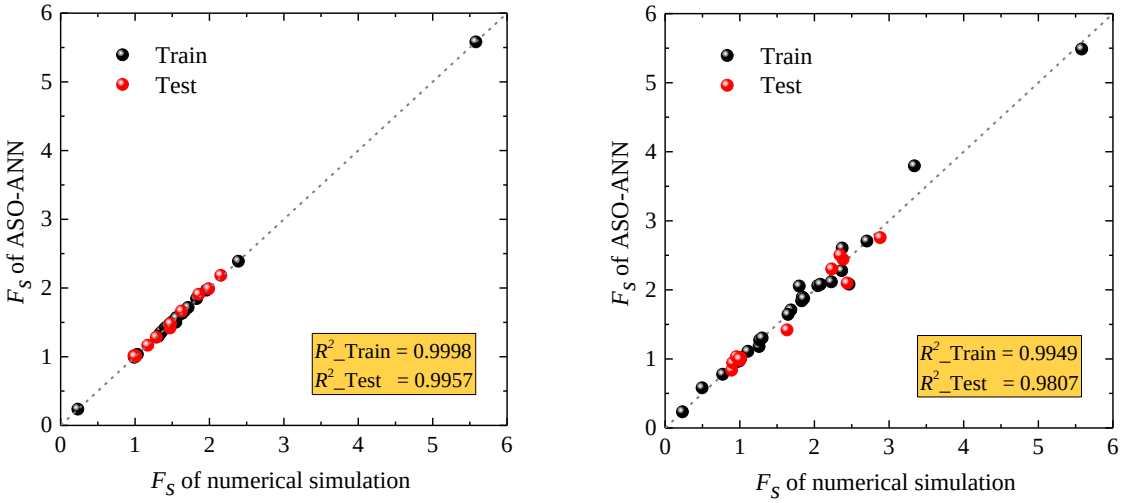

(a) LHS sampling method (b) Uniform sampling method

Fig. 7.6 Comparison of the predictions and numerical simulations for case 1.

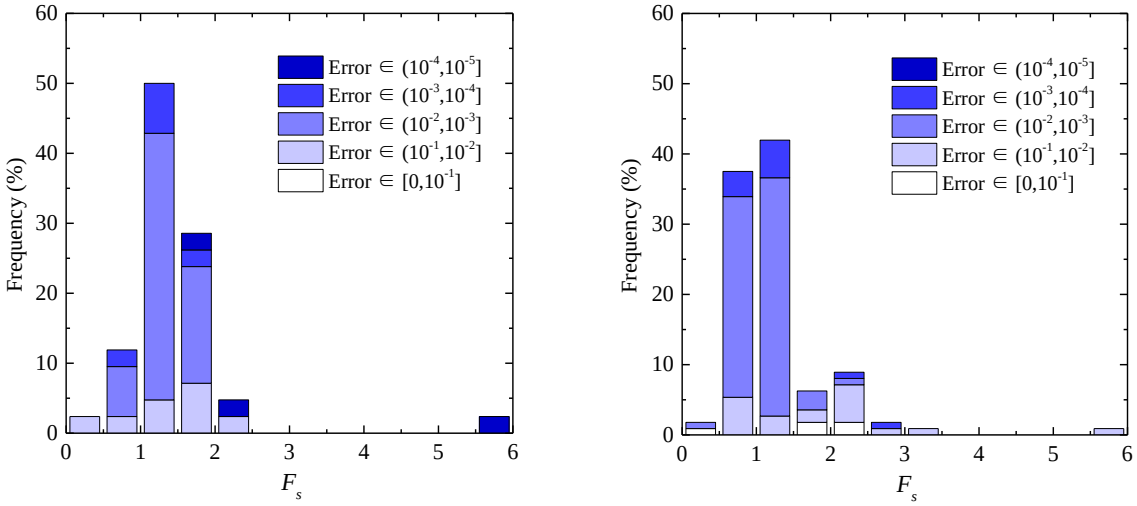

(a) LHS sampling method (b) Uniform sampling method

Fig. 7.7 Predictions error distribution of case 1.

In general, the ASO-ANN surrogate model has good generalization quality and the LHS sampling method performs better for the probabilistic analysis in terms of calculation efficiency and accuracy.

Once the surrogate model (ASO-ANN) is defined, the probabilistic methods can then be performed. The ASO-ANN metamodel-based MCS is implemented first and the results are given in Fig. 7.8. 100,000 calls to the surrogate model to make sure the failure probability accuracy (meets the target COV_{Pf} requirement of 5% and its corresponding value is 0.018. The safety factors are almost distributed asymmetrically and the F_s values are mainly in the range of [0.5, 3]. The mean value and standard deviation (Std.) are respectively 1.546 and 0.294. The sensitivity analysis based on the ASO-ANN model is then performed and the results can be found in Fig. 7.9. The first order and total effect Sobol indices shows that the cohesion is the parameter that contributes the most, which is followed by the permeability anisotropy coefficient r_k. The effects of friction angle φ and soil-wall interface coefficient r_i are relatively slight.

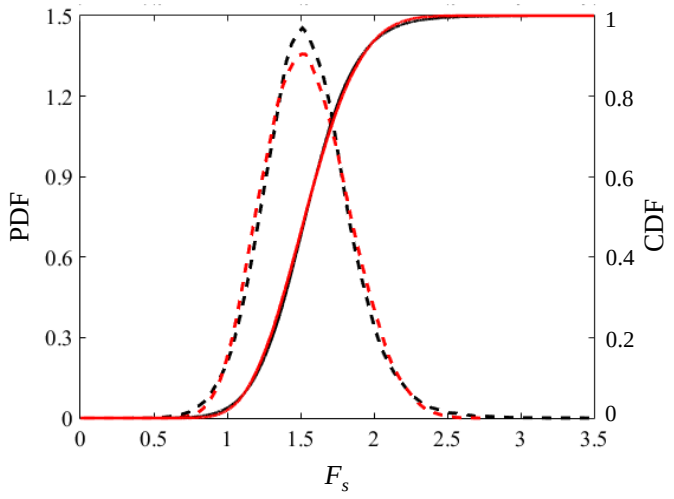

	SPAA	PCK
PDF	- - - -	- - - -
CDF	———	———
P_f	0.018	0.018
Mean	1.546	1.542
Std.	0.294	0.286

Fig. 7.8 PDF, CDF and statistical moments of F_s comparison of case 1.

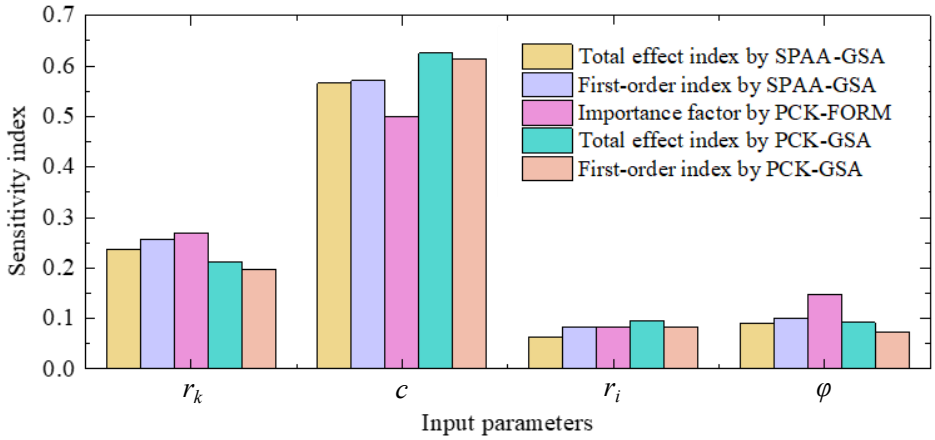

Fig. 7.9 Sensitivity indices comparison of case 1.

In order to validate the proposed SPAA method, the probabilistic results obtained by the existing SS and PCK metamodel-based probabilistic methods, are also given. The comparison can be found in Table 7.2, Fig. 7.8 and Fig. 7.9. It is evident that the P_f values of SPAA-MCS (LHS: 0.018; Uniform: 0.019) are almost identical to the P_f value of PCK-MCS (0.018). SS and PCK-FORM yield relatively larger P_f values (0.021 and 0.024 respectively), but the failure probabilities are generally similar within the same order of magnitudes. It can be observed that the SPAA based on the LHS sampling approach needs the fewest calls to the deterministic model (around 47 evaluations). The PCK metamodel and SPAA-Uniform-MCS follow (80 and 112, respectively). The SS needs around 1898 simulations, which is far larger than the surrogate model-based probabilistic analyses. The proposed LHS-based SPAA surrogate model is also further validated by the comparisons of PDF, CDF and statistical moments of safety factor with the ones of PCK. It can be found that the PDF curves of SPAA and PCK are close and the corresponding CDF curves are almost overlapping. The statistical moments (i.e., mean value

and Std.) are also identical. Besides, the sensitivity indices comparison can be found in Fig. 7.9. It is noted that the considered methods can give consistent results with the same ranking orders, which can validate the sensitivity analysis results accuracy.

Table 7.2 Failure probability comparison of case 1.

Methods	P_f	Number of numerical evaluations
SS	0.021	1898
PCK-MCS	0.018 [a]	80
PCK-FORM	0.024 [a]	80
SPAA-LHS-MCS	0.018	47
SPAA-Uniform-MCS	0.019	112

Note: [a] Based on results given by Zhang et al. (2022)

This section indicates that the LHS-based SPAA performs better than other methods in terms of the deterministic simulations number and results accuracy.

7.3.2 Case 2: undrained circular shaft stability in non-homogeneous soils

A circular shaft in non-homogeneous soils as presented in Chapter 4 is presented. Three input parameters, which include the undrained shear strength at the ground surface S_{u0}, undrained shear strength increase gradient r_g and soil-wall adhesion factor r_i, are considered random variables in the probabilistic analysis. The summary of the parameters' statistics and corresponding distributions refer to Table 4.2.

Table 7.3 presents the iterative procedure, and 10 input samples are initially generated, which is less than 30 samples presented in case 1. This is because the *COV* values of case 2 are less significant with a maximum value of 0.2, while the one of case 1 can be up to 0.5. The relatively insignificant variation leads to a narrow distribution of soil parameters, which requires fewer simulations for the SPAA model construction. It can be observed that the requirement is met in 4^{th} iteration using the LHS sampling method and a total of 27 samples are used for the SPAA model construction. Comparatively, the uniform sampling method needs around 77 simulations and starts to converge at the 12^{th} iteration and the failure probability is around 9.2e-4.

Table 7.3 Probabilistic analysis iterative results of case 2.

Iteration	P_f		Number of evaluations	Iteration	P_f		Number of evaluations
	LHS	Uniform			LHS	Uniform	
1	9.4e-4	8.4e-4	12	8	-	9.2e-4	47
2	8.6e-4	6.4e-4	17	9	-	8.6e-4	52
3	8.6e-4	8.8e-4	22	10	-	8.4e-4	57
4	**8.7e-4**	8.4e-4	**27**	11	-	8.7e-4	62
5	-	8.7e-4	32	12	-	9.1e-4	67
6	-	9.0e-4	37	13	-	9.1e-4	72
7	-	8.8e-4	42	14	-	**9.2e-4**	**77**

*The bold is the converged result.

The trained neural network is verified by comparing the predictions from SPAA with numerical evaluations. It is seen that nearly all of the sampling points are distributed in 45° line in Fig. 7.10, which can demonstrate the accuracy of the ASO-ANN model. Besides, this surrogate model can be further validated as the safety factor evaluation errors are almost within the range of $[10^{-4}, 10^{-2}]$ as depicted in Fig. 7.11.

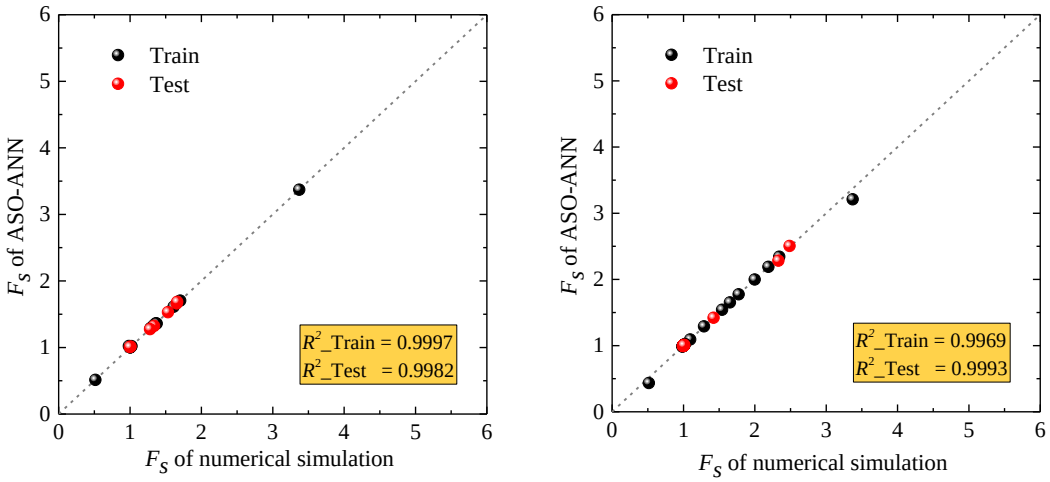

(a) LHS sampling method (b) Uniform sampling method

Fig. 7.10 Comparison of the predictions and numerical simulations for case 2.

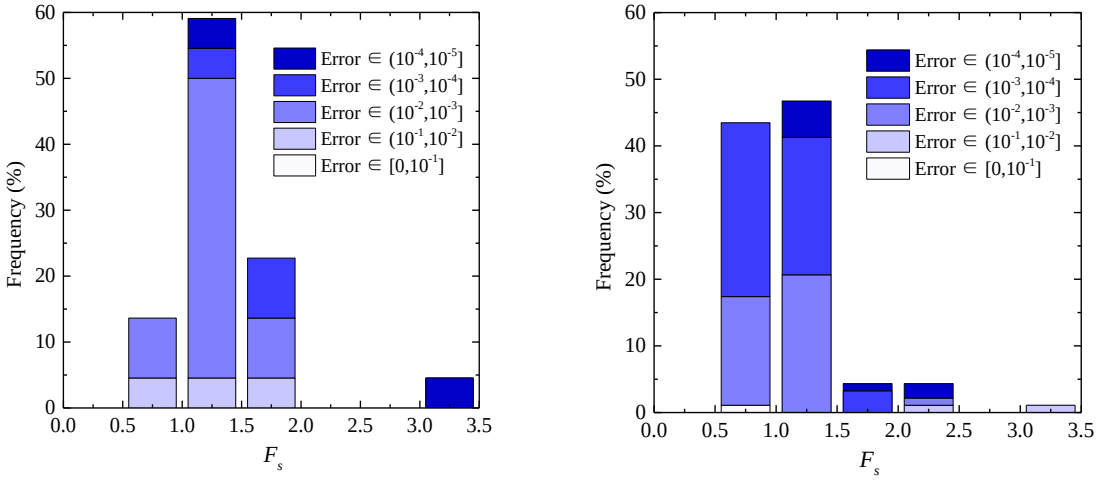

(a) LHS sampling method (b) Uniform sampling method

Fig. 7.11 Predictions error distribution of case 2.

The reliability analysis results and comparison are summarized in Fig. 7.12 and Table 7.4. The P_f values obtained by PCK-MCS and SPAA-LHS-MCS are identical (8.8e-4 and 8.78e-4, respectively) and the PDF/CDF distributions (based on 1000,000 simulations) are almost coinciding. Relatively high P_f values are derived by the SS and PCK-FORM with a difference being about 14%, which is similar to Case 1. SPAA-LHS still needs the fewest deterministic evaluations, which can validate the ASO-ANN model efficiency.

Table 7.4 Failure probability comparison of case 2.

Methods	P_f	Number of numerical evaluations
SS	1.1e-3	2763
PCK-MCS	8.8e-4	43
PCK-FORM	1.0e-3	43
SPAA-LHS-MCS	8.7e-4	27
SPAA-UNI-MCS	9.2e-4	77

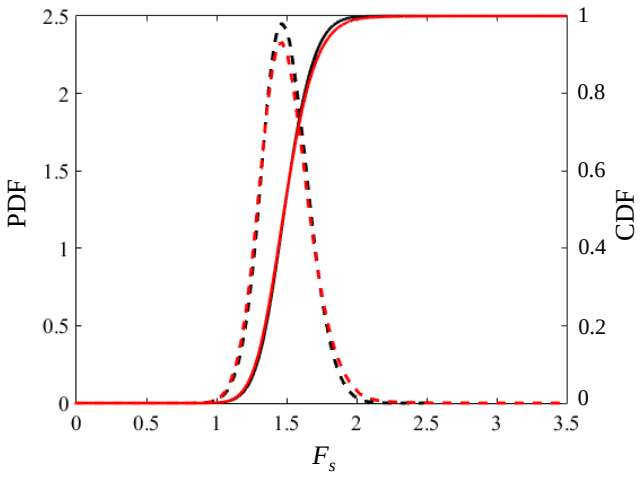

	SPAA	PCK
PDF	- - - -	- - - -
CDF	———	———
P_f	8.7e-4	8.8e-4
Mean	1.493	1.497
Std.	0.165	0.183

Fig. 7.12 PDF, CDF and statistical moments of F_s comparison of case 2.

Fig. 7.13 depicts the sensitivity analysis results for the undrained circular shaft. Although there are differences in the sensitivity index magnitudes, they can give a consistent ranking order. The strength gradient has the highest sensitivity index with a value of 0.4 in this case. The soil-wall adhesion factor r_i sensitivity index is slightly smaller. The undrained shear strength at the ground surface S_{u0} has the least effect on the model response. This discussion indicates the importance of the soil non-homogeneity consideration in the undrained circular shaft, which supports the evidence from previous observations (Goh et al., 2019b). Besides, the soil-wall interface uncertainty has a significant influence on the model response and the values determination should be done with attention.

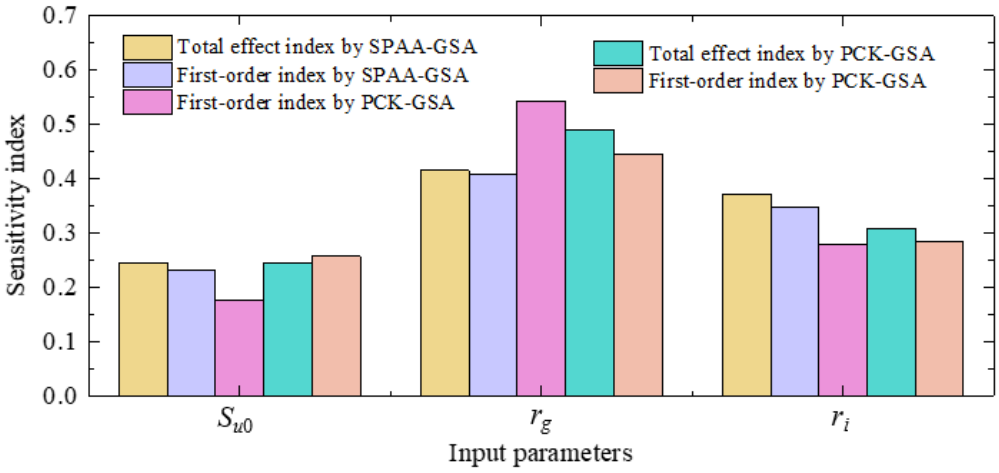

Fig. 7.13 Sensitivity indices comparison of case 2.

7.3.3 Case 3: circular shaft stability considering soil spatial variability

A random field case is considered to discuss the SPAA performance on the high-dimensional problems and the same deterministic model as in case 1 is applied. According to the results presented in Fig. 7.9, the cohesion contributes the most among the four random parameters, and the sensitivity index can be up to 0.6. It is more reasonable to consider the inherent spatial variability of soil cohesion. The other three (i.e., the permeability anisotropy coefficient, friction angle and soil-wall interface coefficient) are modelled using random variables. The K-L expansion is used for the random field generation as presented in Section 6.2.1 and the corresponding autocorrelation lengths are respectively l_h=40 m and l_v=3 m (Luo et al., 2018a). It is noted that 54 variables are necessary for the ratio of expected energy R_e being larger than 0.99 (Marelli and Sudret, 2014). A total of 57 input variables will be considered in this probabilistic analysis, which includes 54 standard normal variables about the cohesion and 3 random variables (r_k, r_i and φ). A random finite element limit analysis is used and the soil properties of each point in the FELA model can be mapped from MATLAB using batch commands. One realization of the cohesion random field is depicted in Fig. 7.14.

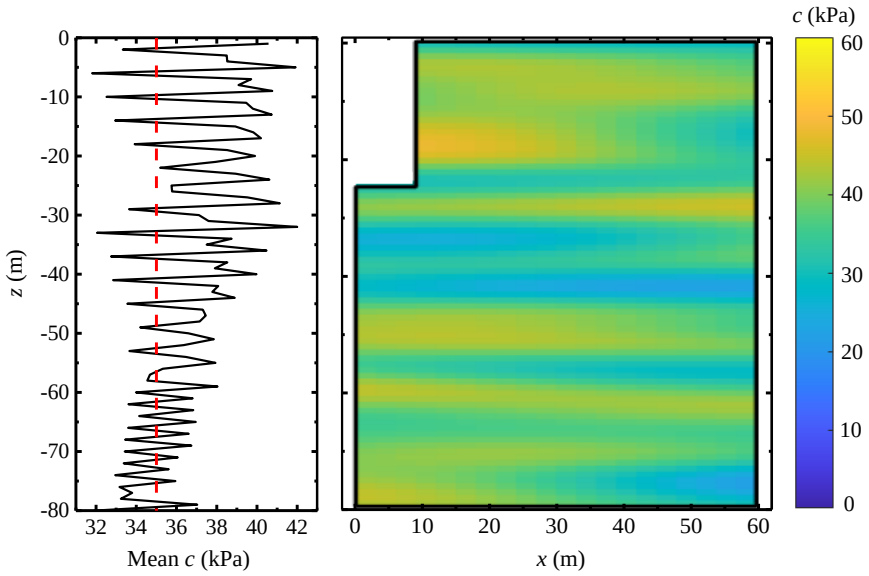

Fig. 7.14 One realization of the random field for cohesion.

The LHS sampling behaves better than uniform sampling as presented in cases 1 and 2. Therefore, only the LHS sampling approach is considered in this case. The iterative procedure can be found in Table 7.5. Due to the high-dimensional random variables, the initial samples are set as 570. The dataset is split into 70% training and 30% testing. The ASO-ANN model can

then be developed to determine the F_S. It can be noticed that the failure probability converges when 870 samples are enriched and the failure probability is around 8.2e-3.

Table 7.5 Probabilistic analysis iterative results of case 3.

Iteration	P_f	Number of evaluations	Iteration	P_f	Number of evaluations
1	8.4e-3	570	5	8.2e-3	770
2	1.1e-2	620	6	8.2e-3	820
3	1.0e-2	670	7	**8.2e-3**	**870**
4	9.2e-3	720			

* The bold is the converged result.

A good correlation is observed between the predictions from ASO-ANN and the numerical evaluations in Fig. 7.15(a). It is seen that the Train and Test sets are distributed in the diagonal line, which can validate the effectiveness of the ASO-ANN model. The prediction tolerances are also primarily allocated in the region of [10^{-4}, 10^{-2}], as illustrated in Fig. 7.15(b).

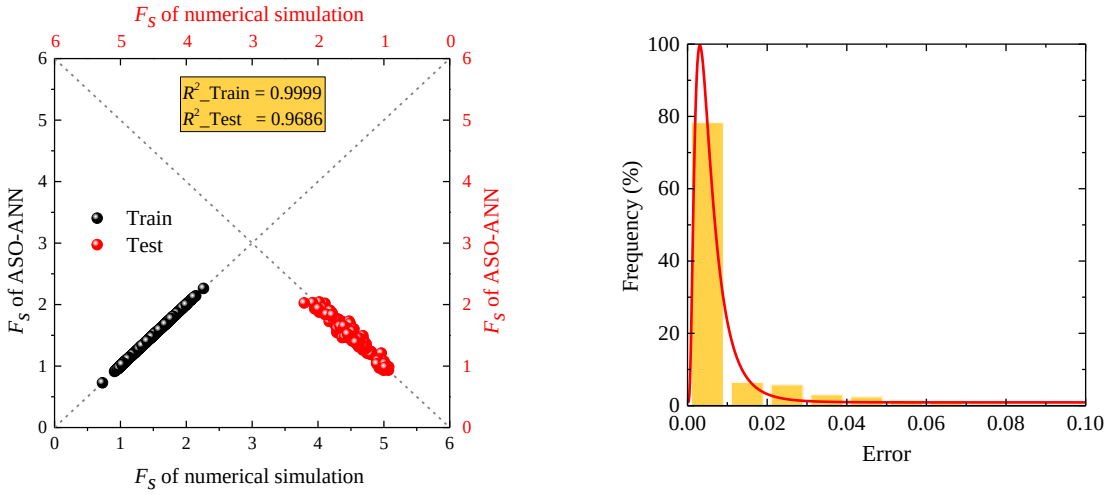

(a) Comparison of the predictions and numerical simulations

(b) Prediction error distribution

Fig. 7.15 Validation of the SPAA model for high-dimensional case.

The comparison with the SPCE-based MCS is presented in Table 7.6 and Fig. 7.16. It is seen that the failure probability, PDF, CDF and the statistical moments are similar to the results determined by the SPCE-based MCS results, which can validate the proposed SPAA effectiveness on high-dimensional problems. However, the SPCE model construction requires around 1945 simulations, while for the SPAA, less half of the simulations number (870) is

necessary. It proves that the SPAA can reduce significantly the evaluation number and improves computational efficiency.

Table 7.6 Failure probability comparison of case 3.

Method	P_f	Number of numerical evaluations
SPCE-MCS	8.7e-3	1945
SPAA-MCS	8.2e-3	870

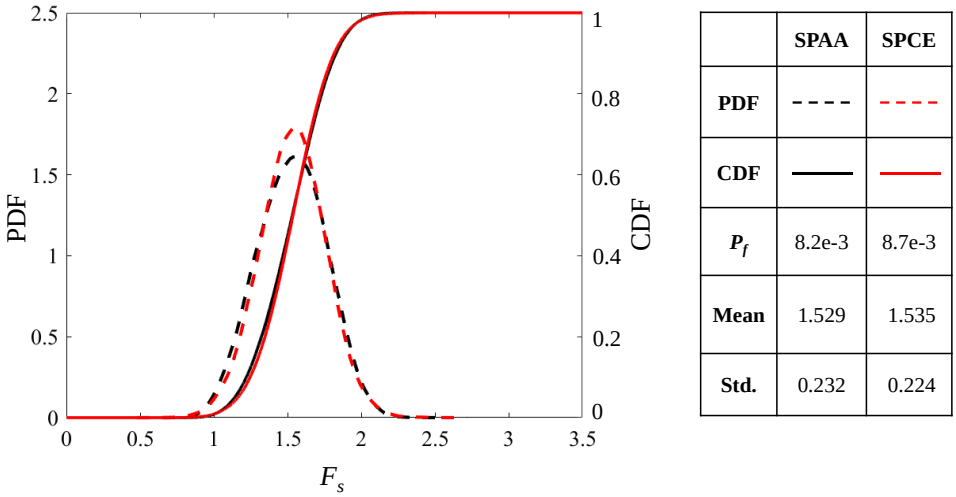

Fig. 7.16 PDF, CDF and statistical moments of F_s comparison of case 3.

7.4 Discussion

This section aims to give some discussions about the SPAA performance, and the importance of spatial variability consideration.

7.4.1 Accuracy and efficiency survey

The ASO-ANN model with the input -1st hidden -2nd hidden -output MLP neuron structure with the maximum determination coefficients R^2 is identified as the optimal model (Bharati et al., 2022). In this study, after being tuned, the ASO-ANN model including two hidden layers and 10 initial population size of ASO proved to be the most effective for the ASO-ANN model construction. The optimal model parameters in 3 cases are listed in Table 7.7. It is seen that the neurons of the 2nd hidden layer are tuned to be equal to the number of variables, while the neurons of the 1st hidden layer are not only determined by the amount of input features, but are also greatly influenced by the sample size. Usually, the neurons of the first hidden layer are

between the amount of input variables and three times of it. It can easily be concluded that the larger the sample size is, the larger the number of neurons in the hidden layer.

Table 7.7 Parameters of ASO-ANN model.

Case	Sampling method	Parameters of model		
		Architecture of ANN layers (input-neurons in 1st hidden layer-neurons in 2nd hidden layer-output)	Sample size	Testing R^2
1	LHS	4-6-4-1	47	0.9957
	Uniform	4-10-4-1	112	0.9807
2	LHS	3-5-3-1	27	0.9982
	Uniform	3-7-3-1	77	0.9993
3	LHS	57-114-57-1	870	0.9686

The failure probabilities and required runs for the ASO-ANN model construction of 3 cases are summarized in Fig. 7.17. It can be observed that the calculated failure probabilities are consistent, whereas the SPAA-LHS requires fewer simulations for the results determination compared to the SPAA-Uniform, PCK and SPCE-based analysis, particularly for the high dimensional stochastic problems, and around 1000 model evaluations are reduced. It indicates that the SPAA based on the LHS sampling technique, introduced in this study, could be a good choice for the shaft probabilistic stability analysis since it is efficient and permits to provide a variety of interesting results.

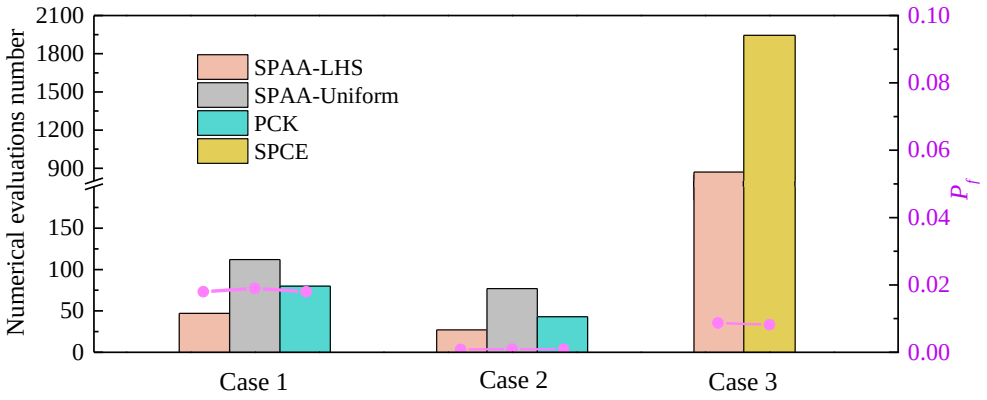

Fig. 7.17 Comparison of deterministic simulations number and P_f of 3 cases.

7.4.2 Initial samples determination

The initial sampling amount is varied for different problems, and it depends on the random variables number and the corresponding *COV*. Case 1 has a maximum *COV* value of 0.5 and 4 random variables, 32 samples are generated in the first iteration. Whereas for the second case, the random variables number is 3 and the *COV* value is relatively small (0.2) and 12 initial samples are considered. For the random field case, 57 random variables are observed, and 570 samples are provided for the initial sample generation.

In general, the initial generated sample number is set to be 3 to 10 times the number of random variable quantities. The larger the *COV*, the larger the recommended initial sample size, and conversely, the smaller the *COV*, the smaller the sample size. The presented initial generated sample number can be regarded as a reference for future discussion using SPAA.

7.5 Conclusion

This chapter proposed a sample-wised probabilistic analysis method SPAA for the excavation stability evaluation in a probabilistic framework. The Latin Hypercube Sampling (LHS) is employed to provide the initial sampling points. The proposed hybrid atom search optimization (ASO) based on an artificial neural network (ANN) approach is then used to construct a fast-to-evaluate surrogate model, which can replace the time-consuming deterministic numerical simulations. Probabilistic methods are employed to provide probabilistic results.

To validate the effectiveness and feasibility of the proposed SPAA approach, 3 circular shaft problems, which include two random variables and one random field cases, are analysed and the results are compared with the existing methods, which include the Subset Simulation, the Polynomial Chaos Kriging based MCS and FORM, and Sparse Polynomial Chaos Expansion based MCS. The comparison demonstrates that the SPAA outperforms other existing methods due to its adaptative capacity of providing satisfactory solutions and excellent powers of improving computational efficiency. It is noted that the ASO-ANN model tuning may also increase the computational effort. Therefore, for the random field case which can reduce around 1000 model evaluations or the deterministic numerical simulation is very time-consuming, the proposed SPAA is more essential. In addition, the samples generation method is also discussed and the results show that the samples generated by the LHS sampling method are more representative and more efficient compared to the uniform sampling method.

Chapter 8

General conclusions, recommendations and perspectives

Contents

8.1 Conclusions and recommendations 204

8.2 Limitations and perspectives 208

8.1 Conclusions and recommendations

This thesis aims to discuss the stability of rectangular- and circular-shaped supported excavations, which are commonly encountered in practical engineering. Probabilistic analyses are also implemented to account for the soil uncertainties and quantify their effects on the excavation stability. Four kinds of excavations cases, which include rectangular- and circular-shaped excavations under undrained and drained conditions, are respectively discussed in deterministic and probabilistic frameworks from Chapter 2 to Chapter 5. In order to further consider the soil spatial variability on the excavation stability, Chapter 6 introduces soil random fields into probabilistic analyses. Chapter 7 proposes a sample-wised probabilistic analysis approach based on an artificial neural network to further improve the computational efficiency.

An improved limit analysis (ILA) mechanism for the rectangular-shaped excavations under undrained conditions is first proposed in Chapter 2. It is found that the proposed ILA can provide an accurate basal heave safety factor in a shorter time (less than one second) compared to the numerical simulations and has a wider applicability compared to the other existing analytical methods. Benefiting from the proposed ILA method efficiency, a comparative study of the probabilistic methods is conducted. It is shown that the proposed probabilistic procedure Polynomial Chaos Kriging-based probabilistic analysis (PCK-PA) can provide a variety of probabilistic results in an efficient way. The excavation stability is increased with the decrease of the excavation depth, width and the increase of embedment depth and soil-wall adhesion factor. Besides, it is found that the soil-wall interface strength significantly influences the failure probability estimation and its influence is important for the larger values of undrained shear strength and embedment depth.

A real case, the Fort d'Issy-Vanves-Clamart excavation (FIVC) with a depth of 32 m is introduced in Chapter 3 to investigate the deterministic and probabilistic stability of deep excavations. The wall deflections and ground surface settlements are evaluated using the finite element method. The distributions of the wall deflections and ground surface settlements are wider with the increase of the soil parameters coefficient of variation (*COV*). However, the maximum horizontal wall deflection δ_{hm} mainly occurs from 24 m to 26 m below the ground surface, and the maximum ground surface settlement δ_{vm} is mainly distributed at the range of [10 m, 12 m] behind the retaining wall. Besides, the δ_{vm}/δ_{hm} ratio is generally in the range of [0.5, 1] and for cases with larger δ_{hm}, a larger δ_{vm}/δ_{hm} ratio should be used. The sensitivity analysis indicates that the friction angle at the excavation bottom layer contributes the most to

the model response variation. In addition, the probabilistic serviceability assessment shows that the serviceability failure probability is significantly affected by the wall deflection limit and the soil coefficient of variation. When the limit value is larger than the deterministic wall deflection, the failure probability P_f increases with the *COV*, conversely, the P_f decreases as the *COV* increases.

Circular shafts considering the soil-wall interface in undrained and non-homogeneous clayey soils are presented in Chapter 4. The coupling of the finite element limit analysis and proposed procedure PCK-PA makes the circular shaft probabilistic analysis possible. The failure probability increases with the coefficient of variation increase and the decrease of the soil-wall interaction coefficient r_i, undrained shear strength at the ground surface S_{u0}, soil non-homogeneity coefficient k and wall embedment depth D. The soil-wall interaction r_i affects considerably the shaft failure probabilities, and its influence is more significant with the increase of the undrained shear strength and wall embedment depth. Besides, the r_i influences the model response greatly when its value is in the range from 0.3 to 0.7. The sensitivity analysis indicates the importance of the soil-wall interaction, soil non-homogeneity and uncertainties consideration.

The stability of circular shafts subjected to hydraulic uplifts is presented in Chapter 5. The effects of the soil-wall interaction, the soil tensile strength and the permeability anisotropy coefficient are discussed. The results show that the safety factor increases with the increase of the soil-wall interface and soil tensile strength, and with the decrease of permeability anisotropy coefficient. It is shown that the permeability coefficient anisotropy increase can lead to more horizontally distributed flow vectors. Its influence is more pronounced when it varies from 1 to 10. Concerning the soil-wall interface effects, the corresponding strength affects significantly the shaft stability when the soil-wall interaction coefficient is in the range of [0.2, 0.8] and the shear failure occurs along the soil-wall interface when the soil permeability is less anisotropic. The tensile strength can also make a significant influence on the circular shaft stability, and the difference can be up to 100%. Besides, the failure probability is increased as the coefficient of variation when the permeability anisotropy coefficient is small (e.g., r_k<10), whereas it is decreased for the case with a large permeability anisotropy coefficient.

Then, an extension of Chapter 3 is presented in Chapter 6 by considering the soil spatial variability. A bootstrap-sparse polynomial chaos expansion is implemented to perform a probabilistic analysis of supported excavations. Three key parameters determined from

sensitivity analysis of Chapter 3, which include the friction angles of the Meudon Marls and Plastic Clay layers, and the initial earth pressure coefficient at rest of the Plastic Clay layer, are modelled using random fields. It is shown that the autocorrelation lengths influence significantly the excavation stability. With the decrease of the autocorrelation lengths, the distributions of the wall deflection contours and the locations where the maximum wall deflection occurs are narrower, whereas the probability of serviceability failure is not monotonously varied with the autocorrelation lengths and is strongly related to the limiting values. The failure probability P_f decreases with the autocorrelation length value when the limiting wall deflection is larger than the deterministic wall deflection. Conversely, the failure probability is increased. Besides, the probabilistic results show that ignoring the soil spatial variability can provide a biased estimation of the excavation stability, particularly the spatial variability in the vertical direction.

At the end of the thesis, a sample-wised probabilistic analysis method SPAA is proposed. The hybrid atom search optimization based artificial neural network approach is used to construct a fast-to-evaluate surrogate model. The initial sampling points are generated by the latin hypercube sampling method and an active learning method is designed to find the informative training samples. The probabilistic methods are then employed to provide probabilistic results. The proposed method is validated by 3 circular shaft problems, which include two random variables and one random field cases. It is found that the SPAA shows a great power of improving computational efficiency. Particularly for the random field case with around 1000 model evaluations being reduced.

In conclusion, this thesis presents several deterministic models of assessing the supported excavations (with rectangular and circular shapes) stability and the surrogate-model based probabilistic methods for computing failure probabilities. A sensitivity analysis is also implemented to determine the input variables information.

Based on the present work, some suggestions can be given to the engineers/researchers, which can improve the understanding of the supported excavations in deterministic and probabilistic frameworks, which include:

- Probabilistic analyses of the supported excavations stability are important, particularly for cases with significant soil uncertainties. They can provide more useful information that can help designers to make more reasonable decisions in practical engineering. One major concern of the probabilistic analyses is the heavy computational effort. In order to improve their computational efficiency, the development of analytical methods is a good idea since

they can significantly decrease the computational time within a reasonable result. However, some cases with complex geometrical and geological conditions are difficult to be analysed by analytical methods. The development of probabilistic methods is necessary. Active-learning methods based on the surrogate models (such as the sparse polynomial chaos expansion, polynomial chaos kriging, and the artificial intelligence method) are powerful for probabilistic analysis because they can significantly decrease the required deterministic simulations. A variety of interesting results can then be provided, such as the failure probability, reliability index, design point and sensitivity index.

- A sensitivity analysis is recommended in practical engineering since it can provide a quantitative measure of the importance of input parameters, allowing for a better understanding of how the model output varies with the input parameters changes. For the input parameters that have a great influence on the model output variability, more attention should be paid to the data collection and variability modelling. Conversely, the insignificant parameters can be considered as deterministic, which can simplify the numerical models and reduce the computational effort. Besides, when the soil spatial variability is considered, the sensitivity analysis can help the parameters selection that need to be modelled by the random field approach.
- The failure probability is significantly influenced by the limiting values (wall deflection, ground surface settlement or basal heave safety factor). The criteria are often given for different areas. However, the excavation stability is also influenced by the soil properties, wall stiffness, excavation geometry, groundwater conditions, etc. A thorough understanding of these factors is essential to ensure a safe and effective design, and construction of excavations.
- Considering the spatial variability or different uncertainty properties of soil can make a significant influence on the failure probability, which may lead to different designs of the excavations. It is thus important to measure and collect more soil information that is used for the soil variability modelling.
- The soil-wall interaction is an essential consideration in the design and analysis of supported excavations and its strength is often considered to be proportional to the adjacent soil strength. It significantly influences the excavation stability, particularly for cases with larger embedment depths of wall or soil shear strength. Besides, the interface effects are more significant when the reduction factor value is in the range of [0.2, 0.8] for circular shafts. Some codes or researches give some information of the reduction factor, for instance, a value of 2/3 is suggested by the Eurocode 7 (Bond et al., 2013), 0.5 and 0.67 are respectively

set for clays and sand materials (Hsi and Yu, 2005). However, the value may be affected by the soil properties, the retaining system type and stiffness, the construction methods, or the quality of the workmanship. In practice, it should be determined with attention by field experiments, such as direct shear tests or pullout tests (Kuntz et al., 1994).

- Considering the hydraulic effects, the anisotropy of the permeability coefficient should also be considered. The excavation stability is significantly influenced particularly when the anisotropy coefficient is in the range of [1, 10]. The determination should be done with attention.

8.2 Limitations and perspectives

This section aims to discuss the limitations of the present work and the corresponding perspectives for future researches considering supported excavations stability.

System failure consideration. As a systematic soil-structure interaction problem, the structural performance is also important for the stability assessment of the supported excavations. This thesis only considers the geotechnical failure modes and the system failure modes which include the geotechnical and structural failures should be examined to better understand the excavation stability.

Analytical methods developments. This thesis improves the failure mechanism of the rectangular-shaped supported excavation under undrained conditions and it can decrease the computational time from 40 s (numerical simulations) to 0.15 s (improved analytical method). However, the wall stiffness effect is not considered, which will be discussed in the future. Besides, the analytical method for the circular shaft basal heave safety factor determination is also of interest to develop since one numerical evaluation is around 180 s.

Back analysis using the Bayesian theory. The soil variability parameters of FIVC excavation are assumed or referenced from existing studies in this thesis. However, the corresponding parameters (such as the coefficient of variation, the autocorrelation lengths) could be updated using complementary data using the Bayesian theory and more reasonable probabilistic stability can be assessed.

Three-dimensional consideration. In practice, the supported excavations are three-dimensional and the soil properties vary in three dimensions. It should be interesting to

investigate the three-dimensional soil spatial variability effects on the supported excavations stability.

Bibliography

Addenbrooke, T.I., Potts, D.M., Dabee, B., 2000. Displacement flexibility number for multipropped retaining wall design. Journal of geotechnical and geoenvironmental engineering 126, 718–726.

Alder, B.J., Wainwright, T.E., 1959. Studies in Molecular Dynamics. I. General Method. The Journal of Chemical Physics 31, 459–466.

Álvarez, M.A., Rosasco, L., Lawrence, N.D., 2011. Kernels for vector-valued functions: A review. Foundations and Trends in Machine Learning 4, 195–266. https://doi.org/10.1561/2200000036

Arai, Y., Kusakabe, O., Murata, O., Konishi, S., 2008. A numerical study on ground displacement and stress during and after the installation of deep circular diaphragm walls and soil excavation 35, 791–807. https://doi.org/10.1016/j.compgeo.2007.11.001

Au, S.K., Beck, J.L., 2001. Estimation of small failure probabilities in high dimensions by subset simulation. Probabilistic Engineering Mechanics 16, 263–277. https://doi.org/10.1016/S0266-8920(01)00019-4

Aye, T.T., Tong, M.S.Y., Yi, K.H., Arunasoruban, E., 2014. Design and Construction of Large Diameter Circular Shafts. Underground Singapore.

Baroth, J., Malecot, Y., 2010. Computers and Geotechnics Probabilistic analysis of the inverse analysis of an excavation problem. Computers and Geotechnics 37, 391–398. https://doi.org/10.1016/j.compgeo.2009.12.006

Bharati, A.K., Ray, A., Khandelwal, M., Rai, R., Jaiswal, A., 2022. Stability evaluation of dump slope using artificial neural network and multiple regression. Engineering with Computers 38, 1835–1843. https://doi.org/10.1007/s00366-021-01358-y

Bjerrum, L., Eide, O., 1956. Stability of strutted excavations in clay. Geotechnique 6, 32–47. https://doi.org/10.1680/geot.1956.6.1.32

Blatman, G., Sudret, B., 2011. Adaptive sparse polynomial chaos expansion based on least angle regression. Journal of Computational Physics 230, 2345–2367. https://doi.org/10.1016/j.jcp.2010.12.021

Bond, A.J., Schuppener, B., Scarpelli, G., Orr, T.L., Dimova, S., Nikolova, B., Pinto, A. V., 2013. Eurocode 7: geotechnical design worked examples, BSI Standards Limited. https://doi.org/10.2788/3398

Boulon, M., 1989. Basic features of soil structure interface behaviour. Computers and Geotechnics 7, 115–131.

Bourinet, J., Riche, R. Le, Lemaire, M., 2018. Reliability analysis and optimal design under uncertainty - Focus on adaptive surrogate-based approaches.

Brault, J., Konrad, J., 2007. Experimental device and testing procedures to determine the hydraulic conductivity anisotropy of compacted tills 127–133.

Breitung, K., 1984. Asymptotic approximations for multinormal integrals. Journal of Engineering Mechanics 110, 357–366.

Burgess, J., Fenton, G.A., Griffiths, D. V, 2019. Probabilistic seismic slope stability analysis and design. Canadian Geotechnical Journal 56, 1979–1998.

Cai, F., Ugai, K., Hagiwara, T., 2002. Base Stability of Circular Excavations in Soft Clay. Journal of Geotechnical and Geoenvironmental Engineering 128, 702–706. https://doi.org/10.1061/(asce)1090-0241(2002)128:8(702)

Cai, L., Zhou, J., Ying, H.W., Gong, X.N., 2018. Stability against basal heave of excavation in anisotropic soft clay. Yantu Gongcheng Xuebao/Chinese Journal of Geotechnical Engineering 40, 1968–1976. https://doi.org/10.11779/CJGE201811002

Canadian, G., 2006. Canadian foundation engineering manual. Canadian Geotechnical Society, Richmond.

Celestino, T.B., Rocha, H.C., Gonçalves, F.L., 2009. Geotechnical aspects of shaft design and construction in São Paulo city, in: Roceedings of the ITA-AITES World Tunnel Congress – Safe Tunnelling for the City and Environment.

Chang, M., 2000. Basal Stability Analysis of Braced Cuts in Clay. Journal of Geotechnical and Geoenvironmental Engineering 126, 276–279. https://doi.org/10.1061/(asce)1090-0241(2000)126:3(276)

Chapuis, R.P., 2002. The 2000 R.M. Hardy lecture: Full-scale hydraulic performance of soil-bentonite and compacted clay liners. Canadian Geotechnical Journal 39, 417–439. https://doi.org/10.1139/t01-092

Chapuis, R.P., Aubertin, M., 2003. On the use of the Kozeny-Carman equation to predict the hydraulic conductivity of soils. Canadian Geotechnical Journal 40, 616–628. https://doi.org/10.1139/t03-013

Chehadeh, A., Turan, A., Abed, F., 2015. Numerical investigation of spatial aspects of soil structure interaction for secant pile wall circular shafts. Computers and Geotechnics 69, 452–461. https://doi.org/10.1016/j.compgeo.2015.06.014

Chen, F., Miao, G., Lai, F., 2020. Base Instability Triggered by Hydraulic Uplift of Pit-in-Pit Braced Excavations in Soft Clay Overlying a Confined Aquifer. KSCE Journal of Civil Engineering 24, 1717–1730. https://doi.org/10.1007/s12205-020-1102-2

Chen, S., Cui, J., Liang, F., 2022. Centrifuge Model Investigation of Interaction between Successively Constructed Foundation Pits. Applied Sciences (Switzerland) 12. https://doi.org/10.3390/app12167975

Cheng, H., Chen, J., Chen, R., Huang, J., 2019. Three-dimensional analysis of tunnel face stability in spatially variable soils. Computers and Geotechnics 111, 76–88.

Cheng, M., Wu, Y., 2009. Prediction of Diaphragm Wall Deflection in Deep Excavations Using Evolutionary Support Vector Machine Inference Model (ESIM), in: 26th Int. Symp. on Automation and Robotics in Construction (ISARC 2009). pp. 176–182.

Cho, S.E., 2012. Probabilistic analysis of seepage that considers the spatial variability of permeability for an embankment on soil foundation. Engineering Geology 133–134, 30–39. https://doi.org/10.1016/j.enggeo.2012.02.013

Cho, S.E., 2010. Probabilistic assessment of slope stability that considers the spatial variability of soil properties. Journal of Geotechnical and Geoenvironmental Engineering 136, 975–984. https://doi.org/10.1061/(ASCE)GT.1943-5606.0000309

Cho, S.E., 2009. Probabilistic stability analyses of slopes using the ANN-based response surface. Computers and Geotechnics 36, 787–797.

Chowdhury, S.S., 2017. Reliability Analysis of Excavation Induced Basal Heave. Geotechnical and Geological Engineering 35, 2705–2714. https://doi.org/10.1007/s10706-017-0272-2

Chua, C.G., Goh, A.T.C., 2005. Estimating wall deflections in deep excavations using Bayesian neural networks 20, 400–409. https://doi.org/10.1016/j.tust.2005.02.001

Clough, G.W., O'Rourke, T.D., 1990. Construction induced movements of in-situ walls, in: In Proc. Design and Performance of Earth Retaining Structure, ASCE Special Conference. pp. 439–470.

Clough, G.W., Smith, E.M., Sweeney, B.P., 1989. Movement control of excavation support systems by iterative design, in: ASCE Conference on Current Principles and Practices on Foundation and Engineering. pp. 869–884.

Cui, J., Nelson, J.D., 2019. Underground transport: An overview. Tunnelling and Underground Space Technology 87, 122–126. https://doi.org/10.1016/j.tust.2019.01.003

Daliri, F., 2011. A Review of theoretical and experimental methods to measure coefficient of permeability of unsaturated soils. Electronic Journal of Geotechnical Engineering 16 U, 1665–1677.

Dang, H.P., Lin, H.D., Juang, C.H., 2014. Analyses of braced excavation considering parameter uncertainties using a finite element code. Journal of the Chinese Institute of Engineers 37, 141–151. https://doi.org/10.1080/02533839.2013.781790

Day, R.A., Potts, D.M., 1998. The effect of interface properties on retaining wall behaviour. International Journal for Numerical and Analytical Methods in Geomechanics 22, 1021–1033. https://doi.org/10.1002/(sici)1096-9853(199812)22:12<1021::aid-nag953>3.3.co;2-d

Desai, C.S., Zaman, M.M., Lightner, J.G., Siriwardane, H., 1984. Thin-layer element for interfaces and joints. International Journal for Numerical and Analytical Methods in Geomechanics 8, 19–43.

Dias, T.G.S., Farias, M.M., Assis, A.P., 2015. Large diameter shafts for underground infrastructure. Tunnelling and Underground Space Technology 45, 181–189. https://doi.org/10.1016/j.tust.2014.09.010

Ding, C., Li, Z., Wu, X., Wu, K., 2014. Analysis on inducing factors to inrushing plastic deformation failure of foundation pit with confined water. In Tunneling and Underground Construction 491–501.

Dong, Y., 2014. Advanced finite element analysis of deep excavation case histories. UNIVERSITY OF OXFORD.

Dong, Y.P., Burd, H.J., Houlsby, G.T., 2016. Finite-element analysis of a deep excavation case history. Geotechnique 66, 1–15. https://doi.org/10.1680/jgeot.14.P.234

Echard, B., Gayton, N., Lemaire, M., 2011. AK-MCS: An active learning reliability method combining Kriging and Monte Carlo Simulation. Structural Safety 33, 145–154. https://doi.org/10.1016/j.strusafe.2011.01.002

Faheem, H., Cai, F., Ugai, K., Hagiwara, T., 2003. Two-dimensional base stability of excavations in soft soils using FEM. Computers and Geotechnics 30, 141–163. https://doi.org/10.1016/S0266-352X(02)00061-7

Faustin, N.E., Elshafie, M.Z.E.B., Mair, R.J., 2018. Case studies of circular shaft construction in London. Proceedings of the Institution of Civil Engineers: Geotechnical Engineering 171, 391–404. https://doi.org/10.1680/jgeen.17.00166

Fell, R., 2005. Geotechnical engineering of dams, 2nd ed. CRC Press, London.

Fenton, G.A., Griffiths, D. V., 2010. Reliability-Based Geotechnical Engineering 41095, 14–52. https://doi.org/10.1061/41095(365)2

Finno, R.J., Atmatzidis, D.K., Perkins, S.B., 1989. Observed performance of a deep excavation in clay. Journal of geotechnical engineering 115, 1045–1064.

Fredlund, D.G., Xing, A., Huang, S., 1994. Predicting the permeability function for unsaturated soils using the soil-water characteristic curve. Canadian Geotechnical Journal 31, 533–546. https://doi.org/10.1016/0148-9062(95)96995-n

Furlani, G., Guiducci, G., Lucarelli, A. Carettucci, A., Sorge, R., 2011. 3-D finite element modeling and construction aspects for vertical shafts in Metro C Rome, in: International Symposium on Geotechnical Aspects of Underground Construction in Soft Ground. pp. 685–692.

Gharehchopogh, F.S., Maleki, I., Dizaji, Z.A., 2022. Chaotic vortex search algorithm: metaheuristic algorithm for feature selection, Evolutionary Intelligence. Springer Berlin Heidelberg. https://doi.org/10.1007/s12065-021-00590-1

Gholampour, A., Johari, A., 2019. Reliability-based analysis of braced excavation in unsaturated soils considering conditional spatial variability. Computers and Geotechnics 115, 103163. https://doi.org/10.1016/j.compgeo.2019.103163

Ghosh, K.K., Guha, R., Ghosh, S., Bera, S.K., Sarkar, R., 2020. Atom Search Optimization with Simulated Annealing-a Hybrid Metaheuristic Approach for Feature Selection. arXiv preprint 2005.08642.

Goh, A.T.C., 2017a. Deterministic and reliability assessment of basal heave stability for braced excavations with jet grout base slab. Engineering Geology 218, 63–69. https://doi.org/10.1016/j.enggeo.2016.12.017

Goh, A.T.C., 2017b. Basal heave stability of supported circular excavations in clay. Tunnelling and Underground Space Technology 61, 145–149. https://doi.org/10.1016/j.tust.2016.10.005

Goh, A.T.C., 1994. Estimating basal-heave stability for braced excavations in soft clay. Journal of geotechnical engineering 120, 1430–1436.

Goh, A.T.C., Fan, Z., Wengang, Z., Yanmei, Z., Hanlong, L., 2017. A simple estimation model for 3D braced excavation wall deflection. Computers and Geotechnics 83, 106–113. https://doi.org/10.1016/j.compgeo.2016.10.022

Goh, A.T.C., Kulhawy, F.H., 2005. Reliability assessment of serviceability performance of braced retaining walls using a neural network approach. International Journal for Numerical and Analytical Methods in Geomechanics 29, 627–642. https://doi.org/10.1002/nag.432

Goh, A.T.C., Kulhawy, F.H., Wong, K.S., 2008. Reliability assessment of basal-heave stability for braced excavations in clay. Journal of Geotechnical and Geoenvironmental Engineering 134, 145–153. https://doi.org/10.1061/(asce)1090-0241(2008)134:2(145)

Goh, A.T.C., Wong, K.S., Broms, B.B., 1995. Estimation of lateral wall movements in braced excavations using neural networks 1064, 1059–1064.

Goh, A.T.C., Zhang, W.G., Wang, W., Wang, L., Liu, H., Zhang, W., 2019a. Numerical study of the effects of groundwater drawdown on ground settlement for excavation in residual soils. Acta Geotechnica 15, 1259–1272. https://doi.org/10.1007/s11440-019-00843-5

Goh, A.T.C., Zhang, W.G., Wong, K.S., 2019b. Deterministic and reliability analysis of basal heave stability for excavation in spatial variable soils. Computers and Geotechnics 108, 152–160. https://doi.org/10.1016/j.compgeo.2018.12.015

Gordan, B., Jahed Armaghani, D., Hajihassani, M., Monjezi, M., 2016. Prediction of seismic slope stability through combination of particle swarm optimization and neural network. Engineering with Computers 32, 85–97. https://doi.org/10.1007/s00366-015-0400-7

Griffiths, D., Yu, X., 2015. Another look at the stability of slopes with linearly increasing undrained strength. Geotechnique 65, 824–830. https://doi.org/10.1680/geot.14.T.030

Griffiths, D. V., Huang, J., Fenton, G.A., 2009. Influence of spatial variability on slope reliability using 2-D random fields. Journal of Geotechnical and Geoenvironmental Engineering 135, 1367–1378. https://doi.org/10.1061/(asce)gt.1943-5606.0000099

Gu, X., Wang, L., Ou, Q., Zhang, W., 2023. Efficient stochastic analysis of unsaturated slopes subjected to various rainfall intensities and patterns. Geoscience Frontiers 14, 101490. https://doi.org/10.1016/j.gsf.2022.101490

Guo, X., 2020. Etude probabiliste de la stabilité d ' un barrage en remblais. Doctor thesis, Université Grenoble Alpes.

Guo, X., Dias, D., 2020. Kriging based reliability and sensitivity analysis – Application to the stability of an earth dam. Computers and Geotechnics 120, 103411. https://doi.org/10.1016/j.compgeo.2019.103411

Guo, X., Dias, D., Carvajal, C., Peyras, L., Breul, P., 2019a. A comparative study of different reliability methods for high dimensional stochastic problems related to earth dam stability analyses. Engineering Structures 188, 591–602. https://doi.org/10.1016/j.engstruct.2019.03.056

Guo, X., Du, D., Dias, D., 2019b. Reliability analysis of tunnel lining considering soil spatial variability. Engineering Structures 196, 109332. https://doi.org/10.1016/j.engstruct.2019.109332

Hamrouni, A., Dias, D., Sbartai, B., 2019. Probability analysis of shallow circular tunnels in homogeneous soil using the surface response methodology optimized by a genetic algorithm. Tunnelling and Underground Space Technology 86, 22–33. https://doi.org/10.1016/j.tust.2019.01.008

Hashash, Y.M., Whittle, A.J., 1996. Ground movement prediction for deep excavations in soft clay. Journal of geotechnical engineering 122, 474–486.

He, Q., Cao, Z., Tang, F., Gu, M., Zhang, T., 2023. Experimental analysis and machine learning research on tunnel carriage fire spread and temperature evolution. Tunnelling and Underground Space Technology 133, 104940. https://doi.org/10.1016/j.tust.2022.104940

Helton, J.C., Davis, F.J., 2003. Latin hypercube sampling and the propagation of uncertainty in analyses of complex systems. Reliability Engineering and System Safety 81, 23–69. https://doi.org/10.1007/3-540-54029-6_187

Herrmann, L.R., 1978. Finite element analysis of contact problems. Journal of the engineering mechanics division 104, 1043–1057.

Hohenbichler, M., Gollwitzer, S., Kruse, W., Rackwitz, R., 1987. New light on first-and second-order reliability methods. Structural safety 4, 267–284.

Hong, Y., 2012. Ground deformation and base instability of deep excavation in soft clay subjected to hydraulic uplift.

Hong, Y., Ng, C.W.W., 2013. Base stability of multi-propped excavations in soft clay subjected to hydraulic uplift. Canadian Geotechnical Journal 50, 153–164. https://doi.org/10.1139/cgj-2012-0170

Hong, Y., Ng, C.W.W., Liu, G.B., Liu, T., 2015a. Three-dimensional deformation behaviour of a multi-propped excavation at a "greenfield" site at Shanghai soft clay. Tunnelling and Underground Space Technology 45, 249–259. https://doi.org/10.1016/j.tust.2014.09.012

Hong, Y., Ng, C.W.W., Wang, L.Z., 2015b. Initiation and failure mechanism of base instability of excavations in clay triggered by hydraulic uplift. Canadian Geotechnical Journal 52, 599–608. https://doi.org/10.1139/cgj-2013-0343

Hou, C., Zhang, T., Sun, Z., Dias, D., Shang, M., 2019. Seismic analysis of nonhomogeneous slopes with cracks using a discretization kinematic approach. International Journal of Geomechanics 19, 1–14. https://doi.org/10.1061/(ASCE)GM.1943-5622.0001487

Hsi, J.P., Yu, J.B.Y., 2005. Jet grout application for excavation in soft marine clay, in: In Proceedings of the 16th International Conference on Soil Mechanics and Geotechnical Engineering. pp. 1485–1488. https://doi.org/10.3233/978-1-61499-656-9-1485

Hsiao, E.C.L., Kung, G.T.C., Juang, C.H., Schuster, M., 2006. Estimation of wall deflection in braced excavation in clays using artificial neural networks 1–6.

Hsieh, P.G., Ou, C.Y., 1998. Shape of ground surface settlement profiles caused by excavation. Canadian geotechnical journal 35, 1004–1017.

Hsiung, B.C.B., 2009. A case study on the behaviour of a deep excavation in sand. Computers and Geotechnics 36, 665–675. https://doi.org/10.1016/j.compgeo.2008.10.003

Hu, Z., Mansour, R., Olsson, M., Du, X., 2021. Second-order reliability methods: a review and comparative study. Structural and Multidisciplinary Optimization 64, 3233–3263. https://doi.org/10.1007/s00158-021-03013-y

Huang, F.K., Wang, G.S., 2007. ANN-based reliability analysis for deep excavation. EUROCON 2007 - The International Conference on Computer as a Tool 2039–2046. https://doi.org/10.1109/EURCON.2007.4400328

Huang, M., Tang, Z., Yuan, J., 2018. Basal stability analysis of braced excavations with embedded walls in undrained clay using the upper bound theorem. Tunnelling and Underground Space Technology 79, 231–241. https://doi.org/10.1016/j.tust.2018.05.014

Huang, M.S., Zuo-long, D.U., Chun-xia, S.O.N.G., 2011. Effects of inserted depth of wall penetration on basal stability of foundation pits in clay. Chinese Journal of Geotechnical Engineering 33, 1097–1103.

Huang, S.Y., Barbour, S.L., Fredlund, D.G., 1998a. Development and verification of a coefficient of permeability function for a deformable unsaturated soil. Canadian Geotechnical Journal 35, 411–425. https://doi.org/10.1139/cgj-35-3-411

Huang, S.Y., Fredlund, D., Barbour, S., 1998b. Measurement of the coefficient of permeability for a deformable unsaturated soil using a triaxial permeameter. Canadian Geotechnical Journal 35, 426–432.

Iooss, B., Lemaître, P., 2015. A review on Global Sensitivity Analysis methods, in: Uncertainty Management in Simulation-Optimization of Complex Systems: Algorithms and Applications. pp. 101–122. https://doi.org/10.1007/978-1-4899-7547-8

Jan, J.C., Hung, S., Asce, M., Chi, S.Y., Chern, J.C., 2002. Neural Network Forecast Model in deep excavation 16, 59–65.

Jen, L.C., 1998. The Design and Performance of Deep Excavation in Clay. MIT.

Jiang, S.H., Li, D.Q., Zhou, C.B., Zhang, L.M., 2014. Reliability analysis of unsaturated slope considering spatial variability. Rock and Soil Mechanics 35, 2569–2578.

Johari, A., Kalantari, A., 2021. System reliability analysis of soldier-piled excavation in unsaturated soil by combining random finite element and sequential compounding methods. Bulletin of Engineering Geology and the Environment. https://doi.org/10.1007/s10064-020-02022-3

Jun, Y.U., Haiming, C., Jun, Y.U., Haiming, C., Training, A., 2009. Artificial Neural Network ' s Application in Intelligent Prediction of Surface Settlement Induced by Foundation Pit Excavation 303–305. https://doi.org/10.1109/ICICTA.2009.80

Kamien, D.J., 1997. Engineering and design: introduction to probability and reliability methods for use in geotechnical engineering. Engineer Technical Letter.

Keawsawasvong, S., Ukritchon, B., 2019. Undrained basal stability of braced circular excavations in non-homogeneous clays with linear increase of strength with depth. Computers and Geotechnics 115, 103180. https://doi.org/10.1016/j.compgeo.2019.103180

Keawsawasvong, S., Ukritchon, B., 2017. Stability of unsupported conical excavations in non-homogeneous clays. Computers and Geotechnics 81, 125–136. https://doi.org/10.1016/j.compgeo.2016.08.007

Khadija, N., Dias, D., Cuira, F., Chapron, G., 2021. Experimental study of the performance of a 32 m deep excavation in the suburbs of Paris. Géotechnique 1–11. https://doi.org/https://doi.org/10.1680/jgeot.21.00017

Kłosowski, G., Rymarczyk, T., 2022. Monitoring of flood embankments through EIT machine ensemble learning. International Journal of Applied Electromagnetics and Mechanics 1–10.

Koltuk, S., Song, J., Iyisan, R., Azzam, R., 2019. Seepage failure by heave in sheeted excavation pits constructed in stratified cohesionless soils. Frontiers of Structural and Civil Engineering 13, 1415–1431. https://doi.org/10.1007/s11709-019-0565-z

Konda, T., Shahin, H.M., Nakai, T., 2010. Numerical analysis for backside ground deformation behaviour due to braced excavation. IOP Conference Series: Materials Science and Engineering 10. https://doi.org/10.1088/1757-899X/10/1/012010

Krabbenhoft, K., Lyamin, A., Krabbenhoft, J., 2016. OptumG2:theory. Optum.

Krabbenhoft, K., Lyamin, A., Krabbenhoft, J., 2015. Optum computational engineering (OptumG2).

Kucherenko, S., Tarantola, S., Annoni, P., 2012. Estimation of global sensitivity indices for models with dependent variables. Computer Physics Communications 183, 937–946. https://doi.org/10.1016/j.cpc.2011.12.020

Kung, G.T.C., Hsiao, E.C., Juang, C.H., 2007a. Evaluation of a simplified small-strain soil model for analysis of excavation-induced movements. Canadian Geotechnical Journal 736, 726–736. https://doi.org/10.1139/T07-014

Kung, G.T.C., Hsiao, E.C.L., Schuster, M., Juang, C., 2007b. A neural network approach to estimating deflection of diaphragm walls caused by excavation in clays 34, 385–396. https://doi.org/10.1016/j.compgeo.2007.05.007

Kung, G.T.C., Juang, C.H., Hsiao, E.C., Hashash, Y.M., 2007c. Simplified Model for Wall Deflection and Ground-Surface Settlement Caused by Braced Excavation in Clays. Journal of Geotechnical and Geoenvironmental Engineering 0241. https://doi.org/10.1061/(ASCE)1090-0241(2007)133

Kuntz, M., Schlapschi, K.H., Meier, B., Grathwohl, G., 1994. Evaluation of interface parameters in push-out and pull-out tests. Composites 25, 476–481.

Lai, F., Chen, F., Liu, S., Keawsawasvong, S., Shiau, J., 2022. Undrained stability of pit-in-pit braced excavations under hydraulic uplift. Underground Space (China) 7, 1139–1155. https://doi.org/10.1016/j.undsp.2022.04.003

Lam, S.Y., 2010. Ground movements due to excavation in clay: physical and analytical models. University of Cambridge.

Lam, S.Y., Haigh, S.K., Bolton, M.D., 2014. Understanding ground deformation mechanisms for multi-propped excavation in soft clay. Soils and Foundations 54, 296–312. https://doi.org/10.1016/j.sandf.2014.04.005

Le, B.T., Goodey, R.J., Divall, S., 2019. Subsurface ground movements due to circular shaft construction. Soils and Foundations 59, 1160–1171. https://doi.org/10.1016/j.sandf.2019.03.013

Leroueil, S., Le Bihan, J.P., Sebaihi, S., Alicescu, V., 2002. Hydraulic conductivity of compacted tills from northern Quebec. Canadian Geotechnical Journal 39, 1039–1049. https://doi.org/10.1139/t02-062

Leu, S., Lo, H., 2004. Neural-network-based regression model of ground surface settlement induced by deep excavation 13, 279–289. https://doi.org/10.1016/S0926-5805(03)00018-9

Li, C., Zhou, J., Armaghani, D., Li, X., 2021a. Stability analysis of underground mine hard rock pillars via combination of finite difference methods, neural networks, and Monte Carlo simulation techniques. Underground Space (China) 6, 379–395. https://doi.org/10.1016/j.undsp.2020.05.005

Li, C., Zhou, J., Armaghani, D.J., Cao, W., Yagiz, S., 2021b. Stochastic assessment of hard rock pillar stability based on the geological strength index system. Geomechanics and Geophysics for Geo-Energy and Geo-Resources 7, 1–24. https://doi.org/10.1007/s40948-021-00243-8

Li, C., Zhou, J., Dias, D., Gui, Y., 2022a. A Kernel Extreme Learning Machine-Grey Wolf Optimizer (KELM-GWO) Model to Predict Uniaxial Compressive Strength of Rock. Applied Sciences (Switzerland) 12. https://doi.org/10.3390/app12178468

Li, C., Zhou, J., Khandelwal, M., Zhang, X., Monjezi, M., Qiu, Y., 2022b. Natural Resources ResearchSix Novel Hybrid Extreme Learning Machine–Swarm Intelligence Optimization (ELM–SIO) Models for Predicting Backbreak in Open-Pit Blasting. Natural Resources Research 31, 3017–3039. https://doi.org/10.1007/s11053-022-10082-3

Li, H., Kayhanian, M., Harvey, J.T., 2013. Comparative field permeability measurement of permeable pavements using ASTM C1701 and NCAT permeameter methods. Journal of Environmental Management 118, 144–152. https://doi.org/10.1016/j.jenvman.2013.01.016

Li, J.H., Zhou, Y., Zhang, L.L., Tian, Y., Cassidy, M.J., 2016. Random finite element method for spudcan foundations in spatially variable soils. Engineering Geology 205, 146–155.

Liao, W., Ji, J., 2021. Time-dependent reliability analysis of rainfall-induced shallow landslides considering spatial variability of soil permeability. Computers and Geotechnics 129, 103903. https://doi.org/10.1016/j.compgeo.2020.103903

Likitlersuang, S., Surarak, C., Wanatowski, D., Oh, E., Balasubramaniam, A., 2013. Finite element analysis of a deep excavation: A case study from the Bangkok MRT. Soils and Foundations 53, 756–773. https://doi.org/10.1016/j.sandf.2013.08.013

Lin, S., Shen, S., Zhou, A., Xu, Y., 2021. Automation in Construction Risk assessment and management of excavation system based on fuzzy set theory and machine learning methods. Automation in Construction 122, 103490. https://doi.org/10.1016/j.autcon.2020.103490

Liu, G.B., Jiang, R.J., Ng, C.W.W., Hong, Y., 2011. Deformation characteristics of a 38 m deep excavation in soft clay. Canadian Geotechnical Journal 48, 1817–1828. https://doi.org/10.1139/T11-075

Liu, Jinlong, Liu, Jiequn, 2011. Abrupt gush problem of foundation pit considering the influence of shear strength of soil. Advanced Materials Research 168–170, 1586–1589. https://doi.org/10.4028/www.scientific.net/AMR.168-170.1586

Long, M., 2001. A case history of a deep basement in London Clay. Computers and Geotechnics 28, 397–423. https://doi.org/10.1016/S0266-352X(01)00006-4

Lü, Q., Chan, C.L., Low, B.K., 2012. Probabilistic evaluation of ground-support interaction for deep rock excavation using artificial neural network and uniform design. Tunnelling and Underground Space Technology 32, 1–18. https://doi.org/10.1016/j.tust.2012.04.014

Luo, Z., Atamturktur, S., Cai, Y., Juang, C.H., 2012a. Simplified approach for reliability-based design against basal-heave failure in braced excavations considering spatial effect. Journal of Geotechnical and Geoenvironmental Engineering 138, 441–450. https://doi.org/10.1061/(ASCE)GT.1943-5606.0000621

Luo, Z., Atamturktur, S., Cai, Y., Juang, C.H., 2012b. Reliability analysis of basal-heave in a braced excavation in a 2-D random field. Computers and Geotechnics 39, 27–37. https://doi.org/10.1016/j.compgeo.2011.08.005

Luo, Z., Atamturktur, S., Juang, C.H., 2012c. Effect of Spatial Variability on Probability-Based Design of Excavations against Basal-Heave 2876–2884. https://doi.org/10.1061/9780784412121.294

Luo, Z., Atamturktur, S., Juang, C.H., Huang, H., Lin, P., 2011a. Computers and Geotechnics Probability of serviceability failure in a braced excavation in a spatially random field : Fuzzy finite element approach. Computers and Geotechnics 38, 1031–1040. https://doi.org/10.1016/j.compgeo.2011.07.009

Luo, Z., Atamturktur, S., Juang, C.H., Huang, H., Lin, P., 2011b. Probability of serviceability failure in a braced excavation in a spatially random field : Fuzzy finite element approach. Computers and Geotechnics 38, 1031–1040. https://doi.org/10.1016/j.compgeo.2011.07.009

Luo, Z., Das, B.M., 2015. System probabilistic serviceability assessment of braced excavations in clays 00, 1–11. https://doi.org/10.1179/1939787915Y.0000000021

Luo, Z., Hu, B., Wang, Y., Di, H., 2018a. Effect of spatial variability of soft clays on geotechnical design of braced excavations: A case study of Formosa excavation. Computers and Geotechnics 103, 242–253. https://doi.org/10.1016/j.compgeo.2018.07.020

Luo, Z., Li, Y., Zhou, S., Di, H., 2018b. Effects of vertical spatial variability on supported excavations in sands considering multiple geotechnical and structural failure modes. Computers and Geotechnics 95, 16–29. https://doi.org/10.1016/j.compgeo.2017.11.017

Lv, G., He, Y., Wei, B., 2020. Dynamic Stability Analysis of Slope Subjected to Surcharge Load considering Tensile Strength Cut-Off. Mathematical Problems in Engineering 2020. https://doi.org/10.1155/2020/5196303

Mahmoodzadeh, A., Mohammadi, M., Farid Hama Ali, H., Hashim Ibrahim, H. Nariman Abdulhamid, S., Nejati, H.R., 2022. Prediction of safety factors for slope stability: comparison of machine learning techniques. Natural Hazards 111, 1771–1799.

Mana, A.I., Clough, G.W., 1981. Prediction of Movements for Braced Cuts in Clay. Journal of the Geotechnical Engineering Division 107, 759–777.

Marelli, S., Sudret, B., 2018. An active-learning algorithm that combines sparse polynomial chaos expansions and bootstrap for structural reliability analysis. Structural Safety 75, 67–74. https://doi.org/10.1016/j.strusafe.2018.06.003

Marelli, S., Sudret, B., 2014. UQLab: A framework for Uncertainty Quantification in MATLAB. Vulnerability, Uncertainty, Risk ©ASCE 2554–2563.

Marten, S., Bourgeois, E., 2006. Three-dimensional behaviour of a circular excavation in Nantes, France, in: Proceedings of the 5th International Conference of TC 28 of the ISSMGE. pp. 867–872. https://doi.org/10.1007/978-3-319-73568-9_174

McNamara, A.M., Roberts, T.O.L., Morrison, P.R.J., Holmes, G., 2008. Construction of a deep shaft for Crossrail. Proceedings of the Institution of Civil Engineers: Geotechnical Engineering 161, 299–309. https://doi.org/10.1680/geng.2008.161.6.299

Milligan, V., Lo, K.Y., 1970. Observations on some basal failures in sheeted excavations. Canadian Geotechnical Journal 7, 136–144.

Mishra, S., 2004. Sensitivity Analysis with Correlated Inputs - An Environmental Risk Assessment Example.

Mollon, G., Dias, D., Abdul-Hamid Soubra, M.A., 2010. Face Stability Analysis of Circular Tunnels Driven by a Pressurized Shield. Journal of Geotechnical and Geoenvironmental Engineering 136, 215–229. https://doi.org/10.4028/www.scientific.net/AMR.378-379.461

Mollon, G., Phoon, K.K., Dias, D., Soubra, A.-H., 2011. Validation of a New 2D Failure Mechanism for the Stability Analysis of a Pressurized Tunnel Face in a Spatially Varying Sand. Journal of Engineering Mechanics 137, 8–21. https://doi.org/10.1061/41095(365)208

Moore, J.F.A., Longworth, T.I., 1979. Hydraulic uplift of the base of a deep excavation in Oxford Clay. Géotechnique 29, 35–46.

Moormann, C., 2004. Analysis of wall and ground movements due to deep excavations in soft soil based on a new worldwide database. Soils and foundations 44, 87–98.

Moustapha, M., Marelli, S., Sudret, B., 2022. Active learning for structural reliability: Survey, general framework and benchmark. Structural Safety 96, 102174. https://doi.org/10.1016/j.strusafe.2021.102174

Mouyeaux, A., Carvajal, C., Bressolette, P., Peyras, L., Breul, P., Bacconnet, C., 2019a. Probabilistic analysis of pore water pressures of an earth dam using a random finite element approach based on field data. Engineering Geology 259. https://doi.org/10.1016/j.enggeo.2019.105190

Nagy, L., Tabács, A., Huszák, T., Mahler, A., Varga, G., 2013. Comparison of permeability testing methods. 18th International Conference on Soil Mechanics and Geotechnical Engineering: Challenges and Innovations in Geotechnics, ICSMGE 2013 1, 399–402.

Nejjar, K., Dias, D., 2019. Comportement des parois de soutènement dans un contexte exceptionnel (grande profondeur , formations déformables , environnement sensible) Application à la gare Fort d ' Issy - Vanves-Clamart. https://doi.org/10.13140/RG.2.2.31102.33607

Ng, C.W., Simpson, B., Lings, M.L., Nash, D.F., 1998. Numerical analysis of a multi-propped excavation in stiff clay. Canadian Geotechnical Journal 35, 115–130.

Ng, C.W.W., Hong, Y., Liu, G.B., Liu, T., 2012. Ground deformations and soil-structure interaction of a multi-propped excavation in Shanghai soft clays. Geotechnique 62, 907–921. https://doi.org/10.1680/geot.10.P.072

Nguyen, T.S., Likitlersuang, S., 2021. Influence of the Spatial Variability of Soil Shear Strength on Deep Excavation : A Case Study of a Bangkok Underground MRT Station. International Journal of Geomechanics 21, 1–12. https://doi.org/10.1061/(ASCE)GM.1943-5622.0001914

O'Rourke, T.D., 1993. Base stability and ground movement prediction for excavations in soft clay. Thomas Telford, London.

Osman, A.S., Bolton, M.D., 2006. Ground Movement Predictions for Braced Excavations in Undrained Clay. Journal of Geotechnical and Geoenvironmental Engineering 132, 465–477. https://doi.org/10.1061/(asce)1090-0241(2006)132:4(465)

Ou, C.Y., 2006. Deepexcavation:TheoryandPractice. Taylor&Francis, London, UK.

Ou, C.Y., Hsieh, P.G., 2011. A simplified method for predicting ground settlement profiles induced by excavation in soft clay. Computers and Geotechnics 38, 987–997.

Ou, C.Y., Liao, J.T., Lin, H.D., 1998. Performance of diaphragm wall constructed using top-down method. Journal of geotechnical and geoenvironmental engineering 124, 798–808.

Ouzaid, I., Benmebarek, N., Benmebarek, S., 2020. FEM optimisation of seepage control system used for base stability of excavation. Civil Engineering Journal (Iran) 6, 1739–1751. https://doi.org/10.28991/cej-2020-03091579

Pan, Q., Dias, D., 2017. Probabilistic evaluation of tunnel face stability in spatially random soils using sparse polynomial chaos expansion with global sensitivity analysis. Acta Geotechnica 12, 1415–1429. https://doi.org/10.1007/s11440-017-0541-5

Pan, Q., Qu, X., Liu, L., Dias, D., 2020. A sequential sparse polynomial chaos expansion using Bayesian regression for geotechnical reliability estimations. International Journal for Numerical and Analytical Methods in Geomechanics 44, 874–889. https://doi.org/10.1002/nag.3044

Pan, Y., Lee, F.H., 2019. Effect of spatial variability on undrained behaviour of tunnel with improved surroundings, in: 13th International Conference on Applications of Statistics and Probability in Civil Engineering, ICASP 2019. pp. 1–8.

Papaioannou, I., Betz, W., Zwirglmaier, K., Straub, D., 2015. MCMC algorithms for Subset Simulation. Probabilistic Engineering Mechanics 41, 89–103. https://doi.org/10.1016/j.probengmech.2015.06.006

Papaioannou, I., Straub, D., 2012. Reliability updating in geotechnical engineering including spatial variability of soil 44–51.

Paul W, M., Fred H, K., 1982. K0-OCR relationships in soil. ASCE GT6 851–869.

Peck, R.B., 1969. Deep excavations and tunneling in soft ground. Proc. 7th ICSMFE 225–290.

Philipponnat, G., Hubert, B., 2016. Fondations et ouvrages en terre. Eyrolles.

Phoon, K.K., Cao, Z.J., Ji, J., Leung, Y.F., Najjar, S., Shuku, T., Tang, C., Yin, Z.Y., Ikumasa, Y., Ching, J., 2022. Geotechnical uncertainty, modeling, and decision making. Soils and Foundations 62, 101189. https://doi.org/10.1016/j.sandf.2022.101189

Phoon, K.K., Kulhawy, F.H., 1999. Characterization of geotechnical variability. Canadian Geotechnical Journal 36, 612–624. https://doi.org/10.1139/t99-038

Pieczyńska-Kozłowska, J., Vessia, G., 2022. Spatially variable soils affecting geotechnical strip foundation design. Journal of Rock Mechanics and Geotechnical Engineering 14, 886–895. https://doi.org/10.1016/j.jrmge.2021.10.010

Powrie, W., Li, E.S.F., 1991. Finite element analyses of an in situ wall propped at formation level. Geotechnique 41, 499–514.

Qin, C., Chian, S.C., 2018. Seismic bearing capacity of non-uniform soil slopes using discretization-based kinematic analysis considering Rayleigh waves. Soil Dynamics and Earthquake Engineering 109, 23–32. https://doi.org/10.1016/j.soildyn.2018.02.017

Qu, J.L., Liu, G.B., Zhang, J.F., 2002. Study on the ground settlement induced by artesian pressure release at Dongchang road metro station. China Civil Engineering Journal 35, 93–98.

Qu, P., Zhang, L., Zhu, Q., Wu, M., 2023. Probabilistic reliability assessment of twin tunnels considering fluid–solid coupling with physics-guided machine learning. Reliability Engineering & System Safety 231, 109028.

Raj, D., Singh, Y., Kaynia, A.M., 2018. Behavior of Slopes under Multiple Adjacent Footings and Buildings. International Journal of Geomechanics 18, 04018062. https://doi.org/10.1061/(asce)gm.1943-5622.0001142

Richards, D.J., Powrie, W., 1998. Centrifuge model tests on doubly propped embedded retaining walls in overconsolidated kaolin clay. Géotechnique 48, 833–846.

Rosenblatt, F., 1958. The perceptron: A probabilistic model for information storage and organization in the brain. Psychological review 65, 386. https://doi.org/https://doi.org/10.1037/h0042519

Rouainia, M., Ph, D., Elia, G., Ph, D., Panayides, S., Ph, D., Scott, P., Asce, M., 2017. Nonlinear Finite-Element Prediction of the Performance of a Deep Excavation in Boston Blue Clay. Journal of Geotechnical and Geoenvironmental Engineering 143, 1–13. https://doi.org/10.1061/(ASCE)GT.1943-5606.0001650.

Sahin, A.U., 2016. A new parameter estimation procedure for pumping test analysis using a radial basis function collocation method. Environmental Earth Sciences 75, 1–13.

Salazar, F., Morán, R., Toledo, M., Oñate, E., 2017. Data-Based Models for the Prediction of Dam Behaviour: A Review and Some Methodological Considerations. Archives of Computational Methods in Engineering 24, 1–21. https://doi.org/10.1007/s11831-015-9157-9

Sasmal, S.K., Behera, R.N., 2021. Prediction of combined static and cyclic load-induced settlement of shallow strip footing on granular soil using artificial neural network. International Journal of Geotechnical Engineering 15, 834–844. https://doi.org/10.1080/19386362.2018.1557384

Schöbi, R., Sudret, B., Marelli, S., 2017. Rare Event Estimation Using Polynomial-Chaos Kriging. ASCE-ASME Journal of Risk and Uncertainty in Engineering Systems, Part A: Civil Engineering 3, 1–12. https://doi.org/10.1061/ajrua6.0000870

Schöbi, R., Sudret, B., Wiart, J., 2015. Polynomial-Chaos-based Kriging. International Journal for Uncertainty Quantification 5(2).

Schwamb, T., Elshafie, M.Z., Soga, K., Mair, R.J., 2016. Considerations for monitoring of deep circular excavations, in: Proceedings of the Institution of Civil Engineers-Geotechnical Engineering. pp. 477–493.

Schwamb, T., Soga, K., 2015. Case studies of circular shaft construction in London. Geotechnique 65, 604–619. https://doi.org/10.1680/geot.14.P.251

Selmi, M., Kormi, T., Hentati, A., Ali, N.B.H., 2019. Capacity assessment of offshore skirted foundations under HM combined loading using RFEM. Computers and Geotechnics 114, 103148.

Sert, S., Luo, Z., Xiao, J., Gong, W., Juang, C.H., 2016. Probabilistic analysis of responses of cantilever wall-supported excavations in sands considering vertical spatial variability. Computers and Geotechnics 75, 182–191. https://doi.org/10.1016/j.compgeo.2016.02.004

Shen, S.L., Wu, Y.X., Misra, A., 2017. Calculation of head difference at two sides of a cut-off barrier during excavation dewatering. Computers and Geotechnics 91, 192–202. https://doi.org/10.1016/j.compgeo.2017.07.014

Shi, Y.-J., Li, M.-G., Zhang, Y.-Q., Li, J., Wang, J.-H., 2018. Field Investigation and Prediction of Responses of Far-Field Ground and Groundwater to Pumping Artesian Water in Deep Excavations. International Journal of Geomechanics 18, 1–12. https://doi.org/10.1061/(asce)gm.1943-5622.0001252

Shoari Shoar, S.M., Heshmati R, A.A., Salehzadeh, H., 2023. Investigation of Failure Behaviour of Soil Nailed Excavations under Surcharge by Centrifuge Model Test. KSCE Journal of Civil Engineering 27, 66–79.

Siacara, A.T., Napa-García, G.F., Beck, A.T., Futai, M.M., 2022. Reliability analysis of an earth dam in operating conditions using direct coupling. SN Applied Sciences 4. https://doi.org/10.1007/s42452-022-04980-7

Sivakumar Babu, G.L., Murthy, D.S., 2005. Reliability Analysis of Unsaturated Soil Slopes. Journal of Geotechnical and Geoenvironmental Engineering 131, 1423–1428. https://doi.org/10.1061/(asce)1090-0241(2005)131:11(1423)

Sobol, I., 1993. Sensitivity estimates for nonlinear mathematical models. Math Model Comput Exp 407–414.

Sudret, B., 2008. Global sensitivity analysis using polynomial chaos expansions. Reliability Engineering and System Safety 93, 964–979. https://doi.org/10.1016/j.ress.2007.04.002

Sudret, B., Kiureghian, A. Der, 2000. Stochastic Finite Element Methods and Reliability. A State-of-the-Art Report 189.

Sun, Y. yong, 2016. Experimental and theoretical investigation on the stability of deep excavations against confined aquifers in Shanghai, China. KSCE Journal of Civil Engineering 20, 2746–2754. https://doi.org/10.1007/s12205-016-0488-3

Takemura, J., Kondoh, M., Esaki, T., Kouda, M., Kusakabe, O., 1999. Centrifuge model tests on double propped wall excavation in soft clay. Soils and foundations 39, 75–87.

Tan, Y., Wei, B., 2012. Observed Behaviors of a Long and Deep Excavation Constructed by Cut-and-Cover Technique in Shanghai Soft Clay. Journal of Geotechnical and Geoenvironmental Engineering 138, 69–88. https://doi.org/10.1061/(ASCE)GT.1943-5606

Tang, Y., 2011. Probability-based method using RFEM for predicting wall deflection caused by excavation. Journal of Zhejiang University-SCIENCE A 12, 737–746. https://doi.org/10.1631/jzus.A1100016

Tang, Y., Kung, G.T., 2014. Influence of Spatially Varying Soil on Basal Heave Analysis of Braced Excavation. In Vulnerability, Uncertainty, and Risk: Quantification, Mitigation, and Management 2439–2448. https://doi.org/10.1061/9780784413609.245

Tang, Y.G., Kung, G.T.C., 2012. Probabilistic analysis of excavation-induced basal heave-a case study, in: 5th Asian-Pacific Symposium on Structural Reliability and Its Applications. pp. 707–712. https://doi.org/10.3850/978-981-07-2219-7

Tang, Y.G., Kung, G.T.C., 2011. Probabilistic Analysis of Basal Heave in Deep Excavation. GeoRisk 2011: Risk Assessment and Management 217–224.

Tang, Z., 2020. Design and construction of the circular shape shaft using the reverse construction method. E3S Web of Conferences 198, 3–7. https://doi.org/10.1051/e3sconf/202019802011

Taylor, P., Wang, Y., 2013. MCS-based probabilistic design of embedded sheet pile walls. Georisk : Assessment and Management of Risk for Engineered Systems and Geohazards 7, 151–162. https://doi.org/10.1080/17499518.2013.765286

Tedd, P., Chard, B.M., Charles, J.A., Symons, I.F., 1984. Behaviour of a propped embedded retaining wall in stiff clay at Bell Common Tunnel. Géotechnique 34, 513–532.

Terzaghi, K., 1943. Theoretical soil mechanics. John Wiley & Sons, New York (USA).

Tokmachev, M.S., 2018. Modeling of truncated probability distributions. IOP Conference Series: Materials Science and Engineering 441. https://doi.org/10.1088/1757-899X/441/1/012056

Tvedt, L., 1990. Distribution of quadratic forms in normal space— application to structural reliability. Journal of engineering mechanics 116, 1183–1197.

Wang, J., Aldosary, M., Cen, S., Li, C., 2021. Hermite polynomial normal transformation for structural reliability analysis. Engineering Computations (Swansea, Wales) 38, 3193–3218. https://doi.org/10.1108/EC-05-2020-0244

Wang, J.H., Xu, Z.H., Wang, W.D., 2010. Wall and Ground Movements due to Deep Excavations in Shanghai Soft Soils. Journal of Geotechnical and Geoenvironmental Engineering 136, 985–994.

Wang, Z.W., Ng, C.W.W., Liu, G.B., 2005. Characteristics of wall deflections and ground surface settlements in Shanghai. Canadian Geotechnical Journal 42, 1243–1254. https://doi.org/10.1139/T05-056

Wei, X., Zhang, Lulu, Yang, H.Q., Zhang, Limin, Yao, Y.P., 2021. Machine learning for pore-water pressure time-series prediction: Application of recurrent neural networks. Geoscience Frontiers 12, 453–467. https://doi.org/10.1016/j.gsf.2020.04.011

Whitley, D., 1994. A genetic algorithm tutorial. Statistics and Computing 4, 65–85. https://doi.org/10.1007/BF00175354

Wijesinghe, D.R., Dyson, A., You, G., 2022. Development of the scaled boundary finite element method for image-based slope stability analysis. Computers and Geotechnics 143, 104586.

Wong, R.C.K., Kaiser, P.K., 1988. Behaviour of Vertical Shafts: Reevaluation of Model Test Results and Evaluation of Field Measurements. Canadian geotechnical journal 25, 338–352. https://doi.org/10.1139/t88-035

Wu, G., Zhao, H., Zhao, M., 2021. Undrained stability analysis of strip footings lying on circular voids with spatially random soil. Computers and Geotechnics 133, 104072. https://doi.org/10.1016/j.compgeo.2021.104072

Wu, G., Zhao, H., Zhao, M., Xiao, Y., 2020. Undrained seismic bearing capacity of strip footings lying on two-layered slopes. Computers and Geotechnics 122, 103539. https://doi.org/10.1016/j.compgeo.2020.103539

Wu, S.H., Ou, C.Y., Ching, J., 2014. Calibration of model uncertainties in base heave stability for wide excavations in clay. Soils and Foundations 54, 1159–1174. https://doi.org/10.1016/j.sandf.2014.11.010

Wu, S.H., Ou, C.Y., Ching, J., 2011. Reliability based design of base heave stability in wide excavations, in: In Geo-Risk 2011: Risk Assessment and Management. pp. 680–687.

Wu, S.H., Ou, C.Y., Ching, J.Y., Hsein, J.C., 2012. Reliability-Based Design for Basal Heave Stability of Deep Excavations in Spatially Varying Soils. Journal of Geotechnical and Geoenvironmental Engineering 138, 594–603. https://doi.org/10.1061/(asce)gt.1943-5606.0000626

Xiao, Z., Lin, J., Tang, D., 2022. A Numerical Study of Ground Displacement and Stress Conditions of Small and Medium Circular Diaphragm Wall during Excavation 2022.

Xu, C., Chen, Q., Wang, Y., Hu, W., Fang, T., 2016. Dynamic deformation control of retaining structures of a deep excavation. Journal of Performance of Constructed Facilities 30, 04015071.

Xu, C., Gertner, G.Z., 2008. Uncertainty and sensitivity analysis for models with correlated parameters. Reliability Engineering & System Safety 93, 1563–1573.

Xue, Y., Miao, F., Wu, Y., Li, L., Meng, J., 2021. Application of uncertain models of sliding zone on stability analysis for reservoir landslide considering the uncertainty of shear strength parameters. Engineering with Computers 1–20. https://doi.org/10.1007/s00366-021-01446-z

Yang, H.Q., Zhang, L., Li, D.Q., 2018. Efficient method for probabilistic estimation of spatially varied hydraulic properties in a soil slope based on field responses: A Bayesian approach. Computers and Geotechnics 102, 262–272. https://doi.org/10.1016/j.compgeo.2017.11.012

Yang, J.M., Zheng, G., 2009. Classification of seepage failures and opinion to formula for check bursting instability in dewatering. Rock and soil Mechanics 30, 261–264.

Yang, Z., Chen, Y., Azzam, R., Yan, C., 2022. Performance of a top-down excavation in shanghai: case study and numerical exploration. European Journal of Environmental and Civil Engineering 26, 7932–7957. https://doi.org/10.1080/19648189.2021.2013950

Ye-Shuang, X., Xue-Xin, Y., Shui-Long, S., An-Nan, Z., 2019. Experimental investigation on the blocking of groundwater seepage from a waterproof curtain during pumped dewatering in an excavation. Hydrogeology Journal 27, 2659–2672.

Yoo, K., Bacarreza, O., Aliabadi, M.H.F., 2022. A novel multi-fidelity modelling-based framework for reliability-based design optimisation of composite structures. Engineering with Computers 38, 595–608. https://doi.org/10.1007/s00366-020-01084-x

Young, D.K., Ho, E.W.L., 1994. The observational approach to design of a sheet-piled retaining wall. Geotechnique 44, 637–654.

Zapata-Medina, D.G., 2007. Semi-empirical method for designing excavation support systems based on deformation control. University of Kentucky.

Zhang, F., Sun, C., Li, F., 2016. Hydraulic heave stability and deformation of braced excavation affected by confined water in soft soil. Electronic Journal of Geotechnical Engineering 21, 7469–7480.

Zhang, J., Dias, D., An, L., Li, C., 2022. Applying a novel slime mould algorithm-based artificial neural network to predict the settlement of a single footing on a soft soil reinforced by rigid inclusions. Mechanics of Advanced Materials and Structures 1–16. https://doi.org/https://doi.org/10.1080/15376494.2022.2114048

Zhang, M., Zhang, Z., Li, Z., Li, P., 2018. Axisymmetric arc sliding method of basal heave stability analysis for braced circular excavations. Symmetry 10. https://doi.org/10.3390/sym10050179

Zhang, R., Wu, C., Goh, A.C., Thomas, B., Zhang, W., 2021. Estimation of diaphragm wall deflections for deep braced excavation in anisotropic clays using ensemble learning. Geoscience Frontiers 12, 365–373. https://doi.org/10.1016/j.gsf.2020.03.003

Zhang, T., Guo, X., Baroth, J., Dias, D., 2021a. Metamodel-based slope reliability analysis—case of spatially variable soils considering a rotated anisotropy. Geosciences (Switzerland) 11, 1–24. https://doi.org/10.3390/geosciences11110465

Zhang, T., Guo, X., Dias, D., Sun, Z., 2021b. Dynamic probabilistic analysis of non-homogeneous slopes based on a simplified deterministic model. Soil dynamics and earthquake engineering 142. https://doi.org/10.1016/j.soildyn.2020.106563

Zhang, W., 2017. Multivariate Adaptive Regression Splines Approach to Estimate Lateral Wall Deflection Profiles Caused by Braced Excavations in Clays. Geotechnical and Geological Engineering. https://doi.org/10.1007/s10706-017-0397-3

Zhang, W., Goh, A.T.C., 2016. General behavior of braced excavation in Bukit Timah Granite residual soils: A case study. ISSMGE International Journal of Geoengineering Case Histories 3, 190–202.

Zhang, W., Goh, A.T.C., Xuan, F., 2015a. A simple prediction model for wall deflection caused by braced excavation in clays. Computers and Geotechnics 63, 67–72. https://doi.org/10.1016/j.compgeo.2014.09.001

Zhang, W., Goh, A.T.C., Zhang, Y., 2015b. Probabilistic Assessment of Serviceability Limit State of Diaphragm Walls for Braced Excavation in Clays. ASCE-ASME Journal of Risk and Uncertainty in Engineering Systems, Part A: Civil Engineering 1, 06015001. https://doi.org/10.1061/AJRUA6.0000827.

Zhang, W., Goh, A.T.C., Zhang, Y., 2015c. Probabilistic Assessment of Serviceability Limit State of Diaphragm Walls for Braced Excavation in Clays. ASCE-ASME Journal of Risk and Uncertainty in Engineering Systems, Part A: Civil Engineering 1, 06015001. https://doi.org/10.1061/AJRUA6.0000827.

Zhang, W., Wang, W., Zhou, D., Zhang, R., Goh, A., Hou, Z., 2018. Influence of groundwater drawdown on excavation responses – A case history in Bukit Timah granitic residual soils. Journal of Rock Mechanics and Geotechnical Engineering 10, 856–864. https://doi.org/10.1016/j.jrmge.2018.04.006

Zhang, W., Zhang, R., Wang, W., Zhang, F., Teck, A., Goh, C., 2019. A Multivariate Adaptive Regression Splines model for determining horizontal wall deflection envelope for braced excavations in clays. Tunnelling and Underground Space Technology 84, 461–471. https://doi.org/10.1016/j.tust.2018.11.046

Zhang, W., Zhang, Y., Goh, A.T.C., 2017. Multivariate adaptive regression splines for inverse analysis of soil and wall properties in braced excavation. Tunnelling and Underground Space Technology incorporating Trenchless Technology Research 64, 24–33. https://doi.org/10.1016/j.tust.2017.01.009

Zhao, G., Yang, Y., Meng, S., 2020. Failure of circular shaft subjected to hydraulic uplift: Field and numerical investigation. Journal of Central South University 27, 256–266. https://doi.org/10.1007/s11771-020-4293-2

Zhao, H., Liu, W., Guan, H., Fu, C., 2021. Analysis of Diaphragm Wall Deflection Induced by Excavation Based on Machine Learning 2021.

Zhao, W., Du, C., Sun, L., Chen, X., 2019. Field measurements and numerical studies of the behaviour of anchored sheet pile walls constructed with excavating and backfilling procedures. Engineering Geology 259, 105165.

Zhao, W.G., Wang, L., Zhang, Z., 2019. Atom search optimization and its application to solve a hydrogeologic parameter estimation problem. Knowledge-Based Systems 163, 283–304. https://doi.org/10.1016/j.knosys.2018.08.030

Zheng, G., Zeng, C., Diao, Y., Xue, X., 2014. Test and numerical research on wall deflections induced by pre-excavation dewatering. Computers and Geotechnics 62, 244–256. https://doi.org/10.1016/j.compgeo.2014.08.005

Zhou, S., Guo, X., Zhang, Q., Dias, D., Pan, Q., 2020. Influence of a weak layer on the tunnel face stability – Reliability and sensitivity analysis. Computers and Geotechnics 122, 103507. https://doi.org/10.1016/j.compgeo.2020.103507

Zhou, W.H., Mu, Y., Q., H., X., Yang, S., 2018. Reliability-Based Design of Basal Heave Stability for Braced Excavation Using Three Different Methods, in: In Proceedings of the 2nd International Symposium on Asia Urban GeoEngineering. pp. 273–283.

Zhu, D., Griffiths, D., Huang, J., Fenton, G., 2017. Probabilistic stability analyses of undrained slopes with linearly increasing mean strength. Geotechnique 67, 733–746. https://doi.org/10.1680/jgeot.16.P.223